THE UNIVERSITY *of* EDINBURGH

THE UNIVERSITY
of EDINBURGH

Development of microfluidic devices for the separation of blood plasma from capillary samples

Giulia Deiana

This thesis is submitted for the degree of

Doctor of Philosophy

August 2022

Lay Summary

The collection and analysis of blood are at the core of modern clinical investigations. Whenever we are ill and go to the doctor, one or more blood tests will likely be ordered for us. Then, we will need to book another appointment to have the blood drawn and wait a few days for the results to come back. Behind the scenes, our sample is transported to a laboratory where trained specialists use expensive equipment to analyse it and produce meaningful results, which are then communicated to your doctor.

For some analyses, this time consuming testing process can instead be performed on the spot using a portable machine that takes in a small fluid sample, such as a blood droplet taken from a finger-prick, and outputs the results in only a few minutes. Biosensing devices capable of performing clinical tests rapidly and at the site of a patients are called point-of-care devices. We all have seen examples of this in the form of pregnancy or rapid Covid-19 tests and, most notably, glucose meters, which allow diabetes patients to monitor their glucose levels to establish a more effective treatment.

Blood is a complex fluid where cells are suspended in a liquid matrix called plasma. Most blood tests are performed using plasma, as red blood cells contain biological material that can potentially alter the results of a wide range of tests. Therefore, a sample must be gently prepared before it can be used for clinical testing, meaning that the plasma needs to be separated from the cells. However, this process is extremely difficult to perform at the micro-scale due.

The objective of this project was to develop small devices for the filtration of cells from finger-prick sized blood samples $\leq$ 100 µL, which could then be attached to or integrated with a biosensor to create a fully functional point-of-care device. A range of sample preparation devices based on microfiltration were developed using two different rapid prototyping techniques. Each prototype was thoroughly tested and its performance analysed in order to compare the pros and cons of various design features until satisfactory designs were developed. The devices are simple to use, as they require minimal steps for their operation, and are fabricated with affordable equipment and materials. This research proved that low cost, effective sample preparation devices that are simple to manufacture and use can be created using rapid manufacturing methods. The results obtained can help in the development of point-of-care devices that require a pre-treated blood sample for their operation.

Declaration

I declare that this thesis was composed by myself, that the work contained herein is my own except where explicitly stated otherwise in the text, and that this work has not been submitted for any other degree or professional qualification.

Giulia Deiana

Aug 2022

Acknowledgements

I would like to thank my supervisor Dr Stewart Smith for his constant presence and guidance throughout my PhD, and my second supervisor Dr Adam Stokes for helping me overcome significant obstacles in my project with his insight and knowledge. I would also like to thank Dr Filippo Menolascina for helping me define my research path during a difficult time in my project.

I am deeply grateful for the help of Mr Colin Wood and Dr Maciej Parys, who both patiently answered at least a thousand questions and kindly taught me everything I needed to complete the biological side of my project.

Special thanks to Dr Chiara Piccinelli for her invaluable help in setting up a collaboration with the Veterinary School, which was crucial for the completion of my project, and to Dr Paola Cazzini for offering precious guidance on techniques and methods to use for my thesis.

Most importantly, I would like to thank my wonderful partner. Without him and his constant understanding and support I would have never been able to complete this project.

Abstract

Point-of-care devices have the potential to revolutionise healthcare as we know it. Sensing platforms capable of performing clinical tests rapidly and at the site of a patient can facilitate early diagnoses and enable continuous patient care in chronic conditions. This has been clearly demonstrated by glucose monitoring devices, which are now the standard of care for patients with diabetes. However, with the exception of glucose sensors and lateral flow devices such as those used in pregnancy or Covid-19 testing, point-of-care devices are not commonly used in modern medicine. One of the main reasons for this is the difficulty in separating blood cells from plasma, the liquid part of blood, without damaging red blood cells and, consequently, releasing haemoglobin in the plasma. The absence of haemoglobin in plasma samples is a strict requirement for many clinical tests and diagnostic procedures. Microfluidic technologies offer an array of tools for understanding and controlling very small volumes of fluids within microchannels. They are a key part of most lab-on-a-chip and biosensing systems used in point-of-care testing and can be successfully used to gently separate blood cells from plasma, thus preparing a sample for analysis.

The microfluidic devices for sample preparation proposed in the literature often require too many complex manual steps to assemble and use, are poorly analysed, can be ineffective under normal clinical circumstances or are too expensive to produce and commercialise. This research seeks to fill the gap in the literature for thoroughly characterised, low-cost, passive microfiltration devices operated without power or specialist equipment for the separation of good quality blood plasma from red blood cells in undiluted capillary samples $\leq$ 100 µL. Two main rapid manufacturing techniques were used and compared, both of which allow the plasma separation devices to be potentially incorporated into, or expanded to become full point-of-care devices: laser cutting with subsequent bonding of a thermoplastic material and 3D printing, the latter using a plant-based biodegradable material and an affordable printer. Several side studies were carried out to assess the suitability of these methods for the manufacturing of microfluidic device prototypes. All iterations of the devices developed were tested extensively with a wide range of whole blood samples and their performance was evaluated by analysing the percentage of available plasma extracted, the time necessary for extraction and the device failure rate. To determine the quality of the plasma collected and its suitability for clinical testing, its haemoglobin concentrations were measured and compared with the concentrations found in control plasma samples prepared using gold standard techniques.

The laser-cut devices were operated without power or specialist equipment, requiring only a commercial metered device used for the collection of blood from a finger prick to actuate the blood flow in a dead-end filtration setup. The best iterations of these devices could extract on average 54.85% of the available plasma volume from 100 µL

of undiluted whole blood in three minutes, with only 7.89%. failing during the testing process. The high concentrations of haemoglobin found in the plasma, however, made the devices unsuitable for a wide range of diagnostic tests.

The 3D printed devices only required a pipette for their operation, with the best iteration recovering on average 56.88% of the total available plasma from 50 µL whole blood samples in 87 seconds. The quality of the extracted plasma was excellent, with a negligible haemoglobin concentration difference with control samples. The plasma collected using the 3D printed devices was 99.9% pure and was tested for Bovine Respiratory Syncytial Virus assay, with the results showing no discernible difference with control samples. The 3D printed devices are easy to manufacture and assemble, with some iterations being reusable after disinfection owing to their simple snap-fit mechanism. No waiting time is necessary for their operation, as only one step is required for a successful extraction. Their designs are parametric and therefore easily scalable and adjustable to accommodate for different microfilters and pipette tips. The possibility of creating fully 3D printed actuating components to integrate in 3D printed microfluidic devices was also briefly explored.

In summary, this project demonstrated how simple rapid manufacturing techniques can be used to develop low cost, yet functional, microfluidic sample preparation modules that require minimal operational steps while also being easy to manufacture and assemble. The devices can be used by the research community to help with the development of biosensing platforms, as they provide a simple and well tested template that can be easily incorporated in lab-on-a-chip setup.

Contents

Chapter 1

Introduction

1.1 Overview

With the aim of shifting the diagnostic and monitoring process from standard laboratory methods to the hands of patients and healthcare practitioners, point-of-care testing is a fast growing field with an increasing number of applications. The newest advances in microelectronics and microfluidics are paving the way for the development of novel miniaturized medical devices capable of producing clinically significant results in a short time while only requiring small, finger-prick sized samples. Glucose sensors serve as a perfect example of the impact that point-of-care testing can have on disease management. These devices have revolutionized the life of diabetic patients, who are now able to better monitor their condition and establish a more effective treatment plan [1]. This successful approach could potentially be applied to the rapid diagnosis and management of a wide range of conditions.

However, with the exception of glucose sensors and lateral flow devices commonly used in pregnancy and Covid-19 testing, point-of-care devices are not widely adopted in modern medicine. There are several reasons for this: lab-on-a-chip technologies so far have not been able to compare in quality and cost-effectiveness with common laboratory equipment and medical professionals are understandably reluctant to change existing protocols and replace expensive machinery in favour of novel methods, creating an "inertia" that will likely require decades to overcome [2]. One of the main barriers faced by developers of point-of-care technologies is the difficulty in performing sample preparation at the micro-scale [3]. The separation of cells from the liquid part of blood is a strict requirement for many clinical tests and diagnostic procedures, as cellular material can interfere with analytical methods. However, whole blood is a complex matrix and is notoriously difficult to handle in microfluidic platforms [2].

As emerging point-of-care microfluidic devices catch up with laboratory methods in terms of sensitivity, selectivity and reliability, there is a growing need for the development of sample preparation modules that can either be connected or embedded in such devices to extract blood plasma in a fast, safe and automated way [3]. Achieving this functionality would allow raw samples to be loaded directly into lab-on-a-chip platforms, an important step towards creating commercially viable products that can one day become part of everyday life. Despite decades of research, simple solutions still elude us. Proposed devices often require too many complex manual steps to assemble and use, are ineffective under normal clinical circumstances or are too expensive to

produce and commercialise. Many studies also omit the data collected to prove their claims or altogether ignore key parameters used to assess the quality of a separation process, hindering their ability to one day reach medical relevance.

This project aims to address these issues and bring us one step closer to bridging the "world-to-chip" gap by providing a range of sample preparation devices that can potentially be used by researchers to develop fully functional point-of-care testing devices. The devices were thoroughly tested and purposefully kept as simple as possible in design and operation without sacrificing the quality of the output. They can be easily fabricated with rapid manufacturing techniques used to create fully functional lab-on-a-chip platforms, which simplifies their replication in research laboratories. The proposed sample preparation devices can be integrated into future works as modules or used as stand-alone devices where quick plasma separation is required, so that more time and resources can be devoted to the challenging process of designing and testing the sensing components.

In the development of the devices, passive sample preparation methods were found to be particularly attractive as they do not require any external power and can therefore be used in any setting. Out of such methods, microfiltration was selected as the main separation technique for its simplicity and amenability to a passive design. Capillary samples $\leq$100 µL were chosen as target volume for their ease of collection. Design-for-manufacturing and assembly principles were kept in mind during the design process so that the devices could potentially be mass-manufactured using standard techniques, such as injection-moulding, with only minor adaptations.

This chapter will provide an introduction to sample preparation methods in research laboratories and a description of common terminology used in the context of blood plasma separation. A literature review of existing passive microfluidic devices that can perform sample preparation from capillary samples will then be given, with a focus on passive microfiltration techniques. The research aims of this project will then be discussed. Finally, the structure of the thesis will be outlined to help the reader navigate its contents.

1.2 Background

1.2.1 Properties of blood

The collection and analysis of blood are at the core of modern clinical investigations in both humans and animals. As it circulates continuously throughout the body, blood provides an enormous amount of information about the health of a patient [4]. However, separation of plasma or serum from whole blood sample is often necessary in order to minimize interference from compounds present in blood cells during measurement. Despite notable advances in the past decades, microfluidic devices still struggle with sample preparation at the micro-scale due to the difficulty of handling blood in a microfluidic setting [3].

Whole blood is a complex fluid that mainly consists of proteins and cells suspended in a liquid phase. In humans:

- Erythrocytes, or red blood cells (RBC) account for $\sim$ 98% of all blood cells. RBCs have a discoid shape, with a diameter between 6 and 8 µm and a thickness of 1.5–2.5 µm [5]. The reference range for healthy individuals is $3.5 - 5.5 \times 10^6$ per µL in

females and $4.3 - 5.9 \times 10^6$ per µL in males [6]. The volume fraction of RBCs in blood is referred to as haematocrit (Hct or HT). The healthy haematocrit range in females is generally 36–46%, while in males it is 41–53% [6].

- Leukocytes, or white blood cells (WBC), comprise less than 1% of the total blood cell volume and are found at concentrations of $4.5–11 \times 10^3$ per µL [6]. Estimated to be $\sim$ 75% of the total WBC count [7], neutrophils are the most abundant type and have a diameter of 9–15 µm. Lymphocytes are the second most frequent type of WBC, accounting for 20–40% of the total, and also the smallest with a diameter of 9–12 µm. Monocytes, the third most frequent type, are the largest ones with a diameter of 15–25 µm [7]. Finally, the last two types of WBC, the eosinophils and basophils have a diameter of respectively 12–17 µm and 10–14 µm.
- Thrombocytes, or platelets (PLT), make up the remaining $\sim$ 1% of the total cell count. Small and irregularly shaped (2–3 µm [7]), they can be found at a concentration of $150–400 \times 10^3$ per µL of blood and are responsible for the formation of blood clots [6].
- Plasma, the liquid matrix, is what remains after the cells are removed. It contains glucose, lipid particles and key proteins including antibodies, enzymes and hormones. Because clotting proteins are also present, anticoagulants are required for storage [6]. Plasma from which fibrinogen and clotting proteins have been removed is referred to as serum.

Red blood cells aggregate at low shear rates leading to an increase in blood viscosity, while at higher shear rates they tend to deform, disaggregate and float along the direction of the flow. This greatly affects the rheological properties of blood, making it a non-Newtonian, shear-thinning fluid [8].

1.2.2 Sample preparation in clinical and research laboratories

Driven by technological advances, laboratory medicine has seen enormous growth throughout the past century [9]. Modern laboratory testing allows physicians to combine physical examinations and patient history with valuable information from specimen analysis, thus helping in the prevention, diagnosis and treatment of diseases [10]. A wide range of disciplines find their application in clinical laboratories, most notably clinical chemistry, molecular pathology, microbiology, haematology, immunopathology, coagulation and medical microscopy [11, 12]. In each of these fields, sophisticated medical equipment capable of performing complex analyses is now widely available to assist, and often replace, manual labour by trained professionals. Automation enables the processing of a large number of samples in a shorter time while simultaneously minimising human errors and increasing safety levels for the working personnel [13, 14]. Common examples are haematology analysers, which automatically produce a detailed blood count report from a small initial blood sample, and immunoassay systems capable of automatic fluid handling and high throughput over a vast assay menu, which are widely used in clinical chemistry for analyte quantification [15, 16].

Due to the high cost of such equipment, the predominant approach utilised in clinical testing worldwide consists in the centralization of all machinery in specialized laboratories where samples collected in the area are sent for evaluation [16, 17]. Blood extraction is executed using standard phlebotomy techniques and venous blood is preferred to ar-

terial, as it is less painful to collect from the patients and more easily accessible, with volumes collected varying from 0.175 to 5 mL [18]. Because extra-analytical phases (which include sample extraction and transportation) are less automated than their analytical counterparts and present a number of labour-intensive activities, they are more susceptible to errors that carry over to the analytical side and can invalidate test results. Almost 70% of all clinical testing errors are due to problems encountered at the pre-analytical phase, with the most problematic one being haemolysis [14, 19, 13, 20]. The word haemolysis describes the rupturing of the cell membrane of erythrocytes with consequential release of haemoglobin and other cellular components into the plasma. Haemolysis is visible without equipment when free haemoglobin is found in high concentrations, which confers a pink to red hue to the plasma or serum affected [14].

Haemolysed samples are estimated to comprise $\sim 3.3\%$ of all routine samples received by clinical laboratories. Out of these, only 3.2% present *in-vivo* haemolysis, which is confirmed by other concurring clinical parameters [21]. As such, most of the time haemolysis occurs *in-vitro* and is the leading cause of sample rejection, with haemolysed samples accounting for 40–70% of all unsuitable specimens [14]. Haemolysis is a difficult problem to study and address effectively. The sample does not appear visibly compromised until after centrifugation and the process of sample collection, transportation and preparation involves several healthcare professionals employed in different locations, often outside of the laboratory setting [19]. The lack of a unifying training regime and policies to regulate the preparation of blood samples leads to a high variability in sample quality and competence of the personnel at each of the required manual steps has been reported to affect haemolysis levels in clinical samples [22].

The release of intracellular components, including haemoglobin, in the plasma can interfere with laboratory testing in a number of ways [14, 19]:

- Diluting the plasma.
- Falsely increasing the presence of some analytes that are normally present in higher concentration inside erythrocytes ($\geq$ 10-fold), such as potassium, magnesium, phosphate, folate and urea.
- Direct interference of free haemoglobin with analytic reactions or spectrophotometric measurements, especially for tests that require absorption measurements at 415, 540 and 570 nm.

In their study on the impact of haemolysis on the output of two common immunological assay systems, Snyder et al. [23] concluded that 0.060, 0.150, and 0.300 $\mathrm{g\,dL^{-1}}$ of Hgb indicate slight, moderate, and gross haemolysis respectively. Grossly haemolysed samples were found to significantly alter results in a range of tests, including B12, testosterone, cortisol and cardiac markers. According to Lippi et al. [24, 25] values of cell-free haemoglobin above $0.05\,\mathrm{g\,dL^{-1}}$ are likely to interfere with haemolysis-vulnerable tests. A detailed overview of all the test affected by haemolysed samples can be found in Table 1 of the study by Lippi et al. "*Haemolysis: an overview of the leading cause of unsuitable specimens in clinical laboratories*" [14].

To prevent issues arising from haemoglobin presence and maximize the sensitivity, reproducibility and accuracy of the analytical methods used, many laboratory analyses requiring blood specimens are performed on blood serum or plasma instead of whole blood. While in large clinical laboratories sample preparation steps are mostly automated, in small laboratories and research facilities the separation of blood serum or

plasma from whole blood is performed with the following steps:

1. The sample is gently mixed by inverting the blood tube 5–10 times and then spun slowly using a bench-top centrifuge. The acceleration forces used range from 1500 to 3000 g with carefully controlled, gradual acceleration and deceleration phases [19].
2. The red blood cells precipitate to the bottom of the blood tube, while the plasma or serum remains at the top. Between the two there is a layer of white blood cells and platelets deposit called the "buffy coat".
3. The plasma or serum is collected manually with a pipette, taking care not to accidentally disturb the buffy coat or include any of the cells [2].

1.2.3 Point-of-care testing

The International Organization for Standardization (ISO) defines point-of-care testing (PoCT) as "testing that is performed near or at the site of a patient with the result leading to possible change in the care of the patient" [26]. Affordable point-of-care testing devices have the potential to lower the time and costs involved in standard clinical procedures. Having devices that can perform low-cost tests on the spot could allow healthcare practitioners to provide an early therapeutic intervention. Moreover, patients affected by chronic diseases could better self-manage their condition, or provide further data to their physicians to establish an effective treatment [17]. Glucose sensors are a classic example, as they are the most studied and widely available commercial PoC devices and now the standard method of care for diabetic patients worldwide [1]. Their success is largely due to their fast turn-around times, low-cost, portability and user-friendliness. While the first generations of glucose monitors required a finger-prick sized blood sample for their operation, modern versions come in the form of small patches worn in the back of the arm that perform continuous glucose monitoring in interstitial fluids and communicate the results through smartphones. Hybrid closed-loop systems that act as an "artificial pancreas" are also available, where an insulin pump is connected to the continuous glucose monitor to semi-automatically calculate and inject the basal insulin doses according to the glucose measurements, with the user only needing to manually input carbohydrate intake for the day [1]. Tests for infectious diseases are also a fast growing area, particularly due to the recent Covid-19 pandemic and the high demand in developing countries, where mortality due to epidemics is especially high and access to medical care is often insufficient [27].

The PoCT market includes both over the counter products and professional devices used by practitioners and trained staff. Glucose monitoring is expected to maintain the largest market share in 2022 (39%), highlighting its importance and impact on the medical system. Predictions then place blood gas testing in second place (15%), followed by cardiac markers (13%), infectious diseases (8%), pregnancy and fertility tests (5%) and others. The reader is referred to the work of Sachdeva et al. for a complete breakdown of the market predictions for 2022, along with a review of the top companies controlling the *in-vitro* diagnostic market [28].

The World Health Organisation published a comprehensive set of guidelines for the development of portable diagnostic systems for the detection of sexually transmitted diseases in developing countries. According to the guidelines, such devices should be [29, 16]:

- **A**ffordable, so that they are available even in resource-limited environments.
- **S**ensitive and **S**pecific, that is capable of producing clinically relevant results with minimal errors.
- **U**ser-friendly, simple to handle and use with minimal training necessary and few manual steps to be performed by the user.
- **R**apid and robust, with the ability of producing an output in a short time (ideally within an hour) and not require any special care in storage and transport.
- **E**quipment-free, with all components directly integrated in the device itself.
- **D**eliverable to all end users in any settings, including resource-constrained ones.

Point-of-care devices that comply to such guidelines are easier to commercialise and distribute to the general public. Lateral flow and glucose monitoring devices are good examples of this trend, as they can be made ASSURED-compliant with relative ease, although for different reasons. Being usually qualitative instead of quantitative, lateral flow devices benefit from low cost, simplicity of fabrication, assembly and use. Glucose sensors, on the other hand, do offer quantitative results. However, because glucose can be found in high concentrations in the bloodstream, its presence can be quantified using both enzymatic and non-enzymatic electrochemical sensors that take in whole blood directly and produce an output without the need of sample preparation and complex analytical steps [1]. This is not the case for analyses that require lengthy, multi-step protocols for the successful detection and quantification of low concentrations of target analytes. For example, point-of-care immunosensors, which rely on antibodies as recognition molecules for analyte capture, need to be able to perform sample preparation, incubation and washing steps, provide an appropriate storage and solid phase for assay reagents, and integrate a signal detection and processing unit.

1.3 Sample preparation in point-of-care testing

Microfluidics is one of the enabling technologies used to create lab-on-a-chip devices that can be tailored to point-of-care applications. It allows the control and manipulation of fluids constrained in sub-millimeter geometries, so that small amount of reagents and samples (tens of µL) can be handled with precision. Microfluidics for medical diagnostics is a growing field with a wide range of applications, with both academic research and industry endeavouring to overcome current obstacles and develop new products. However, micro-scale plasma separation for point-of-care or lab-on-a-chip devices is a challenging problem due to the complexity of blood and its contents.

Researchers have tried tackling the problem using a wide range of techniques and many can be found in the literature. Passive blood plasma separation methods are based on microscale flow properties and do not require any external force other than fluid pumping. Because of this, they hold great potential for point-of-care testing in resource-limited settings [2]. Sedimentation, microfiltration and cell deviation through hydrodynamic effects fall into this category. Active techniques rely on external forces (acoustic, electric, magnetic and optical) and generally require more complex equipment for their operation. The reader is referred to the reviews by Kersaudy-Kerhoas and Sollier [2], Mielczarek et al. [30] and Tripathi et al. [31] for a comprehensive overview of existing techniques. The rest of this section will review studies detailing passive microfluidic devices capable of processing undiluted, whole blood samples $\leq$300 µL.

1.3.1 Terminology

It is useful to first introduce common terms that will later be used to describe the performance of a sample preparation device.

Haematocrit levels: volume percentage of blood cells in whole blood.

Plasma yield: volume percentage of plasma extracted out of total available plasma

$$y = \frac{e_p \times 100}{t_p} \tag{1.1}$$

where e_p is the extracted plasma volume and t_p is the total plasma volume in the sample. For example, a 100 µL blood sample with 45% haematocrit can have a maximum plasma volume of 55 µL, which corresponds to 100% yield, so a plasma separation device that separated 20 µL would have a yield of 36.4%.

Separation efficiency, or **plasma purity**: describes the percentage of red blood cells from the initial sample found in the plasma after extraction

$$se = \left(1 - \frac{c_p}{c_s}\right) \times 100 \tag{1.2}$$

where c_p and c_s are the number of RBCs in the output plasma and input sample respectively [2, 31]. An ideal device would present 100% separation efficiency, meaning that no cells from the original sample can be detected in the extracted plasma.

Haemoglobin levels: used to determine whether and to which extent haemolysis occurred within a device. Because the lysis of erythrocytes can negatively affect a wide range of assays, an ideal system should not induce any haemolysis.

Sample dilution ratio: volume of blood over total volume of sample and diluent. Dilution should be avoided, as it decreases the clinical relevance of the extracted plasma by lowering the concentration of analytes in the sample [31].

1.3.2 Hydrodynamic effects

Methods based on hydrodynamic effects rely on channel geometry and inertial or biophysical forces to manipulate the path of blood cells in a continuous flow. In the context of sample preparation, this can be used to direct cells through specific areas of a microfluidic device and separate them from the bulk of the plasma.

Tripathi et al. developed and compared different PDMS (polydimethylsiloxane) devices, each with distinct features, to determine the best geometrical parameters for optimal plasma separation through biophysical effects [32]. The group reported that their best chip was capable of clog-free operation in the flow rate range of 0.3 to 0.5 mL/min [33]. At a fixed flow rate of 0.5 $\mathrm{mL\,min^{-1}}$, the separation efficiency of the device was 99.5

± 0.35% for samples up to 42% haematocrit, after which it gradually dropped to 84% for artificially high haematocrit levels (60%). The ratio of output plasma obtained to total input blood volume was between 1% and 6% depending on haematocrit levels, giving a plasma extraction rate between 5 and 30 µL/min for 500 µL input samples. This makes the device unsuitable for capillary blood samples as it would be able to extract only 1 µL of plasma out of a 100 µL initial sample volume. To counter this issue, the residual blood could potentially be recycled into the inlet or daisy chained to multiple devices and the separation process carried out again until the haematocrit of the input blood is too high for successful operation. Tripathi and Agrawal have recently modified this chip so that it could be integrated with additional features to carry out an ELISA-based Covid-19 test, but concluded that more work is necessary to produce a field-ready device [34]. Another device from the same group outputted 100% pure plasma from a 20% haematocrit sample, but when tested with undiluted whole blood its separation efficiency dropped to 80%. The yield was not reported [35]. A similar setup was adopted by another group, where it was integrated with a biosensor to detect dopamine levels in blood [36].

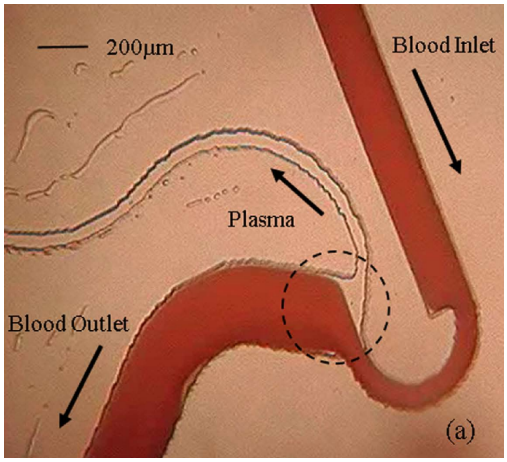

Figure 1.1: Close view of the separation zone of the device developed by Tripathi et al. [32]. The channel is first constricted, then bent and finally expanded again to maximise cell separation under the Zweifach-Fung effect, which describes the phenomenon where particles reaching a bifurcation with different flow rates tend to flow in the channel with higher flow rate. Image reproduced under the Creative Commons Attribution 4.0 International License.

Overall, these methods present significant challenges to their use in point-of-care settings with small capillary samples $\leq 100\,\mu L$ due to their relatively high blood volume requirements, low yield ([37, 32]), frequent need for significant sample dilution and precise fluid control, which is difficult to achieve without expensive microfluidic equipment [38, 35, 39, 40].

1.3.3 Microfiltration

Microfiltration devices rely on either a commercial or inbuilt porous membrane to physically separate plasma from cells. Depending on the configuration of the device and the properties of the membrane used, the input sample volume can go from a few tens of µL to ∼2 mL. In dead-end filtration setups the fluid is placed directly above the membrane, while in cross-flow filtration the fluid flows tangentially upstream of the membrane while the filtrate is extracted downstream. Although haemolysis can be a problem in microfiltration-based devices if excessive pressure is used to drive the

separation, plasma purity is close to 100% unless leakage around the membrane occurs or the blood volume exceeds capacity, leading to membrane damage.

Dead-end filtration

Thorslund et al. developed a disposable, low-cost chip to detect steroid concentration in the low ng/mL range [41]. The device was constructed using two PDMS substrates, the top one containing an inlet and an outlet and the bottom having 40 parallel microchannels converging into a collection channel leading to the outlet. The device can be seen in the left side of figure 1.2. Prior to irreversible bonding of the two substrates, the membrane was cut to a diameter of 13 mm and placed between the microchannels and the inlet. To seal the edges of the membrane, PDMS prepolymer was applied before bonding. Both the membrane and the surface of the device were temporarily activated with oxygen plasma before assembly to render the PDMS surface hydrophilic. The authors tested four different membranes to identify the one with lowest specificity to free and bound testosterone and concluded that a hydrophilic polypropylene filter (Pall Corporation) performed best for both testosterone recovery and blood filtration. The device could process 300 µL of 70–80% diluted blood and produce 100 µL of filtrate, which was manually withdrawn at the collection reservoir. The dilution was necessary to prevent RBC leakage around the membrane. Once assembled, the device had to be used within 30 minutes as the oxidised PDMS surface quickly regained its hydrophobicity, making the separation process noticeably slower after 1 hour and rendering the device unusable after 24 hours.

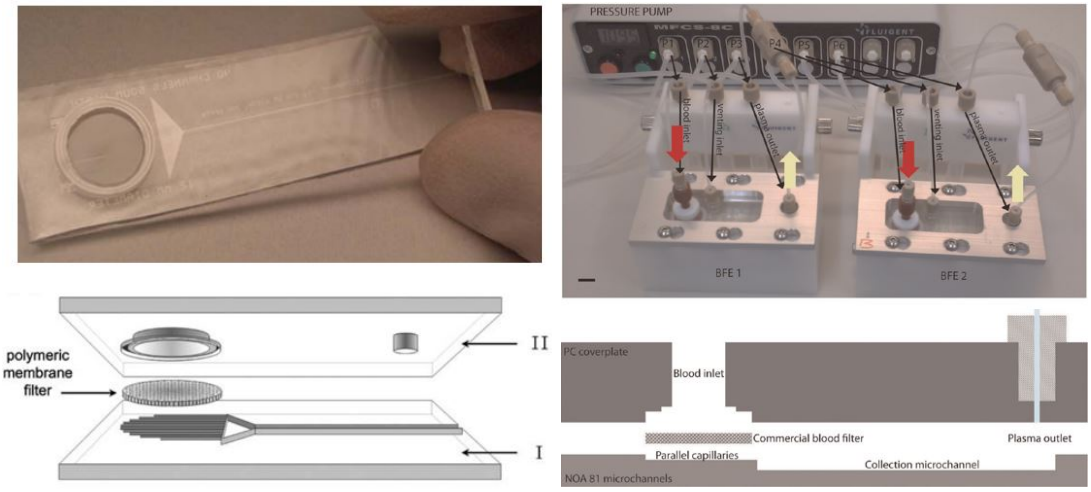

Figure 1.2: Device prototypes and schematics of the dead-end microfiltration devices developed by Thorslund et al. (left, reproduced from ref. [42] with permission from Springer) and Homsy et al. (right, reproduced from ref. [43] with permission from AIP Publishing).

Conversely, the device developed by Homsy et al. did not require any dilution nor plasma activation prior to use [43]. The blood plasma separator (figure 1.2, right) consisted of a polycarbonate cover plate with a blood inlet and plasma outlet, a commercially available plasma separation membrane (Pall Corporation, Vivid^{TM} GR grade filter) cut into a 20 mm diameter circle and a bottom substrate containing microchannels created by soft-embossing of thiolene-based UV-curable adhesive (NOA 81). The latter was selected by the authors because of its long lasting hydrophilicity, particularly when treated with oxygen plasma, and biocompatibility, as well as its ability to be

easily patterned by soft-embossing. The authors determined that haemolysis is likely to happen if blood cells are subjected to shear stress caused by pressures higher than 6.65 kPa, so they limited the pressure applied from a venting inlet to 4 kPa. Although most of the filtration was reported to occur within the first 1–3 minutes, the device was operated for approximately 7 minutes in the experiments and could separate 12 ± 3 µL of plasma from 100 µL of undiluted whole blood. Without the application of external pressure, the collection of the same filtrate volume required over 30 minutes. The authors tested the protein absorption properties of their device by means of interleukins recovery, obtaining rates of 75% for IL6 and IL10 and 37% for IL8, concluding that protein loss can occur to varying degrees within the device during the separation process.

Improving on the conventional flat membrane placement, Hauser et al. developed and patented a device configuration where a commercially available plasma separation membrane is positioned to form a wedge-shaped connection with a capillary channel [44]. The top and bottom parts of the channel were formed by hydrophilic sheets and the sides were defined by double-sided tape, which held the sheets together and connected the membrane to the channel entrance. The favourable angle of the 1 cm^2 membrane allowed the plasma to meet the hydrophilic channel earlier than in a flat configuration, initiating the gradual filling of the 2 mm wide, 100 µm high and 55 mm long channels treated with oxygen plasma for 3 minutes before assembly. A petri dish was used to cover the device during its operation to minimise plasma evaporation. The volume of the extracted plasma was calculated through video evaluation using the software "Tracker". The authors claim that the device could separate a maximum of 21, 18 and 13 µL of plasma from 50 µL samples of undiluted blood with haematocrit values of 35, 45 and 55% respectively. The extraction was reported to occur in less than 10 minutes and haemoglobin levels were ≤ 0.036 g/dL, which indicates low haemolysis within the device. The authors excluded from their analysis any device where blood leakage could be observed visually. A BCA Protein Assay Kit was used to assess protein recovery. The filtrate contained 73% of the protein found in the centrifuged plasma control, a result attributed to absorption at the filter membrane and device material. Although developed for a small sample size, the authors mention that the device could be easily adapted to filtrate larger volume by adding more channels and expanding the membrane surface area.

The device developed by Gao et al. also relied on capillary force to power the extraction of plasma from their microfiltration device [45]. The chip consisted of a Poly(methyl methacrylate) (PMMA) bottom substrate and cover, which were bonded using adhesive tape. The features in both layers were created using a computer numerical control (CNC) milling machine. A commercially available plasma separation membrane (PSM0180-B, Cobetter) was placed in the central gap and secured using a sealing ring constructed using a milled Acrylonitrile butadiene styrene (ABS). The surface of the grooves in the bottom layer was altered to increase its hydrophilicity using a plasma cleaner, with the contact angle (defined in chapter 3, section 3.3.1) decreasing from 77.8° to 37.7°. The hydrophilic channels created by the small gaps between the two layers collected the plasma separated by the membrane by capillary force. A fresh human blood sample was modified to have its haematocrit level in a series of 40, 50 and 60% to assess the haematocrit dependence of the extraction process. The group tested a total of 4 chips for each Hct level and report that the volume of maximum recoverable plasma extracted was 63, 76 and 75% for 40, 50 and 60% Hct samples respectively, with an average yield between them of 71%. The plasma output volume

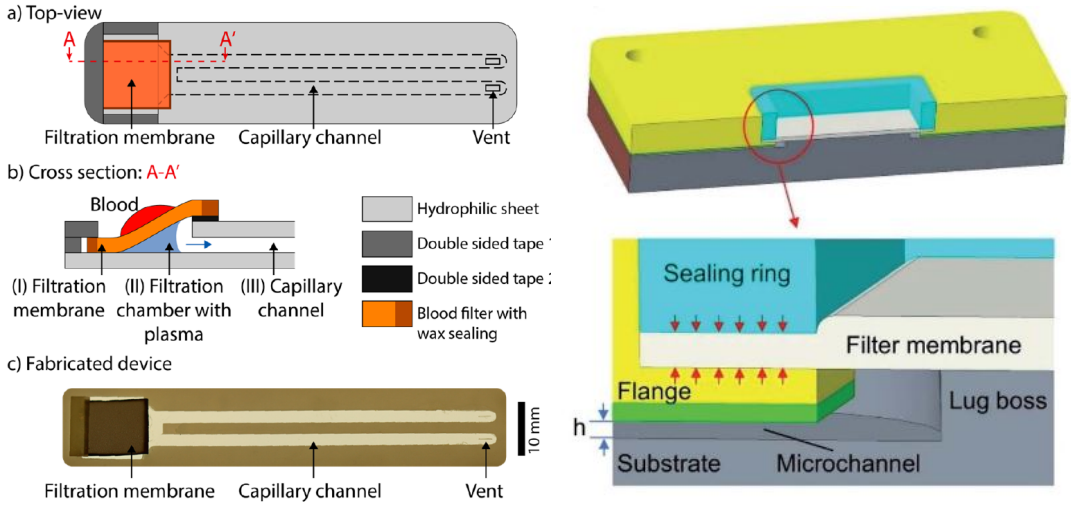

Figure 1.3: On the left, schematic representation of the top view and cross section of the device developed by Hauser et al. (reprinted from [44] with permission from the American Chemical Society). On the right, cross section of the device developed by Gao et al. with a close view of the separation area (image reproduced from ref.[45] with permission from the Royal Society of Chemistry).

was 23 µL for 60 µL samples with 40–50% Hct, which decreased slightly to ∼ 18 µL for 60% Hct samples. The volume of the output plasma was measured via channel imaging and a small 10 µL pipette was used to collect the extracted plasma from the outlets for protein and haemoglobin evaluation. The authors claim that pink fouling in the plasma was not detected upon visual inspection, but then add that the haemoglobin content of the output plasma was measured to be 0.1 g/dL using a haematology analyser (a plasma sample containing 0.1 g/dL Hgb is considered to be grossly haemolysed [23]). The extraction was carried out within 10 minutes of sample insertion. Using gravimetric analysis, the authors concluded that the evaporation rate of the plasma reached 0.3 mL/min when 60 µL blood was placed over the membrane, so the devices were covered with a petri dish during the separation process to lessen the effects of evaporation. Protein recovery was 82.3% for total protein and 77.5% for albumin, the loss due to absorption in the membrane and microchannel walls. The authors noted that although the devices would be cheap to produce in batches, the effect of the hydrophilic treatment starts to significantly fade after 4 days. Once the contact angle returned to its original level, the devices could no longer extract any plasma.

Kim et al. also developed a device powered entirely by capillary force, but without requiring prior plasma activation [46]. The device consisted of a patterned microfluidic base divided in two areas, one hosting the membrane filter and the other a microfluidic channel, each with its own individual cover. The base and both covers were fabricated through polystyrene injection moulding and pressure bonded in the presence of acetone. The filter region contained a pillar array to support the membrane and draw plasma from the filter into the main microfluidic channel. On the sides of the microfluidic channel were sub-micron nano-interstices (NI), which enhanced the wetting capabilities of the main channel by increasing the Young-Laplace pressure at the air-liquid interface, thus driving the flow by capillary action. The main channel was designed to hold 20 µL and the yield was calculated by observing the percentage of the channel filled by the plasma during extraction using a camera. The authors claim that when using a 100 µL

blood sample the channel was filled in 11–16 minutes, meaning that at least 20 µL of plasma could be reliably extracted autonomously by the device. The haematocrit of the sample used for testing was not mentioned, and the authors did not investigate the purity and quality of the plasma or analyte recovery rate for blood testing.

Cross-flow filtration

Dead-end filtration is limited by the volume of blood supported by the membrane. Once the limit is reached, cells start accumulating on the surface of the membrane forming a "cake" layer that leads to a higher plasma flow resistance, increasing the likelihood of haemolysis. A strategy to mitigate this risk is cross-flow filtration, where the blood travels tangentially to a porous membrane sandwiched in between two channels. As the blood flows on the top channel, lift and drag forces move the blood cells towards the centre of the channel where the flow is fastest (a phenomenon commonly observed in blood vessels), hence facilitating the passage of the plasma filtrate across the membrane and its collection in the bottom channel [47].

An example of this method is the device by Aota et al. [47]. Their microchip was fabricated by sandwiching a hydrophilic porous membrane (Cyclopore, Whatman) between two glass plates patterned using a photolithographic wet-etching method to create a microchannel. The surface of the glass plates was modified with octadecyltrichlorosilane and then made hydrophilic by irradiation with UV light in vacuum conditions. The device was assembled by pressing the plates together using stainless-steel holders. The microchannel resistance and flow shear rate were adjusted so that the red blood cells would aggregate towards the centre of the channels, creating a plasma layer that protects the membrane from fouling. The authors claim that the device could separate 68 µL of plasma volume from a 200 µL whole blood sample in 20 minutes, that is 61% of the total available plasma. The haematocrit of the sample was not given, but assumed to be 45%. The plasma collected contained a negligible haemoglobin concentration of 0.000 25 g/dL and was then connected with a micro-ELISA system for C-reactive protein (CRP) analysis.

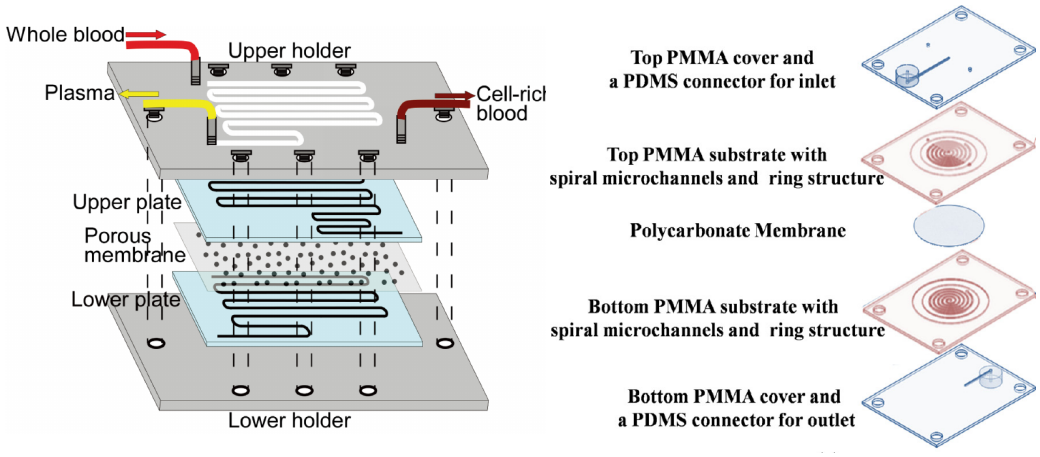

Figure 1.4: Cross-flow plasma separation devices developed by Aota et al. [47] (left) and Chen et al. [48] (right). Both rely on the sandwiching of a membrane between two layers, with the blood flowing tangentially to the membrane in the top layer while the filtrate is collected in the bottom substrate. Images reproduced under a Creative Commons license.

A similar configuration can be observed in the device developed by Aran et al. to

track the concentration of inflammatory biomarkers in blood circulation during cardiac surgery [49]. Although created for large samples well outside the capillary range, this study serves as a good example of the flexibility of microfiltration devices with regards to input sample volume. When connected to an extracorporeal circulatory support (cardiopulmonary bypass or CPB), the authors report that the device could continuously filtrate blood plasma for over 4 hours extracting 2.5 mL of plasma, corresponding to ∼15% of the total plasma volume. The body of the chip consisted of a polycarbonate membrane with 200 nm pore size sandwiched between two PDMS layers, each containing an array of 32 parallel microchannels. The device was connected to a CPB circulation loop primed with 500 mL of fresh human blood diluted to 27–30% haematocrit, which was circulated at a rate of 500 mL/min. The plasma collected was used to perform an immunoassay for the detection of plasma complements and cytokine concentrations. The concentration of haemoglobin was not measured to establish whether or not haemolysis occurred within the device, although the authors claim that the plasma was 100% free of cells and there was no evidence of clogging or cell lysis.

Another example of a cross-flow setup is the plasma separator developed by Chen et al. [48]. The device consisted of four PMMA layers: a top and bottom cover with inlet and outlet connectors and two substrates with micromilled spiral microchannels and a ring structure, between which a polycarbonate membrane (PDC-32G, Harrick Plasma Corp., NY, USA) was placed. The PMMA layers and the membrane were bonded using UV adhesive. To completely seal the gap between membrane and substrates, the adhesive was pipetted in the ring cavity prior to UV irradiation. The study analysed the effect of membrane pore size, haematocrit level and flow rate on plasma separation and haemolysis. The pressure was kept below 50 kPa in all experiments to help prevent cell lysis. No leakage was observed between the layers and the membrane attachment, confirming the effectiveness of the bonding method. The maximum blood volume supported by the device without inducing haemolysis was reported to be 350 µL at 40% haematocrit. The authors compared different flow rates and concluded that the highest separation efficiency occurred at 0.02 mL/min, with the device filtering out 96.86%, 92.51% and 30.12% of WBCs, RBCs and platelets respectively. Out of the membranes tried in the study (5 µm, 2 µm and 1 µm pore size), only the 1 µm was found to be effective in blocking the passage of cells, particularly at higher haematocrit levels. No information on yield, haemoglobin levels or protein absorption was provided.

1.3.4 Pre-filtration methods

Combining other techniques with microfiltration can help remove some of the RBCs from the blood sample prior to filtration, preventing membrane clogging and reducing the risk of haemolysis. Two particularly interesting passive methods are sedimentation and immunological capture. The following section will offer a review of studies that implemented these techniques for blood plasma separation.

Sedimentation-assisted

Sedimentation can be used in conjunction with microfiltration to facilitate the extraction of plasma from undiluted samples. Blood cells have higher density than plasma and tend to slowly sediment through the liquid phase. If undisturbed, they accumulate at the bottom of the device, simplifying the extraction process by limiting the number of cells to filtrate from the plasma itself.

In the device proposed by Liu et al. the membrane (Vivid^{TM} GR) was placed vertically to reduce blockage by red blood cells [50]. The device consisted of two PMMA compartments carved with a CNC milling machine to form a cavity with a micropillar array over which the membrane was placed. The authors aimed to minimise the functional area of the membrane to reduce potential protein absorption in the filter matrix. Held down by double-sided tape, each membrane had a functional area of $\sim 2\,cm^2$ with a combined area of $4\,cm^2$. At the bottom of each compartment was a plasma collection trench of 0.5 mm diameter. Both trenches converged in a conduit leading to a plasma exit port that matched the size of a 200 µL pipette tip used for plasma extraction (figure 1.5). The compartments were solvent-bonded together using acetonitrile and the collection channels were covered by transparent tape. The authors claim that the device separated $275 \pm 35\,\mu L$ of plasma from 1.8 mL of whole blood in 7 minutes. As the haematocrit level of the input sample was not given, it is not possible to calculate the precise yield. Plasma purity was also not assessed. The haemoglobin content of the plasma collected was reported to be $0.35 \pm 0.12\,g/dL$ compared with a centrifuged control of $0.26 \pm 0.09\,g/dL$, which suggests that slight haemolysis took place within the device during the extraction process. To test the protein absorption properties of the device, three independent tests were carried out by spiking blood samples with HIV-1 virus and testing the extracted plasma for recovery efficiency, which was measured to be above 80% in all cases. The authors concluded that the loss of protein might have resulted from non-specific binding to either membrane or device structure.

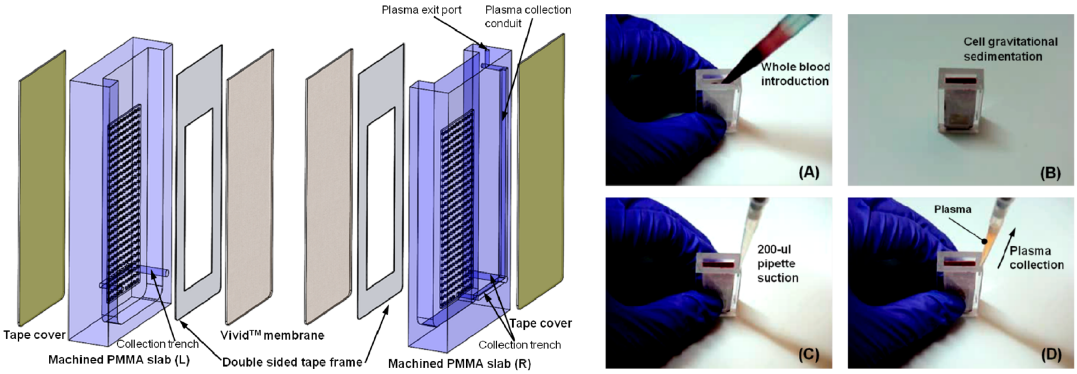

Figure 1.5: Device developed by Liu et al. [50]. On the left is an exploded view of the device, while on the right are its operational steps: whole blood is deposited inside the device (A) and left to sediment for at least 7 minutes (B), after which the plasma can be extracted using a pipette (C and D). Images reprinted from [50] with permission from the American Chemical Society.

Three years later the group developed a new type of device, this time relying on a high sample contact angle to prop the plasma up above the layer of sedimented cells and through a membrane placed above the sample [51]. The 3D printed clamshell-style device consisted of a top cover and bottom substrate treated with a superhydrophobic material (spray-on "Neverwet^{TM}") to reduce loss of target molecules, minimise haemolysis and prevent the spreading of the sandwiched blood. The authors tested the spray, normally sold for coating a variety of objects and clothing, for biomolecular adhesion, blood-clotting time and haemocompatibility, but did not offer a full biocompatibility assessment. Nevertheless, the coating seemed to significantly improve the hydrophobicity of the 3D printed surface, reduce protein loss and prevent blood clotting. To test the devices, the sample was placed in the blood well located in the bottom substrate.

In principle, the high hydrophobicity of the surface ensures that the plasma droplet maintains a high contact angle as blood cells sediment and gather at the bottom of the well. Above the well in the top cover was the membrane, which was fitted on a micropillar array, and an exit port designed to tightly match the tip of a 200 µL pipette. Once the device was closed, the membrane came into contact with the top of the sample, thus filtering plasma with minimal cell content, preventing membrane clogging and haemolysis. The authors report that with this new strategy they were able to decrease the surface area of the membrane by 6.5 times compared to manufacturer guidelines. However, as the membrane grade was not provided, it is not possible to verify this claim. Pall Vivid^{TM} membranes come in GF, GX and GR grades, each with recommended blood volume of 20, 20-30 and 40–50 µL/cm^2 and plasma recovery of ≥60, 60 and 80% respectively [52]. The authors mention a recommended 20 µL/cm^2, suggesting that the filter was of either GF or GX grade. The membrane was cut to 11 mm diameter circles using a laser cutter and surrounded with double-sided adhesive tape before being placed in the device, leaving a 8 mm diameter circle with a 2 cm^2 available surface area for blood filtration, which is about half the recommended size of the GR grade membrane used in their previous device [50]. The authors allowed the sample to sediment for 7-10 minutes before extracting the plasma from the exit port with a pipette. The device separated 65 ± 21.5 µL of plasma from a 200 µL whole sample. The haematocrit level of the sample was not mentioned. The authors instead defined the device yield as:

$$Y = \frac{V_{device}}{V_{centrifugation}} \times 100,$$

that is they compared the plasma volume extracted with the device to the volume collected from a centrifuged sample. This is not standard procedure as it is extremely difficult to extract 100% of the available plasma manually from a spun-down sample. Using this method they reported their device yield to be 70 ± 23% ($n = 10$). Assuming an average 45% haematocrit and a 65 µL output, however, the yield would be 59%. The purity of the plasma was not given. Similarly, haemoglobin levels of the extracted plasma were not mentioned, though the supplementary information contains one graph showing the absorption spectrum of a plasma sample extracted by the device versus the corresponding centrifuged control. While this is not very detailed, it suggests that minimal haemolysis occurred during the extraction process. The devices were tested with blood samples containing variable concentrations of S. *mansoni* genomic DNA to determine the recovery percentage after extraction. The authors reported that the concentration of S. *mansoni* DNA in the filtered plasma was comparable to that of plasma collected by standard centrifugation methods ($> 84.5 \pm 25.8\%$, $n = 3$), meaning that the device material and membrane did not cause significant protein loss.

In a continuation of this work, Kadimisetty et al. modified the 3D-printed clamshell device to become a sample "concentrator" for the rapid detection of HIV in small blood samples of ∼200 µL [53]. As before, the device was pre-treated with the Neverwet^{TM} spray. The membrane was placed in the top substrate of the separation module and held down at the edges by double-sided adhesive. To operate this device, the blood sample was first deposited onto the sample well in the bottom substrate and the clamshell device was closed. A Whatman® FTA® paper disk and a cotton absorbent pad were then inserted in the top substrate above the membrane by means of a 3D printed disk holder with a "twist & lock" mechanism. The paper disk actuated the flow via capillary force by wicking the plasma separated by the Vivid^{TM} membrane. The FTA®

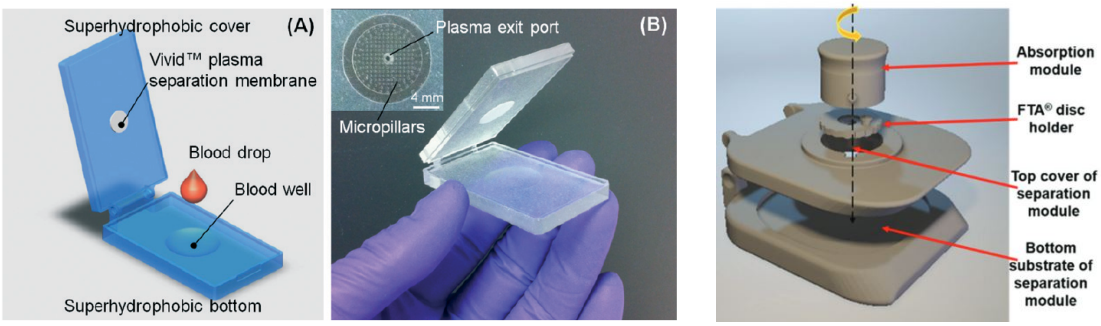

Figure 1.6: Schematic representation (A) and prototype (B) of the 3D printed device developed by Liu et al. [51] (left), along with the sample "concentrator" developed by Kadimisetty et al. [53] (right). The latter uses the same clamshell-style design as the former with the addition of the "twist & lock" absorption module, which self-actuates the plasma flow via capillary action through the FTA® membrane. Images reproduced from ref. [51] and [53] with permission from the Royal Society of Chemistry.

membrane contained chemicals to lyse the membranes of the target virus, leading to the release of nucleic acids that remain entrapped in the cellulose fiber matrix of the membrane. The FTA membrane was kept in the concentrator for approx. 5 min, after which the immobilised nucleic acids were ready for either on-site molecular detection or storage/transportation to a centralized lab at room temperature. The authors experimented with different surface features of the disk holder and reported a significant increase of plasma recovery when a specific pattern was used. They report that their device was able to separate 103 ± 4.4 µL of plasma within 5 minutes, achieving a 94% yield. However, the group did not specify how the extracted plasma volume was measured and did not mention the haematocrit of the sample, instead assuming a standard 45% haematocrit level. No information was given about the purity or the haemoglobin levels of the recovered plasma.

Immunological capture

Su et al. developed a plasma separation device that relied on anti-RBC antibodies immobilized on a glass filter membrane (GFM) to capture RBCs in the sample and facilitate the filtration process [54]. The PMMA cover, channel and support layers were cut to size using a laser cutter and bonded together using double tape and heat pressing. A Vivid™ GR grade filter membrane and the coated GFM were placed between the plates prior to bonding. The gravity-assisted, modular chip is advertised as disposable, low-cost ($2.00–3.00) and simple to use, as it only requires three operational steps. The authors claim that the device could separate 50–70 µL of plasma from 300 µL of undiluted blood in 5 minutes (n = 8) with 100% separation efficiency. The plasma was collected using a pipette. Similarly to previously reviewed studies, the authors did not mention the sample haematocrit and instead compared the device yield with the volume of plasma extracted from a centrifuged control and concluded that the plasma recovery rate was ∼76%. To obtain this value with an average extracted plasma volume of 60 µL, however, the original sample would have needed to have 73.7% haematocrit, which is very far from the normal range [6]. Moreover, assuming an average haematocrit level of 45%, the maximum recoverable plasma volume from a 300 µL sample is 165 µL. With this in mind, 50–70 µL would correspond to 30–42% of the maximum recoverable plasma. To assess the protein recovery properties of the device, the collected plasma was

also analysed for ferritin concentration. When compared to the centrifuged control, the chip recovered 75.48% of ferritin from the input sample, indicating protein absorption within the device, which the authors attributed to changes in the damaged hydrophobic layer of the laser cut PMMA. After cutting or engraving, the contact angle of water was observed to shift from 98.1° to 62.8° . PMMA is generally a hydrophilic polymer with a contact angle of $\sim 68°$ [55]. Changes in wettability properties due to different surface topographies caused by the cutting or engraving of PMMA by CO_2 lasers were also reported in other studies. For example, Waugh and Lawrence [56] observed that 50 µm patterns reduced the contact angle from the material's baseline, while samples with patterns 100 µm or larger increased it to about 90° .

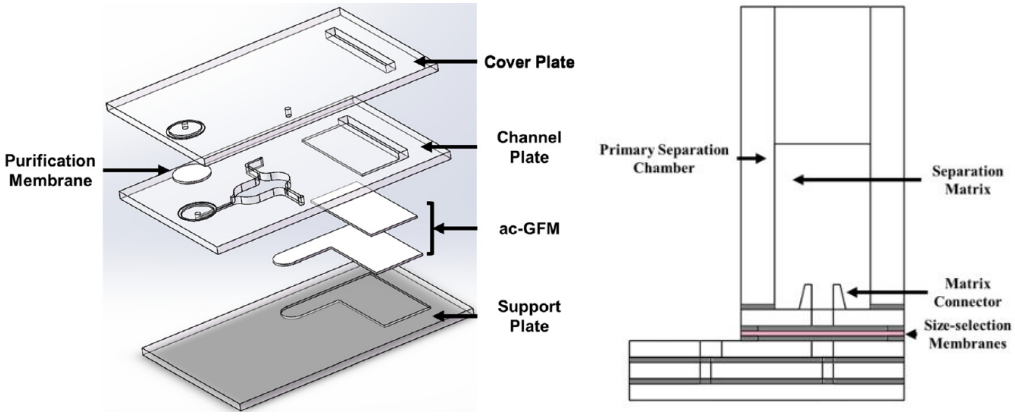

Figure 1.7: On the left is an exploded version of the device developed by Su et al. [54]. A glass filter membrane (ac-GFM) over which anti-RBC antibodies were immobilised was placed between the channel and support plates. The antibodies capture RBCs in the input sample, thus simplify the filtration process through the purification membrane sandwiched between the channel and cover plates. On the right is a schematic representation of the improved device by Su et al. [57] showing the "primary separation" and "purification" chambers assembled together. Images reproduced under a Creative Commons license.

The group then improved on their previous device by developing a new chip that used the same antibody-assisted microfiltration technique in a different configuration [57]. The device comprised two separate components, a "primary separation" and a "purification" chamber. The former consisted of a cylindrical unit containing an acetate fiber pillar coated with anti-RBC antibodies, which could accommodate blood samples up to 400 µL. The purification chamber was fabricated using three laser cut PMMA layers and double-sided tape, which were heat-pressed to reinforce the bonding. This flat PMMA chip contained a channel that connected an 8 mm diameter plasma separation membrane to the outlet. The membrane was placed over the top layer and was held down by double-sided tape. The two chambers were united by means of a connector placed on top of the membrane in the purification chip, which pierced the acetate sheet in the cylindrical chamber with a needle to ensure a tight fit for extraction. To test the devices, first the two chambers were connected, then 400 µL of whole blood was placed in the primary chamber and left there for 5 minutes to allow the antibodies to capture the RBCs. Finally, a 200 µL pipette with matching tip was used to collect the plasma from the outlet. The authors report that the device could separate 131.84 ± 3.4 µL of 99.8% pure plasma from a 400 µL sample with a plasma recovery rate of 97.14 ± 1.13%. They also mention that the samples used were fresh and collected from the researchers and collaborators without manipulation to alter haematocrit level. However, the sample used for testing had haematocrit levels of 65%,

a value much higher than that of an average person [6], meaning that the maximum volume of recoverable plasma was 140 µL. This corresponds almost perfectly to the volume recovered by the authors after centrifugation (136.9 ± 1.6 µL), casting doubt on the haematocrit calculation, for which the methods are not given in the study. The haemoglobin content of the extracted plasma was not mentioned. When compared to centrifuged controls ferritin recovery was ∼87%, indicating a low level of protein absorption in the device. The recovery rate for glucose was 100%.

1.3.5 Creative use of 3D printing in plasma separation

3D printing has recently become a widely available and affordable rapid-manufacturing method. As equipment costs decrease and the quality of the prints improves, 3D printed microfluidic devices are progressively gaining traction in the literature. 3D printing has been used in a number of creative ways to develop new devices for plasma separation. Some of the studies previously described in this chapter featured 3D printed parts within their devices. The following studies rely on a variety of techniques, but are worth reporting for their original approach to the use of 3D printing in the context of sample preparation. For example, Park et al. [58] developed a method to directly 3D print structures onto a plasma separation membrane to create an integrated device for the detection of glucose and potentially other analytes in whole blood. Unfortunately the authors did not include any information on the performance of their plasma separation method.

Kim and Choi [59] relied on 3D printing to develop parts for their "smart pipette", which combines a standard syringe, a 3D printed chamber of fixed volume and a pipette tip to create a system that provides a controllable and stable pressure generation for a predictable and constant flow rate. The smart pipette was used as an actuator to separate plasma from samples of varying haematocrit levels (19 to 53%). The smart pipette was connected to a "microfluidic pipette tip" fabricated in PDMS as a proof of concept, which consisted of a microchannel with ridges that led to the deviation of the cells' trajectory from the fluid streamlines, resulting in the accumulation of cells to one side. The other side, containing a stream of plasma and cells, then went through another grooved channel connected in series with a bifurcation at the end, which allowed a final separation of plasma and cells into different outlets to increase plasma purity. A single run with 1 mL blood volume of a 53% haematocrit sample produced plasma with a purity of 93 ± 0.8%. Depressing the plunger of the smart pipette created a volumetric flow rate within the microfluidic channel of 100.9 ± 7.9 µL min^{-1} after 5 minutes of operation, which led to a yield of 12.3 ± 1.5% with and an extraction rate of 12.1 ± 0.6 µL min^{-1}. The authors claim that the haemoglobin content was comparable to a centrifuged control in absorbance when analysed with a spectrometer.

Vemulapati and Erickson developed a 3D printed "sleeve" designed to enclose a sample collection tube for venous blood containing magnetic beads and an aggregation agent [60]. Within the sleeve are two ball magnets placed in specific chambers. The chamber design allows the magnets to roll in and out of the magnetic field of the beads in the sample tube, creating a side-to-side mixing pattern that increases the overall separation efficiency. During the mixing process, the beads bind to the outside of the cell clump formed by the aggregation agent, therefore separating the cells from the plasma upon exposure to the magnetic field. Once the tube was inserted into the sleeve, it was inverted gently for 8-10 times or 45 seconds, then placed in a magnetic stand for separation. The plasma was then be collected with a pipette without the need for cen-

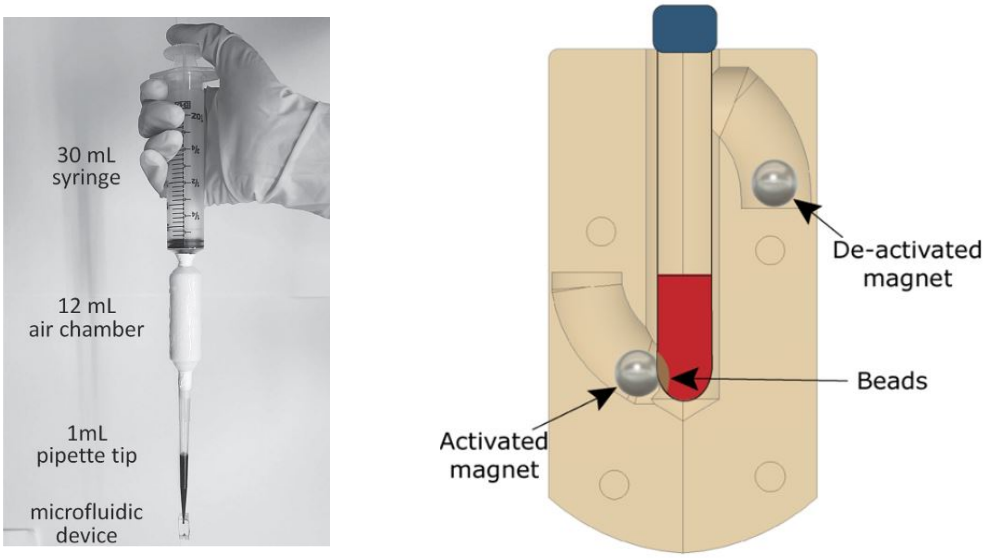

Figure 1.8: "Smart pipette" developed by Kim and Choi (left, reproduced from ref. [59] with permission from John Wiley and Sons) and cross section of the 3D printed "sleeve" by Vemulapati and Erickson (right, reprinted from [60] with permission from the American Chemical Society).

trifugation. The authors report that 76.7 ± 11.5% of the available plasma was collected with the sleeve, against 43.9 ± 13.1% of the sleeve-less inversion using 7 human samples with a normalised haematocrit of 50%. In both cases the sample purity was 99.9%. The authors estimate that the cost for the separation of a 1 mL sample using their methods would be approximately $20-25 due to the cost of the beads and aggregation agent.

1.3.6 Hand-powered centrifugal methods

Lab-on-a-disk systems that use centrifugal forces have been developed to mimic the functionality of centrifuges, but as they often require a power source for their motor they are not optimal in remote and/or resource-poor settings [61, 62]. The following three studies present a rather original approach in transforming common everyday objects into hand-powered centrifugal sample preparation devices.

In 2008, Wong et al. turned an egg beater into a sample preparation centrifuge [63]. The authors purchased an egg beater from a grocery store, then removed one of its two paddles to make space for a 5 cm piece of polyethylene (PE) tubing containing the sample, which was attached to the remaining paddle using adhesive tape (figure 1.9). To fill the tube, a whole blood sample was drawn into the PE tube using a rubber bulb to create a vacuum. The edges of the tube were then melted over a candle and pinched together to create a seal and prevent blood leakage. After centrifugation, scissors or a knife were used to cut the tubing at the interface between plasma and blood cells, so that the plasma could be pushed out of the cut end by squeezing the tube. PE tubing was selected for its safety, ruggedness, transparency and flexibility, which allows it to self-align in a perpendicular direction to the rotational axis during the centrifugation process. The authors report that spinning the handle of the egg beater at a comfortable pace (200 RPM) led to rotational speeds of ∼1200 RPM at the tube connected to the paddle. The farthest edge of the tube, located 12.5 cm away from the axis of rotation, experienced ∼280 g. The separation was completed in around 10

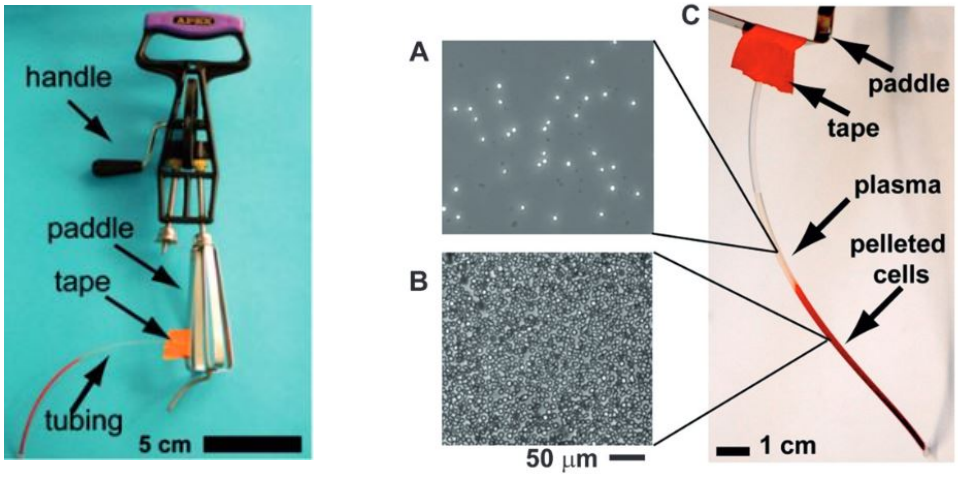

Figure 1.9: Egg beater centrifuge developed by Wong et al. [63]. On the left are the components of the device, showing the store-brought egg beater with one paddle removed and the tubing attached to the other paddle. On the right is a magnified view of the tubing post-centrifugation (C) with phase contrast microscopy images of the residual cells in the separated plasma (A) and in the residual cell portion (B). Reproduced from ref. [63] with permission from the Royal Society of Chemistry.

minutes of continuous spinning and the centrifuge could accommodate up to 20 tubes at once. The authors developed a mathematical model to predict the performance of the centrifuge and concluded that the experimental results closely matched that of the calculations, with a maximum of ∼58 µL of plasma collected from a ∼100 µL sample after 8 min of centrifugation. When the same sample was left to sediment by gravity alone for 4 hours, the authors could only extract ∼27 µL of plasma. The total cell count in the plasma separated by the centrifuge was ∼50000 cells/mL , which the authors claim to be comparable to the density of residual cells in samples spun for 5 minutes at 150 g in standard bench-top centrifuges. No initial sample Hct nor haemoglobin values were given. The plasma collected was then used to perform a cholesterol colorimetric assay in a paper-based platform developed by the authors, who hoped that the method could then be adapted in the future for the detection of infectious diseases in low-resource countries.

Brown et al. turned a salad spinner into a hand-powered haematocrit centrifuge specifically designed to provide an easy reading of haematocrit levels in a sample, rather than separate plasma for further use [64]. The centrifuge was constructed by glueing combs across two tiers to form five "racks" where small samples (14 µL) collected in micro-capillary tubes could be secured. The equipment cost 35$ in total and the rack system allows the simultaneous processing of up to 30 samples. In case of spillage, the plastic surfaces could be sanitised easily suing a 10% bleach solution. The authors used a commercially available haematocrit centrifuge as control (ZIPocrit, LW Scientific Inc.). The authors made sure to test the intra-variability of RPM based on user-performance by recruiting 10 different operators and asking them to run the centrifuge for 10 minutes at a rate of 120 "pushes" per minute, using a metronome as reference. At this rate, the centrifuge had an average RPM of 602 (400–730 range) and 31 g, while the ZIPocrit operated at 11000 RPM and 4370 g. Because of this, the salad spinner centrifuge did not pack the cells as effectively as the control, leading to an haematocrit reading 14% higher than the ZIPocrit. Fortunately for the authors, this difference appeared to be

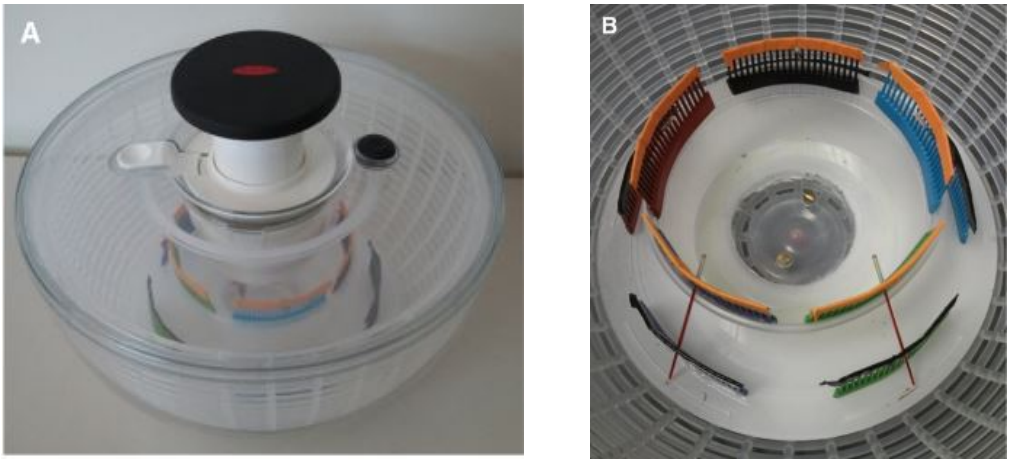

Figure 1.10: Hand-powered centrifuge based on a salad spinner developed by Brown et al. [64]. (A) Overview of the device. (B) Internal rack consisting of combs glued to the main body of the salad spinner with two samples inserted for reference. Images reproduced with permission from The American journal of tropical medicine and hygiene.

consistent across all haematocrit levels, so their solution was to adapt the reading card offered by the ZIPocrit centrifuge to their system in order to obtain the correct reading. The authors conclude that further assessment is necessary regarding durability, user-friendliness and design scalability.

Last but not least is the "paperfuge", a hand-powered centrifuge developed by Bhamla et al. [65]. The authors wanted to address the low RPMs of the previous two studies, claiming that the low rotational speed made for too slow a separation. Their device was reportedly extremely low-cost (< 20 USD cents), lightweight (2 g) and easy to use. The design was inspired by whirligig (or buzzer) toys. The centrifuge was fabricated using paper, but the authors claim that other materials, including 3D printed plastics, can also be used, though they can lower the maximum rotational speed. The device comprises two disks held together by velcro with 40 mm long blood-filled plastic capillaries (ends filled with epoxy) sandwiched in between and two strings passing through the disks. The operational steps of the devices are described in figure 1.11. The centrifuge could achieve speeds of 125000 RPM (30000 g) and separate 8 µL of 100% pure plasma from 20 µL of whole blood in less than 1.5 minutes. The authors conducted 50 trials with two operators using the same sample and the paperfuge had an average haematocrit of 43% against 47% measured by a commercial centrifuge used as control (Critspin, Beckam Coulter). The paperfuge was operated for 1.5 minutes at a maximum speed of ∼20000 RPM (∼ 10000 g), while the Critspin at 16000 RPM (13700 g) for 2 minutes. There was no mention of the original haematocrit value of the sample. Similarly, no haemoglobin values of the extracted plasma were given. High rotational speeds, combined with the difficulty in controlling acceleration and deceleration by hand, have the potential to greatly increase haemolysis rates compared to standard methods, which are purposefully gentle and controlled. As such, it is therefore not clear whether this device can produce plasma with low haemolysis.

1.3.7 Summary

Table 1.1 offers a detailed overview of the studies reviewed with regards to the main criteria used to assess the performance of a plasma separation device. Key parameters

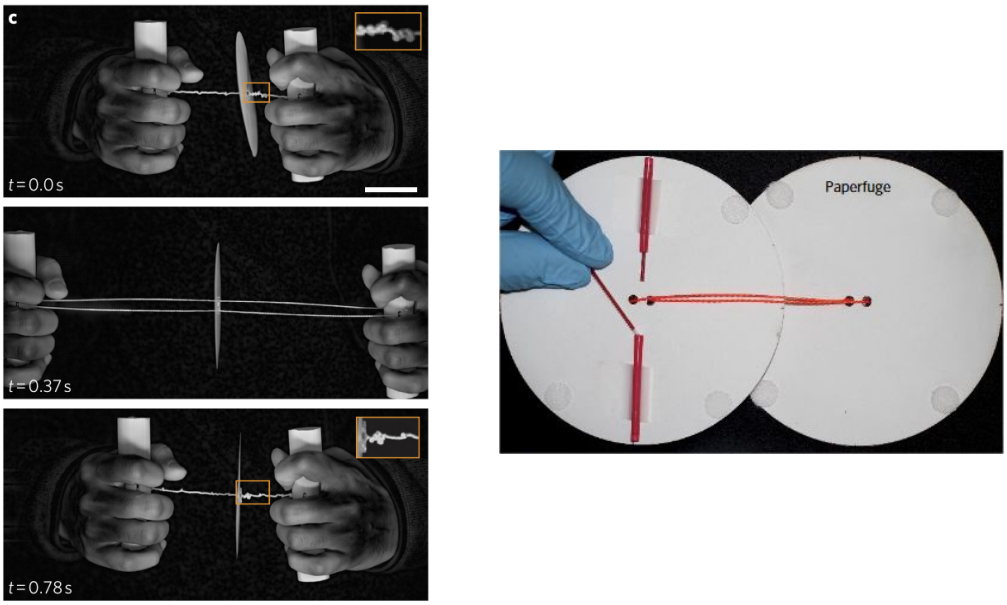

Figure 1.11: "Paperfuge" developed by Bhamla et al. [65]. On the left is a visual description of the device operation: pulling the handles causes the strings to twist and initiates the spinning of the central disks. The image on the right shows the disks loaded with two blood samples, ready to be joined together through the white velcro pads. Reproduced from ref. [65] with permission from Springer Nature.

used to assess the quality of the separation process were missing in most studies, while some omitted the steps used to obtain data presented. Another notable factor is the extraction time, which exceeded five minutes in all devices reviewed.

Table 1.1: Comparison between microfiltration studies described in the literature review. The symbol - indicates that the information was not provided by the authors, while the * symbol means that calculation was not explained in the study.

Study	Sample volume (µL)	Filtrate volume (µL)	Hct (%)	Yield (%)	Purity	Hgb (g/dL)	Dilution	Extraction time (min)	Materials	Biological validation or protein recovery
[42]	300	100	-	-	-	-	70-80%	-	Plasma treated PDMS	Yes
[43]	100	12	-	-	-	-	None	7	Polycarbonate + UV-curable adhesive	Yes
[44]	50	18	45	66	Visual inspection	0.036	None	$\leq$10	Hydrophilic sheets + tape	Yes
[45]	60	23, 23, 18	40, 50, 60	71	-	0.1	None	$\leq$10	PMMA + tape	Yes
[46]	100	20	-	36	-	-	None	16	Polystyrene	No
[47]	200	68	45	61	-	0.00025	None	20	Glass	Yes
[48]	350	-	40	-	95	-	None	-	PMMA + UV adhesive	No
[50]	1800	275 $\pm$ 35	-	-	-	0.35 $\pm$ 0.12	None	7	PMMA + tape	Yes
[51]	200	65 $\pm$ 21.5	-	70 $\pm$ 23*	-	-	None	7-10	3D printed (resin)	Yes
[53]	200	103 $\pm$ 4.4	-	94*	-	-	None	5	3D printed (resin)	Yes
[54]	300	50-70	-	76*	100	-	None	5	PMMA + tape	Yes
[57]	400	131.84 $\pm$ 3.4	65	97.14 $\pm$ 1.13	99.8	-	None	5	PMMA + tape	Yes

1.4 Research aims

As explained in section 1.3.7, there still is a need for comprehensive studies that thoroughly address all the issues in sample preparation for point-of-care-testing. Most methods proposed in the literature often give incomplete or conflicting details of their sample preparation process and the results, use complex methods in assembly and/or usage, and are difficult to mass manufacture as they require manual steps that cannot be automated. Commercial solutions such as disk filters and microfluidic chips [66] are available, but they are expensive and cannot be easily customised, integrated or expanded to become a full lab-on-a-chip system.

With the absolute lack of a simple, low-cost alternative in the literature, the following question springs to mind: is the added complexity of most proposed devices worth it? How do they compare against an extremely simple, no frills type of sample preparation device?

Keeping this in mind, the aim of this research was twofold:

1. To develop successful prototypes of low-cost plasma separation modules that can be fabricated and operated with minimal equipment in low resource environments and have the potential to be incorporated into or expanded to become a full point-of-care device.
2. To offer a comprehensive characterisation of such devices that thoroughly addresses all the issues in sample preparation for point-of-care-testing.

The target objectives were:

- High yield: extract at least 50% of the total available plasma.
- Low Hgb levels, which indicate minimal or no haemolysis occurred during the separation process. The concentration of free haemoglobin in the extracted plasma should not exceed $0.05\,\mathrm{g\,dL^{-1}}$ so that the plasma can be used for haemolysis-vulnerable tests as explained in section 1.2.2.
- High plasma purity $\geq 99\%$, which indicates that no residual cells from the original sample are found in the extracted plasma.
- Quick extraction, within 3 minutes.
- Easy to operate devices without complex steps for the user to follow.
- Low cost (below £1 per piece) and fabrication complexity to make the device amenable to mass manufacturing.

These objective were all met in the last iterations of the devices developed. The proof-of-concept devices were kept as simple as possible to lower expenses and increase reproducibility while retaining excellent usability and performance. Design for manufacturing and assembly principles were kept in mind during the development process, particularly in the last generations, and the devices covered as many of the WHO's ASSURED criteria as possible. Two rapid prototyping techniques, PMMA laser cutting and bonding and 3D printing, were chosen for their ability to create low-cost, full prototypes of point-of-care microfluidic devices. Each will be thoroughly discussed in independent chapters, along with the devices developed and their performance across all sample preparation parameters.

1.5 Structural outline

This thesis is divided into eight chapters.

Chapter 1 introduces the background and terminology necessary for the understanding of the thesis content. A critical review of the relevant literature is then provided, along with a discussion of the research aims of this project.

Chapter 2 describes the materials and equipment used for the fabrication of the devices developed throughout the project.

Chapter 3 provides a thorough description of the experimental methods used during the testing of the devices, along with side studies necessary to establish the correct parameters for the manufacturing procedures.

Chapter 4 describes the development, prototyping and testing of laser-cut PMMA devices.

Chapter 5 offers an analysis of the capabilities of the 3D printer used throughout this project, with an assessment of its suitability for creating microfiltration-based plasma separation devices. The concept of snap-fit mechanisms for device assembly is then introduced, along with the assembly mechanisms that are then used in the development of 3D printed devices. The first attempts at creating 3D printed microfiltration devices are then described in detail.

Chapter 6 describes the development, assembly and testing process of "bonded" 3D printed devices. The Chapter also contains the results of the immunoassay tests performed using the plasma extracted with the devices, along with details on the development and testing of 3D printed devices that resemble the laser-cut PMMA devices.

Chapter 7 describes the development, assembly and testing process of lock-based and locator-based snap-fit 3D printed devices. Different designs are outlined and compared. An analysis on the effect of input sample quality on the device performance is given towards the end of the Chapter.

Chapter 8 discusses additional work not directly related to sample preparation, such as the potential to incorporate integrated 3D printed components into the plasma separation devices (air-tight reservoirs, actuators and valves).

Chapter 9 contains a summary and concluding thoughts on the project and a discussion on future work that could not be completed due to time and laboratory constraints. Interesting potential developments for the devices created throughout the study are also mentioned.

1.6 Publications

The following conference paper described the development and testing process of the PMMA devices:

G. Deiana, A. J. Conde, C. McCarthy, J. Dear, S. Smith, and M. Kersaudy-Kerhoas, 'MICROFLUIDIC DEVICE FOR THE SEPARATION OF BLOOD PLASMA FROM CAPILLARY SAMPLES', presented at the Miniaturized Systems for Chemistry and Life Sciences (µTAS 2019), Oct. 2019. Available online here. The full publication can be seen in appendix D.

Another publication is being prepared describing the development and testing of the 3D printed devices.

Chapter 2

Fabrication Methods

2.1 PMMA devices

2.1.1 Fabrication process overview

Poly(methyl methacrylate) (PMMA) is a biocompatible, optically clear and low cost polymer. As it can be processed using a wide range of techniques that are relatively inexpensive when compared to cleanroom methods used for silicon-based materials, PMMA is particularly suitable for the production of single-use, disposable biomedical microfluidic devices [67]. The PMMA devices developed in this study consisted of separate layers cut to shape using a laser cutter and bonded together with a polysulfone plasma separation membrane (Vivid™ GR, Pall) sandwiched in between. The fabrication steps, described in detail in this section, are listed below:

1. Design of individual PMMA layers.
2. Laser ablation/cutting of layers and membranes.
3. Layer cleaning with optional surface modification.
4. Layer bonding.
5. Device drying prior to use.

2.1.2 Layer design

The individual layers of each device were drawn using a computer-aided design (CAD) software AutoCAD 2019 (Autodesk) in 2D mode. The files were exported as dxf files and then imported into the software used to operate the laser cutter, CorelDRAW Graphics Suite 2013 (Corel Corporation).

2.1.3 Laser ablation procedure

Lasers are commonly used for machining operations due to their ability to selectively etch a material with high precision and speed. Laser cutters operate by focusing a high-powered laser beam onto a substrate. Depending on the reflectivity of its surface, the diameter of the focused beam and the laser power intensity, the material experiences local melting and vaporisation as it partially absorbs the beam of energy [68]. Using

this method, precise patterns drawn using compatible software can be converted to laser paths and then transferred onto a substrate.

The laser cutter used in this study (Epilog Legend Mini 18) was equipped with a 30 W laser. The pulse frequency was set at 2500 Hz. A higher laser resolution directly translates to more detailed engravings at the expense of cutting time. Because microfluidic chips rely heavily on fidelity to the original design, the resolution was kept fixed at the highest setting (1200 DPI) throughout this study. A 1.5 inch focal lens, recommended by the manufacturer to produce smaller cuts and engraving finer details at resolutions $>$ 600 DPI, was used to focus the laser on the target surface.

The laser cutter could be operated in vector (cut), raster (engraving) or combined mode. In vector mode the laser cutter performed a cut by tracing an input vector with the laser. In raster mode the input was a bitmap image file, which contained information about the area to be engraved in the form of a resolution-dependent matrix of pixels. The laser then engraved the area line by line to form the desired pattern. In combined mode, vector and raster cuts were performed automatically one after the other. The depth and width of each cut were dependent on the power/speed setting which were inputted as percentage of the maximum value, 30 W for power and 2.032 m/s for speed (information provided by the manufacturer). To prevent PMMA warping (and fires!) due to excessive heat generated by the laser, suitable parameters relative to substrate thickness needed to be used. Table 2.1 shows the settings adopted in this study, which were partly a result of trial and error and recommendations from experienced lab members. Repeating the cut twice rather than changing the settings (i.e increase the power used or decrease the speed) produced a neater cut and minimised warping. The engravings in raster mode were performed using the "stucki" setting. The parameters necessary to achieve a desired depth were determined empirically using the procedure described in detail in chapter 3, section 3.2.

Table 2.1: Laser cutter parameters (power, speed and number of times the cut needed to be repeated) used to process PMMA of different thickness varying from 0.2 to 3 mm.

Layer thickness (mm)	**Power (% of total)**	**Speed (% of total)**	**Number of repetitions**
0.2	20	14	1
0.3	60	60	1
0.5	60	70	1
1	30	40	2
2	30	80	2
3	25	85	2

Membrane description and cutting parameters

The membrane of choice throughout the project was the Vivid^{TM} GR, an asymmetric polysulfone membrane developed by Pall Corporation. The pore size at the upstream surface is approximately 100 µm and shrinks progressively to around 2 µm at the downstream surface [50]. This asymmetric structure helps trap red blood cells while preventing excessive haemolysis. The membrane can handle human blood volumes up to 40-50 µL cm^{-2} with a plasma recovery rate above 80% in under 2 minutes. A number of studies in the literature adopted this membrane with good results, confirming its

capability to extract a high percentage of available plasma with low haemolysis and low protein binding.

The membrane was supplied in rectangular sheets by the manufacturer and was cut to the desired shape using the laser settings of 20% speed and 7% power.

2.1.4 PMMA cleaning and surface modification

After cutting, the layers were sprayed with ethanol and carefully wiped with cleanroom paper to remove fabrication debris and dust particles. Engraved areas were scrubbed with a cotton swab to further remove melted plastic residues trapped on the rough surface. Any surface modification attempts, as described in chapter 3, section 3.3, were made at this stage.

2.1.5 Layer bonding

The blood plasma separation devices were designed to be actuated with the Minivette® (Sarstedt), a commercially available device for the collection of capillary blood. For a successful operation creation of a pressure differential between inlet and outlet, the main body of the device had to be airtight. As such, any technique used for bonding the device layers had to satisfy this strict requirement. With the available laboratory equipment, the most consistent and successful results were obtained using an optimised ethanol-assisted thermal bonding method described in detail by Liga et al. [69]. Plastics are solid at low temperatures. However, as the temperature increases, the internal molecular motion increases until suddenly, within a few degrees of change, the molecules start moving past each other. This compromises the structure of the material, which becomes more pliable and flexible. The temperature at which this phenomenon occurs is referred to as the glass transition temperature (T_g) [70]. In thermal bonding methods, the PMMA substrates are pressed together and heated above the T_g of the material. As the PMMA melts at the interface between the substrates, the polymer chains intertwine to form a permanent bond [69].

However, at temperatures above its T_g, which is around 105°C depending on the exact composition of the PMMA [71], both the substrate and the features etched into it can experience significant distortion. To minimise warping, the T_g of the thermoplastic material can be decreased using plasticisers, substances that when incorporated into a polymer increase its pliability by reducing the cohesive intermolecular forces in the polymer chains [71]. This enables bonding at a plasticiser-treated surface without allowing the internal regions to reach the glass transition temperature and thus experience distortion. Among all possible solvents, absolute ethanol ($>$ 99.95 %w, Sigma-Aldrich) was chosen for its non-toxicity, low cost and ability to enable bonding at a temperature of 70°C, which is significantly below the T_g of PMMA [69].

The cleaned device layers were stacked on top of each other in the correct order inside custom-made aluminium alignment plates as shown in figure 2.1. The size of the device was therefore restricted by the pins of the plates, which could only accommodate one PMMA piece of dimensions 76.5 × 56.8 mm or two 76.5 × 25.4 mm (the size of a microscope slide) PMMA pieces placed side by side. The top of each layer was lightly sprayed with ethanol before adding the next to ensure a uniform distribution of the solvent and avoid dry patches. Depending on the number of layers, the total amount of ethanol used varied between 50 and 100 µL. As ethanol evaporates rapidly, the process had to be executed as quickly as possible. It was important to not use excessive

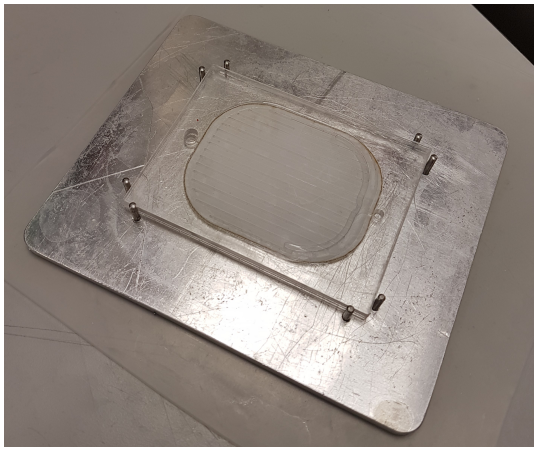

Figure 2.1: Example of a PMMA device placed on the bottom alignment plate with pins. The rig was custom made for this particular application. A range of pins of different lengths was available in order to process devices of various heights, and rubber mats were used above and below the rig to protect the hot press during operation. Up to two microscope-slide devices could be fitted in the area described by the metal pins at one time.

amounts of ethanol, as it was observed that excessive amounts between the layers led to an excess of residual melted material inside the microchannels in the finished device, which often led to clogging during their operation. This issue was particularly evident when the channels were prepared by engraving on the PMMA surface rather than cutting them through the piece. No solution was found to the problem, except avoiding engraved channels whenever possible. Another downside to this method was the inevitable soaking of membrane with ethanol, which had a tendency to shift from its correct position during the layering process once wet.

Once stacked, the layers were placed inside a heated press at 70°C for 3 minutes. Upon removal from the hot plates, the alignment plates containing the PMMA devices were placed between two heavy metal pieces to cool down for 30 seconds. Two press models were used depending on availability: a Bonny Doon Classic 20-Ton Manual Press (Rio Grande, USA) with a custom-made heating plate and control unit (described in detail in the supporting documentation of Liga et al. [69]) and a Carver Bench Top Standard Heated Press (Model 4386, Carver, USA). The latter was only used when the former became defective towards the end of the study. Excessive pressure led to thinning of the ethanol film between the layers and cracking of the PMMA surface, while insufficient pressure prevented the development of a strong bonding. As such, it was important to apply the right pressure to achieve consistently optimal results. Between 200 and 250 bar were applied with the Bonny Doon, while 2-2.5 metric tons were applied at the ram in the Carver press, corresponding to 51-69 bar (750-1000 psi) as read from the pressure gauge. Because the pressure gauge on the Bonny Doon press proved to be defective towards the end of the study (exploding suddenly), it is possible that its output was incorrect, in which case it would be safe to assume that the pressure reading from the Carver press stands correct as the bonding result was the same for both presses.

Visual inspection easily revealed areas with incomplete bonding, which could be seen by placing the device against a direct light source and checking for opaque areas with a defined border. In some cases, partially bonded layers could be salvaged by spraying a small amount of ethanol from the side and placing them back in the press to obtain a complete bond. The Clarex™ (Nitto Jushi Kogyo Co. Ltd, Japan) PMMA, purchased

from Weatherall Equipment & Instruments, was chosen for its ability to work well with this bonding technique, as other types were found to respond differently to this treatment [69, 72].

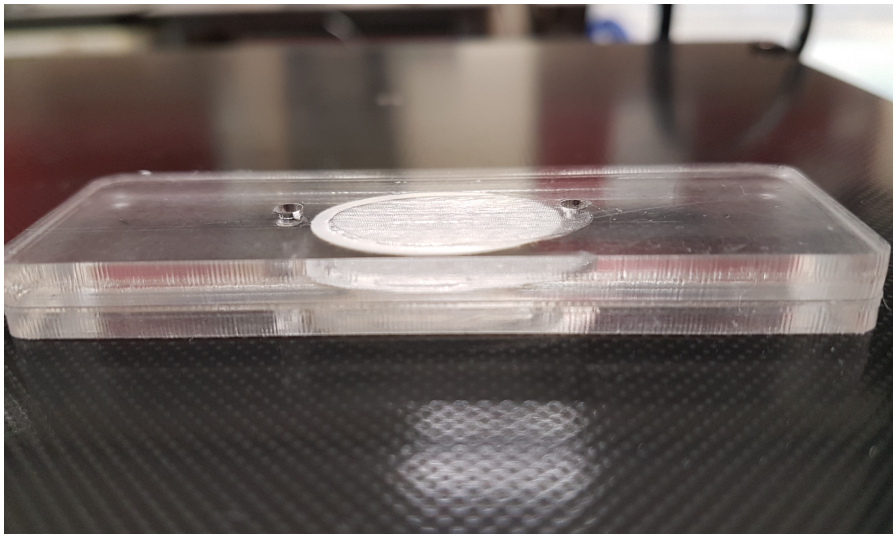

Figure 2.2: Example of a PMMA device successfully bonded using the ethanol-assisted thermal bonding method. The individual layers are still visible and the membrane edges are compressed and secured within internal grooves in dedicated layers to prevent blood spills towards the outlet during operation.

2.1.6 Device drying

There is clear evidence that ethanol can affect the membrane of red blood cells and cause haemolysis [73, 74]. Because the objective of the devices is to perform plasma separation using whole blood samples, the presence of ethanol in the membrane or in the channels would compromise the experiments by inducing haemolysis. Drying the devices completely before use to remove any ethanol residual was therefore an extremely important step. After bonding, the devices were first dried by pushing air inside them with a 10 mL syringe gently to avoid damaging the membrane. Placing the devices in the oven at temperatures above 40°C damaged the membrane, which would darken in colour and become crumbly. Instead, they were placed in a vacuum chamber for at least 24 hours to encourage full evaporation of the ethanol from the soaked membrane. To ensure that the devices were completely dry before major tests, one device was selected at random from the batch and opened up with a scalpel. The membrane was always found to be dry, confirming that the drying procedure was indeed successful.

2.1.7 Alternative layer bonding methods

Because residual ethanol has the chance to induce haemolysis within the devices, other bonding methods that did not require the use of a solvent were explored.

Adhesive bonding

Double sided adhesive (3M, 50 µm thick) was placed on both sides of the PMMA sheets, which were then cut according to the standard parameters previously described. The protection layer was then removed and the layers were stacked in the correct order and then pressed together in a cold press using the same pressure and time applied

in the ethanol-based bonding method. Unfortunately none of the devices prepared with this method were functional, likely due to a combination of poor air-tightness and excessive dead volume within the device caused by the tape, which added an extra 100 µm between each layer. The devices were also quite difficult to prepare using this method, as adhesive placement and alignment of the layers and membrane required considerable manual dexterity and experience.

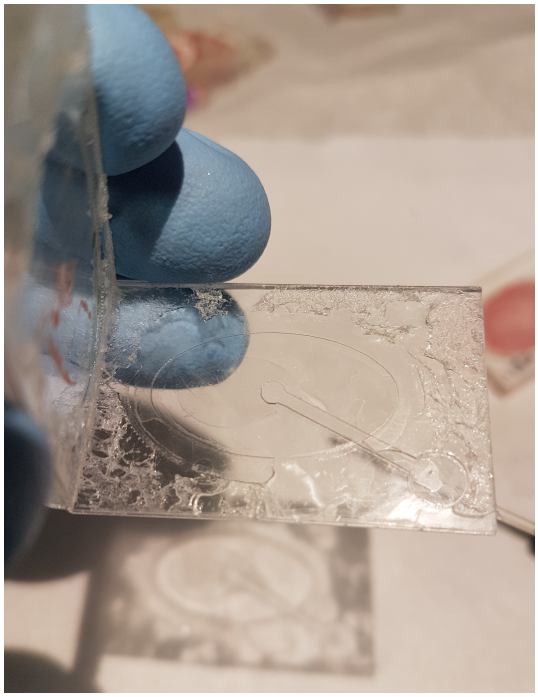

Figure 2.3: Example of a PMMA device unsuccessfully bonded using double-sided adhesive. The glue did not correctly secure the layers together and the layers could be easily separated by hand after blood testing.

UV bonding

Exposure to UV light can be used to activate the surface of PMMA substrates, which can then be successfully bonded by pressing them together. UV bonding was attempted using the following protocol:

- A UV lamp was turned on and left to heat up for 3 minutes.
- The PMMA layers were placed onto a PMMA plate with their bonding side facing upward and exposed to UV light for 45 seconds.
- The layers were removed taking care not to touch the surface, and air-blown briefly to remove potential debris.
- The layers were stacked on the alignment plate and placed inside a heated press at 85°C for 5 minutes, using the same pressure settings as the ethanol-based bonding method.
- Once removed from the press, the devices were left to cool under compression between two metal plated for 2 minutes.

Although the bonding proved to be effective and the device fabricated using this method

were usually functional, this UV bonding technique could not be used for long as the UV lamp was determined to be a health and safety hazard and its use forbidden.

2.2 3D printed devices

2.2.1 3D printer selection

This section will provide a brief introduction to two of the most popular and low-cost modern 3D printing methods to justify the selection of 3D printer and materials used throughout this project. For an in-depth description of the wide range of different 3D printing technologies available, the reader is redirected to chapter 3 of the book "Additive Manufacturing: 3D Printing for Prototyping and Manufacturing" [75].

3D printers based on the fusion deposition modelling (FDM) process are the most affordable and well known type of additive manufacturing technology. With this method, thermoplastic materials provided in the form of filaments are melted and extruded through a nozzle. Upon cooling, the thermoplastic material solidifies and adheres to either the printing platform or to previously deposited layers to create an object from the bottom-up. A wide range of affordable materials are available for this type of printers. Moreover, some FDM 3D printers allow the simultaneous usage of multiple materials in one print. The thickness of each layer is usually in the 0.1 - 0.3 mm range. Layers are evident in the finished product, although post-processing techniques are available for some materials to minimise visible coarseness and "stair-stepping" effects. An example is the exposure of Acrylonitrile Butadiene Styrene (ABS) prints to acetone vapour. When used conservatively, the vapour gradually melts the surface of the print to obtain a smooth and shiny finish [76]. Objects created with typical consumer FDM printers are not completely solid due to voids between layers where the melted plastic did not make full contact. Because of this, air and water-tight prints are extremely difficult to create with standard filaments, although specific print settings and materials can help produce somewhat water-tight parts. Small and intricate features $< 200\,\mu m$ cannot be printed accurately with average FDM printers due to large nozzle sizes. FDM prints are also anisotropic, as the bonding between individual lines of extruded material is much weaker than the material itself, meaning that the 3D printed object is weakest in the axes perpendicular to the deposition axis [77, 78].

Stereolithography (SLA) 3D printers rely on the photopolymerisation of thermosetting liquid resins consisting of monomers and/or oligomers mixed with a photoinitiatior [79]. In most SLA configurations the UV-curable resin is first placed in a resin vat or tank and the object is printed by focusing a laser at a specific wavelegth at the bottom of the vat. The beam can be moved in the desired pattern to create a layer. As the resin cures, it solidifies and adheres to the printing bed, which is kept upside down during the printing process at a distance equivalent to the intended layer thickness (figure 2.5 C).

Digital light processing (DLP) 3D printers operate similarly to their SLA counterparts, but use a digital light projector instead of a laser to cure the resin. This allows entire layers to be printed at once, as opposed to the more time consuming laser-scanning task of SLA printers. This concept is also adopted in Masked Stereolithography (MSLA) 3D printers, which use a monochrome liquid crystal display as a stencil to mask an ultraviolet backlight. With this method, the LCD controls which resin parts are shaded and which are exposed to the light, allowing the resin in one layer to be cured as a whole

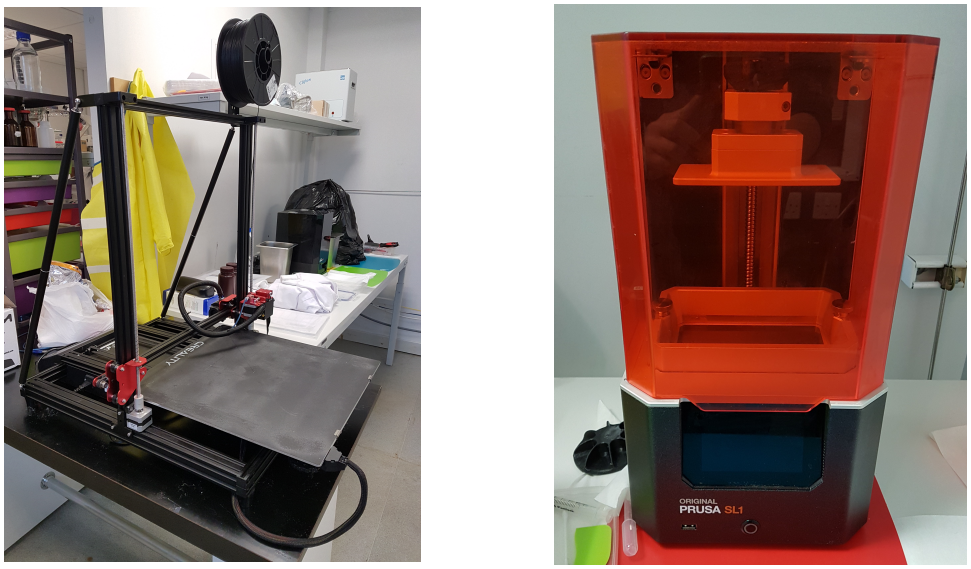

Figure 2.4: Example of an affordable type of FDM (left) and MSLA (right) 3D printer. In the FDM format, a filament is melted and extruded out of a hot nozzle to construct the 3D printer object, while in the MSLA printer liquid resins is polymerised through UV light exposure to form each of the object's layers.

in 3-10 seconds per layer. Many MSLA printers are extremely cheap, with some models available for as little as £250, and can print parts with surprisingly high fidelity to the original designs, even with small features between 200 and 500 µm. Post processing is required to remove excess resin from the prints and fully cure the objects. This is both to ensure that the printed material reaches its full strength and to eliminate any health and safety risk from toxic resin residuals. Once properly post-processed, SLA, DLP and MSLA prints can be considered isotropic [77] as the cross-linking of the polymer in is nearly equal in the Z-axis and XY plane, which leads to a completely solid object with no gaps between printed layers. As such, the resulting prints are solid and air/water-tight by default. Because of the ability to print extremely small features in a short amount of time using a wide range of affordable resins, a low-cost MSLA printer was ultimately selected and used throughout this project to create all the printed components.

2.2.2 Original Prusa SL1

The Original Prusa SL1 3D printer was purchased from Prusa Research along with the Original Prusa Curing and Washing Machine for £1340.73 in February 2020 (both machines have since been discontinued). The print area is relatively small, with a maximum printing volume of 120 x 68 x 150 mm. The XY resolution is determined by the resolution of the LCD screen. The 3D printer has a 5.5" LCD screen with 2560×1440 pixels and XY resolution (pixel size) of 47 µm. The resolution in the Z axis is determined by the layer height, which can be set anywhere between 0.01 and 0.1 mm. The height recommended by the manufacturer is 0.05 mm. Decreasing the layer height results in a smoother finish, but increases the number of layers necessary for each print. As a consequence, the print time increases, along with the chances of print failure due to layer delamination.

2.2.3 Fabrication process overview

The fabrication steps, which will be described in detail in this section, are summarised below:

- Design of 3D printed parts.
- Print settings, orientation and slicing.
- Printing process.
- Clean up and post processing steps.
- Membrane cutting.
- Device assembly.

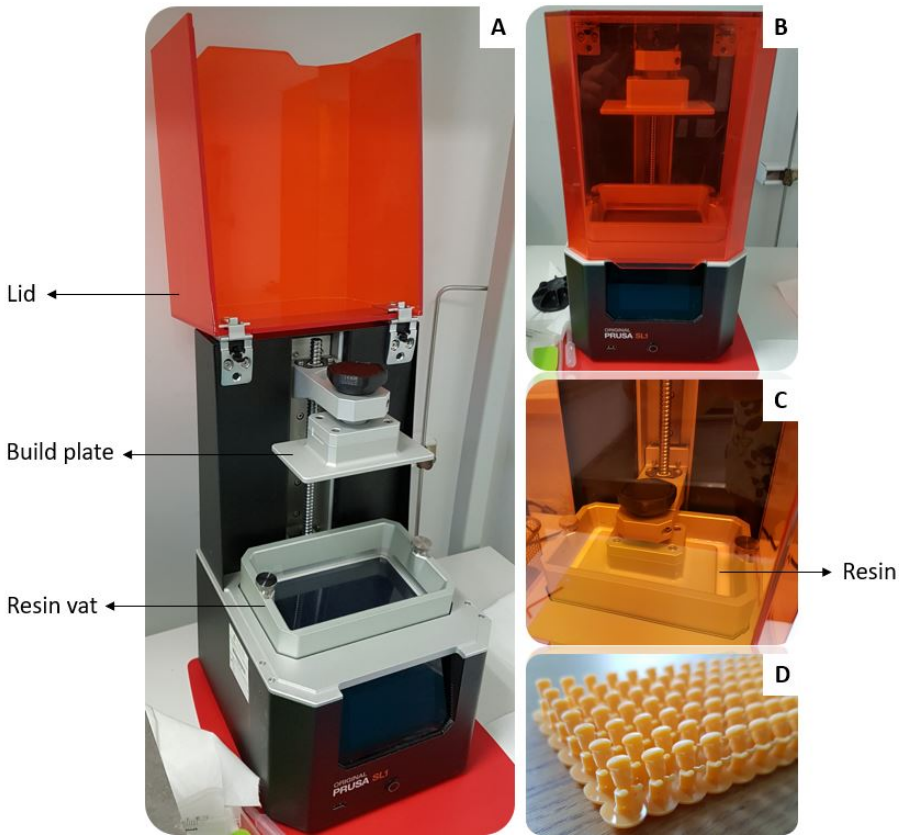

Figure 2.5: A) Labelled picture of open Prusa SL1 3D printer showing the lid, build plate and resin vat placement. B) Front view of the 3D printer. C) Build plate lowered to resin level during the printing process. D) Test object showing the details that can be achieved with the printer.

2.2.4 Design creation

The 3D printed devices were designed using Autodesk Fusion 360, a 3D CAD software for product design and manufacturing. The features in each design were carefully planned to remain within the capabilities of the printer, particularly with regards to overhangs, tolerances/clearances between features and supports.

2.2.5 Print settings and slicing

The finished design was exported as a STL file and imported into a slicing software, which prepared the print by "slicing" the 3D object into a number of layers of a given height. 3D printer manufacturers often develop their own slicing software for maximum compatibility with their printers and ease of use for their customers. The slicing software of choice for this project was the PrusaSlicer, as it was equipped with all the presets for the Prusa resins and printers and offered the ability to control most aspects of the 3D printing process, with the most important ones being:

- Layer height.
- The number and exposure time of the initial layers, which require a longer exposure to ensure adherence to the print platform.
- The exposure time of the subsequent layers.
- Print support features, including automated and manual supports that can be placed anywhere in the print.

The Prusa SL1 printer supports any resin that cures at 450 nm. The settings for each resin vary and are usually specified by the resin manufacturer. Not all resins can be printed at low layer heights, so care must be taken to ensure that the design and settings are tailored to the resin of choice. The photosensitive resins Prusa Tough Transparent, Transparent Flexible and Blue Flexible were purchased from Prusa Research, while the translucent plant-based resin was purchased from ELEGOO. Table 2.2 summarises the settings used when printing with each resin.

The resins listed here cannot be used to create moulds for PDMS, as any PDMS in contact with the resin cannot be polymerized due to the presence of residual catalyst and monomers even in fully post-processed prints [80]. These resins are also non-biocompatible, meaning that they cannot be used in any type of cell culture due to the release over time of materials toxic to cells. Although generally expensive, biocompatible resins are available for purchase from several manufacturers and are widely used in laboratory research and dentistry.

Table 2.2: Print settings used throughout the project. All the Prusa resins were printed at the presets recommended by the manufacturer, while the ELEGOO resin exposure time was a result of trial and error. Fade layers refer to the number of layers used for the smooth transition from the initial layer exposure to the final exposure time. Flexible and coloured resins were only used during early stages of the prototyping process and not for the fabrication of the final devices.

Resin type	Layer height (mm)	Initial layers exposure time (s)	Exposure time (s)	Number of fade layers
Prusa tough orange	0.05	35	7.5	10
Prusa tough transparent	0.05	15	7	10
Prusa tough transparent	0.025	15	6	10
Prusa flexible transparent	0.05	15	5	10
Prusa flexible blue	0.05	15	5	10
ELEGOO plant-based translucent	0.05	30	7	10

The design was loaded into the PrusaSlicer and positioned in the correct orientation

Figure 2.6: Membrane cutting process using 13 mm diameter leather punch. The membrane sheet was laid down on a cutting board and the punch was then used to carve out each membrane individually. Although the process was not significantly more time consuming than laser cutting, the percentage of usable membranes was reduced due to mistakes and defects in the sheet, which could easily bend and be damaged by touch during the process. Each membrane was then carefully inspected before being placed into the devices for assembly.

to ensure a successful print. The print settings were then chosen and supports were applied where necessary. Finally, the object was saved in a 3MF file and loaded into the 3D printer via USB.

2.2.6 Printing process

After filling the vat with a sufficient amount of resin, the printing process was started. The SL1 printer first performed a series of check-ups and then lowered the build plate down into the resin vat, leaving a gap between the build plate and the transparent bottom of the vat equivalent to the layer height setting (figure 2.5 C). The resin between the build plate and the vat was then cured by light exposure. As it cured, the resin adhered to the build plate, which was then lifted up by an amount equivalent to the layer height. The next layer was then cured over the previous one, and the process was repeated until all layers were printed and the intended part constructed.

2.2.7 Washing and drying

At the end of the print, the build plate was extracted from the printer and the printed object was detached from the build plate using a spatula. Supports, if used, were removed at this point. To remove any uncured resin, the object was then placed inside an Isopropyl Alcohol bath (IPA, 99.9% pure purchased from CMC Materials) and thoroughly washed, either manually using a 3 mL pastette (Alpha Laboratories) or automatically using the CW1 machine magnetic mixer. Internal channels, where present, were thoroughly flushed with IPA using either a pastette or a syringe. If undercured resin remained in the channel, a syringe needle was used to displace it before flushing with IPA again. The objects were then dried with compressed air or cleanroom tissue.

2.2.8 Post-processing

The final step in the manufacturing process consisted in placing the printed object under UV light to complete the curing process. The CW1 machine was used for this purpose, as it exposed the objects to light from both sides and bottom. Additionally, the objects

is rotated during the curing process to ensure maximum exposure and an homogeneous cure. As the resin manufacturers did not provide specific curing guidelines, the protocol to ensure that no harmful resin residuals would remain was established by trial and error. Parts that contained integrated membranes were cured for at least 10 minutes on each side. As oxygen is known to inhibit the photocuring process [81], parts that did not contain membranes were instead placed in a clean, transparent container filled with DI water and cured for 10 minutes. In both cases no undercured resin remained as the resin hardened as expected and no sticky resin residuals could be felt or smelled.

2.2.9 Membrane preparation

During the fabrication of the PMMA devices, the membranes were cut to the desired shape using a laser cutter. The membranes used in the 3D printed devices were instead cut manually using a hollow hole punch set (Tooltime UK) that included 14 pieces of varying diameters, from 5 to 35 mm. The tools were sharpened using a knife sharpener before use to minimise the chance of membrane damage. The cutting process is shown in figure 2.6.

Chapter 3

Experimental Methods

3.1 Minivette pressure measurement

As discussed in chapter 1 red blood cells can only withstand a limited amount of shear stress before breaking and releasing their intracellular material in the plasma in a process called haemolysis. Homsy et al. reported significant haemolysis when pressure $\geq 6.65\,\text{kPa}$ was used to drive the blood flow through the same membrane (Vivid$^{\text{TM}}$ GR, Pall Corporation) used in this project [43]. The Minivette™ (Sarstedt), a commercial metered device for the collection of capillary blood from a finger prick, was used to deposit the blood directly over the membrane's surface and actuate the blood flow within the PMMA device. As such, there was a clear need to determine whether the pressure generated by the Minivette could be sufficient to induce haemolysis and thus severely impact the quality of plasma extracted from the devices.

3.1.1 Materials and methods

All blood samples used were collected from the Scottish National Blood Transfusion Service (SNBTS) when at least 3 days old and used as soon as possible after collection. A LabSmith uPS-series (model 0250) pressure sensor and analog manifold were mounted on a LabSmith uProcess™ breadboard and connected to a laptop or tablet. The pressure sensor had a resolution of 1 Pa, obtained one reading per second and was controlled using its corresponding LabSmith software. The input section of the sensor is internally threaded to be used with microfluidic attachments. To ensure a tight fit between the tip of the Minivette and the sensor, the Minivette was securely attached to the pressure sensor by wrapping its tip with Parafilm prior to insertion.

Each measurement was taken by inserting the Minivette, calibrating the sensor and pressing the plunger to initiate the fluid flow though the pressure sensor chamber. The maximum pressure exerted on the fluid by the Minivette was determined by pressing the plunger as fast as possible, while the lower cap was measured by pressing the plunger as slowly as possible. Although still included in the data set, data points $\leq 0.5\,\text{kPa}$ are background noise.

3.1.2 Results and discussion

To determine the maximum pressure that could be obtained with the Minivette plunger, 10 measurements were taken with the 100 µL Minivette when pressing the plunger as

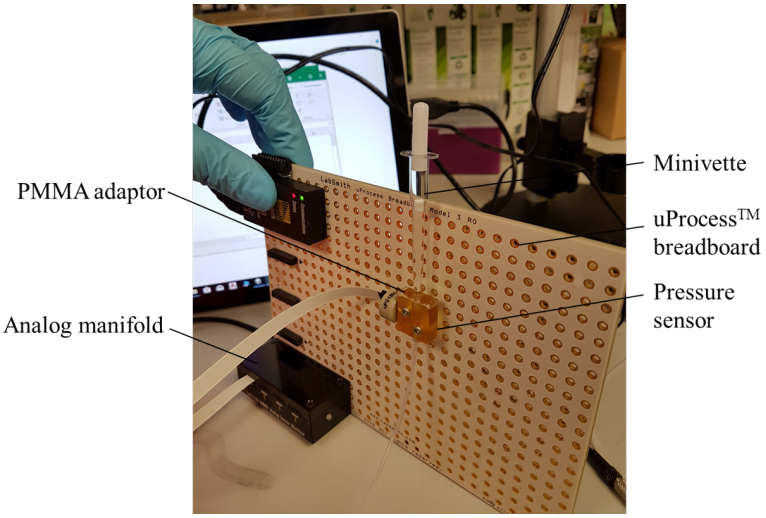

Figure 3.1: Setup for the Minivette pressure measurement. The pressure sensor was connected to a Microsoft Surface and attached to a breadboard as per manufacturer instructions. The filled Minivette was then placed at the sensor inlet and the sensor calibrated before starting the measurement and pressing the plunger.

fast as possible and another 10 when pressing the plunger slowly and in a controlled manner. The process was then repeated with the 200 µL Minivettes with 8 and 12 measurements for fast and slow flow respectively. The results are presented in figure 3.2.

The "slow" graphs for the 100 µL Minivettes show that when pressing the plunger slowly the Minivette empties in 3-4 seconds with a maximum pressure of 2.86 kPa. The peaks average at 2.49 kPa with a 0.27 kPa standard deviation, meaning that, when pressing the plunger slowly, the pressure exerted on the blood is unlikely to cause haemolysis. With the peak average sitting at 4.11 kPa and a 2.85 kPa standard deviation, the "fast" measurements were not as consistent as the "slow" ones, with some data points even falling below the latter. This is likely due to be a combination of manual setup difficulties, Minivette variability and pressure sensor issues. The data clearly shows that the 100 µL Minivettes are capable of exerting a pressure as high as 9.24 kPa.

The 100 µL and 200 µL Minivettes are identical in all aspects except the length of the blood compartment, which is 23 mm long for the 100 µL version and 39 mm for the 200 µL one. The measurements show that a "slow" injection generally lasted 7-8 seconds, with a maximum pressure recorded of 3.91 kPa, a peak average of 2.65 kPa and a standard deviation of 0.77 kPa. Although higher than the 100 µL counterpart, the pressure generated by these Minivettes when pressing the plunger in a controlled manner was still below the 6.65 kPa mark where haemolysis occurs. The data collected in the "fast" tests, however, shows a maximum pressure of 13.08 kPa, with a peak average of 9.66 kPa and a 2.11 kPa standard deviation.

In conclusion, both types of Minivettes are capable of exerting pressure significantly above the 6.65 kPa threshold value observed by Homsy et al. This suggests that haemolysis is likely to occur if the plunger is pressed too fast, while in both cases a slow and controlled injection bring the pressure to acceptable levels at which the damage to red blood cells should be minimal.

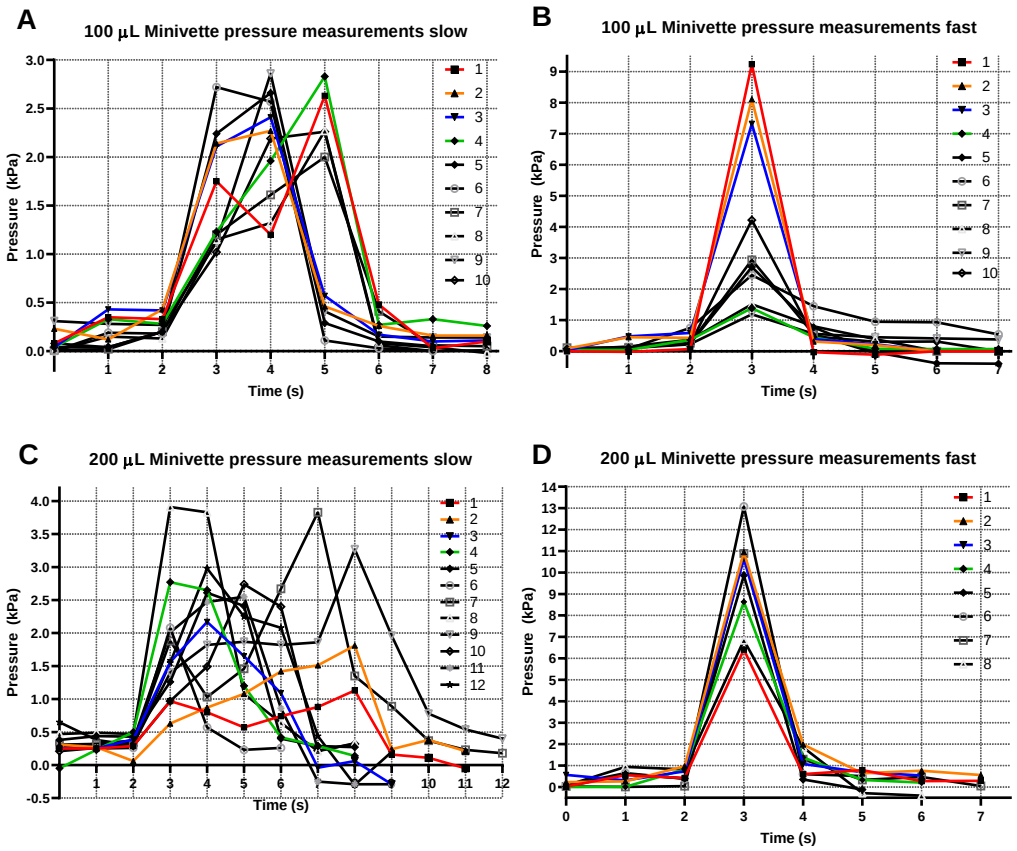

Figure 3.2: Minivette pressure measurements with whole human blood. The plunger press begins at $x = 2$ s in all graphs. The pressure sensor had a resolution of 1 Pa and produced one reading per second. Graphs A and B show the measurements for the 100 µL Minivettes, with the highest pressure recorded being 9 kPa when the plunger was pressed quickly and ∼3 kPa when pressed slowly. Graphs C and D, on the other hand, show the measurements for the 200 µL Minivettes, where a maximum of 13 kPa registered when pressing the plunger rapidly and ∼4 kPa when pressing slowly.

3.2 PMMA cut and engraving analysis

This section describes the attempts at creating small cuts on the PMMA surface using the laser cutter in order to create small channels that could potentially be used for driving the plasma flow through capillary action. As explained in chapter 2, section 2.1.3, a high speed and low power decrease the cut width and depth. Consequently, to achieve the smallest possible cuts the user should set the laser cutter at the highest available speed and lowest power setting. However, because the shape of a shallow cut is a wide parabola, progressively smaller cuts will see the height of such parabola decreased until the cut itself will be indistinguishable from surface imperfections as shown in figure 3.3. As such, it was necessary to find the correct settings that would allow to produce a visible, clear cut that would survive the ethanol-based bonding process without becoming clogged.

Additionally, as the design of some PMMA devices required precise laser cutter engraving of a set depth, it was necessary to also establish a correlation between the engraving settings and the depth generated on the substrate surface by the laser. For engravings,

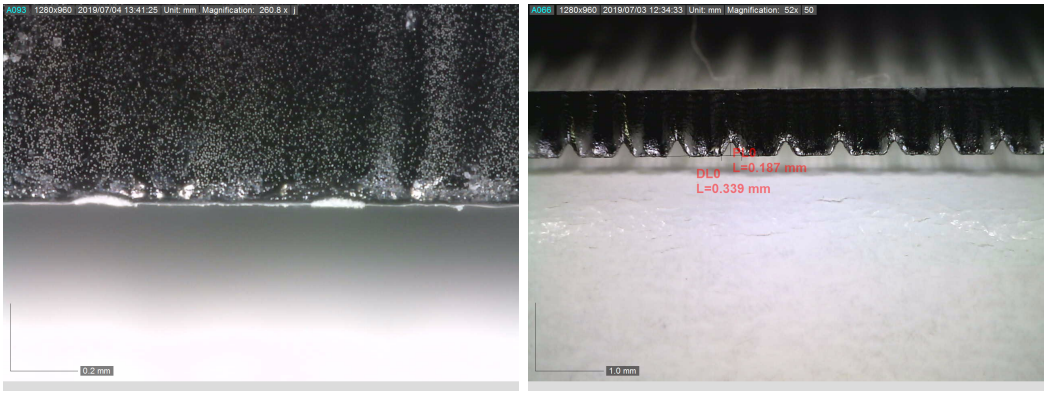

Figure 3.3: Profile comparison of shallow and deep cut. On the left are two cuts produced using 100% speed and 10% power with vector setting. The cuts are barely visible on the surface and would result in a clogged channel when bonded with another layer. On the right are a series of cuts produced using 100% speed and 100% power, repeated twice, using raster setting. The cuts can be seen clearly and would result in viable channels after bonding.

the designs called for depths between 0.2 and 0.8 mm, so the analysis was tailored to finding out the correct settings for this range.

3.2.1 Materials and methods

The laser-cutter (Epilog Legend Mini 18) operated in two different modes: vector for a single cut and raster for engraving patterns and areas. The software used to control the cutting parameters took as settings a percentage of the total power and speed available to produce cuts and engravings of different depths and widths.

For the cut analysis, microscope slide sized PMMA pieces were cut from one long side to the other using a range of different settings. For the engraving experiments, the power was fixed at 100% while the speed was increased by 10% in the 20% to 80% range with a total of 8 samples produced for each step. The laser cutter was operated in raster mode and all the engravings were performed on a 2 mm thick PMMA sheet. Each piece was first cut into rectangles the size of half a microscope slide. The engraving was performed from the middle of the piece to past its edge, so that the depth of the engraving could be easily measured by holding the PMMA piece vertically on the edge opposite the engraving.

In both cases, each piece was then cleaned with ethanol and labelled with a permanent marker and images were collected using a Dino Lite USB microscope as follows:

- The PMMA piece was inserted between two supports.
- The microscope was slid along the edge of the piece and a picture was taken whenever a cut was found.

The magnification used was inputted in the Dino Capture 2.0 software, which then printed two scale bars in the corner of the picture. The ImageJ software was then used to measure the depth and width of each cut by comparing it with the scale bars provided.

3.2.2 Results and discussion

Cut analysis

The results for the cut analysis are summarised in table 3.1 and figure 3.4. As predicted, the minimum cut was obtained using 100% speed and 10% power which produced a parabolic shape on average 126 µm wide and 14 µm deep. The ethanol-based bonding would not allow the creation of channels from this type of cuts, as the melted PMMA creates a residual layer approximately 10 µm deep on the bonded surface and would therefore completely clog the channel.

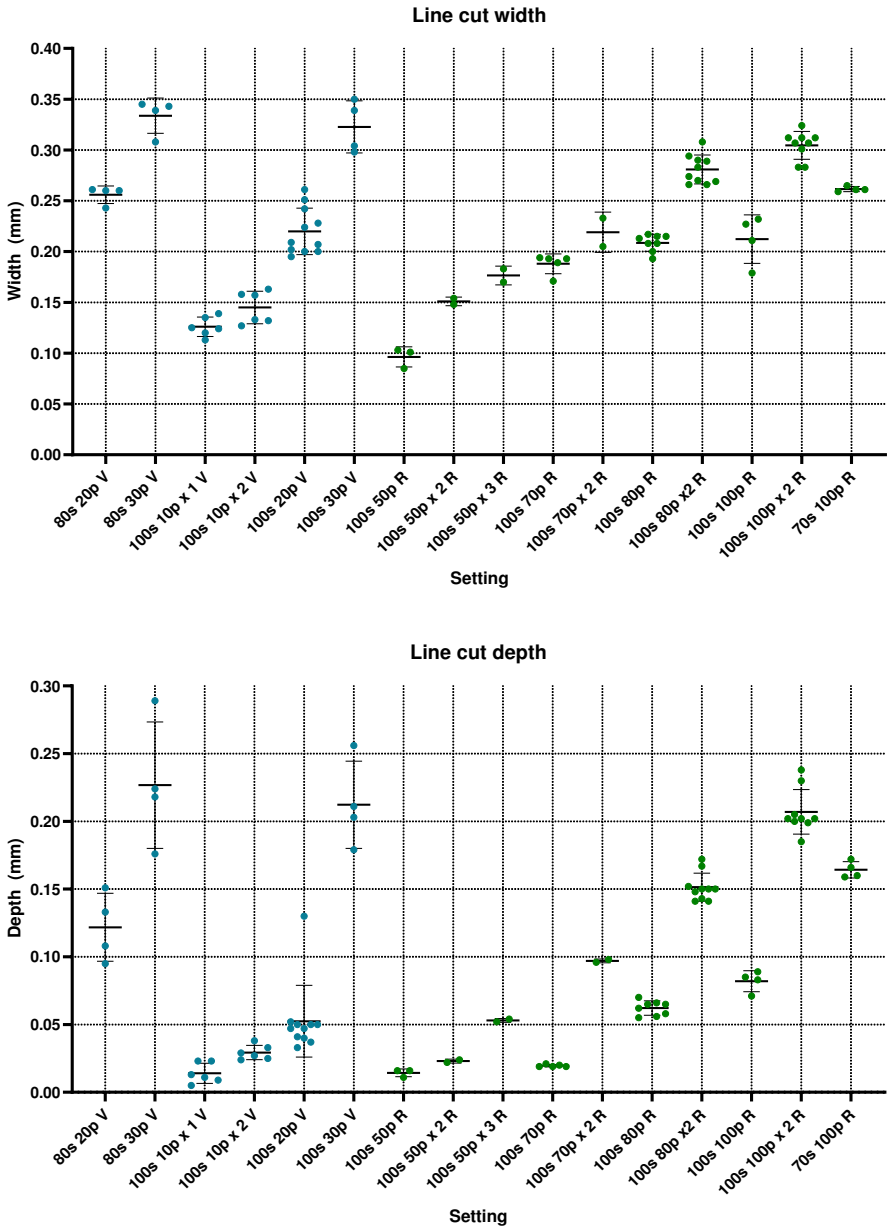

Figure 3.4: Line cut width and depth obtained using different laser cutter settings. The settings notation is an abbreviation for percentage of total speed and power used, i.e. 80s 20p × 2 refers to 80% and 20% of the total available speed and power respectively, while × 2 indicates that the cut was repeated twice. V indicates a vector cut, while R a raster cut. The graphs include mean and SD bars for all settings explored.

Table 3.1: Summary of the data collected during the minimum line cut investigation. The number of independent cuts analysed per setting is noted in the "data points" column, with average width and depth referring to the average of the values obtained across all data points. Whenever a measurement was repeated on the same cut, the average of the repeated measurements on that same cut was used to calculate the overall average.

Speed setting	Power setting	Times repeated	Cut type	Avg width (µm)	Width SD (µm)	Avg depth (µm)	Depth SD (µm)	Data points
80%	**20%**	1	Vector	256.00	7.52	121.75	21.72	4
80%	**30%**	1	Vector	333.75	15.02	226.75	40.42	4
100%	**10%**	1	Vector	126.00	8.52	14.00	7.44	8
100%	**10%**	2	Vector	145.00	14.57	29.33	4.85	6
100%	**20%**	1	Vector	219.91	21.84	52.45	25.22	11
100%	**30%**	1	Vector	322.75	22.20	212.25	27.87	4
70%	**100%**	1	Raster	261.50	2.18	164.25	5.21	4
100%	**50%**	2	Raster	151.00	3.00	23.00	1.00	2
100%	**50%**	3	Raster	176.50	6.50	53.00	1.00	2
100%	**70%**	1	Raster	188.00	8.67	19.60	0.80	5
100%	**70%**	2	Raster	219.00	14.00	97.00	1.00	2
100%	**80%**	1	Raster	208.63	7.83	62.13	4.99	8
100%	**80%**	2	Raster	280.90	13.46	151.40	9.86	10
100%	**100%**	1	Raster	212.25	20.70	82.00	6.71	4
100%	**100%**	2	Raster	304.56	12.90	207.00	15.51	9

Engraving analysis

The engraving depth was obtained using two different methods:

1. Calculated depth by subtracting the thickness of the piece starting from the deepest groove of the engraved area from the thickness of the original PMMA piece, as shown in figure 3.5.
2. Direct measurement of the channel depth using the Dino Lite USB microscope. The measurements were taken by hand and the output values were calculated using two methods, first directly and then by

The results can be seen in figure 3.6. Predictably, a slower speed resulted in a deeper engraving as the laser was focused on the surface for a longer time. As shown in table 3.2, the average depth obtained using both methods was similar, so a curve was fitted to their overall average and used to calculate the final depth corresponding to a given laser cutter speed setting (figure 3.6 C). The MATLAB code used to produce the graph is given in appendix B.

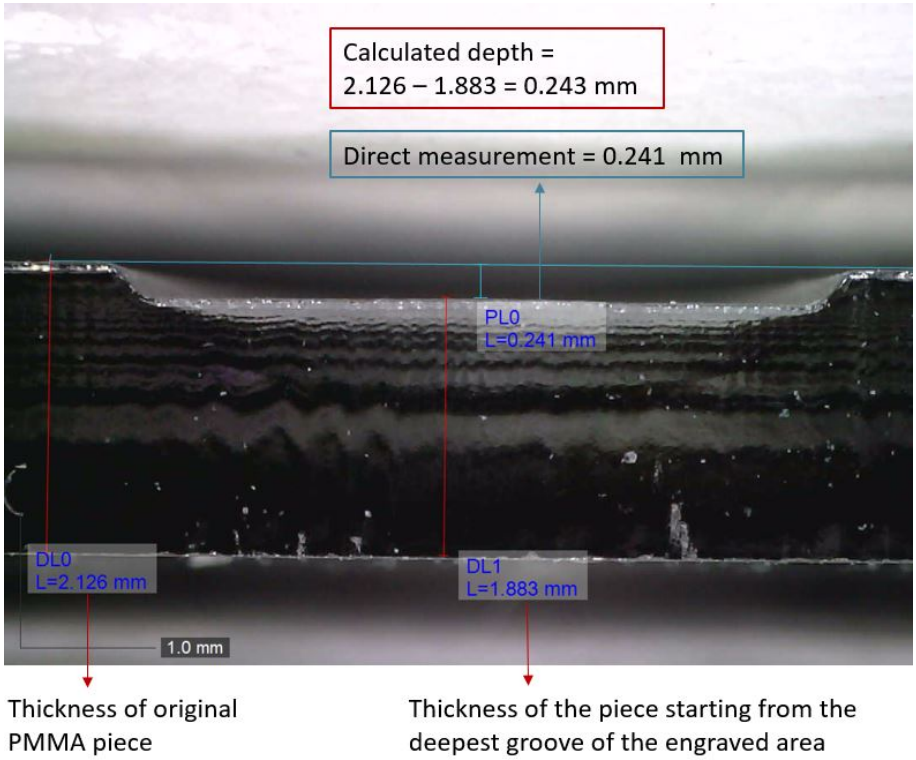

Figure 3.5: Labelled example of the two methods used to obtain the depth of channels engraved in PMMA pieces. The red lines illustrate the values used in the depth calculation through the subtraction of the remaining substrate from the total thickness of the original piece. The blue lines show the direct calculation of the cut's depth. The lines were placed manually using the ImageJ software, which was calibrated using the scale bars at the bottom left as shown in the figure.

Table 3.2: Average and standard deviation of calculated (CD) and measured depth (MD). The difference between the two types of measurements can be seen in Figure 3.5. The overall average between calculated and measured depth is also given, as explained in figure 3.5.

Speed setting	CD Avg (µm)	CD SD (µm)	MD Avg (µm)	MD SD (µm)	CD-MD Avg (µm)
80%	0.191	0.031	0.196	0.030	0.193
70%	0.223	0.029	0.219	0.023	0.221
60%	0.286	0.040	0.281	0.029	0.283
50%	0.342	0.030	0.340	0.025	0.341
40%	0.443	0.029	0.451	0.019	0.447
30%	0.574	0.018	0.586	0.013	0.580
20%	0.857	0.044	0.839	0.045	0.848

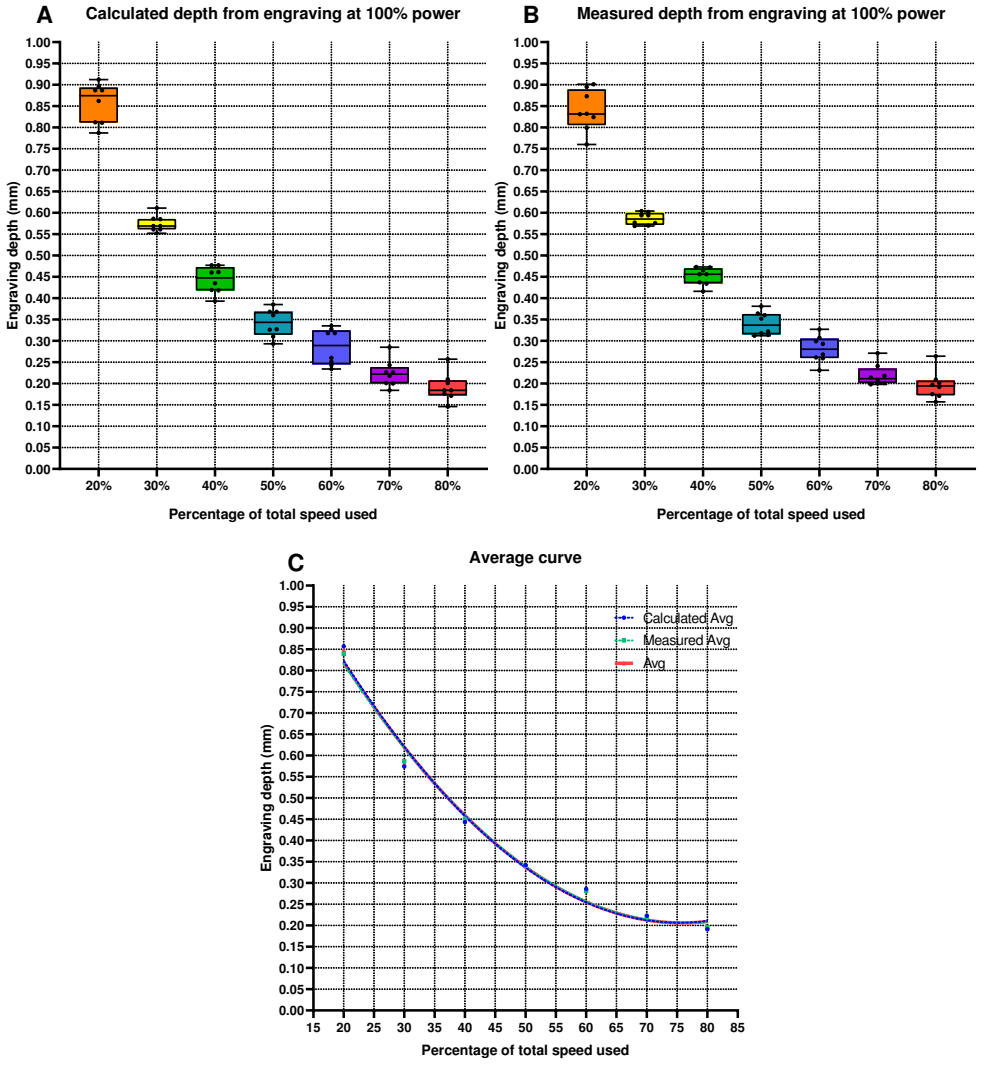

Figure 3.6: PMMA engraving analysis graphs. A) Depth calculated by subtracting the measurement of the engraved surface from that of the original PMMA sheet. B) Depth measured directly using the Dino-Lite software. C) Curve obtained by fitting a 2nd order polynomial curve to the average data points. The MATLAB code used to obtain the curve along with a justification of the fitting method chosen can be found in appendix B.

3.3 PMMA surface modification for increased hydrophilicity

Permanently increasing the surface hydrophilicity of one or more PMMA layers would have allowed the development of PMMA devices that utilised capillary flow to drive the plasma towards the outlet. To increase the hydrophilicity of PMMA, two methods were attempted: surface modification with a sodium hydroxide (NaOH) solution and surface coating with Poly(vinyl alcohol) (PVA).

In this section an overview of contact angle measurements will be given, followed by the literature pertaining the protocols used and the results obtained.

3.3.1 Contact angle background

Surface effects can have a significant impact on the flow of fluids within microfluidic channels. The Gibbs free energy provides a measure of the amount of energy that a system expels or absorbs from its surroundings [82]. Assuming a fixed pressure and temperature, the surface tension γ of an interface is defined as the Gibbs free energy per area:

$$\gamma \equiv \left(\frac{\delta G}{\delta A}\right). \tag{3.1}$$

A liquid molecule at the solid interface has fewer intramolecular bonds compared to its neighbours in the bulk of the material. As such, molecules at the solid interface have a higher energy, with δG indicating the energy provided by the missing intramolecular bonds ΔE. The surface tension can be therefore be expressed as follows:

$$\gamma = \frac{\Delta E}{A} \tag{3.2}$$

where A is the area covered by a single molecule [82].

The term wettability describes the extent to which a solid material can be wet by a liquid and is determined by the molecular interactions at the liquid/solid interface [83]. The contact angle θ, defined as the angle between the solid/liquid and liquid/gas interfaces at the contact line where the three immiscible phases intersect (figure 3.7), is used to describe the degree of surface wetting [82]. In a system at thermodynamic equilibrium with a homogeneous and rigid solid surface, θ is a result of the molecular interactions at the three interfaces, which are described by the surface tensions γ_{sl} (solid/liquid), γ_{lg} (liquid/gas) and γ_{sg} (solid/gas). The contact angle can then be expressed in the most basic way by using Young's equation [82]:

$$\cos\theta = \frac{\gamma_{sg} - \gamma_{sl}}{\gamma_{lg}}. \tag{3.3}$$

A material is said to be hydrophobic (water fearing) if its contact angle with water is $> 90°$ and hydrophilic (water loving) if it is between 0 and 90° [82]. In pressure-driven microfluidic systems, a channel with hydrophobic walls repels water, thus requiring more pressure to be applied for its flow and increasing the likelihood of air bubbles forming and remaining trapped in the channel. On the other hand, hydrophilic walls

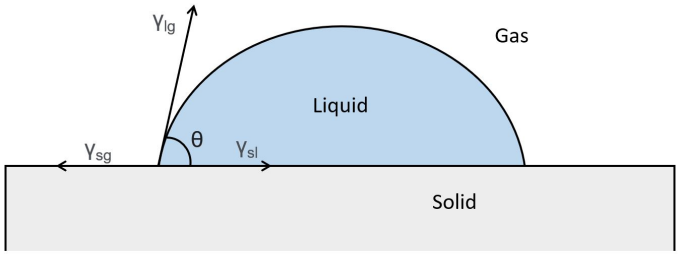

Figure 3.7: Schematic representation of the parameters used in Young's equation.

facilitate (to a degree) the passage of the liquid by capillary effects. Depending on the application, achieving the right contact angle through material selection or surface modification can be extremely important to achieve a desired flow within microfluidic devices.

The same free energy interactions that determine the contact angle also control, along with the solid topography, the shape of a liquid droplet [84]. If the surface is not homogeneous in smoothness and chemistry, the droplet shape can be axis-asymmetric and the contact angle at the extremities can differ, greatly complicating the measurement process. Gravity, which is unaccounted for in Young's equation, can also affect the shape of a droplet having a large enough volume. The equilibrium shape of a free liquid droplet in zero gravity is a sphere (minimal area per volume) [82]. If the effect of gravity on a droplet is insignificant, at equilibrium the droplet will have the shape of a truncated sphere shape, making it possible to measure the contact angle with a circular-fit [83].

As long as the radius of the droplet islower than a threshold value, which for the water/air interface at 20 °C is 2.7 mm [82], the droplet is not significantly affected by gravity as the largest contribution will be that of surface tension. Drelich et al. [84] observed that in smooth and homogeneous surfaces droplet size between 1 and 7 mm base diameter did not cause a change in contact angle. A sphere of 5 µL volume will have a radius of $\sim$ 1.06 mm. Because PMMA is generally smooth and 5 µL droplets on untreated PMMA present was found to have roughly a 2.5 mm diameter, 5 µL was chosen as the droplet volume for contact angle measurements performed in this study to minimise the effect of gravity on the measurement.

Materials and methods for contact angle measurement

The contact angle was measured using the static sessile drop method. A droplet was deposited vertically onto a surface, its profile image was captured with a high resolution camera and the contact angle was measured using a drop shape analysis software. This is done by finding the tangent to the droplet at the intersection point between the three phases and calculating the angle between the tangent and the droplet base line corresponding to the solid surface.

For image capturing either a Dino-Lite AM7013MZT or a Maozua handheld USB microscope, operated with their respective manufacturer's software (Dino-Lite 2.0 and MicroCapture Plus respectivey), were used depending on availability. The microscope was mounted on a stand and the sample placed inside a specifically made apparatus consisting of a box lined with aluminum foil. The foil reflected the light produced by the microscope, which in turn increased the contrast of the droplet against

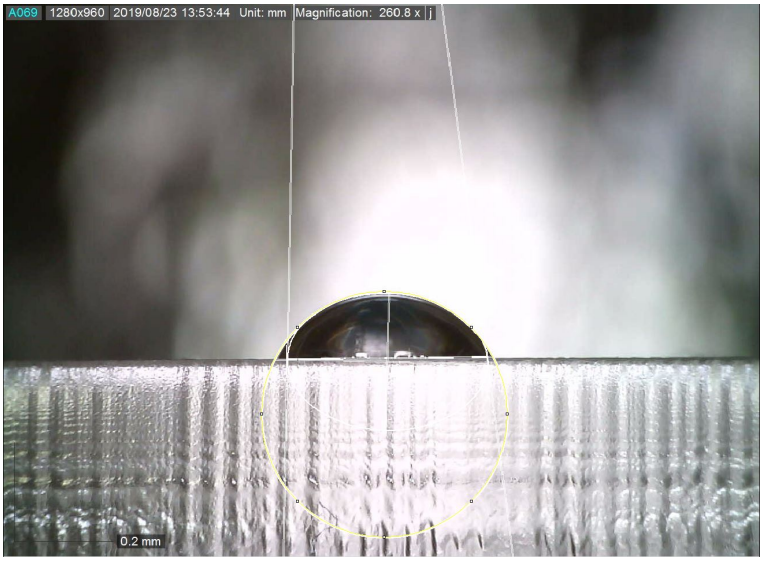

Figure 3.8: Example of an image taken using the apparatus and the Dino-Lite USB microscope. The image was post-processed using ImageJ to demonstrate the contact angle measurement process.

the background, highlighting its boundary. A 5 µL DI water droplet was gently deposited from a pipette fitted with a 1-5 µL tip on the outer edge of the specimen facing the apparatus opening. The USB microscope was then placed in front of the droplet and one or more pictures of the droplet were taken and labelled. The contact angle was then measured from the images using ImageJ with the Contact Angle plugin (https://imagej.nih.gov/ij/plugins/contact-angle.html). ImageJ is an open source software that was developed at the National Institutes of Health, which makes no guarantees on its quality or reliability. As such, the plugin was inspected to ensure the algorithm was legitimate and the results outputted accurate. Although the plugin offered several algorithms, only the basic one, which is based on a circular fit, was used as all droplets could be well approximated to a truncated sphere. Note that for all measurements two points were selected for the base and three for the droplet profile. The algorithm is described in detail in appendix A.

3.3.2 NaOH method

The ester groups in PMMA can be hydrolysed by a strong base such as sodium hydroxide to expose hydroxyl and carboxylic acid groups on the polymer surface. This has the potential to improve hydrophilicity as these groups would then be available to form hydrogen bonds with water molecules [85, 86].

Galin et al. [85] tested this method by leaving small PMMA pieces submerged in a 10% NaOH solution at 20°C for periods varying from 5 min to 4 days at room temperature. The group had no success in changing the contact angle, which remained at 60 ± 2° even after a 1160 hours submersion in the same solution at 50°C. On the other hand, Choi et al. [87] reported some degree of success by pre-treating specimens with ethanol prior to NaOH usage. The group treated PMMA samples by soaking them in 10 mL of 0.1, 1 and 10 M NaOH solutions at room temperature and measured the contact angle at 30 minute intervals between 0 and 90 minutes. At the 90 minute mark, the contact angle was reported to have decreased from 78.19° (untreated PMMA) to 72.74° and

72.10° for the 0.1 and 1 M NaOH solutions respectively. Increasing the concentration to 10 M failed to significantly improve the contact angle. However, when the PMMA was first soaked in ethanol for 10 minutes before being placed in a 10 M NaOH solution, the contact angle decreased to 65.45° and 63.30° after 20 and 30 minutes respectively.

Materials and methods

This method was evaluated in a preliminary study by submerging microscope-slide sized PMMA pieces in 45 mL of a 1M NaOH solution from minutes to hours at room temperature. The solution was prepared by dissolving 1.8 g of NaOH pellets in 45 mL of DI water. The PMMA pieces were cut from sheets of various thicknesses using the laser cutter and cleaned with ethanol and cleanroom tissue before being treated with the sodium hydroxide solution. The contact angle was measured using the method covered earlier in this section. The samples were washed thoroughly with tap water and dried with cleanroom tissue straight after removal from the NaOH bath. Unless otherwise specified, the contact angle was measured without further treatment of the surface.

Results and discussion

The results for each submersion time tested, along with information about the number of PMMA samples used and the data points collected from each piece, are shown in table 3.3.

Table 3.3: Data collected for the preliminary study on PMMA surface modification via submersion into a 1M NaOH solution. In the last row, e.t. refers to "ethanol treated", meaning that the sample was cleaned with ethanol after being washed with tap water. All samples were treated at room temperature with the exception of the 10 min at (50°C) experiment, where the 45 mL container with the sample was left in a hot water bath for the duration of the treatment.

Submersion time	Avg contact angle	Max	Min	SD	PMMA samples	Data points per sample	Total data points
Untreated	64.7	66.6	62.8	1.9	2	1	2
2 min	71.2	71.2	71.2	0.0	1	1	1
3 min	67.3	70.5	59.4	3.3	3	2-3	8
4 min	76	76.1	75.9	0.1	2	1	2
10 min	71.9	71.9	71.9	0.0	1	1	1
10 min (50°C)	70.2	70.2	70.2	0.0	1	1	1
20 h	72.4	80.5	65.8	4.5	1	7	7
20 h e.t.	61.8	78.7	54.7	6.1	2	7	14

With the exception of ethanol-treated samples submerged for 20 hours, this method not only failed to lower, but actually seemed to increase the contact angle compared to untreated PMMA, which was found to have a contact angle of approximately 65°. The 20 hours submersion time followed by ethanol wiping was only marginally better than untreated PMMA (2.9° improvement) and the measurements presented a high degree of variability , suggesting that the treatment was not uniform across the sample's surface. Given such results and the lack of success in the literature, it was decided to drop this method in favour of a stronger coating that would effectively lower the contact angle

at the PMMA surface.

3.3.3 PVA coating

Poly(vinyl alcohol) (PVA, PVAL or PVOH) is a water soluble, biodegradable and biocompatible polymer used in a wide range of sectors. Because it is hydrophilic, non-toxic and presents excellent film forming and adhesive properties, it can be used in the fabrication of microfluidic chips for surface modification purposes [88]. In the literature, PVA has been used to form a film over the surface of PMMA to increase its hydrophilicity. Zhang et al. [89] reported good success by preparing a PVA solution with Tris-boric acid, injecting it in their PMMA devices using a syringe and letting it evaporate freely. The authors kept adding PVA and stirred until the solution appeared homogeneous and transparent, but did not disclose their final PVA concentration.

Shahazahi et al. [90] coated their PMMA devices developed for oil-in-water emulsions with a PVA film to enhance the functionality of their chips using the following protocol:

1. The surface of microchannels within PMMA devices was first activated by argon plasma treatment at atmospheric pressure.
2. The microchannels were then filled with a 2% PVA solution using a syringe and left to rest for 10 min.
3. To remove the excess PVA material and make the coating more uniform, argon gas was passed through the channels continuously for 5 min.
4. The chip was then placed in a vacuum drying oven for 10 min at 70°C, then left to cool down at room temperature in a dry place for at least 12 hours before use.

The authors observed a change in the contact angle from 60°± 3°(untreated PMMA) to 20°± 2 post-treatment.

Yu et al. [91] adopted a similar protocol while also using the PVA coating as a basis for thermal bonding of PMMA layers:

1. The PMMA base was first pre-treated with oxygen plasma to improve its surface free energy, thus increasing the coating uniformity and enhancing the adhesion between the PMMA and the PVA coating layer.
2. A 2% PVA aqueous solution was prepared by dissolving PVA powder into DI water and stirring at 85°C for 24 hours.
3. The PMMA substrates were immersed in the PVA solution at room temperature (22°C) for 10 min.
4. The solution was removed from the substrate, which was then incubated in an oven at 75°C for 10 min for thermal immobilization. The procedure could then be repeated for several cycles to achieve a multilayer coating.
5. After final cycle the substrate was placed in a dry cabinet for 24 hours.
6. Before bonding, the treated PMMA was once again treated with oxygen plasma.
7. The PMMA pieces were pressed together using a custom thermal bonding process at a temperature of 70°C and 1 MPa pressure for 15 min.

The authors observed an improvement in the static contact angle from 75° ± 0.9° for pristine PMMA to 20° ± 2.4° for the post-treated PMMA surface. Low hydrophobic recovery was also observed when the coating was exposed to air and DI water.

Materials and methods

The protocol used in this study was adapted from the work of Yu et al. [91] to fit the equipment available in the laboratory. This method appeared particularly attractive, as it would have allowed simultaneous surface modification for increased hydrophilicity and ethanol-free bonding at low temperatures. The following steps were used to modify the PMMA surface:

1. For the preparation of the PVA solution, 2 g of PVA powder (molecular weight of 31000–50000 $g\,mol^{-1}$, 87–89% partially hydrolysed, Sigma Aldrich, as used by Yu et al. [91]) were dissolved in 100 mL of DI water (2% weight/volume), then mixed with a magnetic stirrer for at least 24 hours at 85°C.
2. The PMMA substrate was placed in a plasma cleaner (Atto, Diener electronic, Germany) for plasma treatment in a vacuum environment (2 min in automatic protocol at 50% power). The plasma cleaner settings could not be changed due to lack of permission.
3. The channels to be coated were carefully covered with the PVA solution with the aid of a syringe and/or a brush and left for 10 minutes at room temperature. Where the whole surface required modification, the entire PMMA piece was directly dipped into the solution.
4. Any PVA excess was then removed and the substrate was blow-dried with compressed air before being placed in the oven at 70°C for 10 minutes.

Results and discussion

To measure the contact angle change, two samples completely coated using this protocol were used. A total of 14 data points, 7 from each sample, were collected. The average contact angle was 57.2°, with a maximum of 69.3° and a minimum of 37.9°, which suggests that the coating was not uniform.

To test the bonding method, the device layers were first coated with PVA as explained above, then stacked to form the PMMA devices and finally placed in the hot press at 70 °C and 2 metric tons at the ram for 5 to 15 minutes. The procedure was repeated for several devices. The bonding was clearly unsuccessful for most of them, as the layers could be easily separated by hand. For the seemingly successful ones, delamination of the microfluidic chips during blood testing confirmed a weak or incomplete bonding, likely caused by the lack of uniformity in the coating. Unfortunately further testing and fine-tuning of the protocol to obtain a more homogeneous result across all surfaces treated could not be pursued further due to a laboratory change.

3.4 Cell measurements for 3D printed devices

In adult humans around 25 trillion RBCs circulate continuously in the bloodstream, with each of these cells containing approximately 260 million molecules of haemoglobin [92]. Given that haemoglobin has a molecular weight of 64500 daltons [93], the weight of haemoglobin contained within a single red blood cell can be calculated as follows:

$$\text{g of Hgb in 1 RBC} = \frac{64000\text{g}}{6.023 \times 10^{23}} \times 260 \times 10^{6} = 2.76 \times 10^{-13}\text{g}$$

To reach the haemolysis threshold of $0.05\,\text{g}\,\text{dL}^{-1}$, approximately 1.81×10^{9} RBCs would need lyse. Assuming an initial sample RBC count of 4.5×10^{11} cells per dL, ~0.4% of the total RBCs would need to be compromised to reach the haemolysis threshold. It was therefore important to measure the number of residual RBCs in the extracted plasma to ensure it was lower than the amount of cells that would push the Hgb concentration over the threshold if lysed.

During the development of the 3D printed devices, no access to a haematology analyser was possible. Haemocytometers, also known as counting chambers, are commonly used to count cells and other particles under a microscope and were readily available in the laboratory. As such, they were chosen as an alternative to haematology analyser readings to calculate the number of residual RBCs in the plasma extracted.

3.4.1 Materials and methods

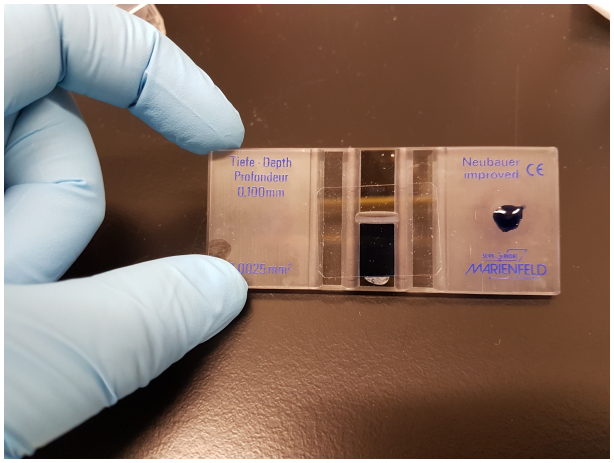

Figure 3.9: Neubauer-improved haemocytometer filled prior to microscope imaging. A small glass slide was used to cover the device channels and ensure their filling by capillary action, as per manufacturer's instructions.

The haemocytometer of choice was the Neubauer-improved from Marienfields, which was used according to the manufacturer's instructions with the following procedure:

1. Using a 20 µL Eppendorf Research pipette, 10 µL of plasma samples obtained from the sample preparation devices were thoroughly mixed with 10 µL of Invitrogen Trypan Blue staining solution.
2. The reusable counting chamber and a glass slide (Thermo-scientific) were cleaned with 70% Ethanol and dried with Kimtech wipes (Kimberly-Clark Professional®) to ensure that no tissue residual would remain on the surfaces. Once dried, DI water was added to the external supports of the chamber and the slide was placed over the chamber base.
3. A droplet of the plasma and ink mixture was carefully placed at the interface between the glass and the chamber base. The counting grid was then immediately filled by capillary force.

4. The counting chamber was immediately placed under a microscope (Leica DMi 1) to prevent the mixture from drying out and pictures were taken at 10x magnification using a camera fitted on the microscope.

The images were then used to calculate the residual cell concentration using the formula in the haemocytometer manual:

$$\frac{\text{cell}}{1\,\mu\text{L of blood}} = \frac{\text{number of cells}}{\text{counted area mm}^2 \times \text{chamber depth mm} \times \text{dilution}} \tag{3.4}$$

where the chamber depth was fixed to 0.1 mm, the dilution used was 1/2 and the area counted was 0.2 mm^2.

3.4.2 Results and discussion

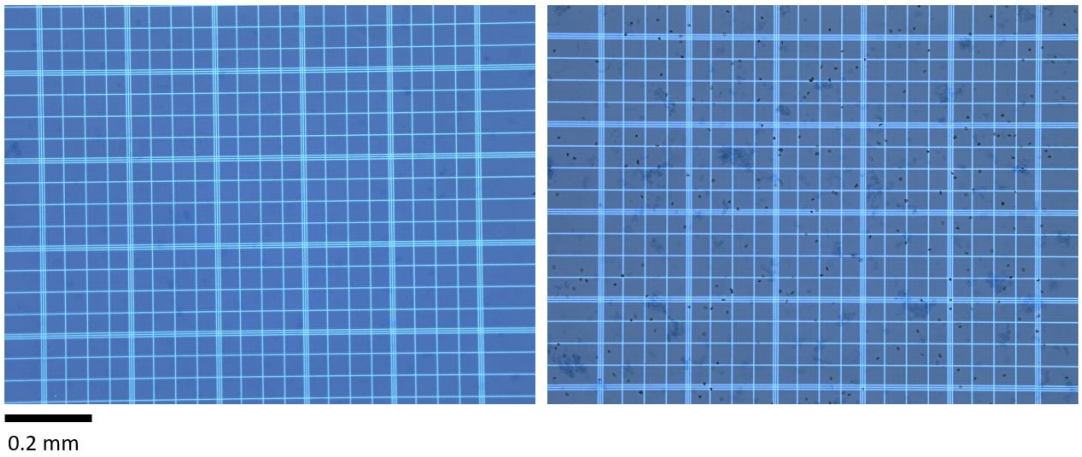

Figure 3.10: Example of plasma samples without (left) and with (right) residual cells on the counting chamber grids when observed under the microscope. The cells within the grids were counted as per manufacturer's instruction and the value obtained used in equation 3.4 to obtain the percentage of residual cells in the plasma collected.

A total of 30 locator-based 3D printed devices were tested using the same equine blood sample with 38% haematocrit. Only 4 devices failed, while the remaining ones successfully extracted at least 15 µL of high quality plasma. Minor amounts of residual cells were observed during 6 of the extractions. The test results are shown in 3.4, while figure 3.10 shows the difference between a sample with and without residual cells. Note that to estimate the percentage of cells filtered from the original blood samples by the device the RBC count for the original equine blood sample would have been required. Unfortunately, this value could not be obtained from the laboratory that provided the sample. Instead, the average RBC count for healthy horses was used, which corresponds to 8.2 µL as the normal equine RBC count is 6.2 - 10.2 µL. As can be seen from the calculation, even in extracted plasma samples with minimal cell residual, the percentage filtered was always ≥99.94%, meaning that the membrane was functioning correctly and the devices successfully prevented blood from spilling over to the outlet.

Table 3.4: Parameters used and results from equation 3.4 for all plasma samples collected. All devices tested, even those that produced plasma with some visible red blood cell residual, obtained a plasma purity $\geq$99.94%, with the number of residual cells being far below the threshold value of 1.81×10^9.

Cell test number	Number of chamber squares	Cell count	Duplicate cell count	Average cell count	Cells/1 µL	Cell count (10^6/µL)	% filtered
CT_1	5	4	4	4	400	0.00040	99.99512
CT_2	5	1	1	1	100	0.00010	99.99878
CT_3	5	0	0	0	0	0.00000	100
CT_4	5	42	50	46	4600	0.00460	99.9439
CT_5	5	1	0	0.5	50	0.00005	99.99939
CT_6	5	0	0	0	0	0.00000	100
CT_7	5	1	1	1	100	0.00010	99.99878
CT_8	5	21	25	23	2300	0.00230	99.97195
CT_9	5	16	21	18.5	1850	0.00185	99.97744
CT_10	5	0	0	0	0	0.00000	100
CT_11	5	1	1	1	100	0.00010	99.99878
CT_12	5	0	0	0	0	0.00000	100
CT_13	5	24	32	28	2800	0.00280	99.96585
CT_14	5	0	0	0	0	0.00000	100
CT_15	5	0	0	0	0	0.00000	100
CT_16	5	0	0	0	0	0.00000	100
CT_17	5	16	17	16.5	1650	0.00165	99.97988
CT_18	5	0	0	0	0	0.00000	100
CT_19	5	0	0	0	0	0.00000	100
CT_20	5	0	0	0	0	0.00000	100
CT_21	5	7	12	9.5	950	0.00095	99.98841
CT_22	5	6	9	7.5	750	0.00075	99.99085
CT_23	5	1	0	0.5	50	0.00005	99.99939
CT_24	5	35	40	37.5	3750	0.00375	99.95427
CT_25	5	1	0	0.5	50	0.00005	99.99939
CT_26	5	5	7	6	600	0.00060	99.99268

3.5 Specimen preparation for device testing

3.5.1 Human whole blood samples

The PMMA plasma separation devices were tested using venous whole blood samples treated with the anticoagulant Ethylenediaminetetraacetic acid (EDTA), either freshly withdrawn from a volunteer donor on the day of the experiments (NHS REC 19/ES/0056) using a EDTA K3 Monovette or collected from the SNBTS (Scottish National Blood Transfusion Service, contract $\sim$ 18 $\sim$ 16). If refrigerated, the samples were left at room temperature for at least 2 hours prior to testing. Before usage, the samples were characterised using an haematology analyser (Coulter Ac·T diff2) meant for clinical use, which requires a 18 µL sample and outputs a wide range of detailed information. This was done to ensure that the main blood count values were within the normal range and the blood sample was not overly compromised by mishandling, age and potential pathologies of the donor and other factors that could lead to excessive release of haemoglobin in the plasma. The linear range where the signal is directly proportional to the concentration, resolution and units of the haemoanalyser with respect to the main parameters are given in table 3.5. The values obtained for the sample(s) used were recorded as part of each experiment.

Table 3.5: Linear range, resolution and units of the main parameters of the haematology analyser as per manual.

Parameter	Linear range	Resolution	Units
Red blood cells	0 - 7.0	0.01	$\times 10^6$/µL
White blood cells	0 - 99.9	0.1	$\times 10^3$/µL
Platelets	0 - 999.0	1	$\times 10^3$/µL
Hemoglobin	0 - 25.0	0.1	g/dL

Preparation of control plasma

The following steps were used to prepare the control plasma from a human blood sample:

1. The sample was mixed gently by inverting it 10 times.
2. 600 µL of blood was pipetted in a 2 mL tube and spun in an Eppendorf Minispin centrifuge at 4800 rpm (1600 g) for 10 min, where g= $1.118 \times 105 \times \text{rpm}^2 \times r_{max}$ (r_{max} = 6 cm for this particular rotor).
3. The supernatant was transferred into a clean tube and spun again in the same centrifuge at 13400 rpm (12045 g) for 10 minutes.
4. The plasma was again transferred into a clean tube and analysed using the haematology analyser and/or the method described in section 3.6.

3.5.2 Equine whole blood samples

The equine blood samples used in the experiments were obtained from the Easter Bush Pathology Laboratory (Royal (Dick) School of Veterinary Studies, The University of Edinburgh). The laboratory was unable to provide date and time of extraction for the

samples. As such, the age and quality varied significantly for each specimen used in the experiments. All samples were treated with Ethylenediaminetetraacetic acid (EDTA) and were used within 24 hours of arrival at the Pathology Laboratory. The samples were stored at 4°C when not in use and were warmed up by leaving them at room temperature for at least 2 hours prior to testing. The haematocrit level of each sample was provided by the laboratory free of charge.

It is important to note that the average diameter of equine red blood cells is 5.66 µm, with a range of 4.72 to 6.07 µm [94], while human red blood cells have a diameter of 6 to 8 µm [5]. This might have a negative impact on the microfiltration process, as the membranes used (Vivid GR™, Pall Corporation) were developed to be used with human blood samples.

Preparation of control plasma

Upon collection of each equine blood sample, a preliminary plasma control was prepared and visually inspected to determine whether the sample was suitable for further analysis. The steps taken were similar to the ones used for human blood samples:

1. The sample was thoroughly mixed for 30 seconds by inversion. For 50 µL samples, no mixing was necessary as they were placed in centrifuge tubes.
2. 100 µL or 50 µL (depending on availability) of blood was pipetted into a 2 mL tube and spun at 1600 g for 10 minutes in an Eppendorf 5418 R centrifuge.
3. The supernatant was transferred into a clean tube and spun again in the same centrifuge at 12000 g for 10 minutes.
4. The plasma was then transferred into a clean tube and kept for haemoglobin measurement.

3.5.3 Sample mixing during device testing

As multiple devices were tested in each experiment, consistency in terms of quality and quantity of the input blood was extremely important to ensure that changes in the output plasma were due entirely to the separation process within the device. Changes in quantity were prevented by using a calibrated laboratory pipette (Eppendorf Research Plus, 20-200 µL) to aliquot the correct blood volume. Changes in quality proved more difficult to address. Samples had to be mixed thoroughly before being inputted into the devices to ensure that the concentration and dispersion of RBCs remained consistent. However, mixing a whole blood sample leads to inevitable damage to red blood cells and consequent haemolysis. The quality of the output cannot be higher than that of the input. If the input sample is already grossly haemolysed, it becomes impossible to tell whether the devices can induce haemolysis.

During the testing of PMMA devices with fresh human blood extracted an hour before testing, the cumulative cell damage from repeated mixing was found to cause haemolysis and significantly alter the haemoglobin levels of the input sample. The steps taken to prepare the control plasma were repeated for the residual sample left at the end of the experiments and the haemoglobin level was found to have changed from 0.1 g/dL to 0.2 g/dL after the sample was mixed 40 times, with 5 gentle inversions per device tested. The change in colour as a consequence of haemolysis can be clearly seen in figure 3.11.

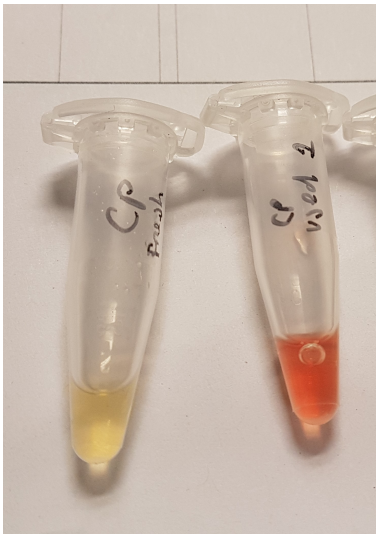

Figure 3.11: Difference between the control plasma prepared before (left) and after (right) an experiment that involved testing 40 devices.

In the final iteration of PMMA devices, the main sample was divided into batches of 600 µL to help prevent this issue. However, sample degradation during testing continued to be an issue. In preparation for the testing of the 3D printed devices, three mixing methods were compared: using and repeatedly mixing a whole sample, splitting the master sample into a few large batches and finally dividing a sample into individual portions, one for each test. The tests were performed using equine blood and the plasma was prepared using the steps described in 3.5.2.

Method #1: keeping the sample whole.

In this method, the entire sample was kept in the same tube it was received in and mixed by inversion 5 times before each test. As can be seen in figure 3.12, significant sample degradation occurred in 3 out of the 4 times this procedure was tested. Clearly, this was an extremely poor mixing method, as the last devices tested received an input blood sample that was already significantly more haemolysed than the first device.

Method #2: splitting master sample into a few large batches.

To reduce the number of times the input sample was mixed before being placed into each device, the master sample was mixed thoroughly by inversion for 30 seconds and split into up to 3 batches before starting the testing procedure. Figure 3.13 illustrates the results for two samples. In particular, the second batch of sample two experienced significant damage, with the Hgb level increasing to $0.175\,\mathrm{g\,dL^{-1}}$ from $0.035\,\mathrm{g\,dL^{-1}}$ in the fresh sample. The variability of the damage in both this and the previous protocol can be explained by both the age and quality of the initial sample and the highly manual nature of the mixing process.

Method #3: individual sample for each device tested.

The final method tested consisted in the division of the master sample into individual batches of 50 µL each, one for each device to be tested. The master sample was

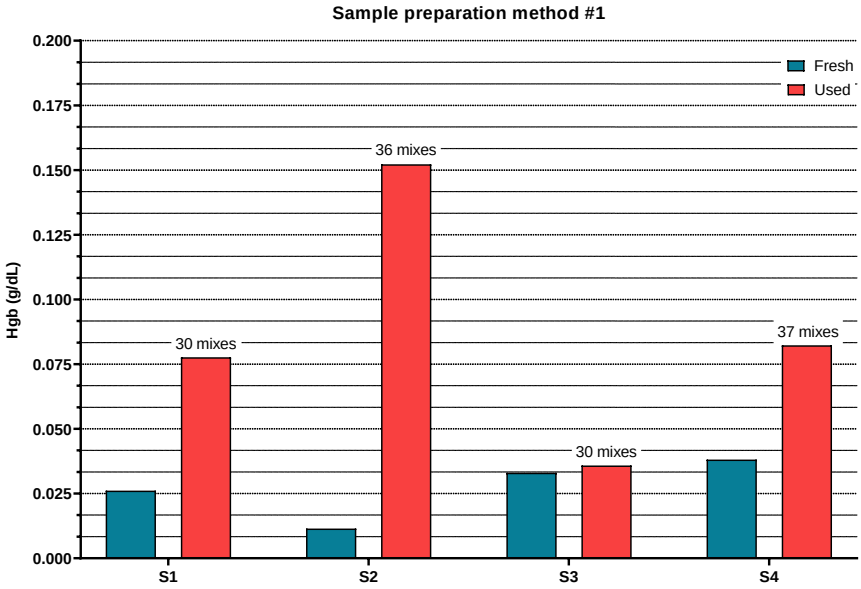

Figure 3.12: Comparison between haemoglobin levels of the plasma collected from the fresh sample versus the plasma collected from the same sample after testing all devices. The term "mixes" above the "used" bars refers to the number of times the sample was mixed before measuring the haemoglobin levels. The inconsistencies between sample behaviour were attributed to sample age and minor differences in the manual mixing process.

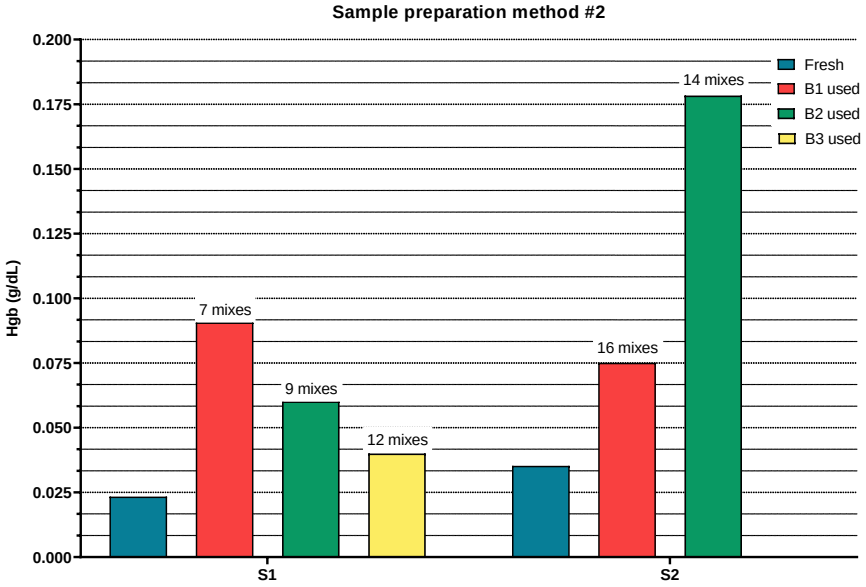

Figure 3.13: Comparison between haemoglobin levels of the plasma collected from the fresh sample versus the plasma collected from each batch at the end of testing. The terms B1, B2 and B3 refer to the batch number 1, 2 and 3 respectively. For sample 2, only two batches were tested. The term "mixes" above the "used" bars refers to the number of times the sample was mixed before measuring the haemoglobin levels.

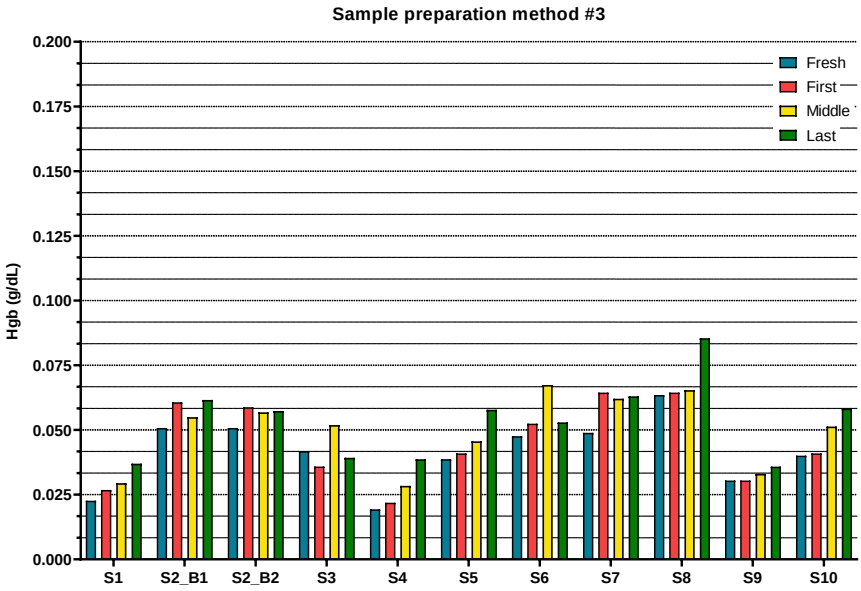

Figure 3.14: Comparison between haemoglobin levels of the plasma collected from the fresh sample versus the plasma collected from the first, middle and last batch.

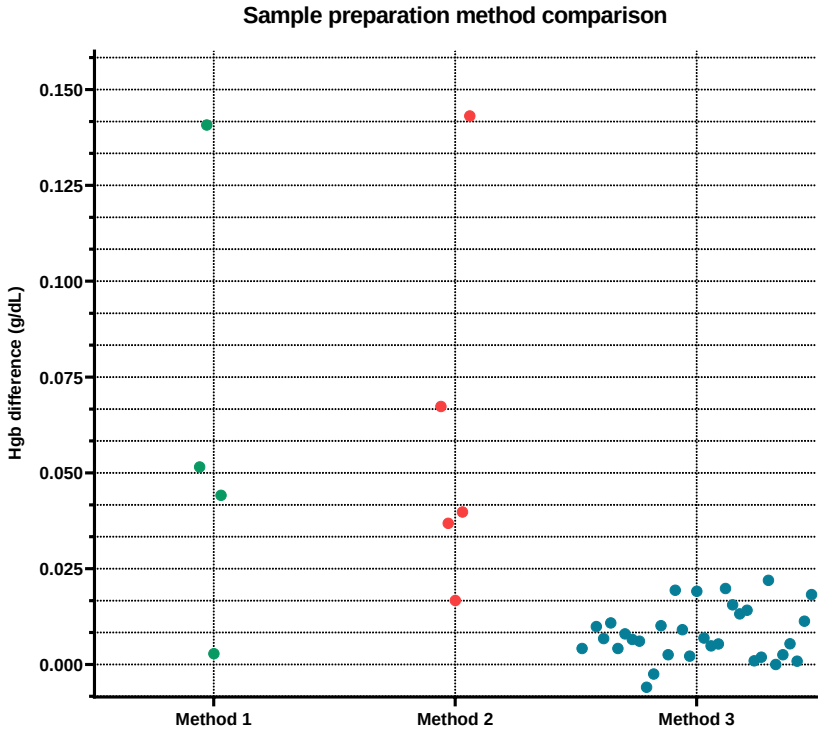

Figure 3.15: Direct comparison between the three different sample preparation methods tested. The values shown are the calculated difference between the haemoglobin level of the used sample (method 1), used batches (method 2) and individual batches (method 3) with the original sample.

thoroughly mixed by inversion for 30 seconds before starting the division in batches, and the sample was re-mixed by inverting it 5 times after every 10 batches. To verify whether this method prevented significant haemolysis, the first, middle and last batches were not used to test the devices, but were instead treated as controls and saved for haemoglobin level testing. As shown in figure 3.14, this method was far more successful than the previous two in keeping the input samples consistent between devices. Although differences still persist, the variability is still far less than the previous two methods. Therefore, this protocol was used in testing all the 3D printed devices described in Chapters 6 and 7.

During device testing, the cells in batches yet to be used quickly settled to the bottom of the tubes. As such, before being placed in the device, each sample was thoroughly mixed using a 200 µL Eppendorf Research Pipette. When using this method, the control haemoglobin concentration was not obtained from the plasma prepared from the master sample, but instead was calculated as the average of the haemoglobin content of the control batches (first, middle and last batch), with the plasma prepared as explained in section 3.5.2. This was done to ensure that damage to the sample done by initial mixing process, which is evident in figure 3.14, would not affect the device results.

3.6 Haemoglobin measurement

As explained in chapter 1, the presence of haemoglobin (Hgb) as a consequence of haemolysis in a blood plasma sample can interfere with a wide range of biomedical assays. A good blood plasma separation device should therefore output high quality plasma containing as low a concentration of haemoglobin as possible, ideally far below the cut-off point for gross haemolysis ($0.05\,\mathrm{g\,dL^{-1}}$ Hgb). In clinical settings, haemoglobin levels are usually quantified using a haematology analyser, which performs the measurement automatically from a small amount of sample. Although access to a haematology analyser was possible during the testing of PMMA devices, its resolution of $0.1\,\mathrm{g\,dL^{-1}}$ Hgb meant that values between 0 and $0.1\,\mathrm{g\,dL^{-1}}$, which is the range of interest for the plasma separated by the devices, could not be detected. During the testing of the 3D printed devices no haematology analyser could be accessed. As such, another method had to be developed for the measurement of low haemoglobin levels in the plasma samples collected from the devices. This section will provide a thorough description and derivation of the protocol used for both human and equine samples.

3.6.1 Background

When irradiated with light, the apparent colour of a sample depends on its selective absorption of certain wavelengths and reflection of the others. The absorbance (A) of a material is defined as

$$A = \log_{10} \frac{I_0}{I}$$

where I_0 and I are the intensity of the light received and transmitted by the material respectively [95]. The spectrum of the material is defined as the curve obtained by plotting A against the wavelength of the incident light and can be determined using absorption spectroscopy instruments such as spectrophotometers. Inside the spectrophotometers, a beam of light from a source is concentrated on a prism or diffraction

grating monochromator. The diffracted light passes through the target sample and is then analysed using a detector. UV-visible spectrophotometers measure the spectrum of electromagnetic radiation with wavelength between 200 and 780 nanometers, commonly defined as the UV-visible spectral region [95].

The spectrum of a substance typically presents characteristic absorption maxima and minima that act as a "signature" and can be used to detect and quantify the target in a solution [95]. The greatest maximum in a specific wavelength range is usually referred to as the peak absorbance. Ideally, by measuring the peak absorbance of a substance at different known concentrations in a range of interest, it is possible to then determine the concentration of the substance in an unknown solution by measuring its absorption at peak wavelength. However, this approach is usually complicated by the presence of interfering substances whose spectrum overlaps with the target substance. If the concentrations of interferants in the compound are always constant, the following correction can be used [96]

$$AT_a = \frac{A_b - K_I A_a}{K_T - K_I} \tag{3.5}$$

where:

$$K_I = \frac{AI_b}{AI_a},\ K_T = \frac{AP_b}{AP_a},$$

and

AT_a = absorption of target substance in solution at wavelength a.

A_a = total absorption measured at wavelength a.

A_b = total absorption measured at wavelength b.

AI_a = isolated interferant absorption measured at wavelength a.

AI_b = isolated interferant absorption measured at wavelength b.

AP_a = isolated pure target substance absorption measured at wavelength a.

AP_b = isolated pure target substance absorption measured at wavelength b.

However, if the concentration of interferants in the solution varies significantly and K_I cannot be determined accurately, the formula can no longer be used. In 1950 Allen [96] published a better correction method that allows the reliable subtraction of the absorption due to interferants from the spectrum of a mixture containing the target substance. A full derivation of the formula developed in his study can be found in appendix C.1. Almost two decades later in 1968 Cripps [97] published his results in applying Allen's correction to the estimation of haemoglobin levels in whole blood. Conditional to Allen's correction is that the spectrum of the interferants has to be linear, or nearly, from two opposite equidistant points to the peak of the target substance. The haemoglobin absorption peak was determined to be 576 nm and the main interferant around this peak was found to be bilirubin, the second major blood pigment affecting the spectrum of blood samples after haemoglobin. Because the individual spectrum of bilirubin can be approximated to a straight line in the 560-592 nm range, with those

points being equidistant from the 576 nm peak, Allen's correction can be applied to obtain the following equation

$$\text{H-value} = Abs_{576} - \frac{(Abs_{560} + Abs_{592})}{2}. \tag{3.6}$$

Cripps then constructed a standard curve, shown in figure 3.16, by measuring the H-value in progressive dilutions of a stock solution of oxyhaemoglobin for which the haemoglobin concentration was determined against an established HiCN standard solution.

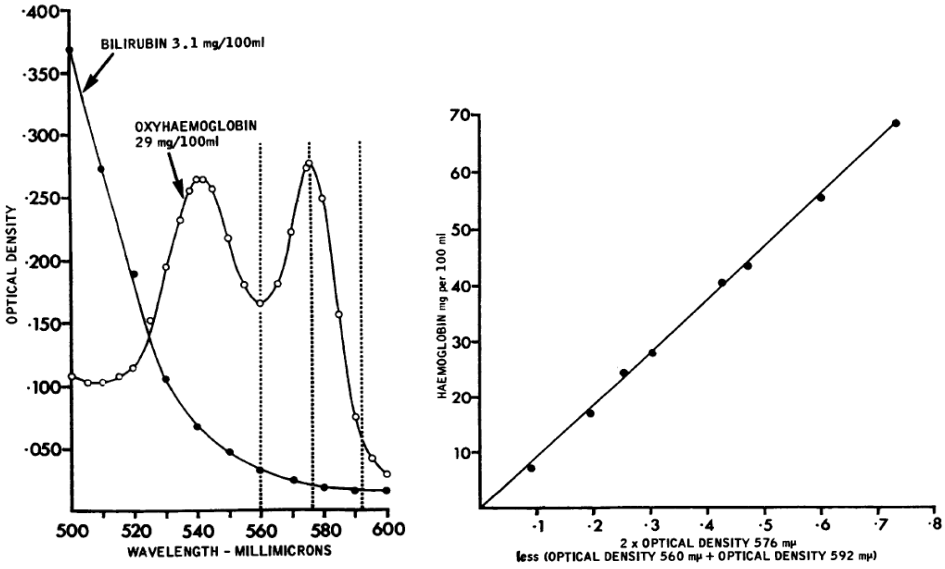

Figure 3.16: Left: absorption curves of oxyhaemoglobin (29 mg/100 mL) and bilirubin (3.1 mg/100 mL). Right: standard curve. Both presented as published in Cripps' work [97].

After comparing nine different methods for haemoglobin quantification, Malinauskas ranked Cripps' method first for use in undiluted plasma to test haemoglobin concentrations between 0.001 and 0.2 $\mathrm{g\,dL^{-1}}$ [98]. Other studies have also used this method to calculate haemoglobin levels in the plasma prepared with their sample preparation devices [99, 100].

In order to use Eq. 3.6 to calculate the unknown haemoglobin concentration in plasma samples, a standard curve had to be constructed first by matching a range of known haemoglobin concentrations to their corresponding H-value. Due to differences between human and equine blood [101] and equipment availability, two standard curves were constructed, one for each blood type.

3.6.2 Standard curve calculation - Human blood

Bilirubin spectrum analysis

As explained in section 3.6.1, when the spectrum of the interferant can no longer be approximated to a straight line Eq. 3.6 becomes invalid. Therefore, it was important to first ensure that the bilirubin spectrum was linear in the region of the haemoglobin peak for the dilution range of interest.

Table 3.6: Concentrations of haemoglobin and bilirubin used in each dilution to determine the detection limits of the UV-Vis spectrophotometer used. The corresponding spectra can be found in figure 3.18.

Dilution number	Dilution ratio	Hgb ($g\,dL^{-1}$)	Solution	DPBS (µL)	Bilirubin ($g\,dL^{-1}$)	Solution	1M NaOH sol. (µL)
1	1	0.05000	250	0	0.00534000	250	0
2	1/2	0.02500	250	250	0.00267000	250	250
3	1/4	0.01250	250	250	0.00133500	250	250
4	1/8	0.00625	250	250	0.00066750	250	250
5	1/16	0.00313	250	250	0.00033375	250	250
6	1/32	0.00156	250	250	0.00016688	250	250
7	1/64	0.00078	250	250	0.00008344	250	250
8	1/128	0.00039	250	250	0.00004172	250	250

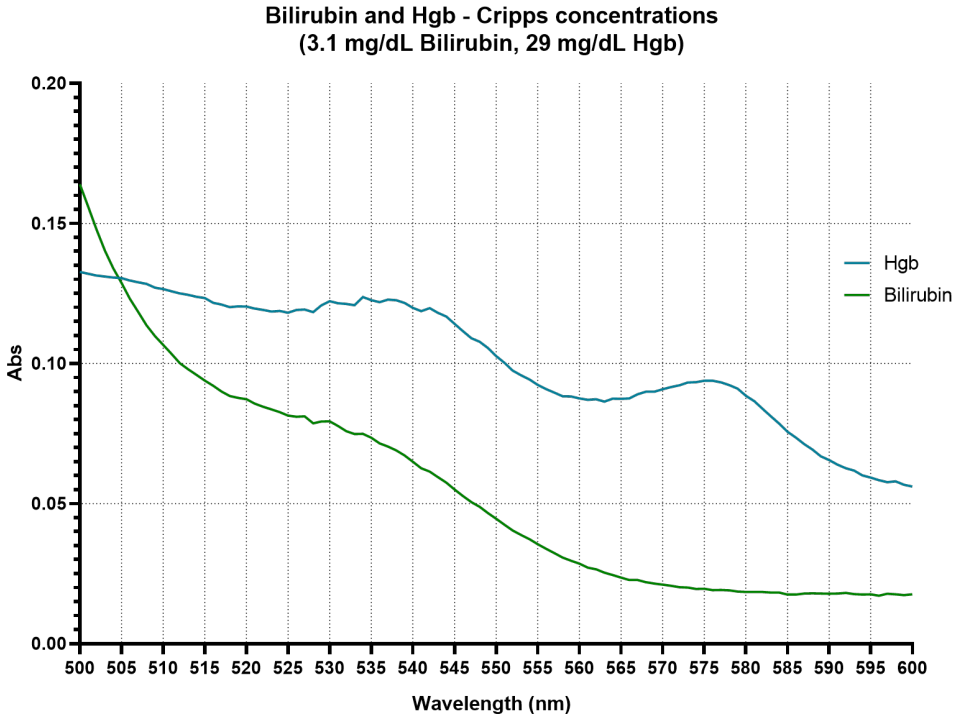

Figure 3.17: Isolated spectrum of bilirubin and haemoglobin at the same concentrations used in Cripps paper ($3.1\,mg\,dL^{-1}$ bilirubin and $29\,mg\,dL^{-1}$ Hgb). The graph strongly resembles that of the work published by Cripps in figure 3.16.

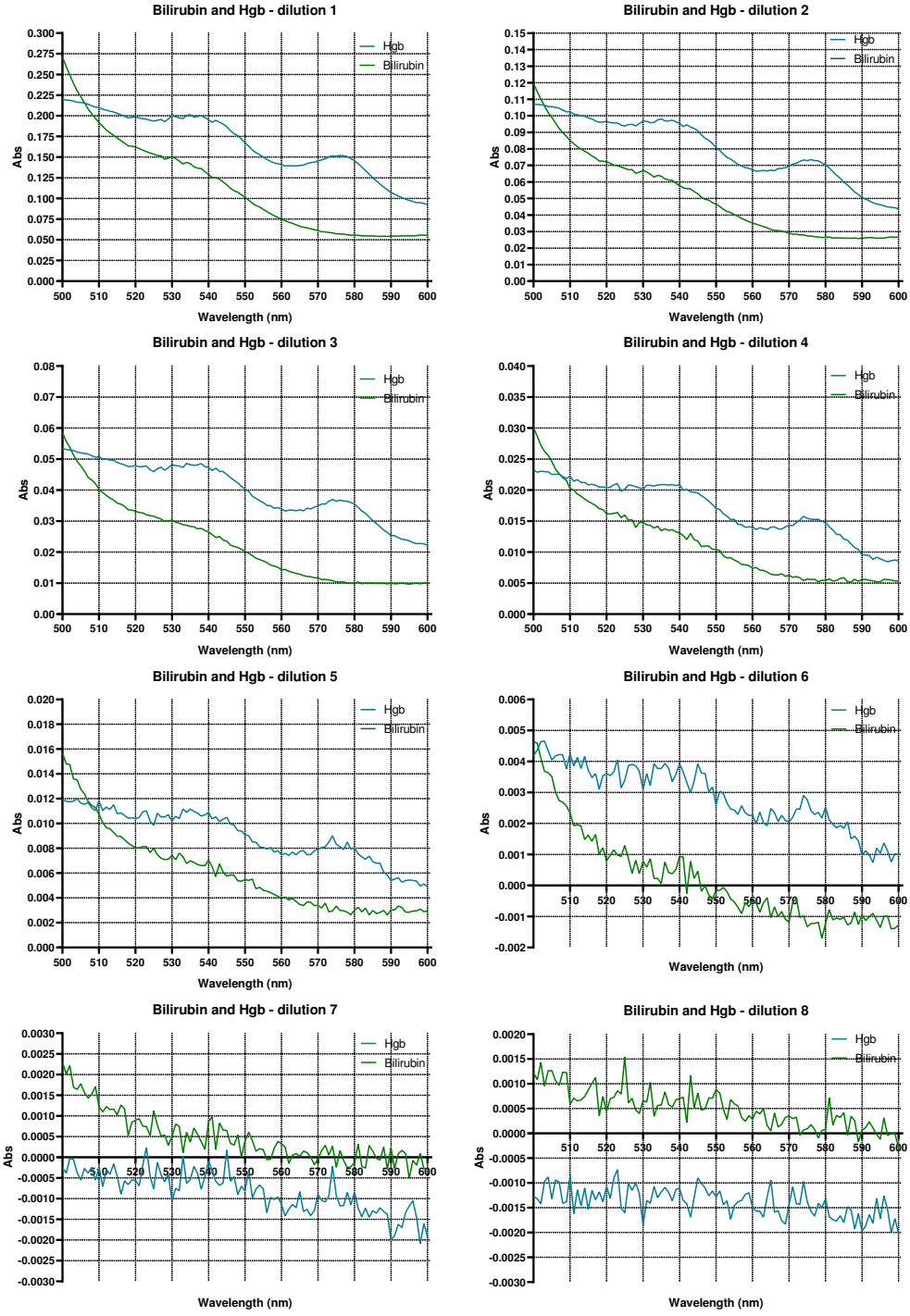

Figure 3.18: Isolated spectrum of bilirubin and haemoglobin at all dilutions shown in table 3.6. As can be seen in the graphs, the spectrophotometer could no longer accurately detect the Hgb and bilirubin values past the 5th dilution, with the lines losing their definition as the concentrations become too low for detection.

To check whether the same graph in Cripps' paper could be reproduced with the UV-Vis spectrophotometer in the laboratory (Agilent Cary 60 UV-Vis Spectrophotometer), $>$ 95% pure bilirubin (Sigma-Aldrich) was diluted in a 1M NaOH solution prepared

by dissolving 1.8 g of NaOH pellets in 45 mL of DI water to reach a concentration of 3.1 mg dL^{-1}, while human haemoglobin in lyophilised powder form (Sigma-Aldrich) was diluted in DPBS to obtain a concentration of 29 mg dL^{-1}. The result can be seen in figure 3.17. After confirming that the spectrum of bilirubin alone can be roughly approximated to a straight line around the haemoglobin spectrum peak at these concentrations, the relationship was checked for the haemoglobin range of interest (0.05 mg dL^{-1} Hgb to 0.001 mg dL^{-1} Hgb). The concentrations and dilutions used are outlined in table 3.6 and the results can be seen in figure 3.18. The relationship held until the 5th dilution, when the concentration became too low for the UV-Vis to detect. As such, it can be said that haemoglobin measurements with the UV-Vis are valid in the 0.05 to 0.003 g dL^{-1} range.

Standard curve construction

A total of 5 SNBTS blood samples, each from a different donor, were well mixed and used as soon as they were acquired. A dilution protocol, previously tested with other samples, was then applied to each sample in order to prepare dilutions with progressively lower haemoglobin concentration. The first dilution, referred to as the "starting solution", was prepared by mixing 500 µL of each sample with 1 mL of lysis solution (Roche) in a shaker at 800 RPM for 10 min at room temperature to reduce the number of intact red blood cells. This step was done to prepare a solution that would closely resemble the plasma extracted by the device, which would not retain red blood cells but might contain residual haemoglobin as a result of haemolysis. The full dilution protocol and values obtained are shown in appendix C.2 (table C.1). The H-values that remained within the valid range established with the haemoglobin and bilirubin study were imported in a MATLAB script, where 5 curves, one for each sample, were first interpolated from the data points independently and then averaged to produce a standard curve, which can be seen in figure 3.19. The full script can be found in appendix C, section C.4.

Device plasma characterisation protocol

The average plasma volume extracted by the PMMA devices was $\leq$ 30 µL. To avoid excessive dilution of the extracted plasma, which might compromise the measurement of very low concentrations of haemoglobin by going below the spectrophotometer limit of detection, a UV-Vis cuvette volume as close as possible to the maximum plasma value had to be used to measure the spectrum of each plasma sample prepared with the devices. The smallest cuvette that could be used (BRAND®) required a minimum of 70 µL and could hold up to 200 µL. To find the minimum dilution necessary to fill the cuvette to operative levels, 1/2 and 1/3 dilutions were compared. Plasma samples were prepared from 4 specimens from different donors using the procedure described in section 3.5.1. Then, 25 µL of each sample were mixed with 50 µL and 75 µL of DPBS to create the 1/2 and 1/3 dilution batches respectively. The results can be seen in figure 3.20. As expected, the spectra of the samples diluted 1/3 was consistently lower than that of the 1/2 dilution. However, in the 1/2 dilution sample #1 could not be measured correctly, which indicates that the cuvette threshold was not met and the light of the UV-Vis did not successfully pass through the sample. In the 1/3 dilution, however, the spectra of all samples was measured correctly.

Given these findings, the following protocol was used to measure the haemoglobin concentration in the plasma extracted from the PMMA devices tested with human

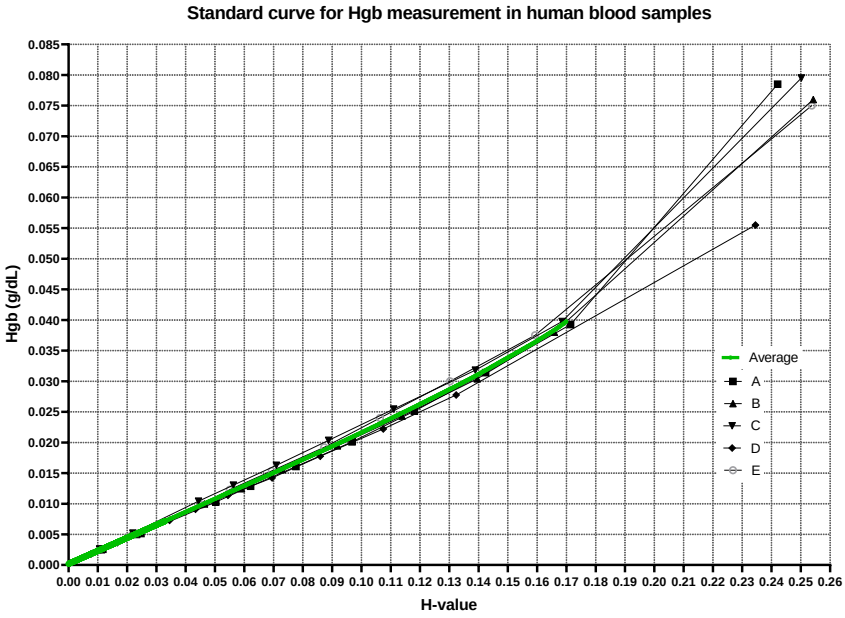

Figure 3.19: Standard curve for the measurement of haemoglobin concentrations in human blood samples using the UV-Vis spectrophotometer. The curve (green line) represents the average of the individual curves obtained through the interpolation of the data points collected for each sample A to E. Note that because the plasma samples from the devices tested are diluted prior to Hgb concentration measurements, most samples will fall within the range of the curve, which is only valid up to $0.04\,\mathrm{g\,dL^{-1}}$ (and hence up to $0.16\,\mathrm{g\,dL^{-1}}$ when correcting for the dilution).

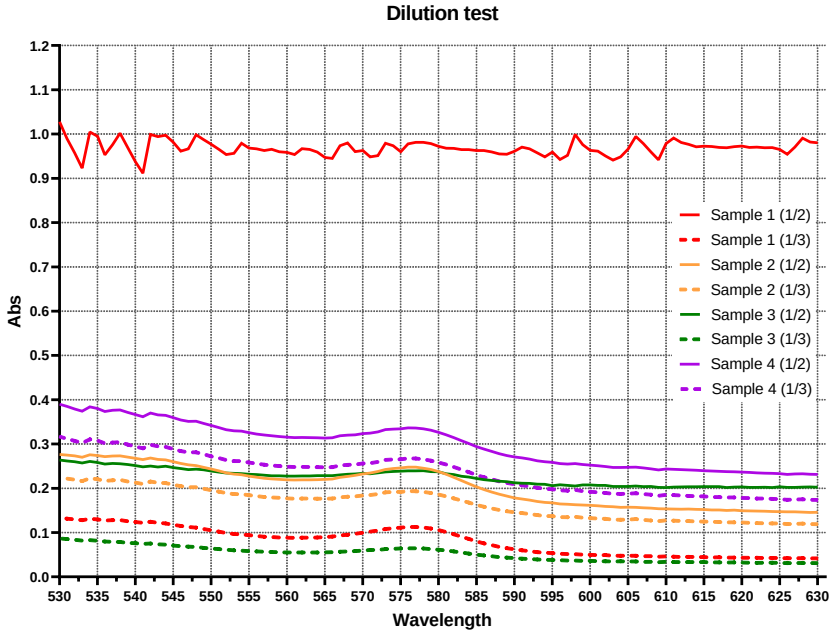

Figure 3.20: Absorption spectra comparison of samples diluted 1/2 and 1/3. As can be seen in the graph, sample 1 diluted 1/2 produced a spurious measurement due to insufficient filling of the cuvette, while no measurement in the 1/3 batch had such problem. This confirms that 1/3 is a more reliable dilution for the protocol.

blood is used:

1. Perform plasma separation with the device and extract at least 25 µL of plasma.
2. Dilute 25 µL of the extracted plasma with 75 µL DPBS (or other suitable buffer) to obtain a 100 µL solution.
3. Mix the solution thoroughly and transfer it in a 70 µL cuvette and calculate the H-value using the UV-Vis spectrophotometer.
4. Fit calculated H-value with Hgb value from standard curve. Multiply by 4 to obtain the actual Hgb value.

3.6.3 Standard curve calculation - Equine blood

In section 3.6.2, the linearity of the bilirubin spectrum in the peak region of haemoglobin was confirmed for the dilutions of interest. This step could not be repeated for equine blood samples, as there was no affordable way to acquire pure equine haemoglobin. As such, it was assumed that the linear relationship would hold as previously demonstrated with human blood samples.

The UV-Vis spectrophotometer available in the laboratory was the NanoDrop 1000 (Thermo Scientific), which did not require any cuvette and instead only needed one small droplet (1.5-2.5 µL) of input solution to be deposited directly in the device using a pipette. To verify the operative range of the spectrophotometer, a 1/2 serial dilution was performed on a test sample with a known haemoglobin concentration to obtain 21 dilutions with a haemoglobin range from $6.4\,\mathrm{g\,dL^{-1}}$ to $0.004\,\mathrm{g\,dL^{-1}}$. Phosphate-buffered saline (PBS) was used as the dilutant. The range that could be measured was 0.8 to 0.01 $\mathrm{g\,dL^{-1}}$, as the spectrophotometer would repeatedly fail to complete the measurement at higher concentrations and would yield the same output as $0.01\,\mathrm{g\,dL^{-1}}$ at lower ones.

Because a haematology analyser was not available, the samples could not be treated with a lysis solution, as it would not have been possible to measure the new haemoglobin concentration post-lysis. Instead, an agreement was reached with the Easter Bush Pathology Laboratory to purchase five EDTA-treated equine samples with varying haematocrit levels where the red blood cells were lysed and removed using the following protocol:

1. The samples were mixed well and the haemoglobin concentration was measured using the Siemens Advia 2120 Haematology Analyser.
2. In order to induce RBC lysis, 1 mL of each sample was diluted with 1 mL of distilled water in a bijou (Thermo Scientific) and mixed in a laboratory roller mixer for 15 minutes.
3. The sample was then centrifuged at 3000 RPM for 5 minutes using a Hettich Universal 320 centrifuge.
4. To make sure that red blood cell that was not lysed in step #2 would remain in the final batch, 1 mL of supernatant was then extracted and placed into a clean bijou.
5. A second spin using the same settings as step #4 was then performed to ensure through visual observation that all red cells that had not lysed were effectively

removed from the sample.

6. The new haemoglobin value was obtained with the haematology analyser.

The dilution protocol used, along with the data collected is shown in appendix C, section C.3. The resulting standard curve is shown in figure 3.21, which was produced with the same MATLAB code used for the human standard curve. As the spectrophotometer only required a few µLs of sample, no dilution had to be performed on the extracted plasma before the spectrum measurement.

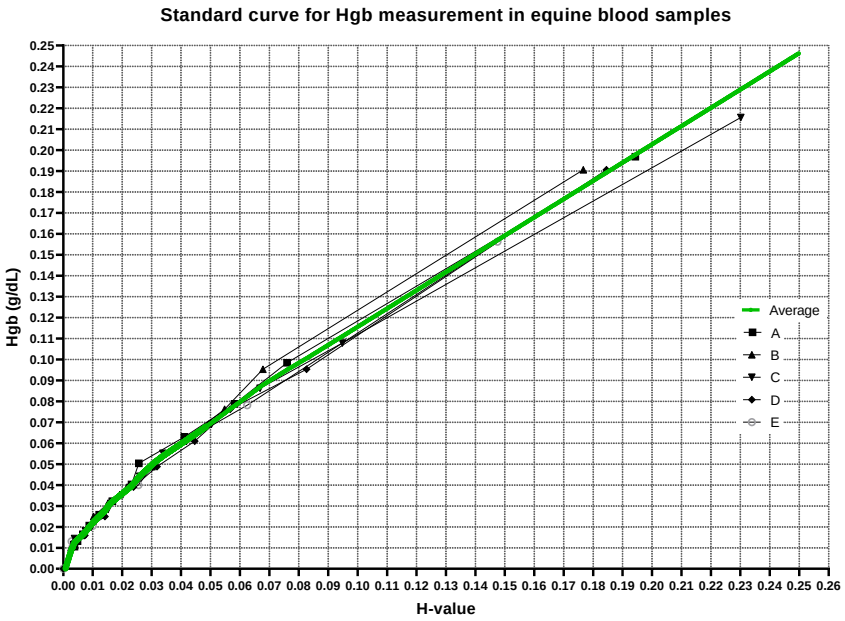

Figure 3.21: Standard curve (green line) for Hgb measurements in equine blood samples. The data points in the curve were the result of the average of the individual curves obtained through the interpolation of the data points collected from samples A to E, which are also shown in the graph.

3.7 Data collection and analysis

This section outlines the procedure used to obtain the data collected from the testing of the assembled PMMA and 3D printed devices.

3.7.1 PMMA devices

The human blood samples used in the experiments were either collected from the SNBTS or extracted from a donor at the testing site. The control plasma was prepared as explained in section 3.5.1. While in earlier device iterations the sample was kept whole and mixed before each test, in later tests the main sample was divided into 600 µL batches to minimise haemolysis induced from repeated mixing, as explained in section 3.5.3.

As mentioned previously, the Minivette™ (Sarstedt), a commercial metered device for the collection of capillary blood from a finger prick, was used to both insert a metered sample inside the devices and actuate the plasma flow during the extraction process. The device operation relied on the air-tightness of all the components. The top of the

Minivette had a small gap that needed to be kept closed to ensure air-tightness during the entire extraction process. Polydimethylsiloxane (PDMS) caps were fabricated from 3D printed moulds, but were not able to adhere correctly to the cap's material. Due to its malleability and adherence properties, Bostik Blu Tack was found to be the best material to cover the Minivette's gap during the testing process of the PMMA devices at the prototype stage. Similarly, to ensure air-tightness at the Minivette-device interface, a small 5 mm piece of silicone tubing (RS Components, 1.6 mm) was cut and fitted on the Minivette's tip. When inserted in the device inlet, the tubing pressed against the edges of the inlet, forming an air-tight seal. The devices were tested using the following procedure:

1. A picture of the front and back of the device was taken using a Microsoft Surface Tablet, so that potential fabrication issues could be seen post-testing.
2. The input sample blood was mixed using a 1 mL pipette fitted with a wide-bore tip.
3. The Minivette was filled with blood and the experiment video was started.
4. A cap (moulded from blu-tack) was placed over the Minivette top hole to form a tight seal upon pressing, taking care not to press the plunger.
5. The Minivette was inserted into the device's inlet. Then, depending on the device tested, one of two methods could be used to push the sample into the device.
6. Method 1, used with the devices developed for the 200 µL Minivettes: the blood was fully pushed inside the device by completely depressing the plunger. Method 2, used with the devices developed for the 100 µL Minivettes: the blood was was either self-absorbed by the membrane by wicking it from the tip of the Minivette, or gently pushed inside the device by pressing the Minivette plunger halfway through or less. After the membrane had absorbed all the input sample, a timer was set for 2 minutes, after which the plunger was pressed all the way through.
7. Regardless of the method used, the video was stopped around the 3 minute mark.
8. If the separation was successful, the plasma in the outlet was pipetted into a clean tube.
9. A picture of the front and back of the used device was taken, along with one of the extracted plasma.
10. The plasma collected was measured with a 100 µL Eppendorf Research Plus pipette and matching tips.
11. If the collected plasma was at least 18 µL, its haemoglobin concentration was measured using the haematology analyser. The UV-Vis protocol was only used in the final PMMA devices tested, if collected plasma was at least 25 µL.

The following values were collected in a spreadsheet during each test:

- Sample information (ID, haematology analyser data).
- Comments on the device performance (ease of use, total or partial failure).
- RBC, WBC, Plt, Hct, Hgb (of raw sample, control plasma and all plasma extracted), when the sample is measured using the haematology analyser.

- H-values when the sample was measured using the UV-Vis.
- Volume of plasma extracted.
- Plasma exit time after injecting the blood inside the device and injection duration.

3.7.2 3D printed devices

The samples of equine blood were collected from the Easter Bush Pathology laboratory and the control plasma was immediately prepared as explained in section 3.5.2. Each sample was divided into individual batches, one per device as per section 3.5.3, method #3. The samples had varying haematocrit levels (28% to 45%). When the haematocrit levels were too low, the sample was centrifuged and a portion of the plasma removed to artificially increase the sample haematocrit to human physiological levels (33-50%). The older the sample, the more degradation of the cells with consequent haemolysis was observed after mixing and centrifugation. Although grossly haemolysed samples were discarded, specimens that were not of optimal quality still had to be used for testing. This is because the sample volume was small and they were received randomly and sporadically depending on patient availability (once or twice a month on average, with a few spikes in sample arrival during horse racing season).

The 3D printed devices were tested using the following procedure:

1. The blood was inserted into the device using a 100 µL Eppendorf Research Plus pipette with 200 µL tips (subject to availability) and operated as per device instructions.
2. The plasma was extracted using another 100 µL Eppendorf Research Plus pipette and placed in a labelled 500 µL centrifuge tube using either 200 µL or 300 µL tips.
3. The plasma was centrifuged at 7000 g for 2 minute intervals in an Eppendorf 5418 R centrifuge until all air bubbles were removed. This step also highlighted the presence of red blood cells, which precipitated at the bottom of the tube if present.
4. The plasma was measured using a 20 µL Eppendorf Research Plus pipette with 20 µL tips. Where the volume exceeded 20 µL, the remaining volume was measured separately using a 5 µL Eppendorf Research Plus pipette with 5 µL tips.
5. Each plasma sample was thoroughly mixed and its spectrum measured with the NanoDrop 100 spectrophotometer along with the control plasma samples.

All tests were recorded using a Microsoft Surface Tablet from blood insertion to full plasma collection. In addition to the spectrum of each plasma and blood sample, the following values were collected in a spreadsheet during each test:

- Input sample information (ID, haematocrit level).
- Details about the extraction, including failure or visual presence of residual cells and ease of operation.
- Sample volume inputted (where it differed from 50 µL).
- Testing order.
- Time waited before extraction.

- Total test duration.
- Number of extractions from each device to obtain the total plasma collected.
- Pipette type and tips used for plasma extraction.
- Volume of plasma collected from each device.

These values were then used to characterise the performance of the 3D printed devices as discussed in chapters 5, 6 and 7. To this aim, the following parameters were used:

- Yield: refers to the percentage of available plasma recovered by the device.
- Plasma quality or Hgb difference: the lower the haemolysis induced by the devices during extraction, the higher the quality of the extracted plasma. The devices were tested with a wide range of small samples, each having different age, quality and haematocrit levels. To remove the effects of initial sample quality from the device analysis, the plasma quality was quantified as the difference between the haemoglobin concentration of the plasma extracted with the devices and the corresponding control plasma. The lower this value, the better the plasma quality extracted from the device as it means that no additional haemolysis occurred during the extraction process. Occasionally, the devices might appear to outperform the control. This is due to difference in input quality due to the sample mixing method used, which is described in section 3.5.3.
- The extraction time indicates the time necessary for the complete extraction process from the moment the sample is placed inside the device.
- The failure rate refers to the percentage of devices that failed completely during testing. A device is considered to have failed when an excessive amount of input blood makes its way from the upstream to the downstream area of the membrane, as a consequence of either membrane damage or insufficient compression at the membrane edges. It is important to note that not all device failure is caused directly by the devices. Parts of the membrane sheets were damaged by improper transportation and storage and were cut by hand. Therefore, although obviously damaged membranes were immediately discarded and utmost care was taken when cutting the membranes and assembling the devices, an unknown percentage of devices was fitted with damaged membranes.
- The residual cell rate refers to the percentage of devices that allowed a visible, but limited amount of residual cells in the output plasma. As discussed in section 3.4, plasma with minimal visible cell residual still maintained a purity >99.9%. Because of this, among the devices flagged for residual cells if the residuals were minimal the device was treated as successful and used as a valid data point for analysis.

Chapter 4

PMMA devices

4.1 Overview

This chapter will explain in detail the designs and testing process of the PMMA plasma separation devices developed in this study. The PMMA devices were designed to be operated with the Minivette® (Sarstedt), a commercial metered device for the collection of capillary blood from a finger prick, and a Vivid GR membrane (Pall Corporation). Figure 4.1 shows the Minivette filling process. During collection, the Minivette has to be kept horizontal and in contact with the blood. Once the Minivette is filled, the blood can be ejected using the built-in plunger. Two types of Minivettes were used, 200 µL and 100 µL, the latter coated with Ethylenediaminetetraacetic acid (EDTA). Other than the coating, the two only differed in the volume of their barrel.

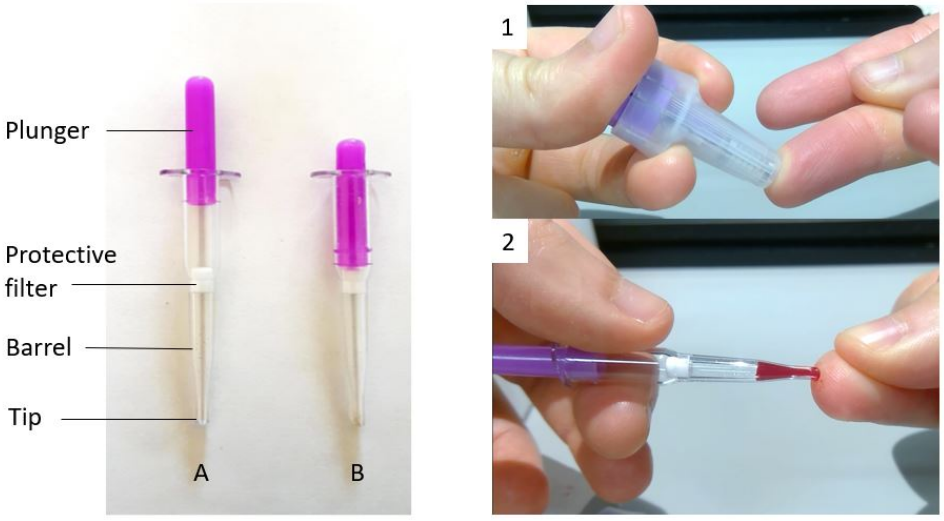

Figure 4.1: Left: annotated picture of a 100 µL Minivette with intact plunger (A) and with plunger pressed (B). Right: Minivette filling process, consisting of finger pricking (1) and blood collection (2).

A thorough description of the device manufacturing process can be found in chapter 2, section 2.1. Due to the method used to bond the PMMA layers together, the overall

size of the devices was constricted to the dimensions of either one or two microscope slides (that is 76.5 × 25.4 mm or 76.5 × 56.8 mm). Up to two devices cut to the dimensions of one microscope slide could be bonded at once. Because of this, although constructing devices the size of two microscope slides was possible, it was discouraged as it doubled both the use of PMMA for device construction and the time necessary for the fabrication of each device. All the PMMA devices developed in this study were constructed using the dimensions of one microscope slide to allow for an easier and faster manufacturing process and lower the overall cost of each device.

The testing process of the PMMA devices is described in detail in chapter 3, section 3.7.1. The next sections will describe the designs for devices operated with each Minivette type, discussing the features implemented, the challenges encountered during the design process and the results obtained.

4.2 Devices for 200 µL Minivettes

To prevent excessive membrane fouling and haemolysis, the manufacturers of the Vivid GR membrane used throughout the project recommend a maximum blood volume of 40-50 µL cm^{-2}. As such, the recommended surface area for a 200 µL input sample was 4-5 cm^2. Due to the size restrictions of the device, the membranes used in most of the devices developed for the 200 µL Minivettes had a slightly smaller surface area than recommended.

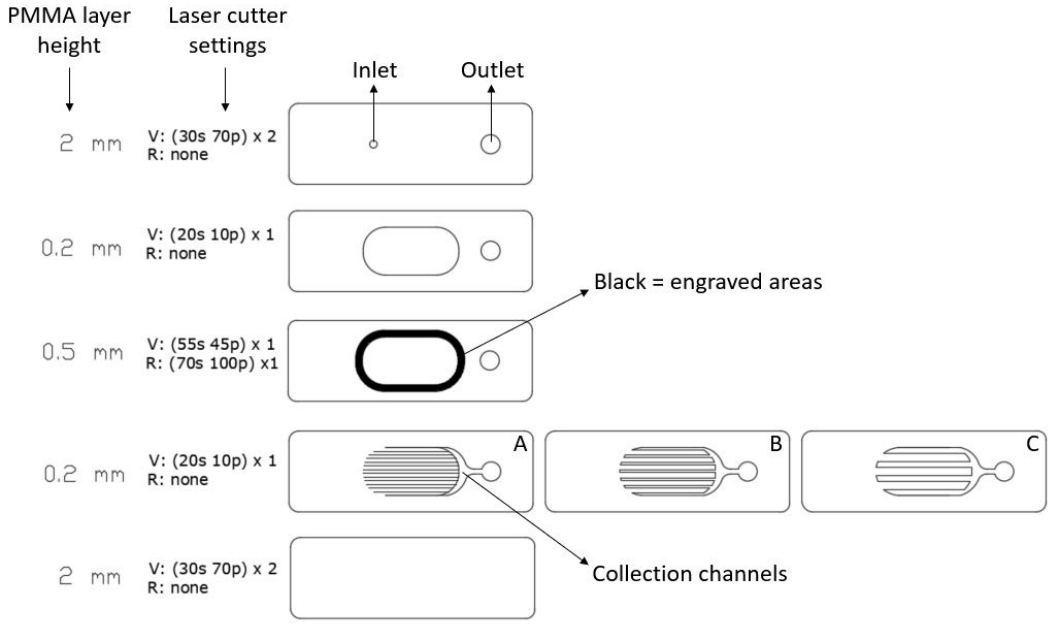

Figure 4.2: Design of each layer of the first PMMA device. PMMA layer height, laser cutting settings and original CAD design showing the engraved patterns are also given. The letters V and R refer to vector and raster respectively, and describe the settings used for the laser cutting process of each layer. For example, if none is given in the R setting, no raster cuts were performed.

Several features were explored during the early phase of the device development, including: cell retention properties of engraved surfaces, capillary flow in small channels, different collection channel designs and various levels of membrane compression and

support. These features will be discussed along with their respective device designs, with some being further explored in the iterations of the devices developed for the 100 µL Minivettes.

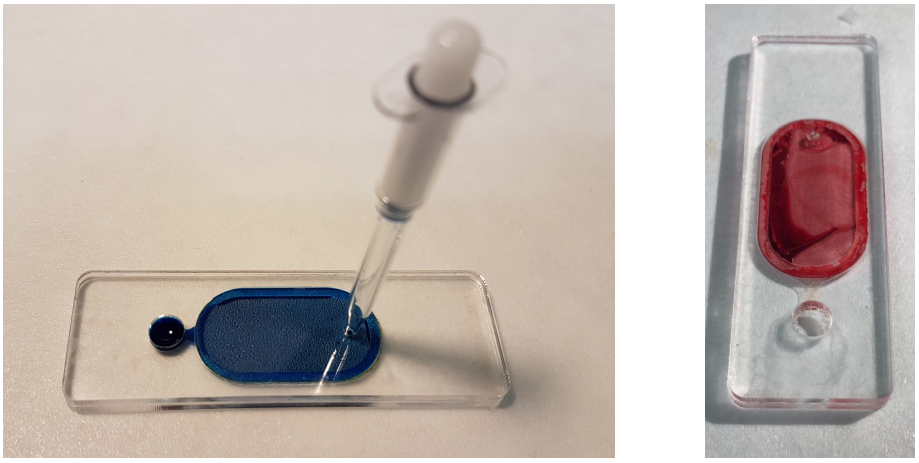

Figure 4.3: Left: first device tested with water and a blue dye. Right: same device tested with human whole blood.

4.2.1 First attempt

The first design attempted is shown in figure 4.2. The functional surface area of the membrane was defined as the area that directly performs the filtration process. To prevent blood from flowing around the edges of the membrane and reaching the outlet, the edges of the membrane were compressed and therefore non-functional. In this device, the total membrane surface area is 576.47 mm^2 and the functional area is 407.93 mm^2.

The first layer supported the Minivette, while the second layer provided enough space for the input blood to prevent backflow at the inlet during injection. The membrane was placed between the second and third layer. A groove was engraved into the third layer to provide support for the membrane and secure its placement during the assembly process. To assess the viability of plasma collection through capillary action, the fourth layer provided 3 different designs of cut-through collection channels for redirecting the plasma from the bottom of the membrane towards the outlet. Design A consisted of small slits through the 0.2 mm PMMA piece, while designs B and C provided progressively wider and more sparse channels.

The device was first tested with dyed water and then with whole blood. As can be seen in figure 4.3, while the device was successful with water, no plasma could be collected at the outlet when blood was used. When looking at the bottom of the device during testing no plasma could be seen within the collection channels of version A, while some plasma could be seen accumulating within the channels of versions B and C. As such, the idea of creating small channels for capillary action was abandoned, as it failed to contribute to the pressure-driven flow induced by Minivette and instead impaired the plasma flow towards the outlet.

4.2.2 Second iteration

The first device that produced a collectable plasma output is shown in figure 4.4. The device features were moved to the edge of the PMMA slide so that two devices could be

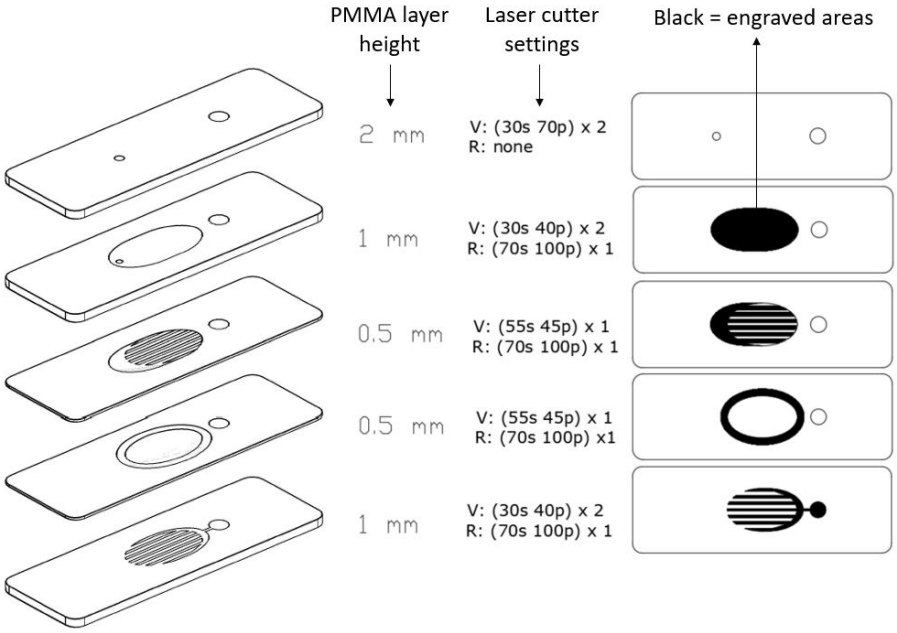

Figure 4.4: Schematic diagram of an early PMMA device designed to be operated with 200 µL Minivettes. The black areas were engraved using the laser cutter raster setting, with the parameters chosen in order to achieve the desired depth according to the curve shown in figure 3.6 of chapter 3.

created simultaneously in one slide. After the bonding process, each piece was cut into two parts using the laser cutter to obtain two devices. Using this method, four devices can be fabricated at the same time as opposed to the two in the previous iteration, thus doubling the fabrication throughput.

The device consisted of five PMMA layers of thicknesses between 5 and 10 mm that contained both cut and engraved features. The top layer supported the Minivette, while the second and the third both contained a rough engraved surface to help retain red blood cells before membrane contact. The fourth layer included the same engraved membrane support as the previous iteration, while the final layer contained seven collection channels, each 0.8 mm wide and spaced apart 1.15 mm, to collect the plasma

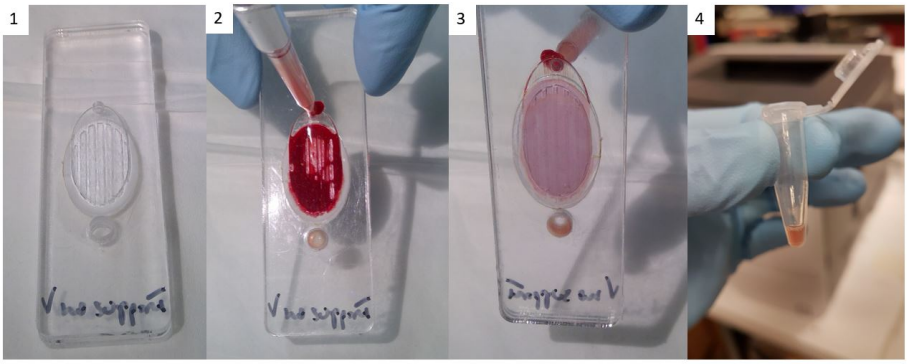

Figure 4.5: Testing process of the early PMMA device described in figure 4.4. 1) The device is ready to be tested. 2) The tip of a filled Minivette is placed into the device inlet and the plunger is pressed all the way to push the blood inside the device. 3) Bottom view of the device while the plasma flows towards the outlet. 4) Plasma collected placed inside a centrifuge tube.

from underneath the membrane and redirect it towards the outlet. The membrane was sandwiched between the third and fourth layer. The surface area of the membrane was significantly reduced from the first attempt, with a total area of 320.35 mm^2 and functional area of 202.24 mm^2.

The testing process of the device is shown in figure 4.5. Due to excessive space above the membrane caused by the engraved surface, a significant portion of the blood volume remained stuck in the upstream area of the membrane. Moreover, the engraved membrane supports in the fourth layer prevented the bottom of the membrane from coming into direct contact with the collection channels. Therefore, only some of the plasma could adhere to the channels, while the rest remained trapped in the downstream area of the membrane. Finally, the engraved collection channels on the bottom layer retained a thin ~ 0.1 mm layer of melted PMMA that resisted all removal attempts and contaminated the small volume of output plasma.

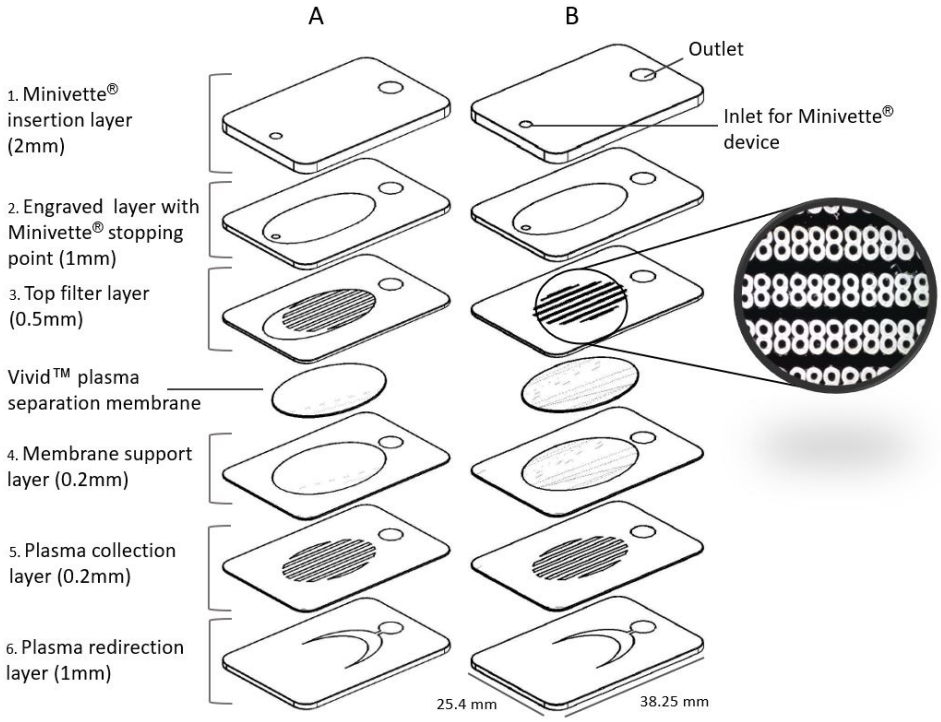

Figure 4.6: Schematic diagram of the final PMMA devices developed for the 200 µL Minivette. A brief description of each layer's function along with the thickness of the PMMA substrate used is given on the left side. The two designs are identical apart from the third layer, with design A having an engraved "landing" are for the inputted blood and B a series of gaps to redistribute the blood more evenly throughout the membrane's surface.

4.2.3 Final iteration

The final iterations of devices created for the 200 µL Minivette retained the membrane surface area of their predecessor. However, the engraved space above the membrane was reduced and the membrane support removed in favour of an entirely cut layer, which kept the membrane steady during assembly without creating a gap between the downstream area of the membrane and the collection zone. To reduce the amount of melted plastic residuals, the collection zone was split into two layers: layer five contained a series of cut-through channels, while layer six included an engraved half-

moon shaped collection area to redirect the plasma from the channels to the outlet. As can be seen in figure 4.6, the two final designs A and B only differ for their third layer.

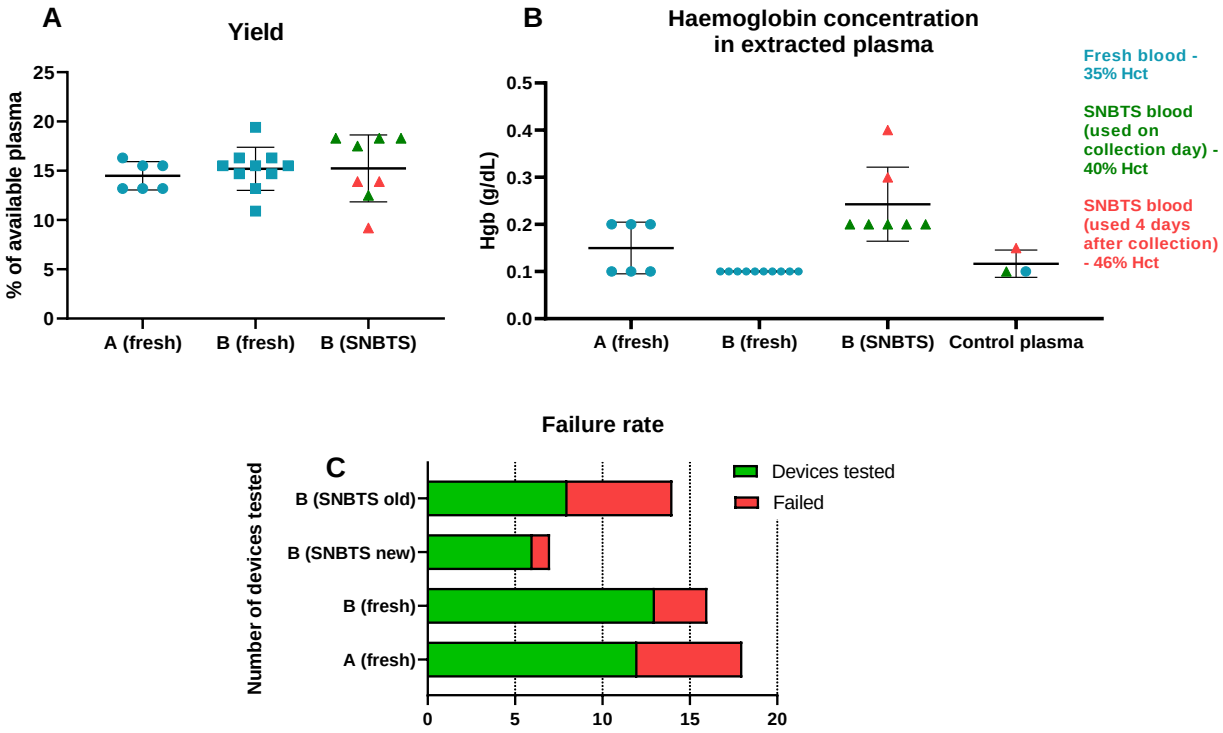

Figure 4.7: Graphs representing the yield (A), haemoglobin concentrations (B) and failure rate (C) of the final devices tested with the 200 µL Minivette. Fresh blood was considerably superior in quality compared with SNBTS blood, which significantly decreases the probability of haemolysis occurring during the extraction process. As can be seen in graph B, devices tested with fresh blood consistently extracted plasma with lower haemoglobin concentrations, with the haematology analyser measuring 0.1 g dL^{-1} Hgb for all devices tested.

The design in device A was similar to the previous iterations, while device B was fitted with an array of cut-through holes to better distribute the blood over the membrane surface during injection. The devices were tested with both fresh human blood and SNBTS samples of different age. The results are summarised in figure 4.7. Overall, the yield was low and the quality of the plasma extracted poor, particularly when the devices were tested with older blood. The B devices performed better than the A designs in all aspects. This is likely due to the tendency of the engraved and cut third layer of the A device to have sharp edges that occasionally damaged the membrane during assembly, as shown in figure 4.8.

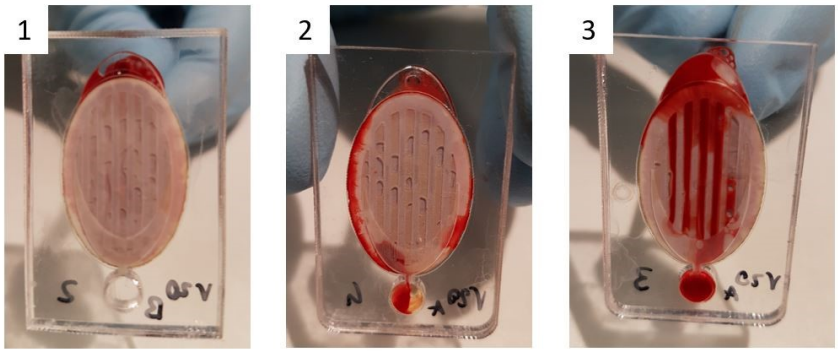

Figure 4.8: Bottom view of a device that did not fail (1) and two others that experienced the two most common types of device failures. 2) Blood passed around the membrane and mixed with the plasma in the outlet. The problem affects both A and B devices. 3) The membrane was damaged by sharp design features (only occurs in design A).

Despite the attempts at improving the quality of the plasma, the output remained visibly haemolysed, as can be clearly seen in figure 4.9. Moreover, the 200 µL Minivettes proved to be extremely difficult to fill with capillary blood. Any blood collected from a finger prick coagulated quickly, blocking the Minivette tip and preventing the barrel to be fully filled.

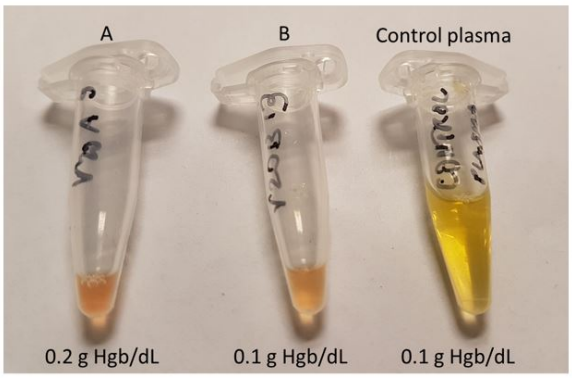

Figure 4.9: Visual comparison of centrifuged control plasma and best plasma samples collected from A and B devices.

To resolve both plasma quality issues and Minivette filling difficulties, the 200 µL Minivettes were replaced by 100 µL Minivettes coated with EDTA. The addition of the anticoagulant prevented blood coagulation during collection. Because the membrane surface are of the devices remained similar to the previous versions, more area per blood volume was available, decreasing membrane fouling and consequent haemolysis.

Minivette plasma collection

An interesting idea explored at this stage consisted of trying to use another Minivette to collect the extracted plasma. This concept was explored using the final devices developed for the 200 µL Minivettes. As can be seen in figure 4.10, the Minivette at the outlet managed to collect some of the plasma, but a significant amount was left behind and had to be collected using a pipette instead.

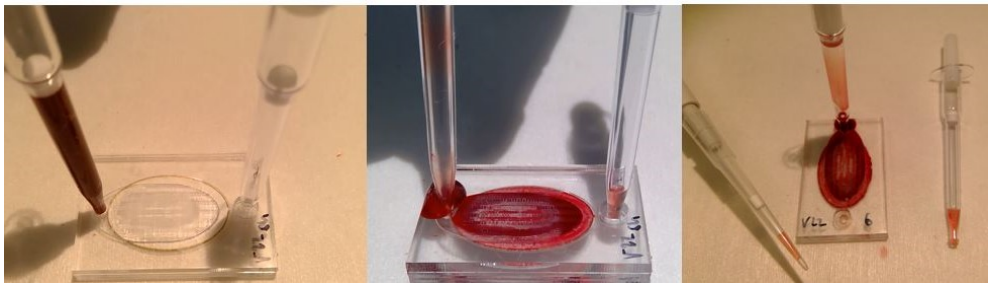

Figure 4.10: Testing process of the "double Minivette" setup, where a second Minivette was used to collect the plasma from the output. Left to right: the blood is pushed inside the Minivette. The second Minivette starts absorbing the output plasma, but fails to complete the collection process, which was finished using a pipette.

4.3 Devices for 100 µL Minivettes

The first step in the development of the devices for the 100 µL Minivettes consisted in resolving a common issue with the previous iterations. As shown in figure 4.11, when the Minivette was placed directly over the inlet the input blood would often backflow out during injection. Placing a small piece of laboratory tubing (1.57 mm I.D. and 3.18 mm O.D.) cut to 3 mm height around the Minivette tip created an air-tight seal that prevented blood backflow at the inlet.

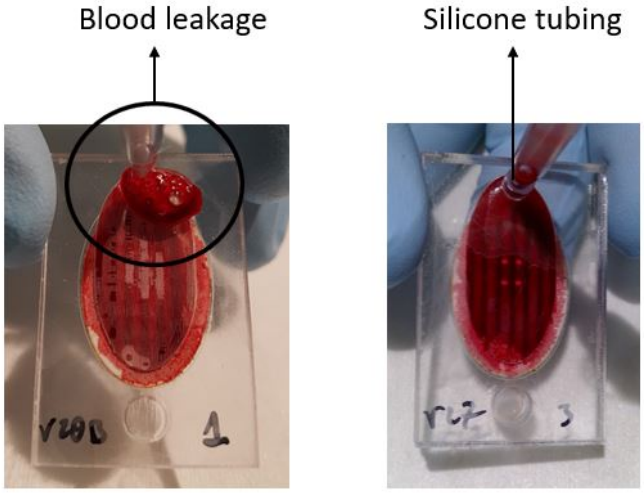

Figure 4.11: Left: blood leaking from inlet when injected from a Minivette directly placed over the PMMA. Right: issue resolved by placing a piece of silicone tubing around the Minivette tip, so that when pressed against the PMMA at the inlet an air-tight seal would be formed.

The final devices developed for the 200 µL Minivettes were heavily modified to correct the main issues that caused device failure. A successful device version (V4) is shown in figure 4.12. The inlet in the first layer is cut to perfectly accommodate the Minivette tip fitted with the silicone tubing. The second layer prevents the Minivette tip from piercing the membrane. The third and fourth layers host the membrane, ensuring that the edges are properly compressed and that the downstream side remains in contact with the collection channel in layer five. This device, along with its testing results, was presented in a poster at the MicroTAS 2019 conference in Basel, Switzerland, where the

matching paper was also published. A link to the publication can be found in appendix D.

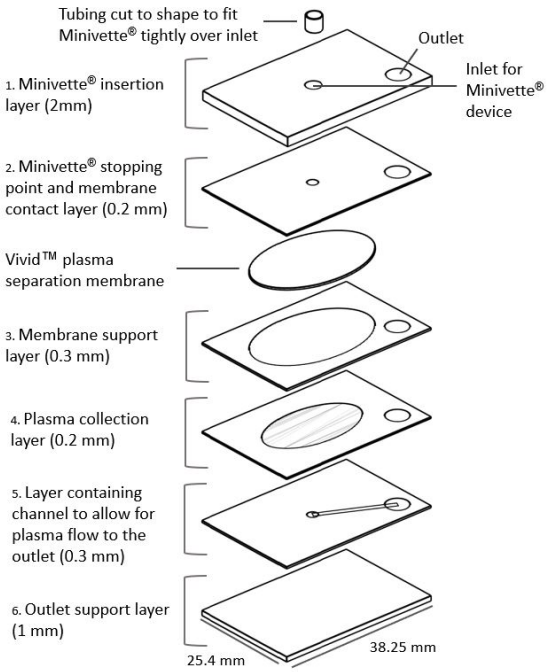

Figure 4.12: Schematic diagram of design V4, along with a description of each layer's thickness and function.

Several modifications were attempted in order to improve the performance of the V4 devices. In the design V7 (figure 4.13, left), a thicker first layer allows to better stabilise the Minivette during extraction and an extra layer was added to separate the downstream area of the membrane from the collection channel. This extra layer was removed in design V9 (figure 4.13, right), which retained the thicker first layer while including a thinner third layer to increase membrane compression.

Design V9 was further modified by including a leaf-shaped plasma collection channel in layer five, as shown in figure 4.14. The design seemed to improve the plasma quality and lower the failure rate, as the red blood cells tended to concentrate on the inlet area, while the outlet area remained clear compared to V4.

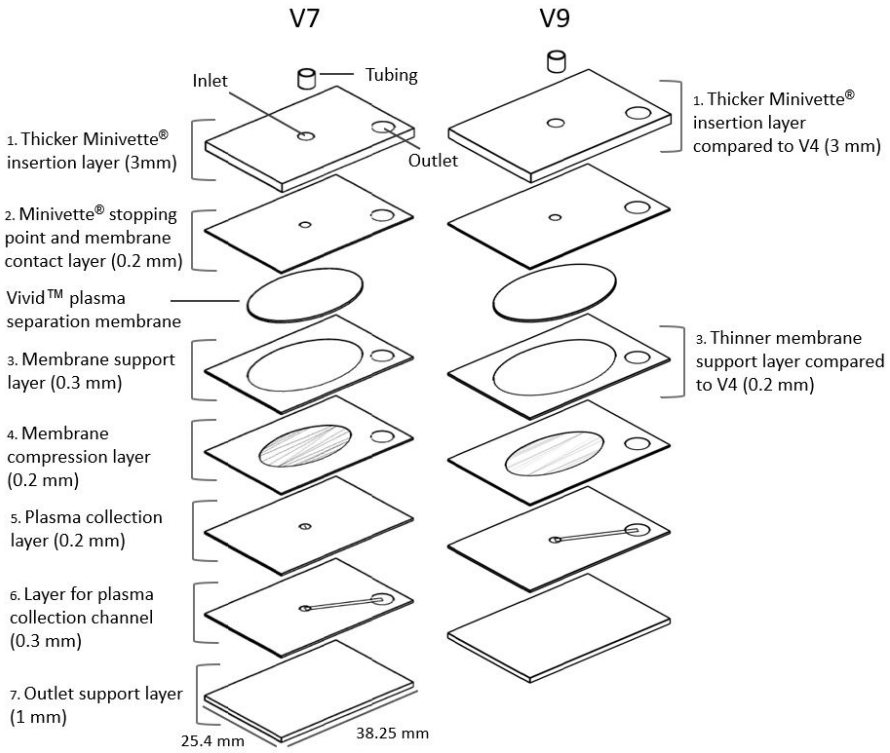

Figure 4.13: Schematic diagrams of designs V7 (left) and V9 (right). The only difference between the two designs is the presence of an extra layer between layers 4 and 6 in V7, with the objective to test the effect of separating the membrane compression layer from the plasma collection channel.

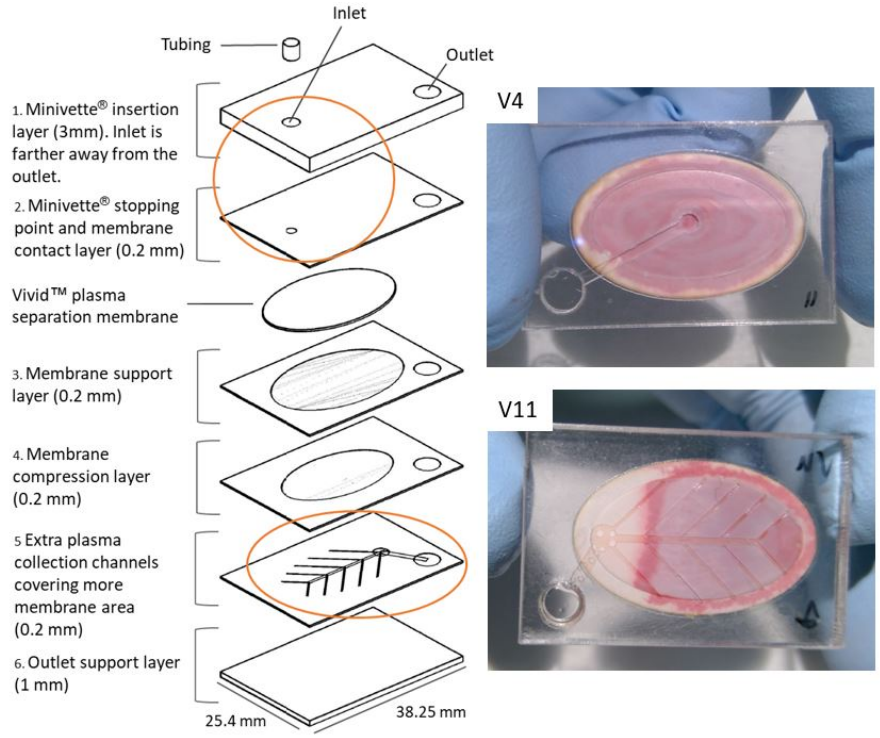

Figure 4.14: Left: schematic diagram of design V11 and highlighted differences with design V4. Right: comparison of bottom of devices V11 and V4 after blood testing.

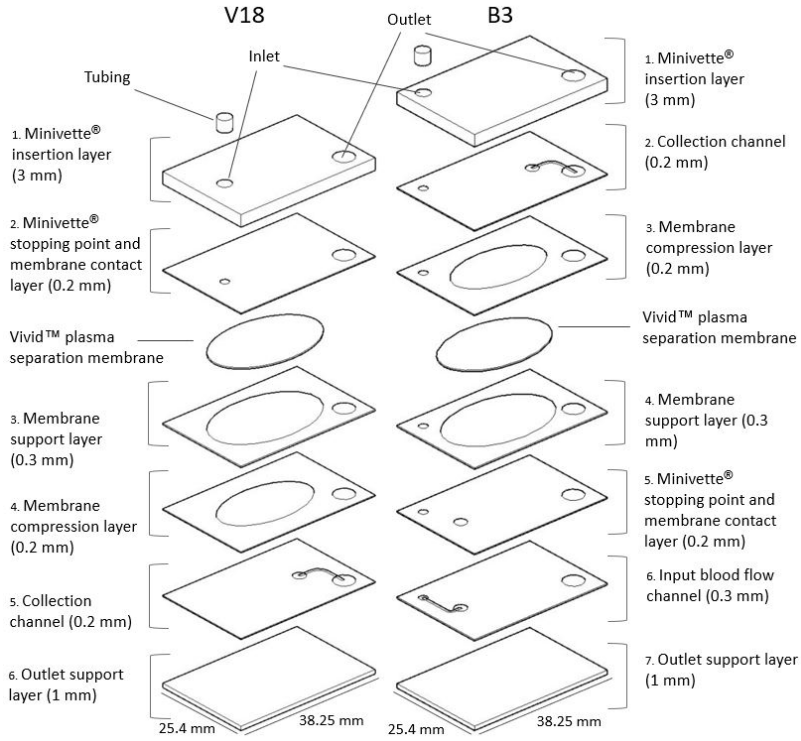

Figure 4.15: Left: schematic diagram of design V18. Right: labelled diagram of design B3. The designs were meant to explore the differences between a top-down (V18) and bottom-up configuration (B3). In the former, the upstream side of the membrane faces upwards, while in the latter the upstream side faces downwards, meaning that the blood is loaded from the bottom side of the device.

The final PMMA design iterations tested are shown in figure 4.15. V18 was the last iteration of the "top-down" designs, where the upstream part of the membrane faced upwards and the plasma was collected from underneath the membrane. V18 was similar to V11, but with a thicker membrane support layer and a curved collection channel that replaced the leaf-shaped pattern. B3, on the other hand, was part of the "bottom-up" series of devices, where the upstream side of the membrane faced downwards towards the bottom of the device and the plasma was collected from the downstream area above the membrane. The device was fitted with an inlet to bring the blood to the bottom of the device, where it was then redirected towards the upstream area of the membrane. The plasma was then pushed from the top of the membrane towards the outlet.

4.3.1 Operational steps

The operational steps of the PMMA devices developed for the 100 µL Minivettes are shown in figure 4.16. The steps correspond to method 2 as explained in section 3.7.1 of chapter 3.

4.3.2 Results and discussion

This section discusses the performance of the devices developed for the 100 µL Minivettes in terms of percentage of total available plasma extracted, plasma quality and failure rate. For the purpose of this analysis, only the performance of the main devices described in the previous section will be analysed. The "missing" device IDs in the

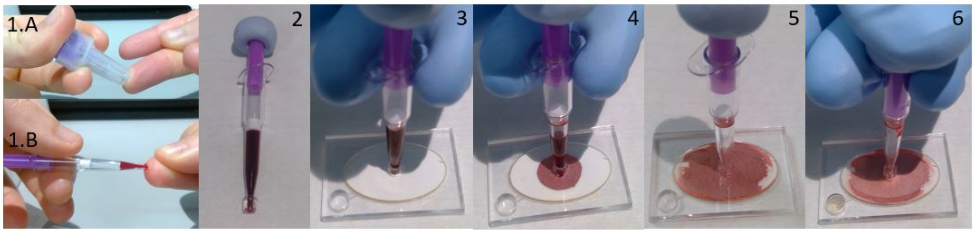

Figure 4.16: 1.A and B) The Minivette is filled with capillary blood. 2) Blu-tack cap and laboratory tubing are fitted on the Minivette. 3) The Minivette is then inserted into the device inlet. 4) The user presses the plunger gently and immediately releases it. This allows the membrane to start wicking the blood out of the Minivette. 5) Once the Minivette is completely emptied, the user waits 2 minutes for the plasma to accumulate in the collection layer. 6) The user presses the Minivette plunger and the plasma fills the outlet, ready for collection or further analysis downstream.

sequence belong to devices that either performed extremely poorly or could not be manufactured successfully.

Some of the devices were colour-coded to highlight their similarities. Devices with the same colour are identical but for one feature used to establish the effect of feature modifications. For example, devices V4 and V9 are identical except for the height of layer three, which is 0.1 mm thinner in V9, and therefore share the same colour (blue). Designs without a colour tag are independent from the others.

All devices were first tested with a range of SNBTS samples of varying haematocrit. Only some devices with V4, V18 and B3 designs were then tested with fresh blood. The results are summarised in table 4.1, which includes values obtained using both SNBTS and fresh blood.

Table 4.1: Average of yield, haemoglobin concentrations, failure rate and percentage of devices that extracted at least 25 µL of all devices tested for each design. The device types were color-coded in blue, red and green depending on feature similarity.

Device ID	Yield (%)	Hgb (g dL^{-1}) (analyser)	Hgb (g dL^{-1}) (UV-Vis)	Failure rate (%)	% with plasma $\geq$ 25 µL
V4	47.66	0.1256	N/A	26.23	47.54
V9	50.88	0.3333	N/A	7.69	61.54
V7	60.91	0.3000	N/A	50.00	28.57
V10	50.86	0.3400	N/A	16.67	66.67
V11	54	0.1944	N/A	7.14	85.71
V12	25	0.1500	N/A	50.00	16.67
V13	49.09	0.2111	N/A	0.00	87.50
V15	44.67	0.1000	N/A	50.00	33.33
V17	47.86	0.1143	N/A	25.00	75.00
V18	57.27	N/A	0.0900	33.33	66.67
B3	54.85	0.1313	0.0960	7.89	89.47

Yield analysis

Figure 4.17 shows the percentage of available plasma recovered by each device. The devices with the highest average yield were V7 (60.91%) and V18 (57.28%). B3 and V11 also performed well, having achieved an average of 54.86% and 54.01% respectively. With a low yield of 25%, V12 was the least impressive design, although only a few data points were collected for its evaluation.

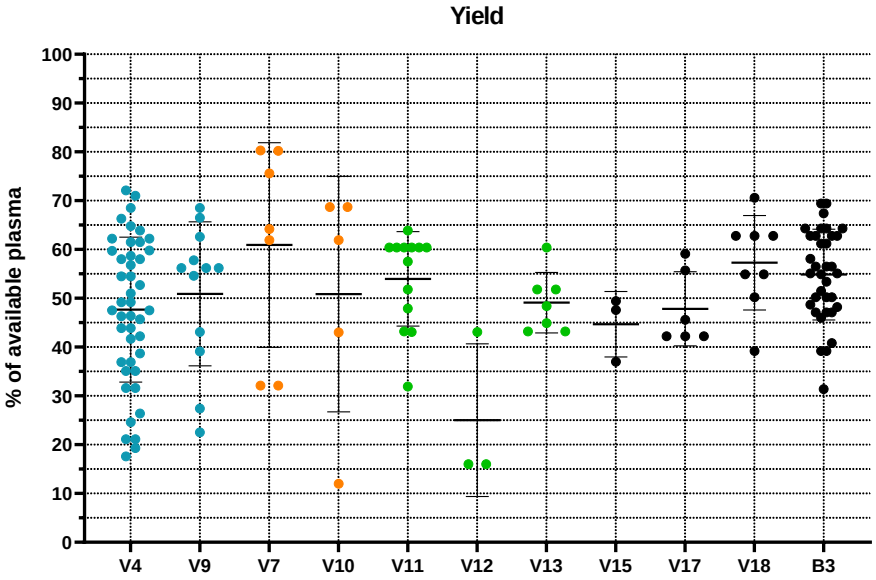

Figure 4.17: Yield of all devices developed for the 100 µL Minivettes. As the devices were tested with different blood samples of varying haematocrit, the results are given as volume percentage collected out of the total available plasma volume in order to make the values comparable. V4, V18 and B3 designs were mostly tested with fresh blood, while SNBTS blood samples were used for the remaining devices.

Plasma quality analysis

An increased haemoglobin concentration when compared to a centrifuged plasma control sample indicates that haemolysis occurred within the device during the extraction process. To be of high quality, plasma should contain as little additional haemoglobin as possible when compared to the control. The haemoglobin concentration of most plasma samples collected with the PMMA devices was measured using the haematology analyser, which could not detect any residual RBCs in any of the extracted plasma. The results can be seen in figure 4.18.

The data was not presented as the difference between haemoglobin concentrations of device plasma and corresponding control, but rather as a collection of all data points collected for each device along with the controls prepared from the samples used to generate the points. If the Hgb concentration difference would have been used, most data points in designs V4, V17 and B3 (and all from V15) would have been zero. This would have misled the reader into thinking that the devices performed perfectly, when the result would have been caused instead by the rounding of the Hgb concentration to the first decimal point in the analyser. The reader is encouraged to look back to figure 4.9 to observe how vastly different in colour two samples measured at 0.1 g dL^{-1} Hgb with the haematology analyser can be. Multiple controls were taken during the testing

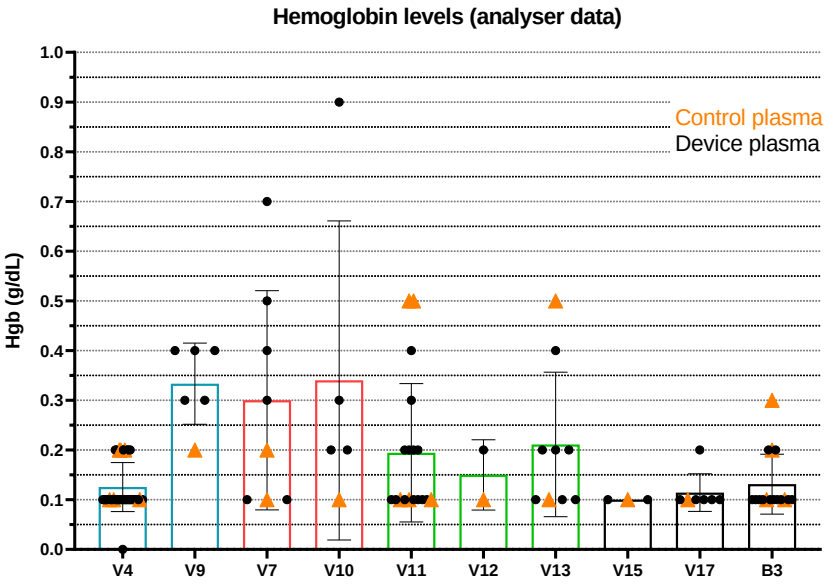

Figure 4.18: Haemoglobin concentrations of all devices developed for the 100 µL Minivettes along with the respective centrifuged controls. All measurements were taken using the haematology analyser.

process to evaluate the mixing procedure as explained in chapter 3, section 3.5.3. As the sample degraded during testing due to frequent manual mixing, haemolysis occurred and the haemoglobin concentrations of the controls increased, as can be clearly seen in the graph.

Despite the flaws in this haemoglobin measurement method, this data offers some insight into the quality of the extracted plasma. Devices V15, V17, V4, and B3 achieved the best average Hgb concentrations, with 0.1, 0.1143, 0.1256 and 0.1313 $\mathrm{g\,dL^{-1}}$ respectively. Once the UV-Vis protocol was established, the haemoglobin concentration of plasma samples $\geq 25\,\mu\mathrm{L}$ could be measured more accurately. This method was used to evaluate the plasma collected from all V18 and most B3 devices, which were tested using the same fresh blood sample. The results can be seen in figure 4.19. The average Hgb was 0.09 and $0.096\mathrm{g\,dL^{-1}}$ in both cases, while the centrifuged control was $0.0058\,\mathrm{g\,dL^{-1}}$ when fresh and degraded to $0.3\,\mathrm{g\,dL^{-1}}$ throughout the testing process. While it is not possible to entirely attribute these high haemoglobin concentrations to the devices due to sample degradation, not a single device produced plasma of quality close to the fresh control, indicating that significant haemolysis does indeed occur within the devices.

Failure rate

Figure 4.20 shows the number of failed devices for each design tested. Particularly successful devices that collected at least 25 µL, the cut-off volume for the UV-Vis analysis, were used as a benchmark of design success. B3 proved to be the most successful device type, with a low failure rate of 7.89% and 89.47% of the devices outputting $\geq$ 25 µL of plasma. V11 and V13 were also extremely successful, with 85.71% and 87.5% of the devices producing $\geq 25\,\mu\mathrm{L}$ of plasma respectively and a 0% failure rate for V13, although less data points were collected compared to B3.

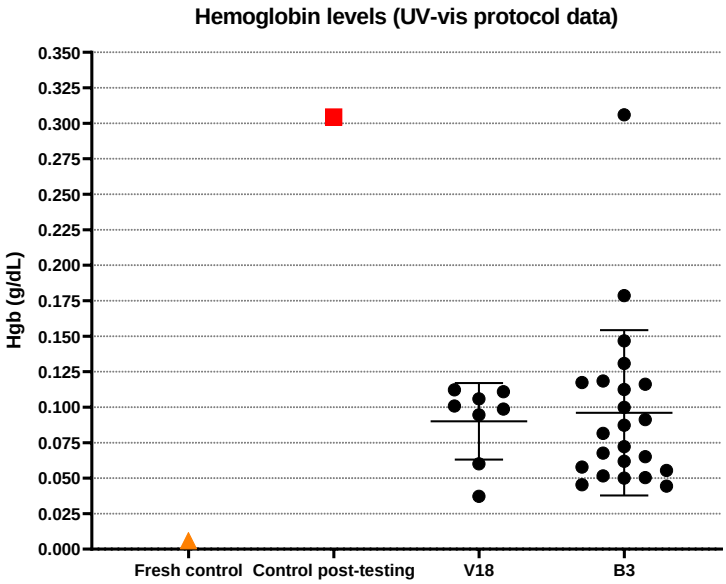

Figure 4.19: Haemoglobin concentrations of all V18 and B3 devices tested with fresh human blood. The measurement were taken using the UV-Vis protocol.

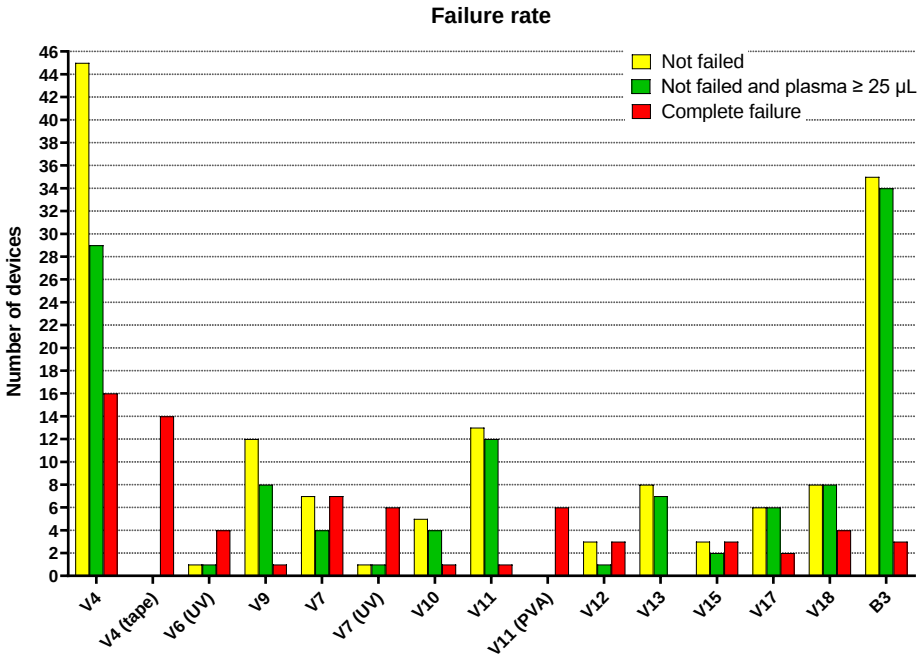

Figure 4.20: Failure rate of all devices developed for the 100 µL Minivettes.

4.3.3 Effect of feature modifications

Table 4.2 offers a summary of the feature modifications attempted and their effect on the devices developed. The colour coding previously introduced was retained for visual guidance on device similarities. Each feature is discussed in detail in the sections below.

Table 4.2: Feature modifications attempted during the development of the PMMA devices for 100 µL Minivettes. The device types were color-coded in blue, red and green depending on feature similarity as explained in section 4.3.2.

Device ID	Membrane support layer height (mm)	Collection channel height (mm)	Collection channel pattern
V4	0.3	0.3	Single channel
V9	0.2	0.3	Single channel
V7	0.3	0.3	Single channel
V10	0.2	0.3	Single channel
V11	0.2	0.2	Pattern 1
V12	0.3	0.2	Pattern 1
V13	0.2	0.3	Pattern 1
V15	0.2	0.2	Pattern 2
V17	0.2	0.2	Pattern 3
V18	0.3	0.2	Single channel
B3	0.3	0.2	Single channel

Membrane compression

The membrane experiences a uniformly higher compression in designs V9, V10 and V11 compared to designs V4, V7 and V11 respectively. The design pairs are otherwise identical in all other aspects. In the first device group, the membrane support layer height is 0.3 mm, while in the second 0.2 mm. The haemoglobin concentration of the devices with a higher membrane compression was consistently worse than their less compressed counterpart. However, the devices with a 0.2 mm thick membrane support layer were far less likely to fail and had a much higher percentage of devices that produced at least 25 µL of plasma. This is likely due to the fact that extra compression at the edges prevents blood from passing around the membrane and reaching the outlet, causing device failure. In conclusion, compression at the edges of the membrane is highly desirable as it reduces the likelihood of failure, while compression on the functional area of the membrane negatively impacts plasma quality by inducing excessive haemolysis.

Collection channel height

Devices V11 and V13 were identical but for the height of their collection channel, which was 0.2 mm in V11 and 0.3 mm in V13. Changing this feature did not appear to have any major impact on device performance, with V11 and V13 having similar yield (54 and 49%), plasma quality (0.19 and 0.21 $g\,dL^{-1}$ Hgb), failure rate (7.14% and 0%) and percentage of successful devices from which at least 25 µL of plasma were collected (85.71% and 87.5% respectively).

Collection channel patterns

With the relative success of the pattern placed in V11 (pattern 1), two more pattern were explored as shown in figure 4.21. Although few V15 devices were tested, the high failure rate and low yield indicated that pattern 2 was not an improvement over its predecessor. The V17 devices fitted with pattern 3 performed slightly better than its

V15 counterpart, although the yield was still lower than V11 and the failure rate higher. As such, pattern 1 remained the most successful of the three.

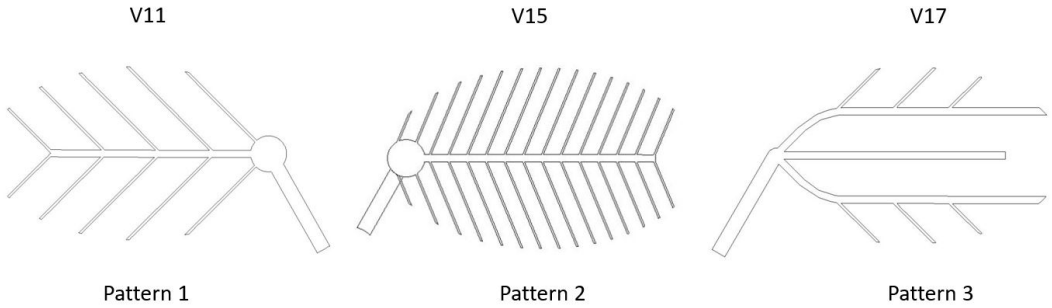

Figure 4.21: Three patterns tested during the PMMA devices development, matched to the ID of the designs where they were featured.

4.4 Summary

This chapter discussed the development and testing process of the PMMA devices, which consisted of multiple laser cut PMMA layers joined together using ethanol, which acted as plasticiser, and a heated press. The devices were designed to work in conjunction with a commercially available capillary blood collection device called Minivette. The first iterations of PMMA devices were designed for the 200 µL version of the Minivette, while the latest versions used 100 µL EDTA coated Minivettes. This change was both due to difficulties in the collection of 200 µL volumes of capillary blood and the necessity to reduce the membrane surface area needed for the successful filtration of a relatively large sample volume.

After the switch to the 100 µL Minivettes, a few successful devices were developed and the testing results for version V4 were published at the µTAS 2019 conference. The best device versions V18 and B3, however, were created and tested after the conference and consisted in identical designs, with the first using a top down configuration and the second a bottom up one. Both were tested with fresh blood and achieved a yield of 57.27% and 54.85% respectively. Although better than previous PMMA device versions, the plasma quality was still low, with a Hgb concentration around $0.1\,\mathrm{g\,dL^{-1}}$ for both despite being tested with fresh blood. Version B3 proved to be extremely reliable, with a low failure rate and most devices extracting at least 25 µL of plasma and can therefore be considered the most successful out of all the PMMA device versions tested.

Issues with sample mixing and haemoglobin concentration measurements limited the usefulness of the haemoglobin data collected, with V18 and B3 being the only versions where haemoglobin could be detected at concentrations below $0.1\,\mathrm{g\,dL^{-1}}$. Despite many iterations aimed at optimising the devices, plasma quality could not be significantly improved due to the excessive shear forces on the red blood cells caused by the pressing of the Minivette plunger, which was necessary to generate a pressure difference and drive the plasma towards the outlet. Nevertheless, in situations where higher Hgb concentrations are acceptable, the good yield and low failure rate of the devices make them useful tools for plasma separation using capillary blood collection tools such as the Minivette.

Other problems with these devices included:

- Difficult fabrication steps, which required extensive experience in order to minimise manufacture failure rate.
- The requirement for expensive equipment throughout the manufacturing process.
- Multi-step device operation with a significant waiting time for the user and the necessity to modify the Minivette before each use by adding tubing and Blu Tack at the top of the plunger.

All of these issues were resolved in the next iterations of devices, which are introduced in the following chapter, with a complete change in manufacturing methods and operational steps aimed at simplifying the fabrication, assembly and use of each device while simultaneously reducing material and equipment costs and increasing plasma quality.

Chapter 5

Early development of 3D printed devices

5.1 Overview

Additive manufacturing refers to the technologies that construct objects by adding layers of materials on top of each other until the whole object is complete. This is in contrast with subtractive manufacturing methods, such as machining processes, which rely on the removal of materials from a block to obtain the intended object. Early additive manufacturing technologies were developed and patented in the 1980s. Since the expiration of the fusion deposition modelling patents in 2009, 3D printing has gradually become an affordable and reliable rapid prototyping method [102]. As the technology progresses, print quality increases, making 3D printing an increasingly attractive technology for the development of microfluidic devices, as it enables the manufacturing of components with internal features without the need for layer bonding. This and the next chapter are dedicated to exploring ways to satisfy the original hypothesis, that is to develop good microfiltration plasma separation devices that can achieve the following objectives:

- Extract as much of the available plasma as possible.
- Leave no residual red blood cells in the extracted plasma.
- Avoid inducing haemolysis, that is the rupturing of red blood cell membranes.
- Provide quick extraction, with little to no waiting time for the user.
- Be low-cost, easy to fabricate and amenable to mass manufacturing.
- Be easy to assemble and use without prior expertise, with no complex steps for the user to follow.

5.2 Preliminary work

The following tests were carried out as a means of getting acquainted with the new printer and explore its strengths and limitations, particularly with regards to producing micro-scale features for the fabrication of microfluidic devices.

5.2.1 Smallest feature analysis

Minimum external channel width

The theoretical minimum XY resolution of the 3D printer was 47 µm. However, the limit for clearly defined features is bound to be higher and resin-dependent, and therefore needs to be established empirically. To determine the minimum open channel width that could be achieved with the 3D printer and the resin available, a test piece consisting of 0.2 mm deep open channels in the 10 to 300 µm width range was printed using the Prusa Tough Transparent resin with standard presets and two different layer heights: 0.05 mm and 0.025 mm. No supports were used and the part was printed flat on the platform without pads. The channels were printed in horizontal, vertical and diagonal orientations to observe the potential effect on print quality. The channels with widths between 10 and 100 µm were analysed under a Leica Microscope in both brightfield and darkfield mode, while the remaining channel images were taken using the Maozua handheld USB microscope. A summary of the results can be seen in figure 5.1.

As expected, the channels were non-existent until the 50 µm mark and not well defined until the 200 µm mark width was reached. The difference between channels printed with 0.05 and 0.025 mm layer was minimal, meaning that both are valid options for printing open channels in the micro to millimetre range. An open channel width of 200 µm is therefore the minimum that can be achieved with this 3D printer. However, a 300 µm channel width is recommended, as it leads to a better defined channel.

Measuring the depth of each channel was attempted with a Dektak® stylus profiler, but the instrument could not produce meaningful readings due to the original roughness of the resin. A channel-less sample can be seen in figure 5.2 for reference. Visual and tactile observation proved sufficient for this type of test, as it was clear that the channels were simply not defined enough at widths $\leq$200 µm.

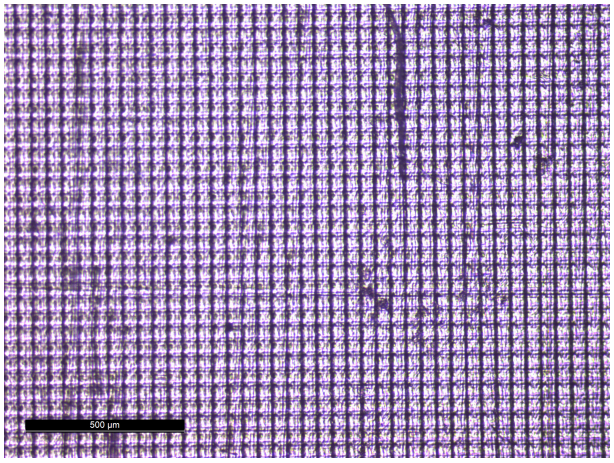

Figure 5.2: Surface of a 3D printed part. Although it appears rough, the pixel size is small and the surface feels smooth to the touch.

Minimum engraving and embossing

The objective of this test was to identify the minimum printable height of engraved (sunken) and embossed (raised) features. The parts were printed using the Prusa Tough Transparent resin with standard presets and 0.05 mm layer height. No supports or pads were used, as the parts were printed flat on the platform. The test piece consisted of

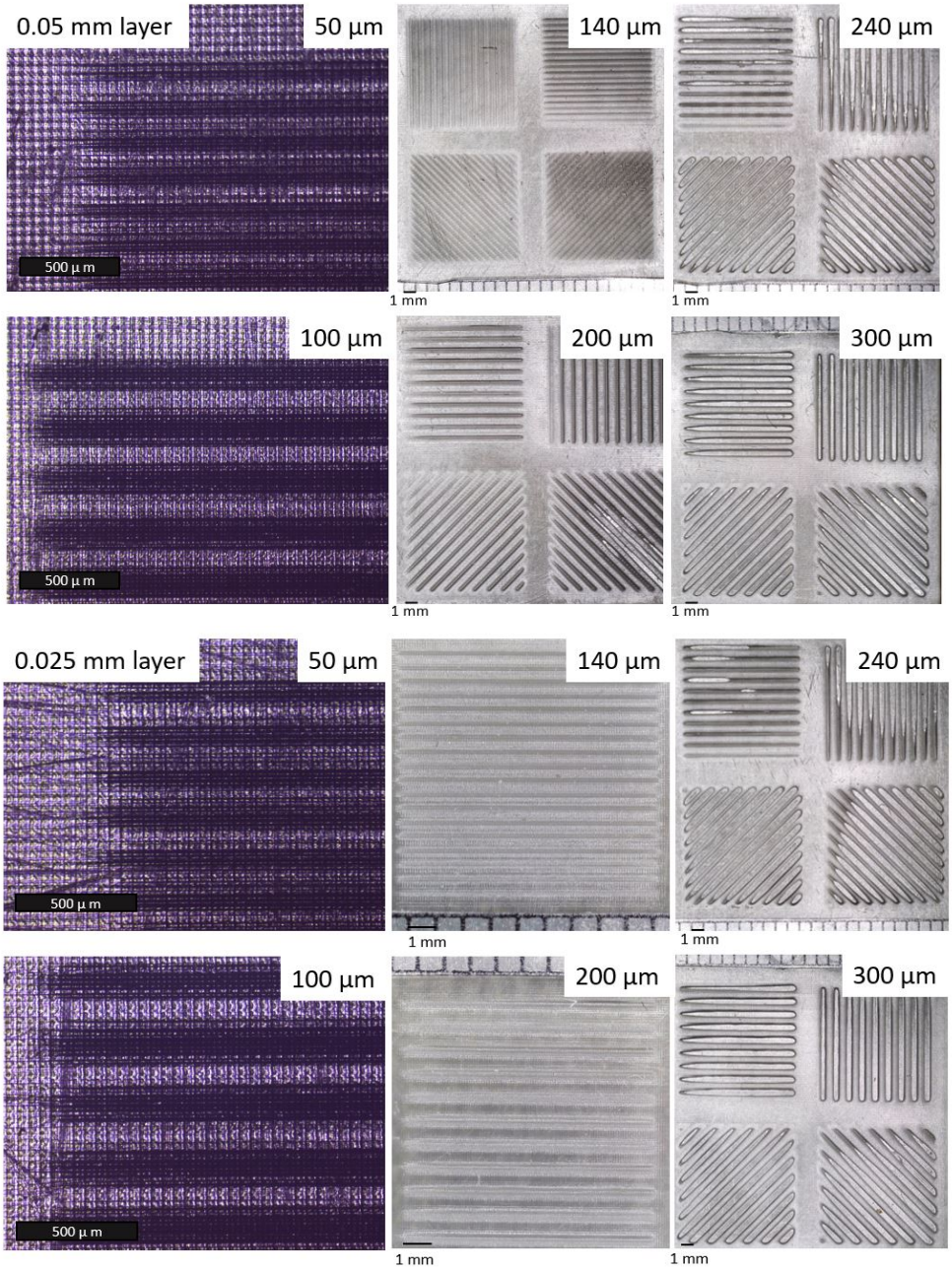

Figure 5.1: Microscope images of 3D printed channels with widths 50, 100, 140, 200, 240 and 300 µm at different orientations and magnification levels. The printing test was performed to determine the minimum possible channel width and was repeated for layer heights 0.025 mm and 0.05 mm.

a 50 × 20 × 1 mm^3 rectangle where 1 mm wide lines connecting the long edges were printed with the following settings:

- Engraving depth of 0.6, 0.4, 0.3, 0.2, 0.1 and 0.05 mm.
- Embossed height of 0.4, 0.2, 0.1 and 0.05 mm.

All of these features were successfully produced in the printed part as shown in figure 5.3.

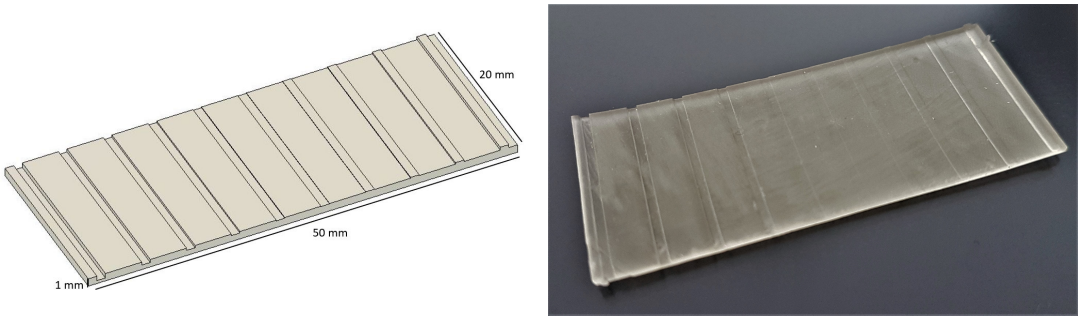

Figure 5.3: Design of the test parts developed for measuring of the minimum height of engraved and embossed features (left) and corresponding printed part (right). Although poorly visible, the features were correctly reproduced in the 3D printed part.

To measure the minimum printable width of engraved and embossed features, a rectangular test piece of size 50 × 20 × 2 mm^3 was printed with lines of 1 mm width going from one long edge to the other as shown in figure 5.4. The following widths were tested:

- Engraving width of 0.6, 0.4, 0.3, 0.2, 0.1 and 0.05 mm.
- Embossed width of 0.4, 0.2, 0.1 and 0.05 mm.

For the engraved features, the minimum width was 0.2 mm (with 0.1 mm leaving a faint mark). The minimum embossed width was 0.2 mm, as the two smaller lines did not survive the printing and curing process.

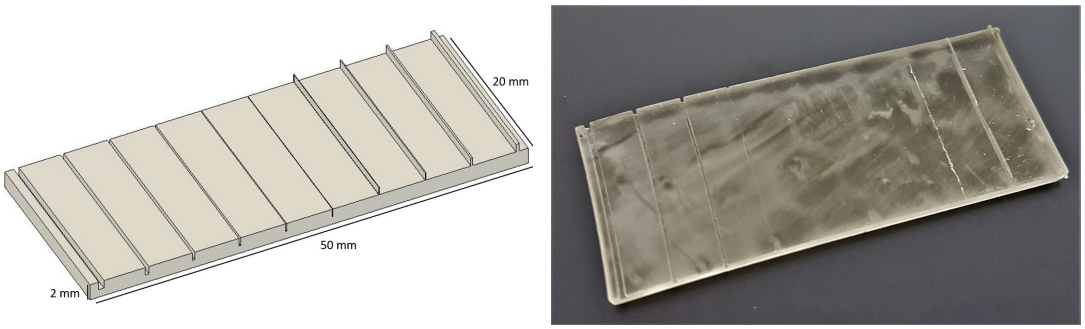

Figure 5.4: Design of the test part developed for the measurement of the minimum width of engraved and embossed features (left) and corresponding printed part (right). Both embossed and embedded channels failed to print at widths below 0.2 mm.

Minimum internal channel cross section

One of the advantages of 3D printing as a manufacturing method for microfluidic devices is the ability to create parts containing internal channels without needing to prepare

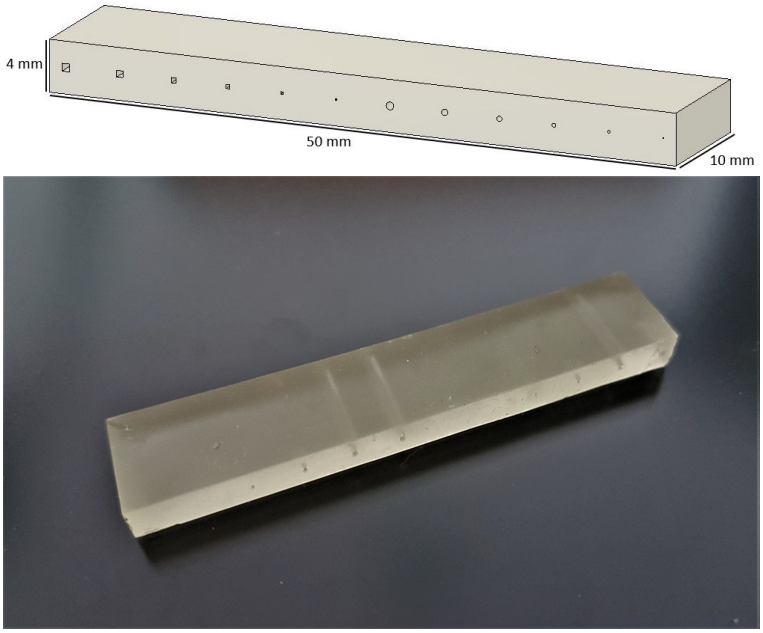

Figure 5.5: Top: design of the test part developed to determine the minimum internal channel width and diameter that can be printed with square and circular cross section respectively. Bottom: corresponding printed part.

and bond separate layers. To identify the minimum cross section of internal channels, a series of channels with square and circular cross sections were printed in the middle of a 4 mm thick, 50 × 10 mm^2 rectangular piece as shown in figure 5.5. The widths and diameters used were the following:

- Square cross sections with dimensions 0.6 × 0.6, 0.5 × 0.5, 0.4 × 0.4, 0.3 × 0.3, 0.2 × 0.2 and 0.1 × 0.1 mm^2.
- Circular cross sections of 0.6, 0.5, 0.4, 0.3, 0.2 and 0.1 mm diameter.

Only the circular 0.5 and 0.6 mm diameter and 0.6 mm width square channels were printed successfully, as shown in figure 5.5.

To explore the effect of orientation on the success of the print, a series of channels with square cross sections were printed in a 91 × 10 × 10 mm^3 rectangular piece divided into 10 sections, each containing 4 internal channels in different orientations: vertical, horizontal and both diagonals. The range of widths went from 50 to 500 µm with 50 µm increments for each part. The design can be seen in figure 5.6. The test was repeated twice and the only channels to consistently survive the printing and curing process were the 500 µm diagonal channels, while the 450 µm diagonal channels were successfully printed in only one test. None of the channels placed in other orientations were successfully printed. Given that in the first test both circular and square cross sections printed correctly with a diameter or width of 0.6 mm in a horizontal orientation, it was determined that the device channels should be at least 0.6 mm wide to ensure their correct printing.

In both the cross section and orientation tests, the objects were printed flat on the platform using the Prusa Tough Transparent resin with standard presets, no supports and no pads. The layer height was 0.05 mm for the cross section test and 0.025 mm for the orientation test.

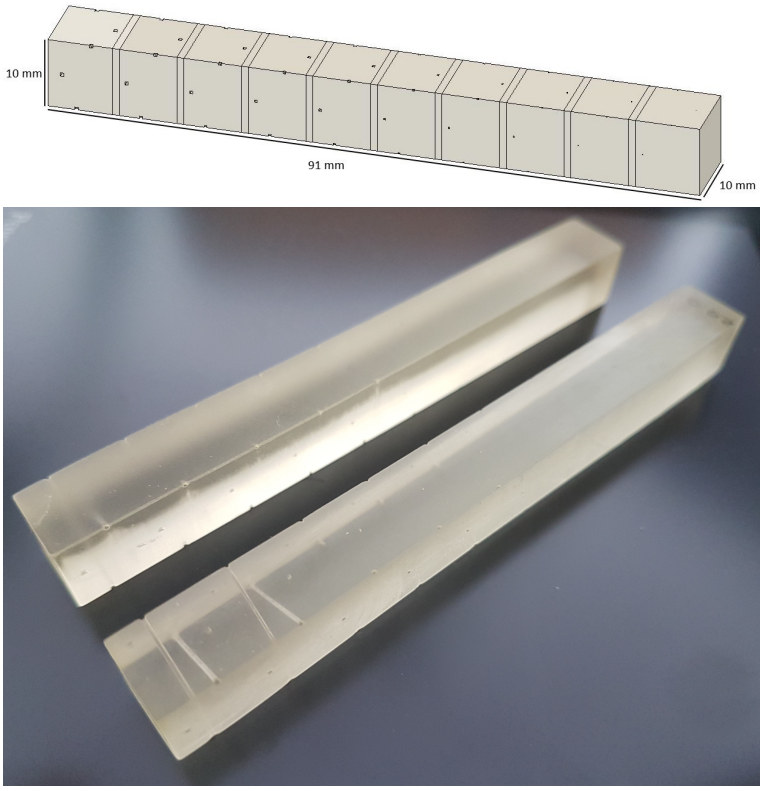

Figure 5.6: Top: design of the test part developed to observe the effect of orientation on the printing of internal channels. Bottom: corresponding printed parts.

Minimum wall thickness

To minimise the amount of material used to create each device, the minimum printable wall and surface thickness were determined by printing a hollow 50 × 20 × 10 mm^3 rectangular test piece with walls connecting each long side. A total of 6 walls 10 mm apart were printed with the following widths: 0.8, 0.6, 0.4, 0.3, 0.2 and 0.1 mm. The test object was printed flat on the print platform using the Prusa Tough Transparent resin with standard presets, no supports and no pads. All but the 0.1 mm walls survived the printing, although the 0.3 and 0.2 mm walls experienced significant warping as shown in figure 5.7.

Clearance

To identify the minimum clearance between interlocking pieces, three 30 × 30 × 10 mm^3 cuboids were divided into an inner part and outer part as shown in figure 5.8 and printed separately. All test objects were printed flat on the platform using the Prusa Tough Transparent resin with standard presets, no support and no pads and a 0.05 mm layer height. The inner and outer parts were separated with the following clearances: 0.2, 0.1 and 0.05 mm. While 0.2 mm proved to be an excessive amount of clearance, 0.1 mm was only marginally loose and 0.05 mm too tight, causing deformation of the outer part upon assembly. As such, the ideal clearance for two parts that need to maintain close contact is likely to be slightly lower than 0.1 mm.

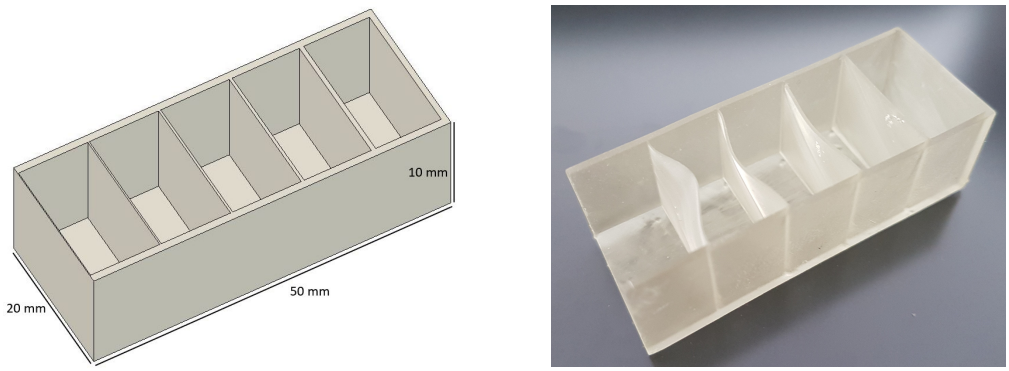

Figure 5.7: Left: design schematic and cross section of the test piece developed to test the minimum wall thickness. Right: corresponding printed part. Walls with thickness of 0.3 and 0.2 mm were bent significantly during the printing process, while the wall with 0.1 mm thickness failed to print altogether.

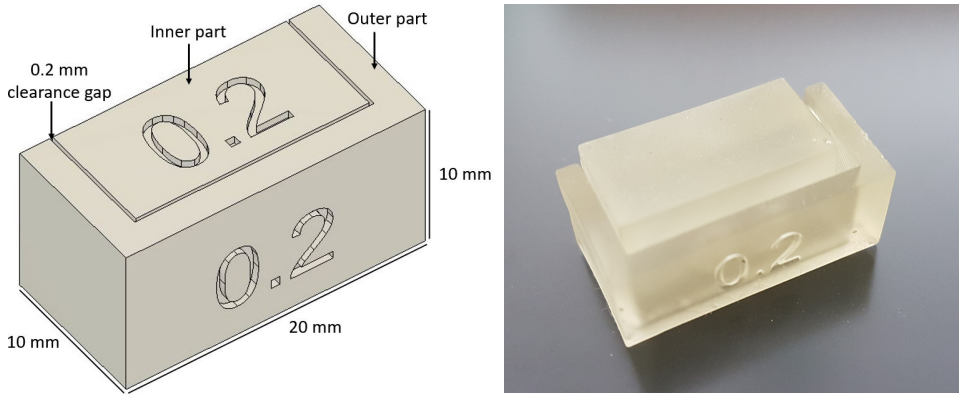

Figure 5.8: Left: labelled design schematic of a test set developed to determine the ideal clearance between interlocking objects. The example given is for a 0.2 mm clearance. Right: 3D printed and assembled object.

Fabrication tests summary

Table 5.1 summarises the results of the fabrication tests covered in this section.

Table 5.1: Summary of minimum feature values obtained during preliminary fabrication tests.

Feature	Minimum value
External channel width	200 µm
Internal channel circular cross section	500 µm diameter
Internal channel square cross section	600 µm width
Engraving depth	0.05 µm
Engraving and embossing width	200 µm
Wall thickness	400 µm
Clearance between parts	$\geq$ 75 µm, $\leq$100 µm

5.2.2 Parameter selection

Sample and membrane size

Because the equine samples available were generally small (<1 mL) and their availability limited, the volume used in the PMMA devices (100 µL) had to be halved so that the amount of 3D printed devices tested with each sample could be doubled.

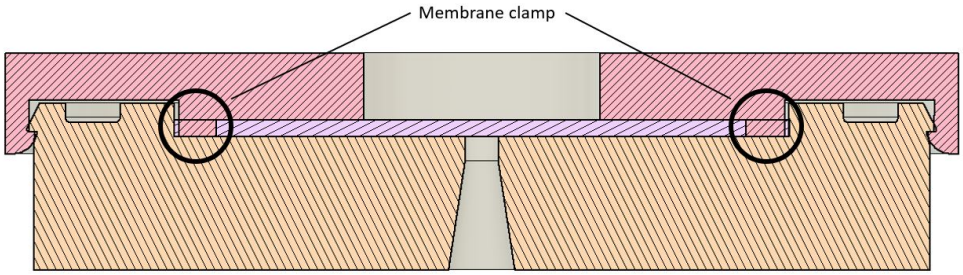

Figure 5.9: Cross section of a 3D printed bonded device (covered in detail in the next chapter), highlighting the membrane clamp that compresses the edges of the membrane to prevent blood spills during testing.

To prevent haemolysis and membrane damage leading to residual cells in the plasma, the surface area of the membrane should be large enough to accommodate the input blood volume. Similarly to the PMMA devices covered in chapter 4 4 the Vivid^{TM} GR grade filter (Pall Corporation) was used throughout the development of all the 3D printed devices. In order to prevent excessive membrane fouling, which leads to haemolysis, the manufacturer recommends a maximum blood volume of 40-50 µL cm^{-2}. As such, the membrane required a surface area of at least 1 cm^2 to accommodate a 50 µL input sample. As explained in Chapter 2, Section 2.2.9, the membranes were cut manually using a hollow hole punch set and were therefore fixed to a circular shape, with the diameter dictated by cutter size. In order to obtain a 1 cm^2 area, a circular membrane would require a 11.28 mm diameter. To prevent blood from spilling over the edges of the membrane during testing, the membrane was clamped down with a 0.8 mm protrusion as shown in figure 5.9. As this reduces the active surface area of the membrane, the total diameter had to be at least 12.9 mm. The hollow hole punch set included a 13 mm and a 16 mm cutter. When devices were fitted with a 16 mm diameter membrane, they were not able to produce any plasma due to the excess surface area of the membrane, which being strongly hydrophilic retained most of the plasma within the pores free from blood. On the other hand, the 13 mm membranes proved to be the perfect diameter for the devices and were therefore used throughout the development of all device types.

Selecting size of pipette and tips

The laboratory provided 1000 µL, 200 µL, 100 µL, 20 µL and 5 µL Eppendorf Research Plus pipettes. The 1000 µL pipettes generated too strong a vacuum, which resulted in gross haemolysis of the blood sample. On the other hand, the 20 µL and 5 µL failed to extract any plasma from the devices. To compare the performance of the 200 µL and 100 µL pipettes, fifteen 3D printed bonded devices (introduced in chapter 6) were tested with each pipette for a total of 30 tests using the same sample. The average output was 14.56 µL and 12.93 µL, while the average Hgb measurement was 0.0541 g dL^{-1} and 0.0483 g dL^{-1} for the 100 µL and 200 µL pipette respectively. As

the differences between the two were minor, the 100 µL pipette was selected and used throughout the experiments.

Selecting the wait for extraction time

The ideal sample preparation device should only require a one-step operation with no waiting time for the user. A quick extraction also helps prevent any plasma evaporation, which was deemed to be an important issue in a few studies where plasma separation devices were developed [44, 45]. As such, it was decided that the plasma would be extracted from the devices as quickly as possible without any waiting time. A few early devices were still tested with a delay of 60 and 120 seconds to evaluate any change in device performance. The results are summarised in table 5.2. Due to a lack of data points, these results are not conclusive, although they suggest that waiting not only provides no advantage but has the potential to worsen the quality of the extracted plasma for this type of 3D printed devices. Overall, more work is needed to conduct a thorough investigation of the effect of different waiting times.

Table 5.2: Preliminary testing of waiting times before extraction using an early iteration of bonded 3D printed devices. 5 devices were tested per setting, although not all were successful.

Devices tested	Time (s)	Output AVG (µL)	Yield AVG (µL)	H-value AVG	Hgb AVG ($g\,dL^{-1}$)
3	0	17.33	49.24	0.0210	0.037
4	60	16.75	47.59	0.0250	0.043
4	120	20	56.82	0.0468	0.066

5.3 Early 3D printed devices

The work described in Sections 5.2 and 5.2.2 set the foundation for the development of the first 3D printed devices. The three main features of a microfiltration device are the inlet, from which the sample is loaded into the device, the filter, which separates particles larger than the filter pore size from the input fluid, and the outlet, from which the filtrate is connected. In any pressure-driven filtration process, the fluid flows from areas of high pressure to areas of low pressure. While the PMMA devices were actuated by the Minivette, which provided high pressure at the inlet compared to the atmospheric pressure at the outlet, it was decided early in the development process that the 3D printed microfiltration devices were to be actuated by suction applied at the outlet using a laboratory pipette. As with their PMMA counterpart, the dead volume within the device had to be kept to a minimum to maximise the efficacy of the pipette extraction. Moreover, the membrane had to be correctly sealed within the device layers and no blood was to spill outside of the device during its operation.

FDM 3D printers allow the user to interrupt the printing process, place objects within the printed structures and then resume the print. This method can be used to potentially integrate membranes into a device, provided that potential issues with high temperatures and melted plastic damaging the membrane surface are resolved first. Although integrating objects mid-print was theoretically possible with the DLP 3D printer available, any membrane placed in the devices during the printing process would have been inevitably soaked with resin and permanently damaged. As such, the only way to integrate a filter in the 3D printed devices was to enclose it within two or more parts.

Therefore, a fundamental requirement to satisfy was the creation of enclosures strong enough to compress the edges of the membrane, while also being easy to manufacture and assemble.

Depending on the material, a wide range of methods are available for permanently or temporarily joining two plastic parts. Some methods rely on changes at the atomic or molecular level caused by the formation of chemical bonds, such as in adhesive bonding and welding, while others utilise mechanical forces without altering the material itself. Commonly employed in everyday plastic objects are adhesives and glues, mechanical fasteners and integral mechanical attachments. Mechanical fasteners make use of external items such as nuts and bolts to join two or more parts. Integral mechanical attachments, on the other hand, allow two parts to be joined without using any external component. Instead, geometric features already present in the mating parts are used to create mechanical interference that prevents the parts from moving and/or separating [103]. A common example of integral attachments are snap-fit lock mechanisms, which immediately appeared particularly attractive in the context of this work as they require no external materials or equipment and can be assembled by any person with minimal or no experience. This makes them an extremely quick and cost-effective method for connecting two parts both permanently and temporarily. As shown in the preliminary printing tests, parts 3D printed using thermosetting tough resins could contain features as small as 200 µm, meaning that the 3D printer could successfully create parts with small interlocking features. This section will provide an overview of the different type of attachments tested and then describe the early attempts at using them to produce 3D printed devices for sample preparation.

5.3.1 Overview of integral snap-fit mechanisms

The term snap-fit traditionally only refers to the lock features of integral attachment interfaces. In this text, however, it will be used to refer to the entire interface, which can include locators, locks and various enhancements that contribute to the creation of a mechanical attachment between two or more parts [104]. Snap-fit mechanisms take advantage of the viscoelastic property of polymers, which allows them to deflect under the application of force and gradually return to their original position once the force is no longer applied. A protruding part in one component can be briefly deflected to fit into the undercut of another component. Once assembled, the material is no longer under stress and will relax into its original shape, preventing or restricting the movements of the parts across one or multiple axes. Snap-fits take their name from the tendency of the lock features to produce a “snap” sound during assembly. Although calculations for predicting the behaviour of snap-fit mechanisms are usually intended for thermoplastic materials, they can also be used for thermosetting materials that display similar behaviours, such as the resins commonly used in modern SLA and DLP printers. Important properties to consider during the design of snap-fit mechanisms are stress (σ) and strain (ϵ), which are defined as follows [70]:

$$\sigma = \frac{F}{A}[\mathrm{N\,m^{-2}}] \tag{5.1}$$

$$\epsilon = \frac{\Delta L}{L_{orig}} \tag{5.2}$$

where ΔL refers to the change in dimensions of the body and L_{orig} to the original dimensions.

Stress refers to the amount of force that a material experiences at its surface, while strain describes the displacement of the material under force. Both properties can be found in Hooke's Law, which states that the deformation of an object is directly proportional to the deforming force:

$$\text{Hooke's Law} = F/A = \sigma = E\epsilon \tag{5.3}$$

where E is Young's Modulus.

Figure 5.10 illustrates the relationship between stress and strain in thermoplastic plastic materials. Young's Modulus is calculated in the initial linear region, where Hooke's Law holds and stress and strain increase at a proportional rate. Once the elastic limit, or yield point, is reached, the material sustains irrecoverable damage and will no longer be able to return to its original shape when the external force ceases to be applied. If the stress continues, the material will reach a breaking point where its polymer chains are pulled apart and eventually rupture. The maximum stress that a material can sustain before breaking is referred to as its tensile strength.

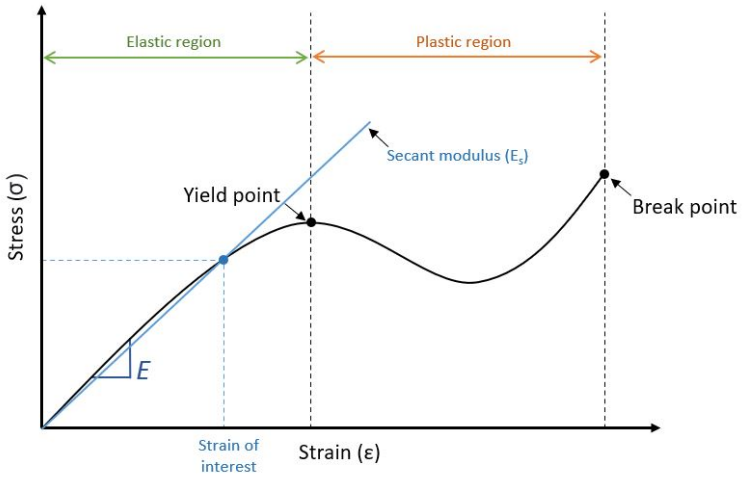

Figure 5.10: Annotated example of a stress-strain curve of a viscoelastic material. The elastic region refers to the amount of strain that the material can experience without compromising its structure permanently. Once the yield point is passed, the material can no longer regain its initial properties.

The stress-strain curve provides important information for the development of snap-fits. The protruded material needs to be able to bend, but not excessively as to exceed its recoverable region, as it needs to return to a stress-free condition at the end of the assembly process. The calculation process for common snap-fit features take into account both the mechanical load sustained by the parts during assembly and the force required for the parts to be assembled successfully. Several books and online resources were used during the development of the snap-fit attachments, most notably Chapter 4 of the "Integral Mechanical Attachment" by Robert Messler [105], "The First Snap-Fit Handbook" by Paul Bonenberger [104] and "Plastics Product Design" by Paul F. Mastro, particulalry Chapters 2 [70] and 9 [106].

Cantilever beams

Cantilever-based snap-fits are the most common and used type. The main parameters used in their characterisation are:

- Beam length L.
- Beam base width (b) and thickness (h_0), and for tapered beams the thickness at the tip (h_L).
- K, the proportionality ratio constant for the ratio h_L/h_0, to be used for calculations involving tapered beams.
- Beam undercut (y), that is the beam deflection needed to engage the snap.
- ϵ = material specific maximum allowable strain, calculated as a percentage of strain at break point ϵ_{break} or strain at yield point ϵ_{yield}, both shown in figure 5.10.

Values for both K and ϵ, along with equations to calculate y using the other parameters, can be readily found in the resources provided, particularly table 4.1 in [106] and [105]. For example, to calculate the deflection necessary for an ABS cantilever beam of rectangular cross section with $L = 20\,\text{mm}$ and $h = 5\,\text{mm}$, the following equation would be used:

$$y = 0.67 \times \frac{\epsilon L^2}{h} \tag{5.4}$$

The maximum permissible strain for ABS is 6-7% [106]. As such, if the snap-fit is to be designed for single use, Eq. 5.4 would become:

$$y = 0.67 \times \frac{0.06 \times 20^2}{5} = 3.2\,\text{mm} \tag{5.5}$$

For snap-fits that require to be disassembled and re-assembled multiple times, it is recommended to use half of ϵ. In our case, this would lead to the following:

$$y = 0.67 \times \frac{(0.5 \times 0.06) \times 20^2}{5} = 1.6\,\text{mm} \tag{5.6}$$

Should a tapered beam with height going from h_0 to h_L be used instead, the Eq 5.4 would change to:

$$y = 0.67 \times \frac{\epsilon L^2 K}{h_0} \tag{5.7}$$

In the previous example, if the height of the beam changes from $h_0 = 5\,\text{mm}$ to $h_L = 2.5\,\text{mm}$, we would know from table 9,1 in [106] that $K = 1.636$, and therefore:

$$y = 0.67 \times \frac{0.06 \times 20^2 \times 1.636}{5} = 5.261\,\text{mm} \tag{5.8}$$

which is a significant improvement over the non-tapered version as it allows the beam to be deflected a longer distance before breaking. Another significant advantage consists in applying a radius to the base of the cantilever, shown in figure 5.11 as R. This is because the bending stress tends to concentrate at the attachment of the cantilever beam to its support structure, which can easily lead to cracking in more rigid materials when the snap-fit is used repeatedly. By rounding the intersection between the beam and the base object, the stress relative to beam thickness can be relieved by R/h_0, with the recommended ratios being 0.5 and 0.6 [106].

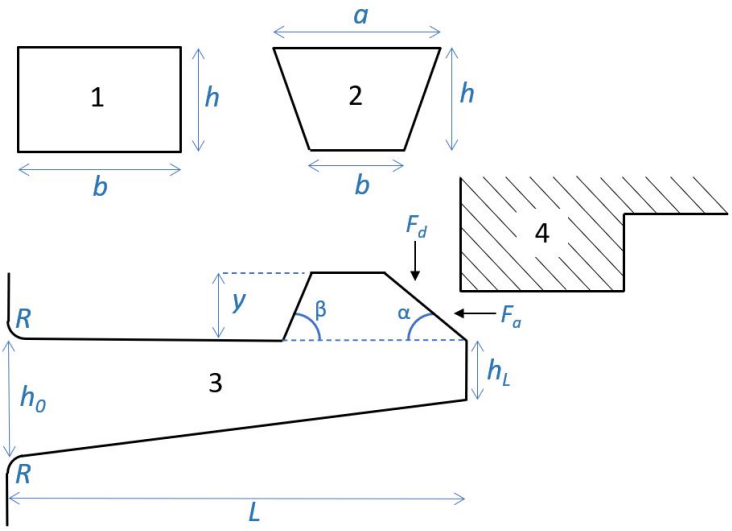

Figure 5.11: Labelled schematic representation of a cantilever beam approaching a catch. 1) Rectangular beam cross section. 2) Trapezoidal beam cross section. 3) Example of a tapered cantilever beam. 4) Catch object to be engaged with the cantilever.

It is also important to calculate the forces acting on the beam to ensure that they are appropriate for the given application. To this purpose, the following parameters are required:

- Material specific coefficient of friction μ.
- Insertion angle α: a steeper angle leads to a more difficult assembly experience and an increased deflection of the beam.
- Retention angle β: the higher this angle is, the harder is becomes to disassemble the snap-fit. Angles $\geq 90°$are often found in non-releasing snap-fit hooks that are not meant to be disassembled [104].

The assembly force is the force required to assemble the snap-fit, that is to deflect the beam and overcome the friction between the materials of the mating parts. It is highly dependent on the insertion angle and is calculated as:

$$F_a = F_{df} \frac{\mu + \tan\alpha}{1 - \mu \tan\alpha} \tag{5.9}$$

Similarly, the disassembly force required to disengage the beam and disassemble the snap-fit can be calculated as:

$$F_d = F_{df} \frac{\mu + \tan\beta}{1 - \mu \tan\beta} \tag{5.10}$$

where the retention (or disengagement) angle is used instead of the insertion angle. In both equations, F_{df} refers to the deflection force, which is defined as:

$$F_{df} = \frac{b h_0^2 \epsilon E_s}{6L} \tag{5.11}$$

where E_s is the secant modulus obtained by dividing the stress by the strain of interest ϵ, which is shown in figure 5.10, and b, h_0 and$L$ are the dimensions in figure 5.11.

Annular snap-fits

Annular snap-fits are another extremely popular type of snap-fit mechanism that can be used in rotationally symmetrical parts. They require larger assembly forces than cantilever beams and their behaviour is more difficult to predict mathematically due to the total deformation area of both hub and shaft components being harder to establish. However, an estimation can be made under the assumption that deformation only occurs in the hub. The variables used in the following equations are illustrated in figure 5.12.

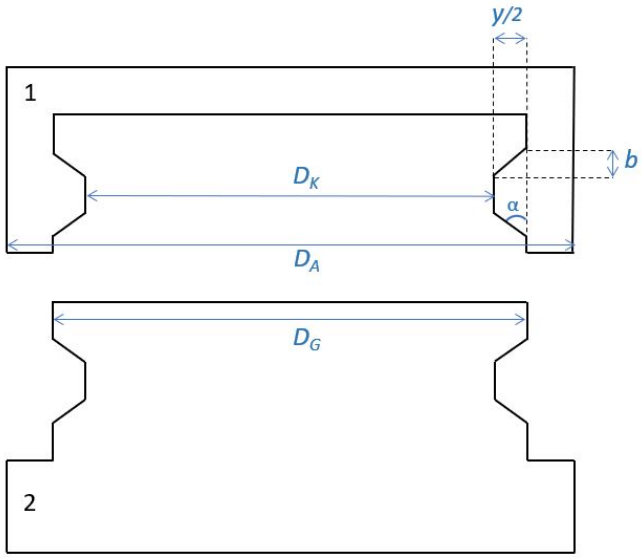

Figure 5.12: Labelled schematic representation of an annular snap-fit comprising a hub (1) and matching shaft (2).

The pressure on the joint is expressed by the following [106]:

$$P = \frac{y\, E_s}{D_k\, K} \tag{5.12}$$

where E_s is the secant modulus of the material and K is a geometric factor calculated as

$$K = \frac{(D_A/D_G)^2 + 1}{(D_A/D_G)^2 - 1} \tag{5.13}$$

The assembly force required to assemble an annular snap-fit can be approximated as follows:

$$F = P \times \pi \times D_G \times 2b \times \frac{\mu + \tan\alpha}{1 - \mu\tan\alpha} \tag{5.14}$$

Snap-fit adaptations for low-cost 3D printers

The first barrier to the adaptation of these calculations to this project was the lack of technical data for the resin used (Prusa Tough Transparent, which has since been discontinued), as the manufacturer had not tested their products to obtain a stress/strain curve and did not know what the tensile strength of the cured resin was. The second barrier was the inability of the 3D printer to produce overhangs that matched exactly those of the original design. As such, any calculation would have been far from the actual result. Figure 5.13 highlights the disparity between design and printed parts with regards to overhang lengths, depths and angles. Clearly, the insertion and retention angles are extremely different between the printed objects and the design. However, because the design was made with this issue in mind, it still resulted in a functional snap-fit mechanism in the finished product. A year into the development of successful 3D printed snap-fits, technical data sheets for commercial resins became the industry standard. By then, effective 3D printed snap-fit mechanisms for the plasma separation devices were already developed by adopting most recommendations offered in the snap-fit resources used and determining feature dimensions by trial and error. As such, calculations were deemed to be redundant.

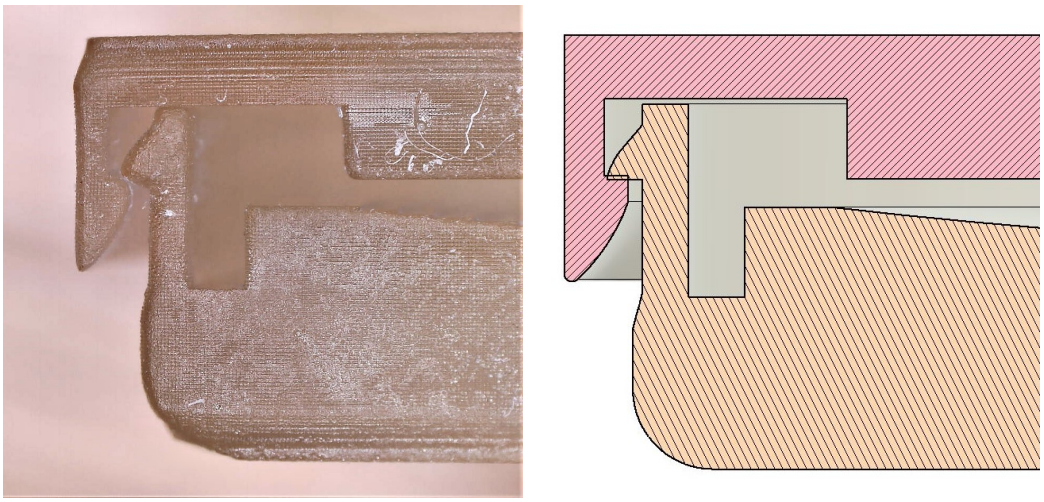

Figure 5.13: Comparison between cross sections of the same early-stage prototype of 3D printed device. This image highlights the disparities between the design and actual printed part, particularly with regards to the the retention and disengagement angles and clearances. These differences limit the usefulness of calculations to predict part behaviour.

5.3.2 Threaded devices

Integrally threaded parts are rigid interlocks that are assembled by repeatedly twisting a mating part into a base part. Effective threads can be printed within the limits of the 3D printer. Fusion 360 offers a range of in-built threads with pre-calculated clearances that can be automatically applied to circular surfaces. Custom threads can also be created either manually or using the "coil" command, which allows the user to control the following:

- Number of revolutions and rotational direction of the coil.
- The distance between threads (referred to as pitch) and total height of the coil.
- The size and shape of the coil cross section (triangular, circular and squared options available).
- An angle option for the creation of tapered threads.

Establishing thread type

In the first attempts, standard ISO pipe threads and ISO metric profile threads were applied to the designs with no added clearance (the default gap between the mating parts was 0.1 mm). Although the resulting prints were successful, the parts could not be assembled due to the excessive friction. At this stage it was also observed that the tough resins used were brittle, quick to break and easily damaged by friction, with powdery residuals being released from parts sliding against one another during assembly. Adding an extra 0.1 mm and 0.2 mm for a total clearance of 0.2 mm and 0.3 mm respectively significantly improved the assembly process, but led to some play between the parts in the Z-axis. Movement in the Z-axis needed to be minimised to clamp down the membrane effectively and prevent blood spilling around the edges of the membrane during testing. With this objective in mind, custom threads were built using the coil command. The pitch, revolutions, shape and width were progressively adjusted until a satisfactory result was reached with the following settings: 13 mm diameter coil, with two revolutions, a circular cross section with a diameter of 0.8 mm, a thread pitch of 1.05 mm and 0.1 mm clearance between mating and base parts. The resulting thread design can be seen in figure 5.16. This design allowed for an easy assembly process while at the same time creating a tight connection with minimal movement between the two parts.

Grip supports for easy assembly

With the addition of the membrane, threaded parts that were previously effortless to combine suddenly required a much larger assembly force due to the membrane matrix resisting compression. This made the assembly difficult and often impossible to complete by hand. To resolve this issue, several methods were developed to facilitate the assembly process. The first attempt consisted in adding two "handles" to the top layer and four in the bottom so that the user could have a surface to leverage on while twisting the parts (figure 5.15 A). When the handles in the top and bottom overlapped, however, completing the revolution proved to be extremely difficult. In the second design two more handles were added to the top layer to correct this problem (figure 5.15 B). Additionally, the handles were rotated by 45°compared to the bottom ones so that at the end of the last revolution, as the assembly force grew, the user could reach the handles more easily and without overlap to complete the assembly. While theoretically

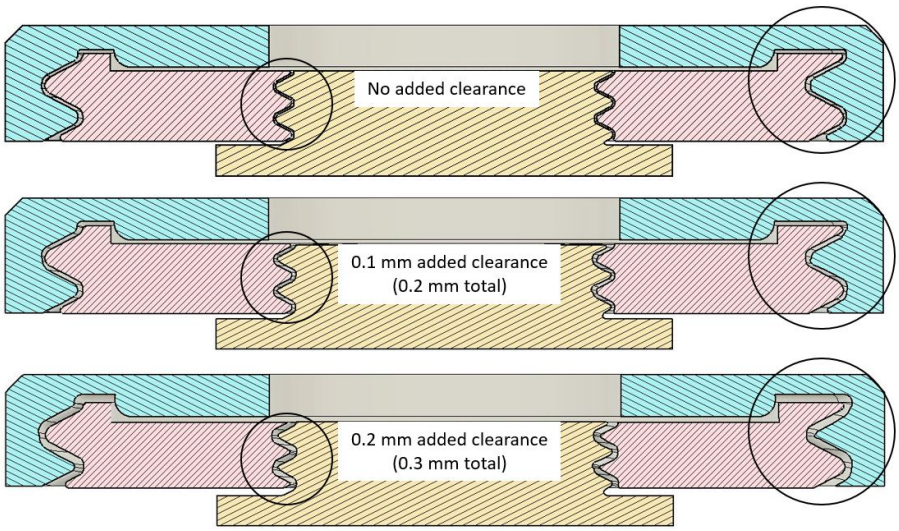

Figure 5.14: Test components highlighting the difference between ISO pipe threads of size 22.911 (pink and blue) and 9.728 mm (pink and yellow), class A, with no added clearance (0.1 mm default), then with 0.1 mm and 0.2 mm mm added to the original clearance.

sound, this method proved to be extremely uncomfortable for the user as the handles dug deep into the skin, making the assembly process rather painful when performed by hand. To resolve this issue, but still include a feature that would improve the grip over the parts to facilitate their assembly, the handles were then removed in favour of a knurled top (figure 5.15 C). Although less painful to operate from a user's perspective, completing the assembly by twisting the top for the correct amount of revolutions was often difficult without the use of any tools. Pliers were used during the assembly of test devices to prevent blisters and excessive discomfort.

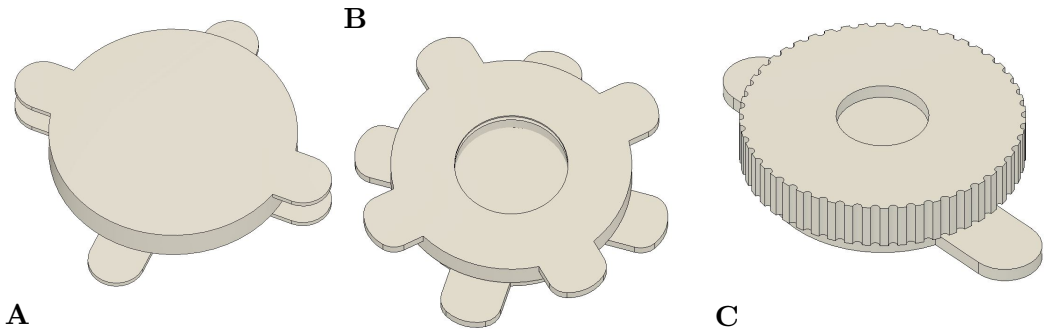

Figure 5.15: Comparison of three main methods used to facilitate the assembly of threaded parts. A) Because the tabs on the top and bottom parts are aligned, the assembly is difficult to complete towards the end of the rotation as the user's fingers overlap. B) The top tabs are shifted 90°compared to the bottom one, effectively resolving the problem in design A. However, assembly can be painful for the user as the twisting forces are relatively high and the tabs thin. C) To help resolve comfort issues during use, the tabs in the bottom part are replaced by grooves that help the user maintain a tight grip over the part during assembly.

Compression methods for membrane edges

Compressing the edges of the membrane correctly prevents blood from reaching the outlet and is therefore a fundamental feature of successful microfiltration plasma separation

devices. Figure 5.16 shows three membrane clamping methods where the compression is provided by protruding features in the top and bottom layer. When assembled correctly, designs A and B both compressed the membrane adequately, while C proved ineffective as the devices could not be fully assembled and a gap would form under the membrane, increasing the dead volume and leading to device failure during testing. Four A and B device types were tested with whole blood to see if significant differences could be seen between the methods. The average yield was 25.75% and 22.17% for A and B respectively, with no blood reaching the outlet of the device in either case. As the difference was minimal, it was decided to only proceed with one method and the configuration displayed in design A was adopted for subsequent designs.

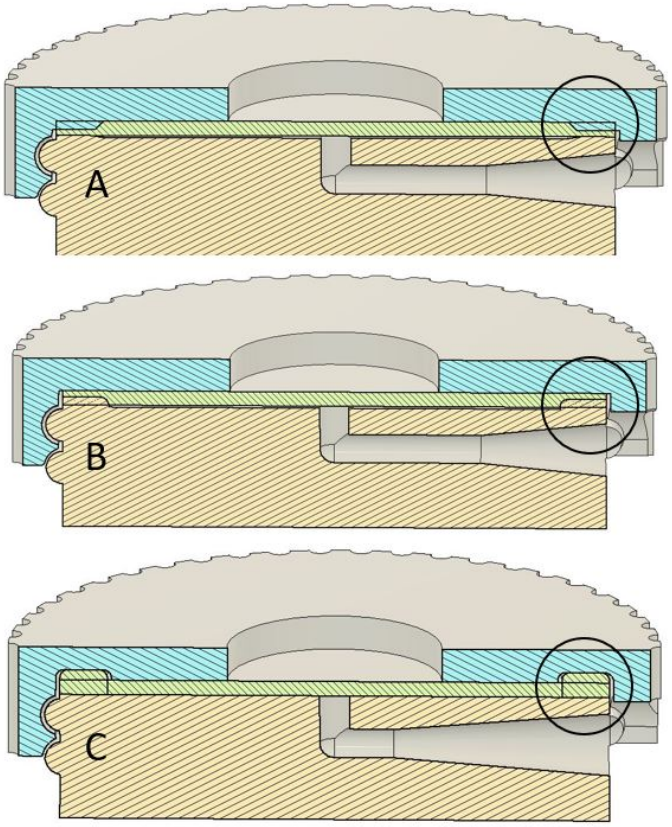

Figure 5.16: Cross section difference between different clamping methods. A) The membrane is partially compressed by a protrusion in the top layer. B) The protrusion is placed in the bottom layer. C) As (B) but the membrane is fully compressed when assembly is complete as the clamp reaches all the way up to the top layer.

Another version of this clamping method, shown in figure 5.17, used a double thread with the intention to further prevent the inner part springing back after compressing the membrane. This method failed to provide significant improvements on the membrane clamping and instead made twisting of the top part into the thread grooves more difficult. As such, it was quickly abandoned in favour of the simpler original version.

Using these clamping methods, the membrane had a tendency to resist the twisting motion due to friction and sustain damage during the assembly process. To prevent this issue, another method was explored where the clamping mechanism was detached from the layers as shown in figure 5.18. This allowed the top layer to rotate over the extra component, which itself experienced minimal twisting motion due to it being in

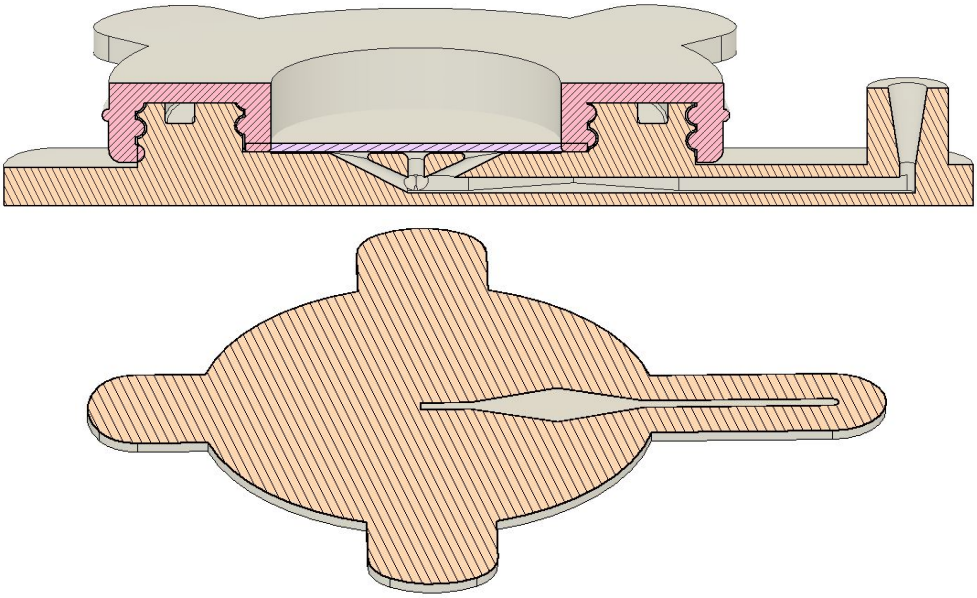

Figure 5.17: Top: example of multi-channel early device with an alternative clamping method consisting of two threads, one internal and one external, to provide extra support for membrane compression. Bottom: cross section of the plasma collection chamber, situated between the channels connected to the membrane and the outlet.

contact with the membrane. Although easier to assemble, these devices were not as successful in preventing spills of liquid around the membrane and therefore the idea had to be abandoned to once again return to the first idea.

Multiple collection channels

The possibility of using multiple collection channels was explored using the most successful version of the threaded devices. The testing procedure can be found in section 3.7.2 of chapter 3. The tests were performed with the following devices:

- T1, shown in figure 5.16 A, with one collection channel.
- T2, same as T1 but with 3 collection channels.
- T3, again same as T1 but with 5 collection channels.

Table 5.3: Comparison of threaded devices. Failure rate and visible cell % refer to the percentage of total devices tested that completely failed and that produced plasma with visible RBCs respectively.

	Average			Standard Deviation				
Device ID	**Yield (%)**	**Hgb diff. ($g\,dL^{-1}$)**	**Extraction time (s)**	**Yield (%)**	**Hgb diff. ($g\,dL^{-1}$)**	**Extraction time (s)**	**Failure rate (%)**	**Visible RBCs (%)**
T1	43.21	0.0350	161.60	8.12	0.0176	31.24	0.00	10.00
T2	41.62	0.0206	195.27	13.02	0.0129	48.97	0.00	10.00
T3	47.42	0.0310	266.34	11.96	0.0233	41.28	31.25	12.50
T4	0.00	0.00	0.00	0.00	0.00	0.00	100.00	0.00

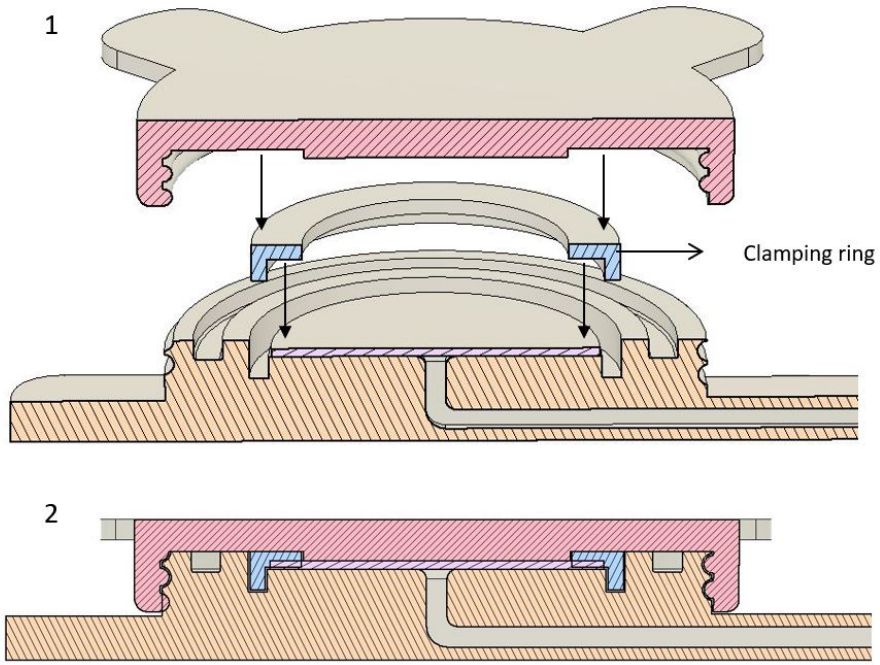

Figure 5.18: 1) Exploded view of clamping ring and top/bottom layers of the test device. 2) Cross section of assembled device.

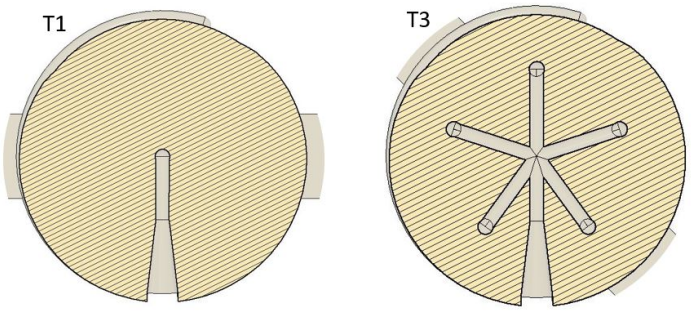

Figure 5.19: Comparison of the horizontal cross sections of devices T1 and T3 to highlight channel structure and differenced between the designs.

The results are summarised in table 5.3, which also include the results of the failed device shown in figure 5.16 C (here labelled T4). Out of the other designs, T3 had the highest yield, but also the longest extraction time and worst failure rate. T1 and T2 performed similarly in terms of failure rate and yield, with T1 having a faster extraction time and T2 outperforming the other devices with regards to plasma quality. However, the T2 design had a higher dead-volume than T1 due to the extra channels, meaning that the plasma was more easily retained in the extra channel volume rather than flowing towards the outlet. This translated to the user having to repeatedly extract the plasma with the pipette. With design T2, the user required no more than 2-3 extractions to collect the plasma, while 4-5 were needed with T3 devices, making the collection process more laborious. As more research was needed to establish the best type, and particularly whether having multiple channels improved plasma quality, more multi-channel devices were tested with devices developed in future iterations, which are discussed in the later chapters.

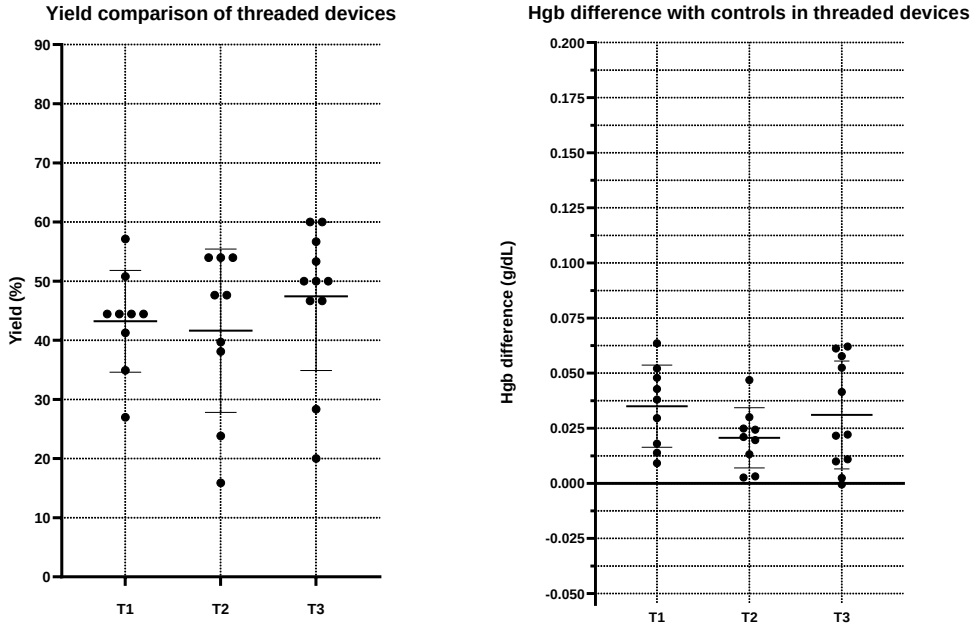

Figure 5.20: Comparison of plasma yield and quality between threaded 3D printed devices. The devices extracted a comparable percentage of the total available plasma in the sample. Plasma quality, measured as the difference in Hgb concentration with centrifuged control, was slightly higher for T2 compared to the other two versions.

Plasma collection chamber

figure 5.17 also highlights another feature tested at this stage where the plasma was pulled into a collection chamber before being pulled out through the outlet. This attempt was made to explore the possibility of inserting antibodies or sensors in the collection chamber that could potentially react with an analyte in the plasma. More work is needed to expand on this idea, as the concept was then not used for the final devices due to lack of time for thorough testing.

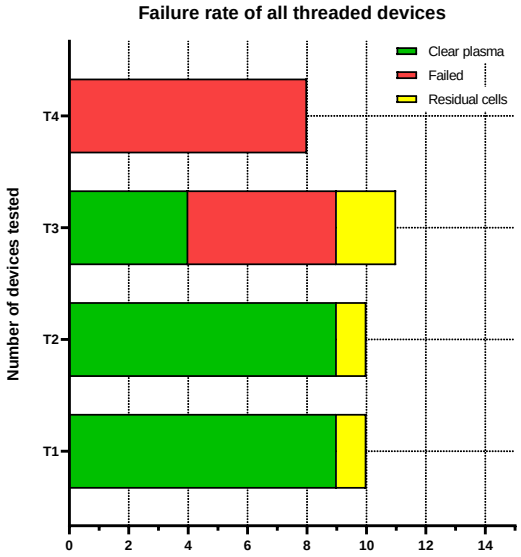

Figure 5.21: Failure analysis of threaded devices tested. As can be seen in the graph, none of the T4 devices were successful during testing and nearly half of the T3 devices failed completely. Designs T2 and T1, on the other hand, were successful in all tests performed, and only one in each version produced plasma with slight visible RBC residual.

5.3.3 Twist-lock

Despite the efforts at facilitating the assembly process of threaded mechanisms, the addition of the membrane made for an uncomfortable (and at times blister-inducing) experience for the user. Moreover, the membrane was often damaged by the twisting motion. To safeguard the membrane (and the user's fingers), a method that required less force had to be adopted. Twist-locks are a popular snap-fit method to connect two cylindrical parts where one is fitted with protruding lugs and the other cavities to match the twisting motion of the lug. A spring or similar object pushes the lug-fitted part against the slot to prevent disassembly. After several iterations, the most successful twist-lock example can be seen in figure 5.22. the assembly steps are described in figure 5.23.

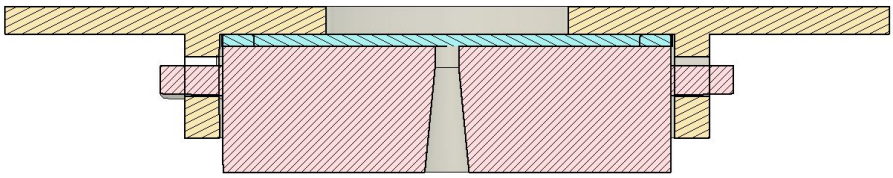

Figure 5.22: Cross section of the twist-lock test device with integrated membrane.

Although slightly easier to assemble than the threaded devices, the force required to operate the twist-lock mechanisms was still excessive with the membrane in place, and assembly by hand was often difficult. As such, more classic snap-fit designs were sought to simplify the assembly process while still maintaining an effective membrane clamping.

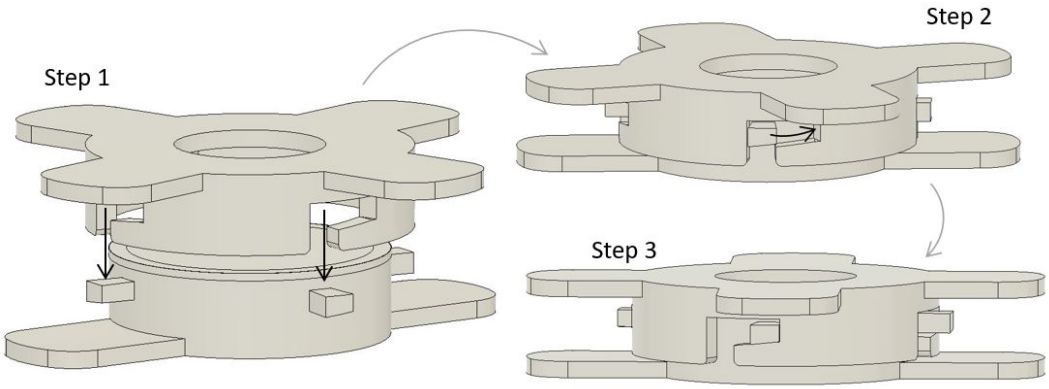

Figure 5.23: Assembly steps of twist-lock devices. Step 1: the user has to align the top and bottom part and press them together, so that the protruding lugs at the bottom layer can fit into the slots of the top layer. Step 2: the top layer is twisted and the lugs slide deep into the slots. Step 3: the device is assembled. The membrane pushes back against the bottom layer to ensure that the layers are locked.

5.3.4 Annular snap-fits and bonded devices

Annular snap-fits appeared to be a valid alternative to twist-based lock mechanisms, as they allow the membrane to be pressed from all sides almost simultaneously during assembly, minimising its chance to move in an incorrect position or to be damaged by twisting motions. Although many different types were tested, the three main iterations of annular snap-fits developed for the devices are shown in figure 5.24. The designs are presented in order of development, with A being the first type tested and C the last.

Design A was impossible to assemble without significantly damaging the parts and manual assembly was only possible before the curing step in post-processing. Once cured, forcing the parts together with external tools, such as pliers, resulted in either the snap-fit or the top layer breaking. While design B could be assembled by hand with cured components, the snap-fit was not strong enough to keep the membrane compressed. Design C could be assembled by hand with difficulty using cured parts, with the high assembly force required often resulting in damage to one or more components. When successful, however, the snap-fit proved strong enough to compress the membrane and prevent blood spillage during testing. This design was easy to assemble when the resin was not yet fully cured and therefore more pliable, although this also resulted to damage in the snap-fit making it less effective at compressing the membrane post-curing.

In conclusion, when used alone annular snap-fits did not prove to be a successful mechanism to be used with the brittle tough resin available. Design C, however proved to be the basis of an extremely successful method of producing usable devices that were simultaneously leak-proof around the edges and easy to assemble. By pouring fresh resin in a specifically designed channel as shown in figure 5.25, the uncured annular snap-fit was strong enough to hold the two parts together while the resin cured. The devices produced using this technique were called “bonded” devices and their performance is covered in detail in Chapter 6.

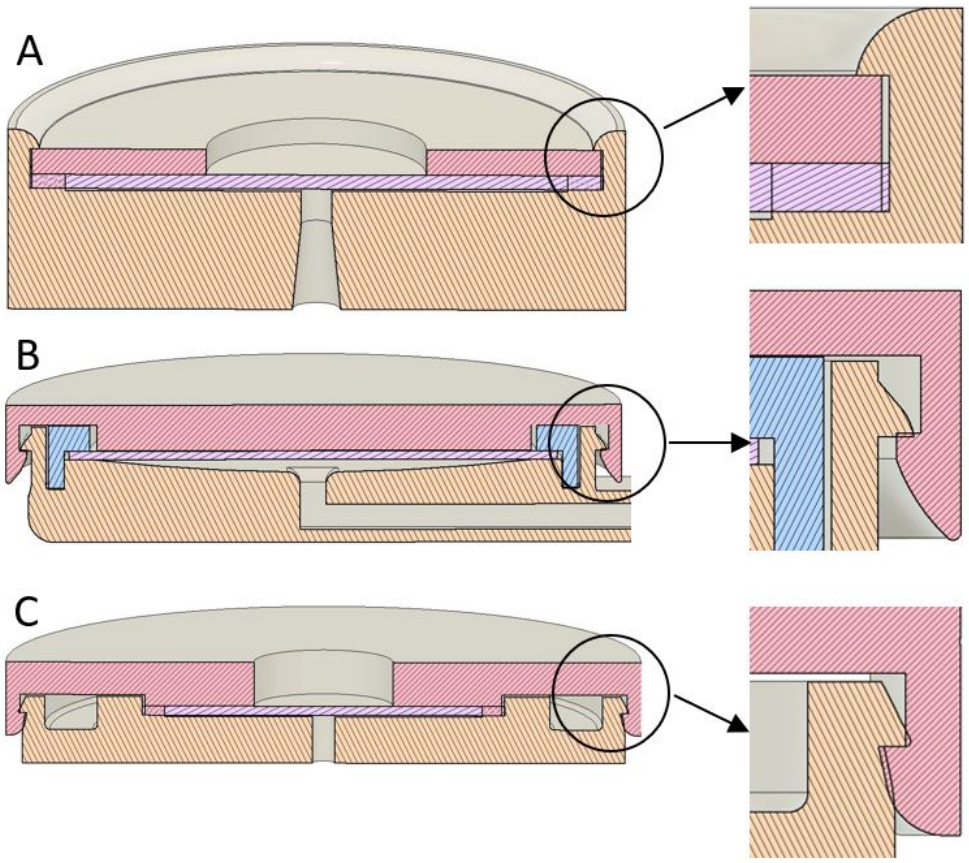

Figure 5.24: Cross section of the design of the three main types of annular snap-fits developed, along with a magnified version of the lock mechanism.

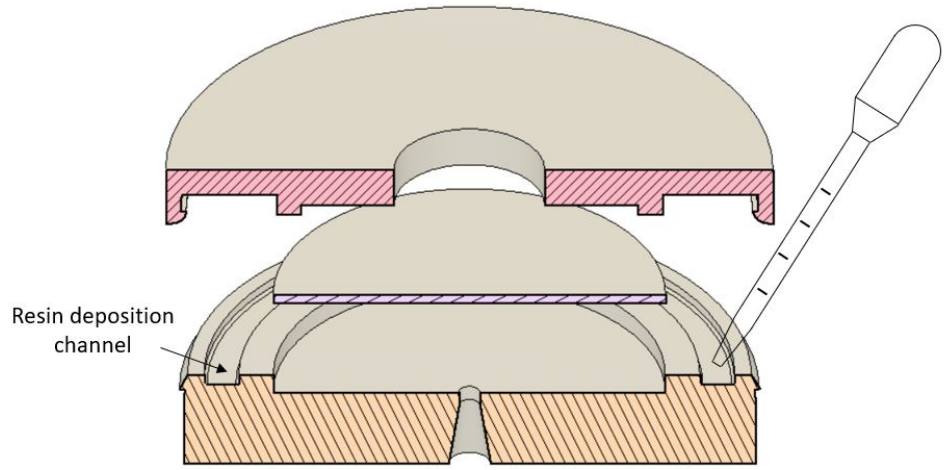

Figure 5.25: Schematic representation of the resin deposition process. During the manufacturing process, a pastette is used to fill the resin deposition channel with raw resin prior to assembly of the top and bottom layer.

5.3.5 Cantilever snap-fits

To decrease the assembly force while maintaining good compression of the membrane edges, curved cantilever snap-fits were created by cutting off parts of the annular snap-fit. Different options were explored to create the ideal compromise between snap-fit strength and ease of assembly. As the tough resin was stiff and brittle, care had to be taken when designing the cantilever beams. A taper was applied to both beam cross-sections to decrease the amount of strain sustained by the beam at the base and therefore reduce its likelihood of breaking during assembly and disassembly [104]. Wider cantilevers make for a stronger snap-fit and allow a quicker assembly/disassembly, but increase the assembly force required, along with the likelihood of each beam breaking during the assembly process. Conversely, thinner cantilever beams decrease the force needed to assemble each beam and the likelihood of one of them breaking, but a higher number of beams is required to create a strong snap-fit, making the assembly and disassembly process fiddly and time consuming for the user. The snap-fit itself had to be customised to take into account membrane compressibility and 3D printer inaccuracies, so several iterations were needed to establish the ideal clearance between parts that allowed the edges of the membrane to be compressed correctly while ensuring that the snap-fit would return to a relaxed position after completing the assembly process. The final iteration is shown in figure 5.26.

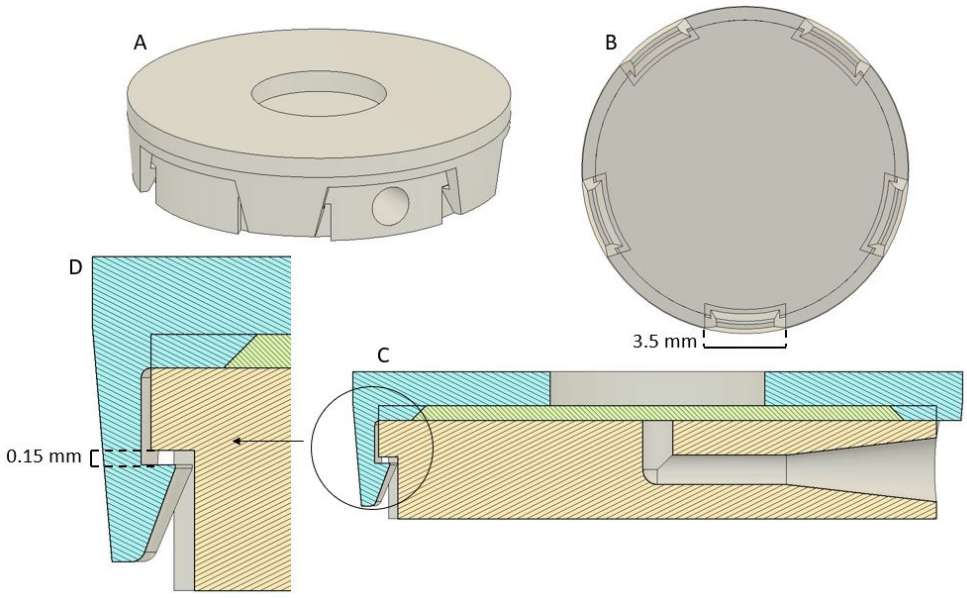

Figure 5.26: Final iteration of cantilever-based snap-fit devices. A) Top view of the assembled device. B) Bottom view of the assembled device with measurement of arm length. C) Cross section of the device. D) Details of cantilever design with measurement of clearance between parts.

5.3.6 Locator-based snap-fits

In the book "The First Snap Fit Handbook" [104], locators are defined as strong and generally inflexible physical features in the mating and base parts that when engage constrain the two parts. They are used along with locks to create more intuitive and stronger snap-fits that are less likely to experience the type of early failure often observed in snap-fits where only flexible parts are present. Low-deflection lock features

can also be used as locators. Different types of protrusion-based locators such as pings, prongs, tabs (commonly found in battery slots), tracks, wedges, catches and lugs can be found in a wide range of everyday products. In this work, lugs were chosen to replace the cantilevers on one side of the devices, while a curved cantilever lock secured the top layer to the bottom one.

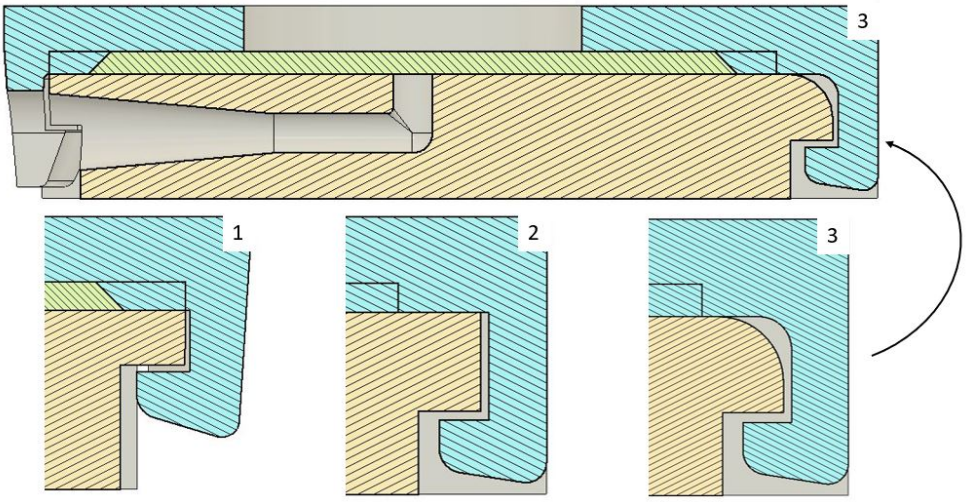

Figure 5.27: Locator shapes attempted before reaching the final design. Design 1 could not be assembled, as the lug arm is too short to allow for a full rotation around the bottom layer locator. Design 2 addressed this issue, but the sharp corner at the interface between top and bottom layer prevented a successful assembly. Design 3 allowed a smooth and painless assembly process for the user, while providing the correct amount of membrane compression necessary for the functioning of the plasma separation devices.

The three iterations needed to produce a suitable locator that would not need to flex during the assembly/disassembly process are shown in figure 5.27, while the mechanisms developed are shown in figure 5.28 and 5.29. The former was difficult to assemble due to the top and bottom layers interfering during assembly, while the latter addressed this issue by removing the interfering material from the bottom layer without compromising the device functionality. The bottom layer was instead fitted with grooves to prevent the membrane from slipping to the back of the device during assembly.

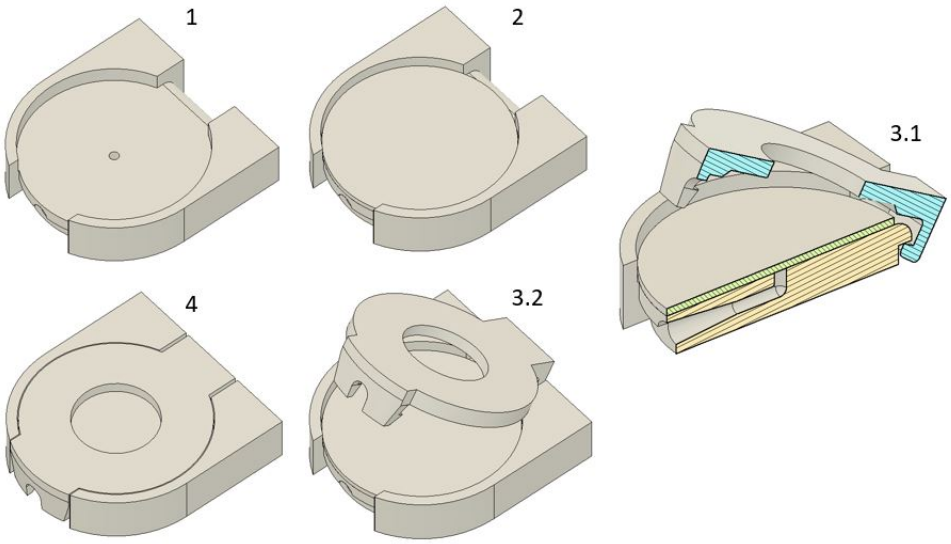

Figure 5.28: First lock mechanisms developed for the locator-based snap-fit devices. The numbers indicate the assembly steps. In step 1, the bottom layer of the device is shown as the device is prepared for assembly. In step 2 the membrane is added, while in step 3 the cap is assembled by pivoting the lug at the top layer around the locator in the bottom layer. Image 3.1 offers a view of the cross section of the device during step 3. In step 4 the device is shown fully assembled.

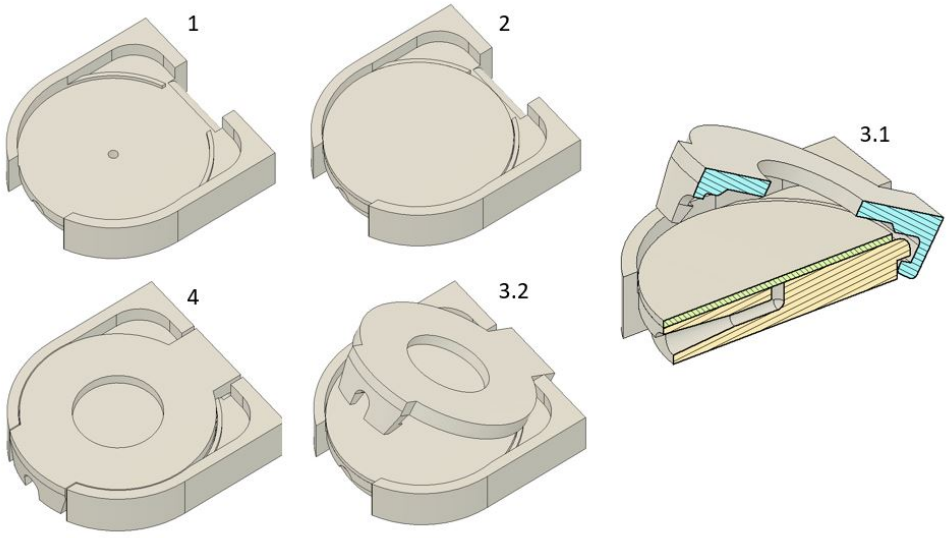

Figure 5.29: Second mechanism developed for the locator-based snap-fit devices. The notation used in this image is identical to figure 5.28. The only difference between the two versions is the removal of material in the bottom part of the device to enable the top part to pivot more easily around the locator and engage the lock without added assembly stresses.

5.4 Summary

This chapter introduced 3D printing as a rapid prototyping method for micro to mesofluidic devices. The capabilities of the 3D printer used throughout this project

were first assessed so that the designs could be adjusted according to its strengths and weaknesses. The selection of important parameters such as sample volume, membrane size and which pipettes to use for extraction was then discussed along with the effect of waiting time between blood deposition and plasma extraction. An introduction to integral snap-fit mechanisms was then given, along with a description of the preliminary versions of the 3D printed plasma separation devices.

The first mechanism explored consisted is a threaded connection between the two device parts to allow for an easy integration of the sample preparation membrane. However, the assembly process proved to be difficult and often painful for the user due to the excessive force necessary to achieve the correct level of membrane compression. In an attempt to reduce the assembly forced required to join the device parts while adequately compressing the membrane edges, a twist-lock mechanism was then introduced. While this improved the device usability compared to the threaded devices, the assembly process was still excessively difficult without the use of external tools.

The next mechanism attempted consisted in an annular snap-fit running along the edge of the parts. While in theory ideal due to the round shape of the devices, annular snap-fits were not feasible with the type of tough resin used to fabricate the parts as the parts proved to be not flexible enough after the resin curing process. This type of mechanism, however, proved successful in holding together parts not yet cured in the post-processing steps. As such, it was found that by coating the edges of the uncured parts with resin and then joining them together through the annular snap-fit, a strong bond could be obtained that completely sealed the membrane within the device.

By cutting slits through the annular snap-fits, effectively creating radial cantilever beams in a “lock-based” mechanism, the assembly was greatly simplified while retaining its efficacy. A natural progression to further simplify the assembly of the two parts consisted in the addition of a fixed locator feature, which meant that the device could be secured with a single cantilever beam placed at the front (“locator-based” mechanism). The manufacturing process, along with the operational steps and full performance analysis of bonded, lock-based and locator-based devices will be thoroughly discussed in the following chapters.

Chapter 6

Development and testing of bonded 3D printed devices

6.1 Design and print settings

The bonded devices comprised a top and bottom part bonded together by photopolymerisation of the same resin used during the printing process. The top and bottom parts of the device are distinct objects that are printed separately, as shown in figure 6.1.

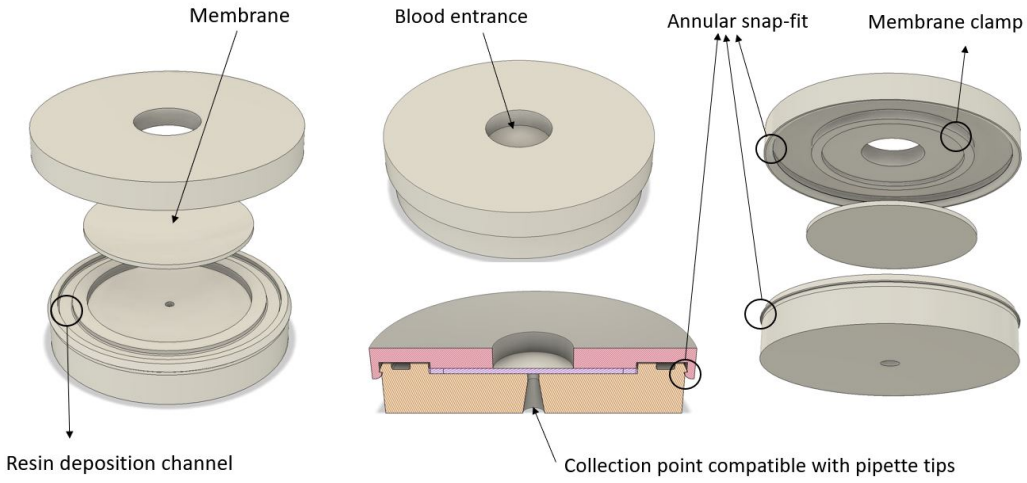

Figure 6.1: Top and exploded view and cross-section of the final prototype of bonded 3D printed devices. The first image (left) highlights the resin deposition channel, where raw resin is deposited prior to assembly and bonding, while the last (right) shows the annular snap-fit holding the device together before bonding and the membrane clamp.

The recommended orientation for SLA and DLP objects is the one that minimises the surface area of the layer to be cured while simultaneously minimising the angle of any overhang present in the design. Overhangs are features that extend outward without direct support underneath. At angles below 45°, unsupported overhangs longer than 3 mm are extremely likely to fail during the printing process. This risk can be minimised by not including unsupported features in the design or by orienting the printed object so that overhangs are printed at angles between 45 and 90°.

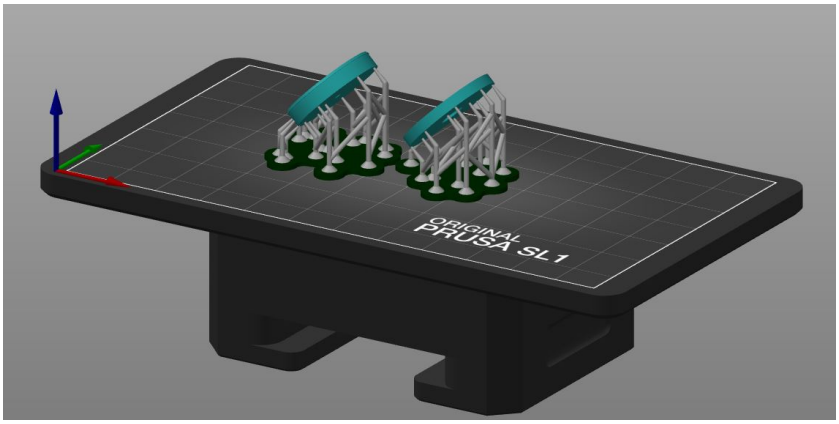

Figure 6.2: Example of device parts printed using pads (dark green) and supports (grey). The objects (blue) were tilted at 45°as per recommendation.

During the print setup, temporary printing supports can be placed underneath unsupported featured using the slicing software of choice. Such supports are then removed after the print is complete. Pads are initial layers placed under the print. The first layers are printed using a longer exposure time to help the resin adhere to the printing platform. This can sometimes create an "elephant feet" phenomenon where the bottom layers are larger than the subsequent ones as a consequence of increased exposure. Pads prevent this while reducing the chance of support failure, as thin supports are far more likely to adhere to an existent resin layer than directly to the printing platform. Figure 6.2 shows the top and bottom objects that make up a bonded 3D printed device, oriented using recommended settings with pads and supports in place.

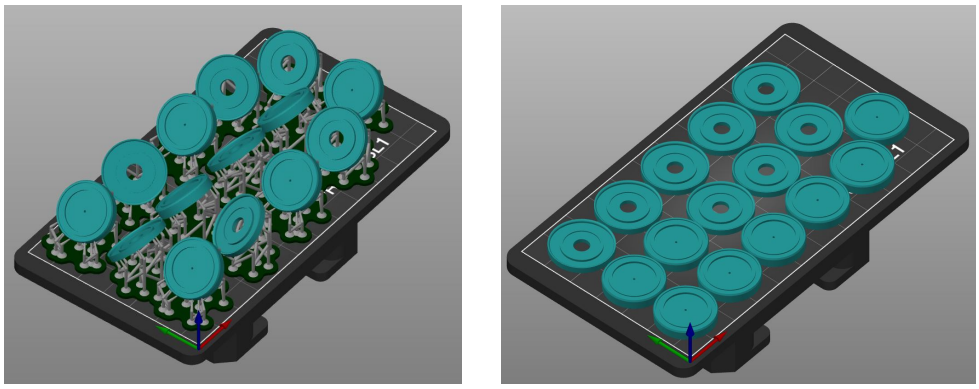

Figure 6.3: Difference in orientation and support use between recommended settings (right) and custom arrangement (left) to produce one batch of bonded device as shown in the PrusaSicer software.

To facilitate the fabrication process, the 3D printed plasma separation devices were designed so that they could be printed flat on the printing platform with no supports and no pads underneath the objects. This method offers several advantages:

- A much shorter print time, as the number of layers is dramatically decreased in a flat orientation. Using the Elegoo plant-based translucent resin as example, the print time for the flat orientation is 18 minutes against 1 hour and 33 minutes with the recommended settings.
- Reduced resin consumption from not having to print pads and support features.

Again using the Elegoo resin as example, the total material consumption to print a batch of 7 devices with recommended settings is 17.36 mL split in 8.8 mL for the objects and 8.56 mL for the supports. As 1 kg cost £34, the cost per batch is £0.59 (0.084 per device). Using the custom settings, 9.99 mL of resin are used per batch for a total of £0.34 (0.0425 per device), which is nearly half the cost. If an expensive resin was used instead, such as biocompatible resins, the reduction in cost would be a significant advantage.

- Easier and faster post-processing procedure, as there is no need to remove supports and sand down the protrusion left behind by the support heads.
- Increased print quality for the snap-fit features. Some areas that require support when printed at an angle are extremely difficult to reach for proper smoothing and the residual hardened resin from the support heads can create obstacles that prevent the assembly of snap-fit features. Moreover, scratches left behind by smoothing procedures impact the translucency of resins marketed as transparent, unless time consuming polishing steps are performed.

To account for the "elephant foot" phenomenon, no features other than the inlet and outlet were placed in the initial layers to be printed, so that potential layer deformation would not have any practical effect on the finished device. Figure 6.3 highlights the difference between a device batch to be printed with recommended settings and one with custom ones.

6.2 Assembly process

Due to the small printing area of the 3D printer used, a maximum of 8 devices could be fabricated in one batch as shown in figure 6.3. Once the device layers were fabricated using the process described in chapter 2, the assembly process required the following steps:

1. The membrane was placed on the bottom layer and a small amount of resin was pipetted within the resin deposition channel shown in figure 6.4.
2. The top and bottom were then joined and held together through the annular snap-fit. The membrane clamp provided a barrier that helped prevent the resin from reaching and soaking the membrane, while also preventing blood from freely flowing around the edges of the membrane during testing.
3. The assembled devices were then cured under UV-light for 10 minutes on each side, after which they were ready to use.

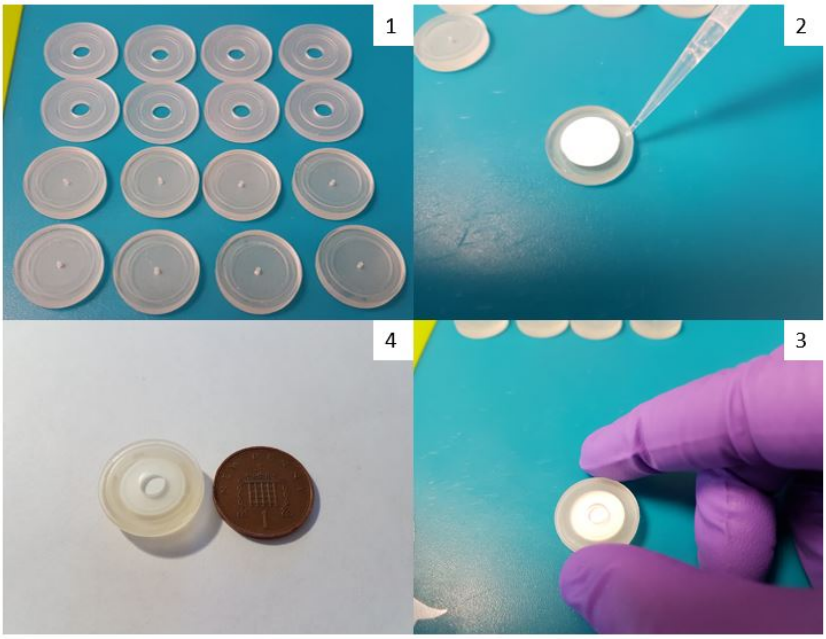

Figure 6.4: Assembly process of the 3D printed bonded devices. 1) The cleaned 3D printed layers are ready for assembly. 2) The membrane is placed inside the device and fresh resin is pipetted within the boundaries of the resin deposition channel. 3) The top layer is aligned over the bottom layer and pressed down to engage the annular snap-fit and connect the two parts. 4) Post-processed device ready for use, placed next to a one penny coin.

The total fabrication time for one batch was 53 minutes, subdivided in 18 minutes printing, 10 minutes washing and drying, 5 minutes assembly and 20 minutes curing, with approximately 6 minutes per device. Figure 6.1 illustrates the final prototype and highlights its main features, which will be discussed in detail in the following sections. The design was made to be parametric so that it could be easily adjusted to include a membrane with larger thickness or diameter.

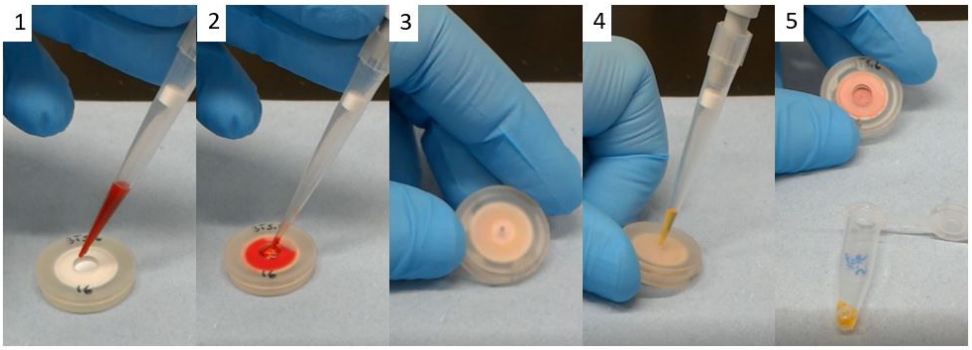

Figure 6.5: Operational steps of the 3D printed bonded devices. 1) The assembled device is ready to be used. 2) Blood is placed inside the device. 3) The device is flipped upside-down to place the outlet in a favourable position for extraction. 4) The plasma is collected immediately using a 100 µL pipette. 5) The plasma is transferred inside a centrifuge tube for further assessment and the device can be safely discarded.

6.3 Operational steps

The steps needed to operate the bonded devices are shown in figure 6.5. After depositing the blood inside the device, the user can extract the plasma immediately using a pipette. In correctly manufactured devices the blood is completely absorbed by the membrane, so that no blood flows outside the device occurs during use.

6.4 Results and discussion

6.4.1 Effect of feature modifications

Once a basic functional version of the bonded devices was created (B1), several features were tested to assess whether there would be improvements over the baseline device. This section describes the effects of feature modifications on both the manufacturing and the plasma separation process of bonded 3D printed devices. The features explored were mapped to the corresponding device IDs in table 6.1 so that they can be more easily identified.

Table 6.1: Feature modifications attempted during the development of bonded 3D printed devices.

Device ID	External resin loading	Membrane compression	Resin channel height (mm)	Inlet placement	Outlet placement	Membrane supports	Orientation
B1	N	N	0.50	Central	Central	N	Horizontal
B2	Y	N	0.50	Central	Central	N	Horizontal
B3.1	N	Y	0.25	Central	Central	N	Horizontal
B3.2	N	Y	0.25	Central	Central	N	Horizontal
B4.1	N	N	0.40	Central	Side	N	Horizontal
B4.2	N	N	0.40	Central	Central	N	Horizontal
B4.3	N	N	0.40	Side	Side	N	Horizontal
B4.4	N	N	0.40	Side	Central	N	Horizontal
B5	N	N	0.40	Central	Central	Micropillars	Horizontal
B6	N	N	0.40	Central	Central	0.1 mm gap	Horizontal
B7.1	N	N	0.40	Central	Central	SP pattern	Horizontal
B7.2	N	N	0.40	Central	Central	SF pattern	Horizontal
B7.3	N	N	0.40	Central	Central	K pattern	Horizontal
B8.1	N	N	0.25	Central	Central	N	Vertical
B8.2	N	N	0.40	Central	Central	N	Vertical

External resin loading

In the normal fabrication process of the bonded 3D printed devices, the membrane is placed on top of the bottom layer, the resin is pipetted inside the deposition channel and finally the top layer is assembled through the annular snap-fit. Injecting the resin after assembling the cap would provide a slight advantage in the fabrication process, as

it would allow the devices to be bonded at any time after being assembled instead of during the assembly process. The device B2 was developed to investigate the feasibility of post-assembly bonding by having a top layer with slits through which the resin could be poured after its assembly with the bottom layer. No advantage was observed using this method, as the resin was too thick to be easily injected into the channel and excess quantities had to be used, leading to partial soaking of the membrane with raw resin and consequent reduction in the active surface area available for plasma separation post curing. Although this did not negatively affect the yield, haemolysis was observed as a consequence of plasma being forced through a smaller membrane. Moreover, the fresh resin proved to be difficult to cure in a reasonable amount of time, as it remained under-cured even after doubling the time used in the normal procedure, creating a potential health and safety hazard for the user. For these reasons, this idea was quickly abandoned and all subsequent models made use of internal resin deposition for bonding.

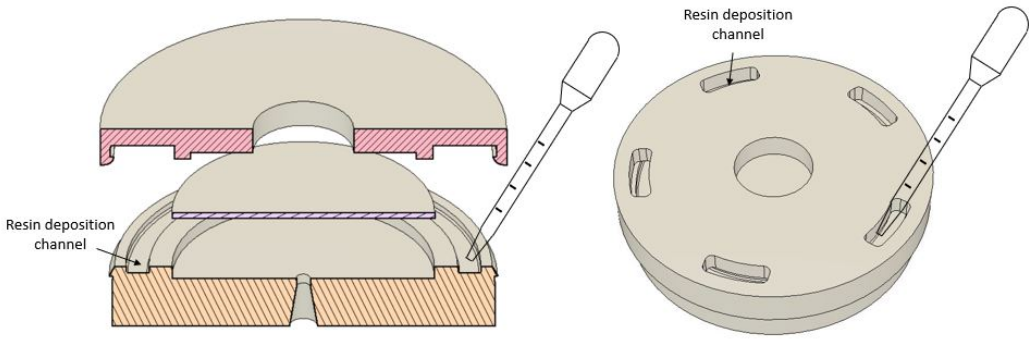

Figure 6.6: Difference between resin loading of standard B devices (left) and B2 (right), where the resin is poured through slits on the top layer rather than during the assembly process.

Membrane compression

To investigate the effect of membrane compression on the plasma extraction process, the designs B3.1 and B3.2 included a smaller membrane slot of 0.3 mm height, compared to all other devices that have 0.35 mm high slots. The height of the Vivid GR membrane is advertised as $330 \pm 20\,\mu m$ by the manufacturer, so while the 0.35 mm slots provides no compression, the 0.3 mm slots compressed the membrane between 3.22 and 14.28%. The compression had a significant negative effect on the quality of the plasma extracted, as B3.1 and B3.2 produced the lowest quality plasma out of all bonded devices with a Hgb difference with controls of 0.739 and 0.0745 $g\,dL^{-1}$ respectively. The yield was also negatively affected, with B3.2 in particular performing the worst out of all other bonded devices with only 29.89% of the total available plasma extracted. The extraction also took longer, with 120.17 s and 152.49 s on average for B1 and B2.

Resin deposition channel height

In an attempt to minimise the amount of raw resin deposited in the channel (figure 6.7), in the designs B3.1, B3.2 and B8.1 the resin deposition channel height was reduced from 0.5 to 0.25 mm. As the groove filling process was done by hand with a pastette of fixed size, the height reduction meant that the pipette tip would often fall out of the groove, spilling resin in unwanted areas. Moreover, it was extremely easy to overfill the channel, leading to resin soaking the membrane and a significant reduction of usable

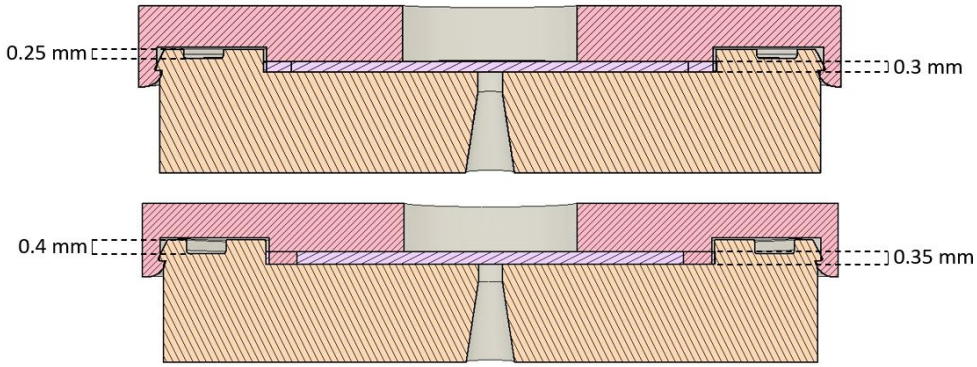

Figure 6.7: Design cross-section of B3.2 (top) and B4.2 (bottom) highlighting the different height of the membrane slots and the resin deposition channels.

membrane surface area. Compromised devices were excluded from the testing process. All subsequent devices were designed with a 0.4 mm deep groove, which was found to be ideal from a manual assembly standpoint.

Blood inlet and outlet placement

When blood was deposited inside the device, it initially came into contact with the portion of the membrane directly below the inlet before spreading to the remaining surface. To investigate whether extracting the plasma farther away from the inlet has any positive effect on the quality of the extracted plasma four designs were developed (B4.1, B4.2, B4.3 and B4.4), each with a different outlet placement with respect to the inlet (figure 6.8). This setup also allowed to explore whether placing the outlet or the inlet close to the edge of the body might increase the likelihood of cells passing around the edges of the membrane, thus causing device failure by contaminating the plasma with whole blood. The devices performed similarly in terms of quality, yield and extraction time. The Hgb difference with controls was negligible and the extraction time was similar across all devices. The amount of available plasma extracted was 50.1%, 51.34%, 54.84% and 53.11% for B4.1, B4.2, B4.3 and B4.4 respectively. There was, however, a significant difference in the failure rate between the models, with B4.2 having by far the lowest (4.65%), followed by B4.4 (12.5%), B4.3 (16.66%), and B4.1 (20%). While B4.2 and B4.4 have central outlets, in the B4.1 and B4.3 models the outlet is placed along the edge of the device, increasing the likelihood of cells being pulled through from around the edges of the membrane and hence device failure. Placing the inlet near the edge as in B4.4 has also a negative effect compared to a central inlet, such as B4.2. A central inlet with central outlet was therefore selected as the best design option.

Membrane supports and patterns

Suction can occasionally cause the membrane to adhere to the edges of the outlet, preventing the plasma from easily exiting the device. Other studies mentioned in the literature relied on membrane supports, such as patterns and micropillars, to prevent this issue and enhance the plasma separation properties of their devices. To investigate the efficacy of micropillar-based supports, the design B5 was fitted with an array of micropillars, each with a diameter of 0.6 mm and height of 0.1 mm spaced $\sim$ 0.55

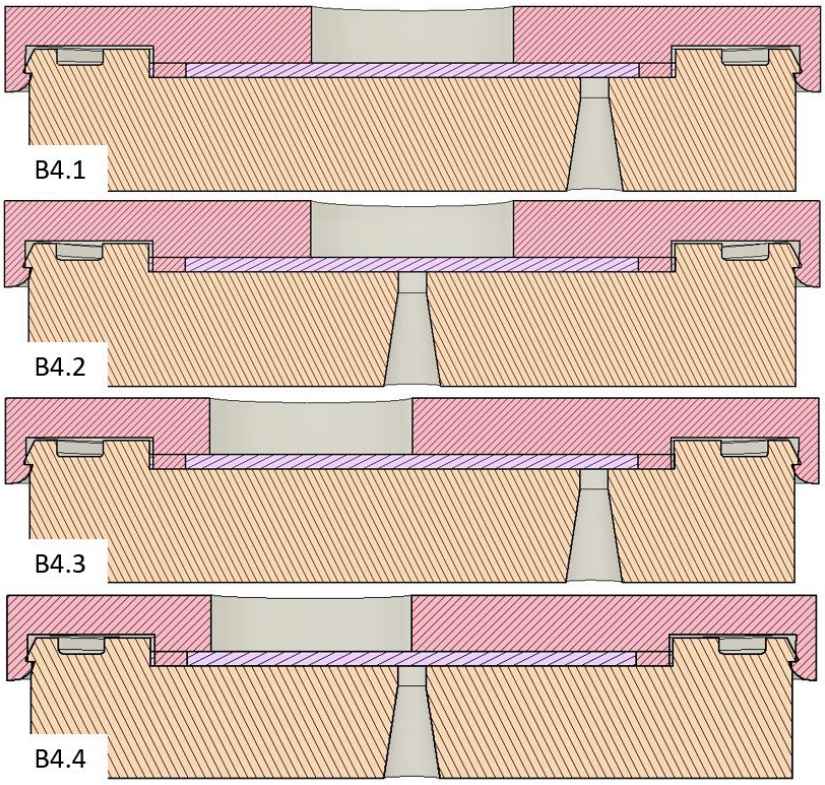

Figure 6.8: Design cross section of all B4 devices, showing the difference between inlet and outlet placement in each design.

mm apart from one another. B6 acts as control with a gap of 0.1 mm underneath the membrane to ensure that the differences observed in B5 are not due to the space between membrane and collection channel (figure 6.9). The plasma quality remained high in both B5 and B6 designs, but the yield of the micropillar-based model was significantly lower (43.07%) than the micropillar-free gap (50.16%) and the gap-free B4 devices (52.47% combined). However, despite the similarity in yield, the extraction time was significantly slower for B6 than the B4s. Not leaving a gap below the membrane, and thus decreasing dead space within the device, therefore leads to a faster extraction process.

To determine whether support patterns can increase the volume of plasma collected and/or improve the extraction time, three different patterns were developed and tested in the devices B7.1, B7.2 and B7.3. With the exception of the patterns, the designs were identical and can be seen in figure 6.10. All patterns were 0.1 mm deep and 0.5 mm wide. Out of the three, B7.1 had the highest yield (56.89%) but lowest plasma quality, with an Hgb difference of $0.0174\,\mathrm{g\,dL^{-1}}$, and highest average extraction time of 96.55 seconds. While the B7.2 and B7.3 designs were comparable in terms of extraction time (75 and 70.90s respectively), B7.3 had the lowest yield (45.4%) and poorest quality (Hgb difference of $0.0174\,\mathrm{g\,dL^{-1}}$), while B7.2 extracted 49.44% of the available plasma and had the highest quality among the patterned designs, with an Hgb difference of $0.0039\,\mathrm{g\,dL^{-1}}$. At 6.25%, B7.1 had the lowest failure rate against the 12.5% of B7.2 and B7.3, with the latter version having the highest percentage of devices that produced plasma with visible residual cells out of all bonded devices (18.75%). Overall, there was no improvement compared to the B4 devices, so the installation of supports and

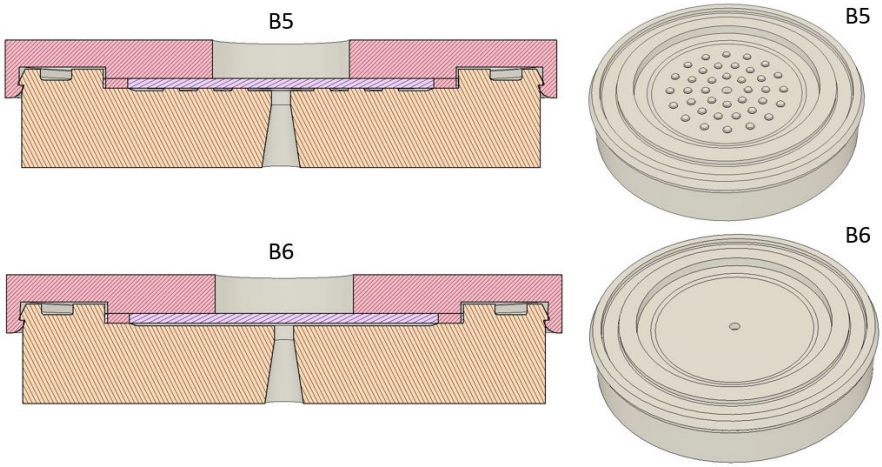

Figure 6.9: Difference between micropillars membrane supports (B5) and gap without supports (B6) shown in design cross section and full CAD of bottom layer.

patterns was considered unsuccessful for bonded devices.

Figure 6.10: Difference between patterns of devices B7.1, B7.2 and B7.3 (left to right). While the "spiral" (SP) and "snowflake" (SF) patterns are original, the pattern in B7.3 (K) was adapted from the work of Kadimisetty et al. [53], where it was claimed to have significantly improved the yield of their devices.

Extraction orientation

Occasionally, when a significant percentage of the available membrane surface area has been compromised by cured resin, the blood might not be absorbed correctly within the device. When flipping the device upside-down for extraction, these faulty devices might leak blood at the inlet. A vertical extraction orientation was explored as a means to address this issue with the devices B8.1 and B8.2, as shown in figure 6.11.

A side effect of such measure is the increase in the length of the collection channel. The Hagen-Poiseuille equation for laminar flow in a channel of circular cross section can be used to predict whether the longer collection channel would have a significant impact on the yield of the devices:

$$\Delta p = \frac{8\mu Q L}{\pi R^4} \tag{6.1}$$

where Δp is the pressure difference between inlet and outlet, Q is the volumetric flow

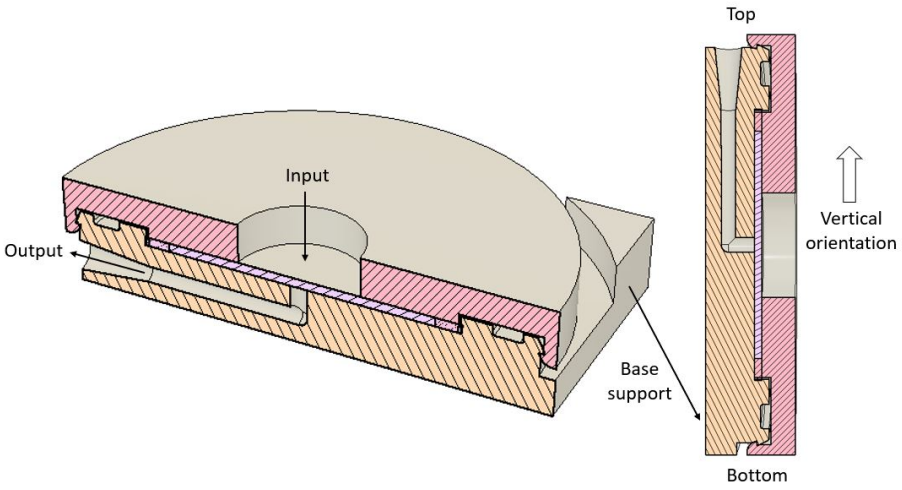

Figure 6.11: Annotated design cross section of device B8.2 in a flat and vertical orientation, to show the use of the base support and the full length of the extraction channel.

rate, L is the pipe length, R is the channel radius and μ is the density of the fluid passing through the channel.

However, for this equation to be used, the flow within the device has to be demonstrated to be laminar using the Reynolds Number calculation for flow in a pipe:

$$Re = \frac{uD_H}{v} \tag{6.2}$$

where u is the fluid velocity ($\mathrm{m\,s^{-1}}$), D_H is the inner diameter of a circular piper (m) and v is the kinematic viscosity. The kinematic viscosity can be calculated as follows:

$$v = \frac{\mu}{\rho}\ (\mathrm{m^2\,s^{-1}}) \tag{6.3}$$

where ρ is the density of the substance. For practical purposes the temperature dependency will be ignored in this calculation, as the experiments were carried out at room temperature. The normal dynamic viscosity of blood plasma at 37°C is ~ 0.00125 Pa s [107] while plasma density is dependent on sample haematocrit and on average estimated to be $1025\,\mathrm{kg\,m^{-3}}$ [108]. This means that the kinematic viscosity $v \sim 1.22 \times 10^{-6}$. The inner diameter of the channel was 0.7 mm and its length 6.5 mm. As it was filled in 1 second during the experiments, the velocity is $0.0065\,\mathrm{m\,s^{-1}}$. With this information, the Reynolds Number can be calculated as 3.731, which is well below the threshold for turbulent flow.

Now that the flow has been demonstrated to be laminar, the Hagen-Poiseuille equation can be used. In equation 6.1, Δp is directly proportional to the channel length, meaning that a larger pressure difference is needed to move the same fluid volume at the same rate along a longer pipe. According to the equation, a yield reduction can therefore be expected as a consequence of the increased channel length, as the exact same pipette with the same settings was used in all experiments.

The experimental data confirms this prediction as the longer collection channel caused

a sharp yield reduction, with B8.1 and B8.2 recovering only 41.19 and 45.12% of the total available plasma respectively. Both devices also had extremely high extraction times (132 and 126 seconds). However, the plasma quality was much lower in B8.1 than in B8.2 (Hgb difference of 0.0495 and -0.0086 $g\,dL^{-1}$ respectively). Given that the only difference between the designs is the resin channel height, the incomplete bonding between the top and bottom is likely that to be the reason behind the poor performance.

6.4.2 Data analysis

All bonded 3D printed devices were tested as described in section 3.7.2 of chapter 3. Table 6.2 summarises the results of all iterations of the bonded 3D printed devices.

Table 6.2: Data analysis summary of all bonded devices. The yield refers to the percentage of total available plasma extracted. The Hgb difference was calculated by subtracting the measured Hgb concentration of each device from a centrifuged control. The extraction time was calculated from blood sample insertion to complete plasma collection. Failure rate % refers to the percentage of the total devices tested that failed to produce any measurable volume of plasma or that experienced a significant amount of blood leakage towards the outlet. The Visible RBSs % describes the percentage of the total devices tested that produced plasma with a small quantity of visible RBCs.

	Average			Standard Deviation				
Device ID	**Yield (%)**	**Hgb diff. ($g\,dL^{-1}$)**	**Extraction time (s)**	**Yield (%)**	**Hgb diff. ($g\,dL^{-1}$)**	**Extraction time (s)**	**Failure rate (%)**	**Visible RBCs (%)**
B1	57.70	0.0147	183.84	7.72	0.0161	41.29	28.57	0
B2	55.18	0.0247	104.00	8.48	0.0142	27.45	20	0
B3.1	45.63	0.0739	120.17	7.12	0.0561	23.40	0	0
B3.2	29.89	0.0745	152.49	23.32	0.0355	18.14	0	0
B4.1	50.59	-0.0011	68.43	9.03	0.0114	12.68	20	13.33
B4.2	51.34	-0.0005	76.11	10.35	0.0095	14.82	4.65	9.3
B4.3	54.84	0.0001	71.53	5.02	0.0074	6.02	16.66	4.16
B4.4	53.11	-0.0016	70.00	7.79	0.0053	5.20	12.5	8.33
B5	43.07	0.0001	84.92	8.16	0.0062	19.81	12.5	6.25
B6	50.16	0.0020	91.85	6.77	0.0047	20.43	6.25	12.5
B7.1	56.89	0.0174	96.55	10.00	0.0098	18.35	6.25	25
B7.2	49.44	0.0039	75.00	10.34	0.0104	7.94	12.5	12.5
B7.3	45.40	0.0096	70.90	10.24	0.0159	13.90	12.5	18.75
B8.1	41.19	0.0495	131.83	7.28	0.0302	32.49	12.5	0
B8.2	45.12	-0.0086	126.00	2.40	0.0095	7.35	0	0

Yield

The yield obtained by all device iteration is summarised in figure 6.12. All devices except B3.1, B3.2, B5, B7.3, B8.1 and B8.2 had an acceptable average yield $\geq$50%. Designs B1 and B7.1 had the highest percentage of plasma recovery with 57.7 and

56.89% respectively. However, arguably fewer devices were tested with these designs compared to B4.2, which despite having the highest number of devices tested still maintained a 51.34% yield.

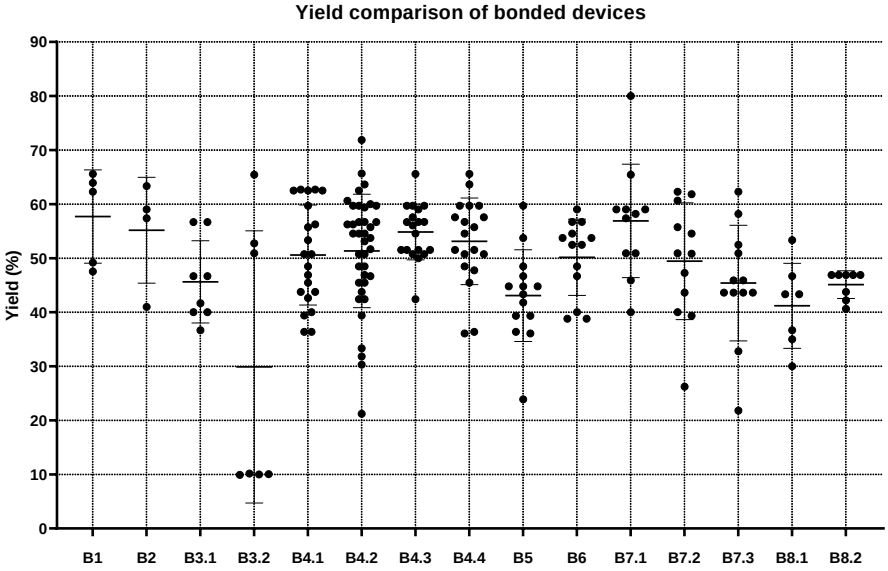

Figure 6.12: Yield comparison of all iterations of 3D printed bonded devices.

Plasma quality

figure 6.13 shows the difference in haemoglobin concentration between the plasma extracted from the devices and the plasma control for the same sample. All the B4 devices had a good performance, followed by B5, B7.2 and B8.2, while haemolysis occurred at higher rates in the remaining ones.

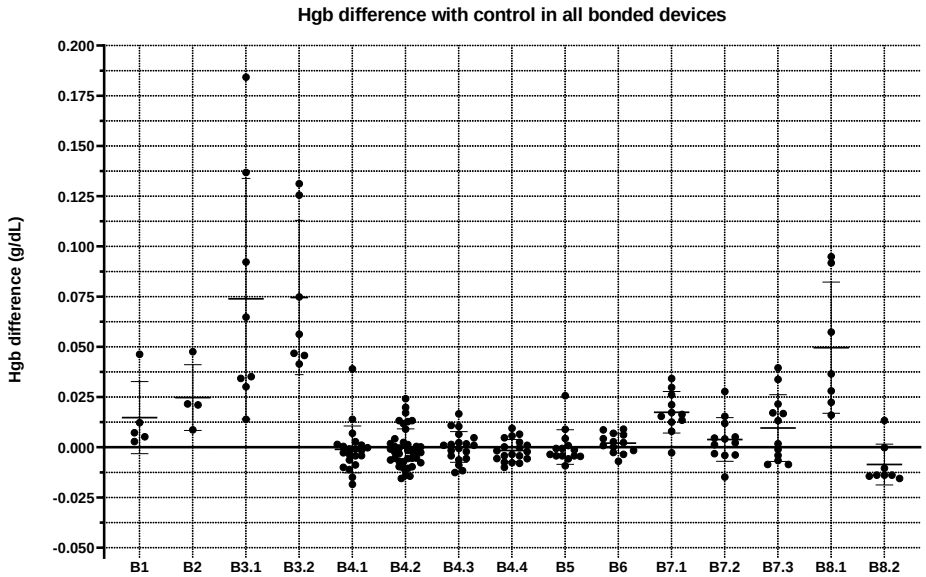

Figure 6.13: Comparison of plasma quality among all iterations of 3D printed bonded devices, measured as haemoglobin concentration difference with centrifuged controls.

Failure rate

Figure 6.14 shows the total number of devices tested along with the percentage of those that failed or had visible residual cells in the output plasma. Design B4.2 stands out as the most tested type and proved to be extremely reliable, as only 4.65% of the devices failed and 9.3% produced plasma with some visible residual cells.

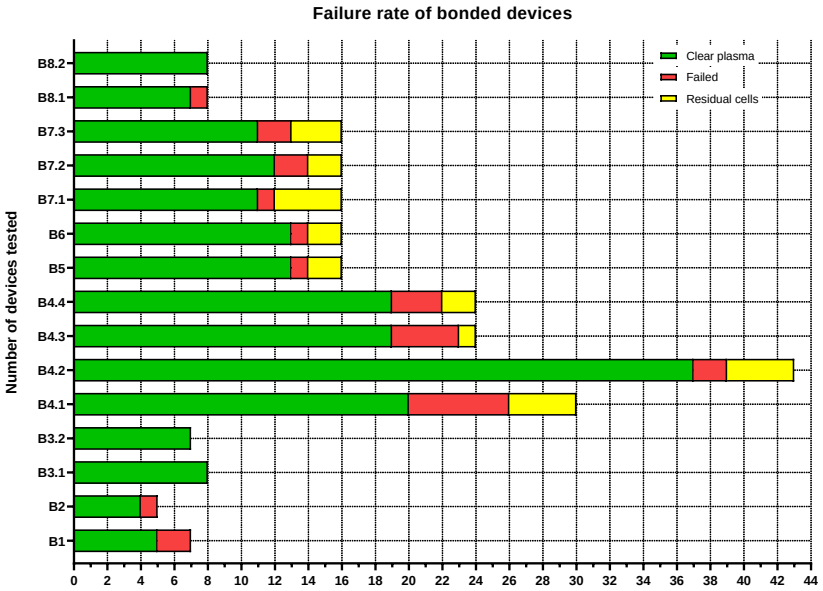

Figure 6.14: Total and partial failure rate comparison of all iterations of 3D printed bonded devices.

6.5 Immunoassay

To ensure that low levels of protein retention occurred within the 3D printed devices and that the plasma collected could be used for blood testing, the devices with the lowest failure rate that still displayed a good overall performance (B4.2) were selected for immunoassay testing. Despite having a good average yield of 51.33%, the average volume of plasma produced by the devices was 16.63 µL due to small input samples. As such, a test that required an input plasma sample $\leq$ 15 µL had to be selected to avoid having to poll plasma from multiple devices to reach the required assay volume. Most animal assay kits called for plasma volumes $\geq$ 50 µL, meaning that at least 4 devices would have been required to produce one data point. To avoid this, the testing was outsourced to a local company (Biobest Laboratories Ltd, https://biobest.co.uk/), which offered a range of assays that only required 5 µL of plasma per test. The plasma produced by the 3D printed devices was tested with a two-step competitive enzyme-linked immunosorbent assay (ELISA) for the detection of antibodies to the Bovine Respiratory Syncytial Virus (BRSV), which infects the respiratory tract of cows resulting in a mild to life-threatening respiratory disease. Antibodies to this virus are commonly found in local cattle.

Six bovine samples were used to test 36 plasma separation devices, with 6 devices being used per sample. In the procedure of this competitive ELISA test, the sample was first incubated in antigen-coated wells to allow the antibodies in the sample to bind to the antigen in the wells. After a washing step to eliminate sample residuals, a

Device ID	Sample 1	Sample 2	Sample 3	Sample 4	Sample 5	Sample 6
Control	>100	>100	59	26	14	<1
D1	>100	>100	67	20	11	<1
D2	>100	>100	73	25	9	<1
D3	>100	>100	52	28	12	<1
D4	>100	95	>100	30	11	<1
D5	>100	>100	85	24	11	<1
D6	91	>100	80	24	11	<1

Table 6.3: Comparison of ELISA results of centrifuged control against 6 devices for 6 different samples for a total of 36 devices tested.

solution of conjugated antibody (that is, antibodies that have been linked to a label) was added to the well and incubated to allow the conjugated antibodies to bind to residual antigen spots left in the well. The wells were washed again and a substrate was added to the wells to react with the label and create a signal, in this case a change in colour and therefore absorption at a specific wavelength. In this case, a stronger signal corresponded to a lower concentration of the target antibody, as more antigens in the wells remained free for binding with the conjugated antibodies instead. The absorption of each well was then measured and fitted to an 8 point standard curve to determine the concentration of antibodies present in the sample. The results are shown in table 6.3, where a result $\geq$3 indicates antibody presence. Other than a few inconsistencies due to inter-test variability (as confirmed by the provider), the results from the devices closely matched those of the centrifuged control, meaning that they can be safely used in immunoassays.

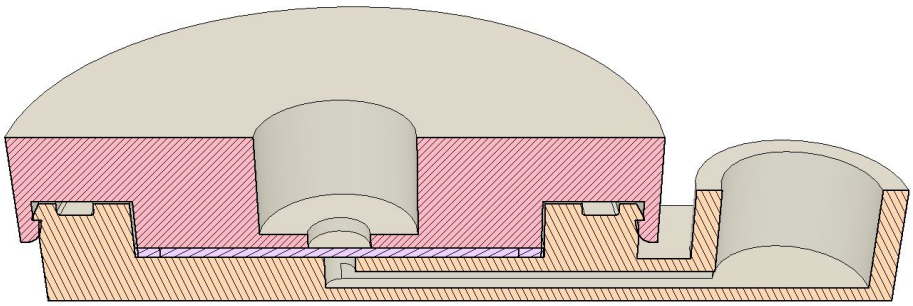

Figure 6.15: Cross section of the 3D printed device that resemble closely those developed in chapter 4.

6.6 Adaptation of laser-cut PMMA designs to 3D printing

To compare the performance of the same design fabricated through different methods, the design of the PMMA devices described in chapter 4 was adapted for 3D printing using the same concept used in the development of the bonded devices. The design of the 3D printed design is shown in figure 6.15. The devices were fabricated and assembled in the same way as the bonded devices, while the operational steps for their use (summarised in figure 6.17) were identical to those of the PMMA devices. A total of 14 devices (3 of which failed) were tested with equine blood prepared as described

in section 3.7.2 of chapter 3 and the results are shown in figure 6.16.

The 3D printed devices displayed the same issues as the PMMA ones, mainly:

1. After the Minivette plunger was fully pressed, the plasma was partially or totally reabsorbed by the hydrophilic membrane, leading to device failure or low yield.
2. The high pressures induced by the Minivette caused significant haemolysis that affected the quality of the plasma.

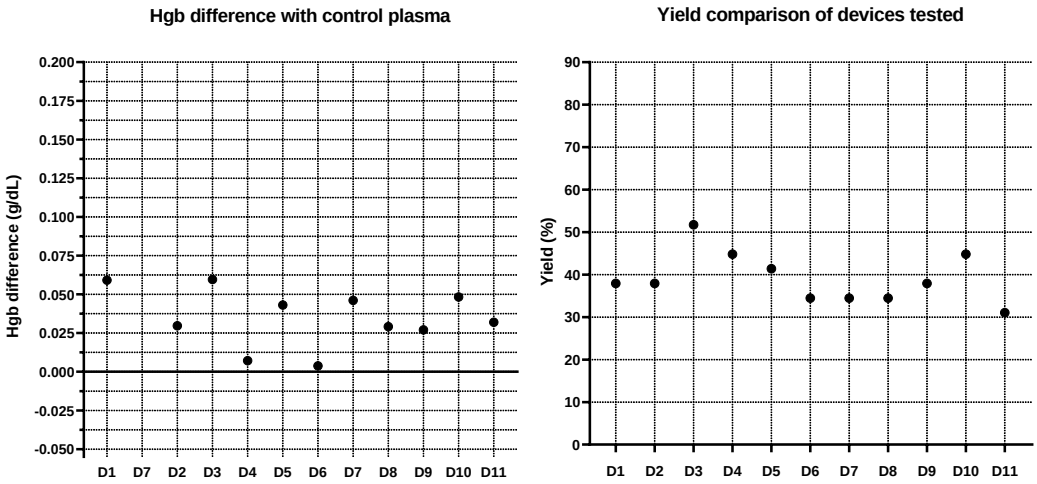

Figure 6.16: Yield and Hgb difference of PMMA-like 3D printed devices that did not fail during the testing process.

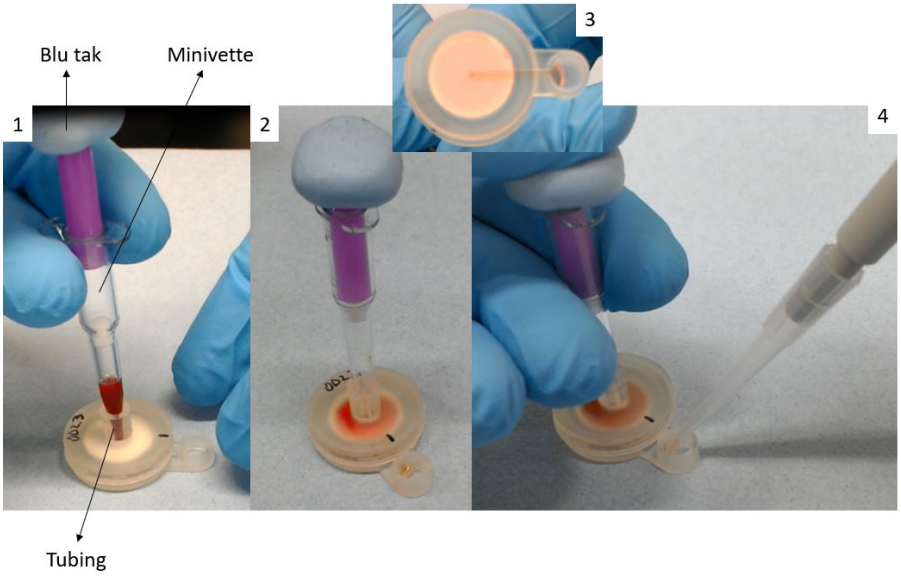

Figure 6.17: Operational steps of the PMMA-like devices fabricated by 3D printing. 1) A piece of Bostik Blu Tak® is placed over a Minivette as described in chapter 4. The Minivette is filled with blood and placed over the device inlet using silicone tubing to create an air-tight seal. 2) The plunger is pressed slightly, initiating the blood flow on the membrane. 3) After 3 minutes, the plunger is pressed completely and the plasma flows towards the outlet. 4) The plasma is collected using a pipette.

The failure rate of the devices was 21.5% and the average yield 39%. The average Hgb difference with controls was $0.035\,\mathrm{g\,dL^{-1}}$ and the extraction time was approximately 4 minutes per device. Overall, this design failed to compete with the one of the B series of devices described in section 6.4 in terms of yield, plasma quality and extraction time.

6.7 Summary

This chapter described the development and testing process of the bonded 3D printed devices, which were created to overcome most of the challenges in manufacturability, usability and performance seen with the PMMA devices described in chapter 4. The manufacturing procedure took full advantage of the type of 3D printer adopted, as the same resin used for the printing of the individual parts was also used to bond them together with an integrated plasma separation membrane in between. This method proved extremely successful, with the devices performing well and proving to be reliable in extracting a high percentage of good quality plasma. The best version (B4.2) had an average yield of 51.34% and a slightly lower Hgb concentration than centrifuged controls, indicating that haemolysis did not occur during the separation process. The low failure rate $< 5\%$, combined with one simple operational step and a total average extraction time of 76.11 seconds, makes these devices quick, easy and reliable to use, with only a manual pipette required for the extraction. The plasma collected with this device version was also used to test six bovine samples for the presence of antibodies to BRSV using an ELISA test. The results were comparable to centrifuged controls, proving the suitability of the extracted plasma for immunoassay testing.

The main downside of these devices is the manual fabrication step required to deposit the correct amount of resin in the deposition channel. If an excessive volume of resin is poured, the membrane can easily absorb part of the resin, which then hardens up during the curing process and reduces the usable surface area of the membrane. On the other hand, an insufficient amount of resin can lead to blood leaking to the downstream side of the membrane and contaminating the plasma. Overall, the devices perform well and could be easily integrated in any resin-based, 3D printed lab-on-a-chip platform. However, a simpler solution would be welcome that would allow joining the two layers together in the same effective manner while eliminating manufacturing difficulties.

Chapter 7

Development and testing of snap-fit 3D printed devices

7.1 Design and print settings

The next generation of 3D printed devices consisted of two separate objects assembled through a snap-fit connection. This chapter discusses the development and testing of snap-fit devices based on lock (figure 7.1) and locator features (7.2). All components were printed in a flat orientation to save time and resin as discussed in chapter 6, section 6.1. The interlocking features were designed to be printed successfully in this orientation, with unsupported overhangs that could be handled well by the 3D printer without the use of external supports. The final designs are parametric so that the user can easily adjust them to accommodate a larger membrane or different pipette tips.

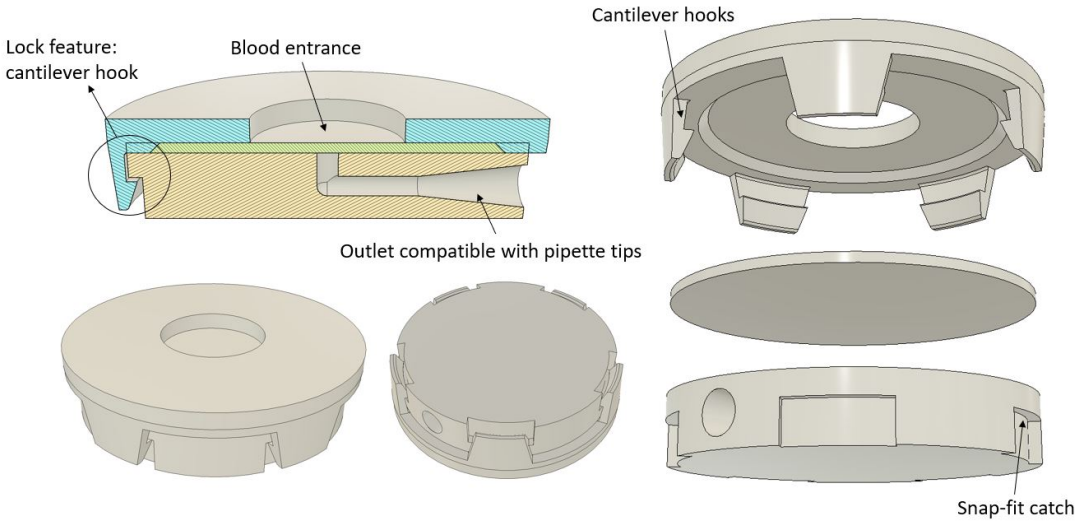

Figure 7.1: Cross-section, top, bottom and exploded view of the final iteration of lock-based snap-fit devices. When engaged, the cantilever hooks hold the top and bottom parts together while compressing the edges of the membrane to prevent spills towards the outlet.

The top and bottom parts of the bonded devices were firmly locked together by cured resin. In the snap-fit devices, on the other hand, the top and bottom parts can experience some lateral play due to the clearances included in the design for the assembly

of the snap-fit features. When the snap-fit devices were flipped upside down and operated as the bonded 3D printed devices described in chapter 6, lateral movement during extraction occasionally caused the membrane to shift sideways and let blood through the edges.

To resolve this issue, both types of snap-fit devices were designed to be operated vertically instead of horizontally. The design included a short channel with a 90° bend directly connected to an outlet shaped to match the pipette tips used. This setup offered two advantages compared to the more straightforward design used in the bonded devices:

- Easier fabrication, as the outlet channel of the bonded device often remained open during the printing process when placed on the back of the printing platform, forcing the user to remove the half-cured resin from the channel manually to save the printed part.
- A larger amount of the pipette tip can be inserted in the device and can be pushed deeply into the channel to create an air-tight seal without the risk of puncturing the membrane. When pushed all the way in, the pipette tip is close to the channel bend, so the channel length is not long enough to negatively affect the extraction process.

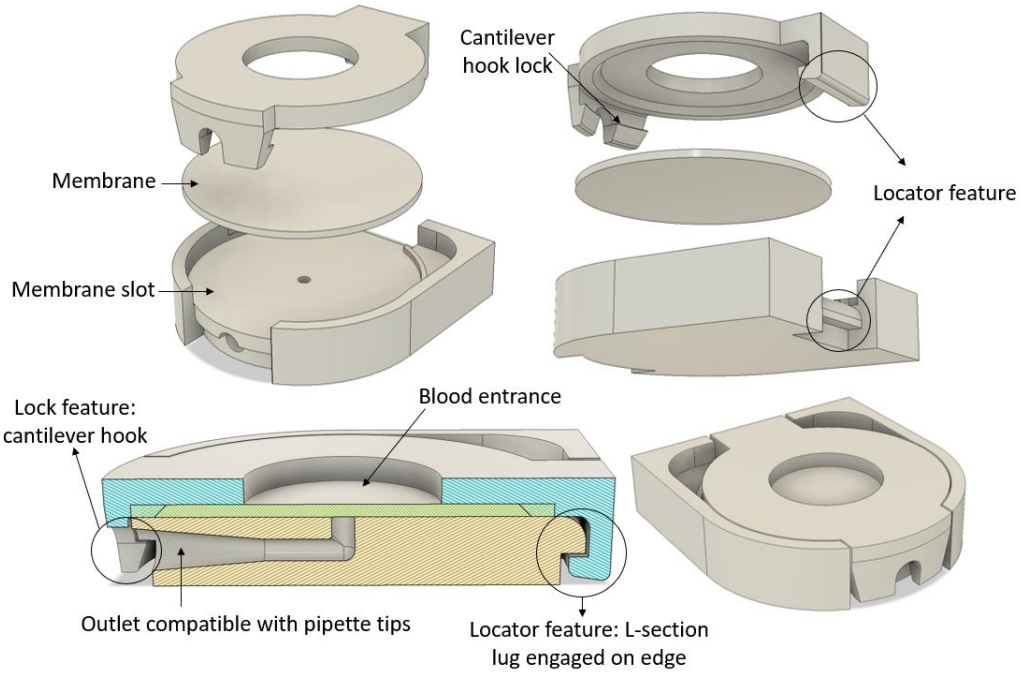

Figure 7.2: Cross-section, top and exploded view of the final iteration of locator-based snap-fit devices. The inflexible locator offers more stability than a cantilever-hooks only configuration, meaning that the membrane can be better compressed at the edges. Having only one locking feature, these devices are also easier to assemble and disassemble than their lock-only counterpart.

During blood testing, the lock-based devices were difficult to grip during plasma extraction without compressing one or more of the cantilever hooks. Compromised hook could be accidentally released from their lock, easing the pressure on the membrane edges and causing blood to pass around the membrane and reach the outlet. The locator-based devices resolved this issue by providing a firm locator-lock mechanism that was safely

surrounded by the bottom layer with no features along the sides, allowing the user to grip the device tightly during the plasma extraction process.

7.2 Assembly process

The manufacturing process was similar for both lock and locator-based snap-fit devices. The objects were first printed as described in chapter 2 and then cured under UV light in a clean, transparent container filled with water. As the curing process is faster with reduced oxygen exposure, the prints were only cured for 10 minutes instead of the 20 minutes required for the bonded devices. Once the objects were removed from the water bath, they were dried with compressed air and cleanroom tissue. The devices were then assembled as follows:

- The membrane was placed in its slot in the bottom layer, as shown in figure 7.2.
- Lock-based devices: the cantilever hooks in the top layer were aligned with the catches in the bottom layer and the two were then joined as uniformly as possible until all cantilevers were engaged against their respective catch.
- Locator-based devices: the top layer was assembled by first aligning the lug under the locator feature, then pivoting the cap and finally snapping the cantilever hook to the lock in the front of the device.

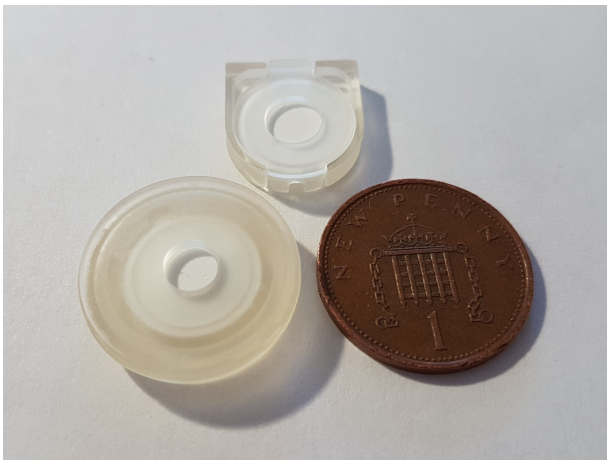

Figure 7.3: Assembled locator-based device placed next to a bonded 3D printed device and a one penny coin. The snap-fit device is smaller and less material-consuming than its bonded counterpart.

The snap-fit devices could also be easily disassembled, which allowed them to be disinfected, re-assembled and re-used when needed. A maximum of 15 snap-fit devices could be fabricated in one batch as shown in figure 7.4. Each batch required a total fabrication time of 45 minutes (15 minutes printing, 10 minutes washing and drying, 10 minutes curing and 10 minutes for drying and assembly), which corresponded to approximately 5 minutes per device.

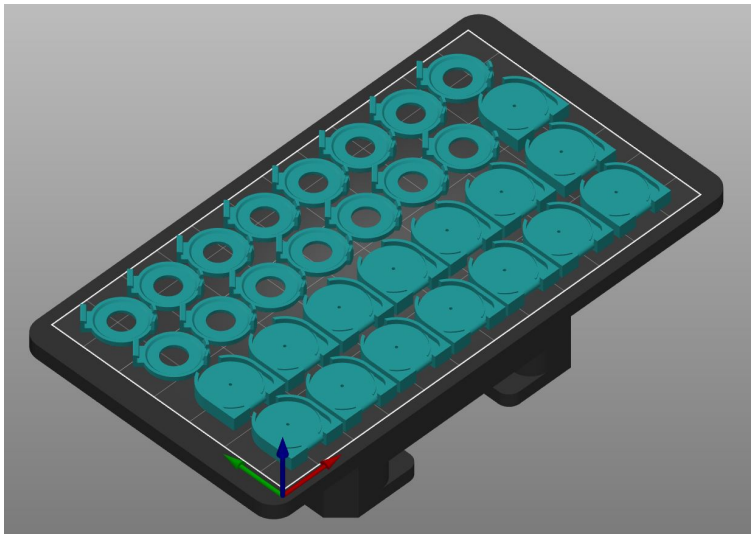

Figure 7.4: A ready-to-print batch of locator-based 3D printed devices placed on the printing platform of the PrusaSlicer software.

7.3 Operational steps

The steps required for operating both the lock and locator-based devices are identical. Figure 7.5 illustrates the steps using the locator-based devices as an example. Once the blood is placed inside the device, the user can immediately extract the plasma using a pipette. The blood is absorbed by the membrane so that the user does not risk direct contact with it while extracting the plasma.

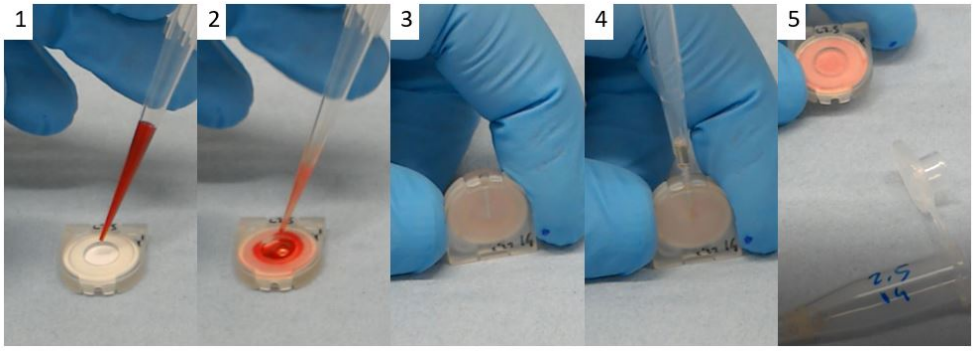

Figure 7.5: Operational steps of the 3D printed snap-fit devices. 1) Assembled device ready to be used. 2) Blood is placed inside the device. 3) The device is placed on its side to place the outlet in a favourable position for extraction. 4) The plasma is collected immediately using a 100 µL pipette. 5) The plasma is placed inside a centrifuge tube for further assessment.

7.4 Results and discussion of lock-based "snap-fit" 3D printed devices

7.4.1 Effect of feature modifications

After creating a functional version of the lock-based 3D printed devices (S1.1), multiple features were tested to improve the baseline results. This section explores the effects of feature modifications attempted on the lock-based 3D printed devices. Table 7.1 offers

a summary of the features covered and maps them to the corresponding device IDs.

Table 7.1: Feature modifications tested during the development of lock-based 3D printed devices.

Device ID	Outlet channel location	Blood inlet diameter (mm)	Membrane support	Membrane slot h. (mm)	Plasma collection channels	Direct plasma exit	Channel diameter (mm)
S1.1	Central	5	N	0.35	1	N	0.70
S1.2	Side	5	N	0.35	1	N	0.70
S2	Central	8	N	0.35	1	N	0.70
S3.1	Central	6	0.1 mm gap	0.35	1	N	0.70
S3.2	Central	6	Micropillars	0.35	1	N	0.70
S3.3	Central	6	Micropillars	0.30	1	N	0.70
S3.4	Central	6	Micropillars	0.35	1	N	0.70
S3.5	Central	6	Micropillars	0.40	1	N	0.70
S4.1	Central	6	N	0.30	1	N	0.70
S4.2	Central	6	N	0.30	1	N	0.90
S5.1	Central	6	N	0.35	1	N	0.70
S5.2	Central	6	N	0.40	1	N	0.70
S6.1	Central	5	N	0.35	5	N	0.70
S6.2	Central	5	N	0.35	5	N	0.70
S7	Central	5	N	0.35	1	Y	0.70

Outlet channel location

The S1 devices were created as a control (S1.1) and test (S1.2) pair to study the consequence of having a longer outlet channel placed on the side of the device farthest from the inlet (figure 7.6). The devices performed similarly in terms of failure rate, but the S1.1 devices outperformed the S1.2 ones both in terms of yield (43.61% vs 38.8%) and plasma quality ($0.0012\,\mathrm{g\,dL^{-1}}$ vs $0.0151\,\mathrm{g\,dL^{-1}}$.

Blood inlet diameter

To test the effect of a larger blood inlet diameter on the device performance, the S2 devices were designed with a larger inlet diameter than their predecessors, as shown in figure 7.6. Their results were among the best of the lock-based devices, with a high yield of 50.88%, a low Hgb difference of $-0.0038\,\mathrm{g\,dL^{-1}}$ and no failures observed among the 13 devices tested, with only one having visible residual cells in the plasma extracted. The extraction time, however, was extremely high (163 seconds). Moreover, disassembly was complicated by the fragility of the top layer, which had less material in the centre than the devices with narrower inlets and tended to snap in two parts easily. As a compromise, the subsequent devices were fitted with a slightly larger inlet than the S1 devices.

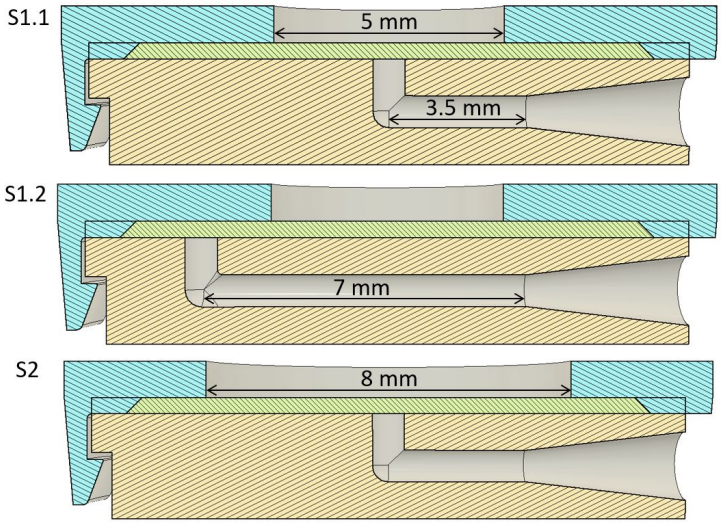

Figure 7.6: Cross sections of the design of devices S1.1, S1.2 and S2 with measurements of the inlet diameter and outlet channel length.

Membrane support

As mentioned in chapter 6, many devices found in the literature use micropillar arrays to support the membrane in their plasma separation devices. The S3 devices were created to determine whether micropillar arrays are a good form of membrane support for the 3D printed devices. S3.1 was a control device with no micropillars and a gap of 0.1 mm under the membrane. S3.2 had two rows of 0.5 mm diameter micropillars, with each row spaced apart by 2.56 mm. Designs S3.3, S3.4 and S3.5 had 3 rows of micropillars with ∼1.125 mm of space both between rows and between each micropillar. The designs can be seen in figure 7.7.

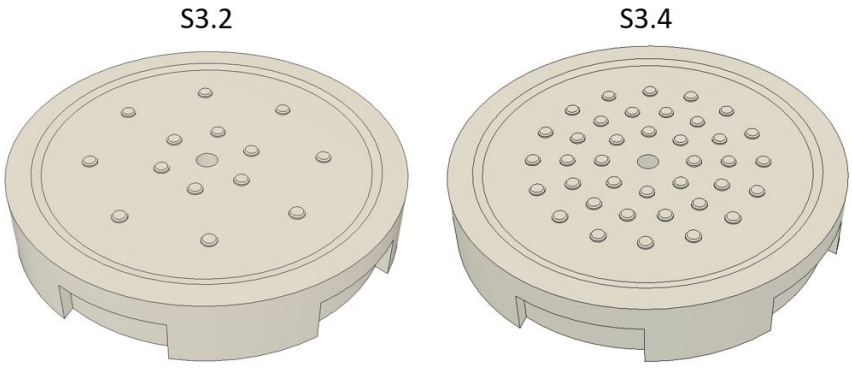

Figure 7.7: Difference between micropillars of designs S3.2 and S3.4. The height of the micropillars was 0.1 mm in both designs.

The S3.1 devices performed poorly, with the lowest yield among functional devices (25%) and a 33% failure rate. S3.2 were slightly better, with a 36.44% yield and 18% failure rate. Both types had, however, extremely good plasma quality with a Hgb difference of $-0.0026\,\mathrm{g\,dL^{-1}}$ and $-0.0067\,\mathrm{g\,dL^{-1}}$ for S3.1 and S3.2 respectively. Out of the other S3 devices, S3.4 was the only one to have the same membrane slot height as S3.1 and S3.2 and was therefore used to compare the second micropillar array pattern. The yield was dramatically improved (47.75%), along with the extraction

time and the failure rate (0%). However, this came at the expense of plasma quality $0.0412\,\mathrm{g\,dL^{-1}}$. Overall, neither of the micropillar arrays were successful in improving the plasma separation devices.

Membrane slot height

Differences in device performance induced by membrane slot heigh were examined using both normal devices (S4.1 and S4.2) and devices fitted with micropillar arrays (S3.3 and S3.5). The height of the membrane slot in designs S3.3, S4.1 and S4.2 was 0.3 mm, while S3.5 had a larger, 0.4 mm high membrane slot.

The designs S4.1 and S4.2 were identical except for the diameter of the plasma collection channel connected to the outlet, which was increased from 0.7 mm in S4.1 to 0.9 mm in S4.2. The wider channel in the S4.2 devices had positive effects both on yield (from 43.18% of S4.3 to 48.08% of S4.2) and failure rate (from 30% to 0%). However, the membrane compression seriously compromised the plasma quality in both cases, with a Hgb difference of $\sim 0.4\,\mathrm{g\,dL^{-1}}$. Increasing the collection channel diameter should be explored further in future work on the devices.

Although the extraction time was significantly improved compared to the other lock-based iterations, both the S3.3 and S3.5 devices had a high failure rate (30% and 37% respectively) and poor plasma quality, with an average Hgb difference of $0.0281\,\mathrm{g\,dL^{-1}}$ and $0.0745\,\mathrm{g\,dL^{-1}}$ respectively.

These findings corroborate the results from the bonded devices, where it was also concluded that membrane compression has a negative effect on plasma quality. The S3.5 devices also performed poorly, likely due to excess dead volume caused by the space between micropillars combined with the excess space above the membrane.

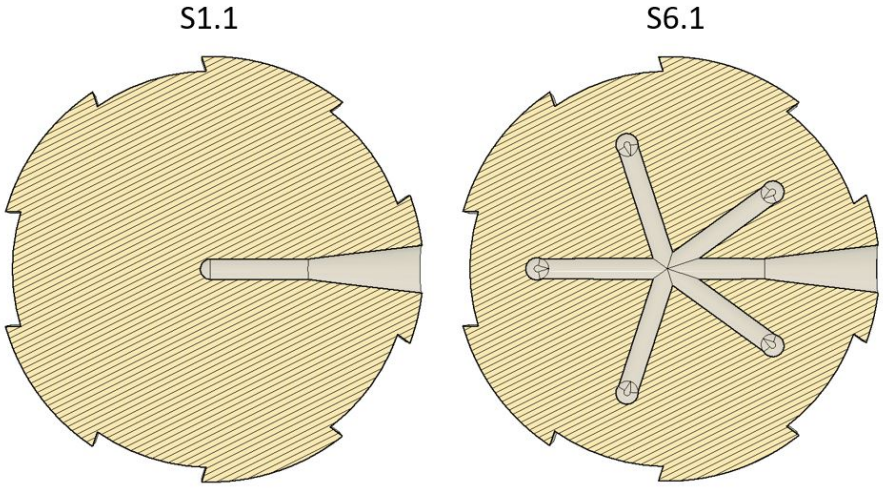

Figure 7.8: Comparison between horizontal cross section of S1.1 and S6.1.

Number of plasma collection channels

To compare the effect of having multiple plasma collection channels, the design S6.1 was fitted with 5 plasma collection channels as show in figure 7.8. Both yield and plasma quality were low (35% and $0.0211\,\mathrm{g\,dL^{-1}}$ respectively). The average extraction

time was also longer than any other lock-based device (173 seconds), suggesting that devices with multiple collection channels do not perform better than those with a single channel.

Direct plasma exit

The design S7 was fitted with the same outlet channel as the bonded devices (figure 7.9). The S7 devices performed poorly, with an average yield of 42.36%, a Hgb difference of $0.0212\,\mathrm{g\,dL^{-1}}$ and a high failure rate of 36.36%.

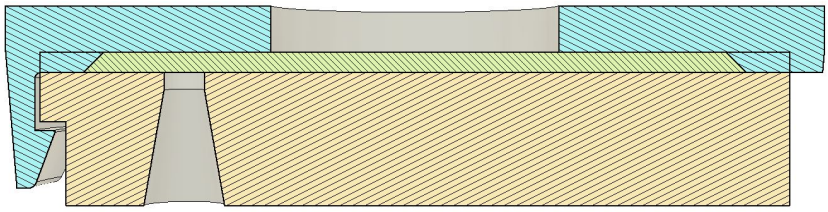

Figure 7.9: Cross sections of the design S7.

Larger membrane

Increasing the membrane size from 13 mm diameter to 16 mm while still using a 50 µL input blood sample caused complete failure in the S6.2 devices, which were otherwise identical to the S6.1 ones. This result was expected, as the membrane area is far too large for the input sample volume. Using a larger sample size was not attempted at this stage, although it is considered an integral part of future work on these devices.

7.4.2 Data analysis

All the devices were tested as described in section 3.7.2 of chapter 3. The results are summarised in table 7.2.

Yield

Figure 7.10 shows the percentage of the total plasma available extracted by each iteration of lock-based devices. Only S2 and S5.2 reached an average yield≥50%. S3.4 and S6.1, on the other hand, were the most consistent type of device as they displayed the least amount of variation between devices tested.

Plasma quality

The difference between the haemoglobin concentration of the plasma extracted with the devices and the centrifuged control is shown in figure 7.11. Only the first five iterations (S1.1, S1.2, S2, S3.1 and S3.2) had an acceptable plasma quality, while the other devices produced plasma with haemoglobin concentrations well above that of the centrifuged controls, meaning that significant haemolysis occurred during the separation process.

Failure rate

Figure 7.12 compares all iterations of lock-based devices in terms of number of devices tested, their failure rate and percentage of devices that produced plasma containing visible residual RBCs. Other than the S6.2 devices, which failed completely, S3.1, S3.3, S3.5, S4.1 and S7 experienced the highest number of failures, with a failure rate ≥30%.

Table 7.2: Comparison of lock based snap-fit devices. The parameters used are described in table 6.2 of chapter 6.

	Average			Standard Deviation				
Device ID	**Yield (%)**	**Hgb diff. ($g\,dL^{-1}$)**	**Extraction time (s)**	**Yield (%)**	**Hgb diff. ($g\,dL^{-1}$)**	**Extraction time (s)**	**Failure rate (%)**	**Visible RBCs (%)**
S1.1	43.61	0.0012	167.64	12.79	0.0153	44.89	18.60	0.00
S1.2	38.80	0.0151	138.40	6.48	0.0259	35.33	25.00	0.00
S2	50.88	−0.0038	163.91	6.98	0.0100	36.55	0.00	8.33
S3.1	25.09	−0.0026	126.30	11.44	0.0212	35.86	33.33	0.00
S3.2	36.44	−0.0067	131.48	7.06	0.0070	47.59	18.18	9.09
S3.3	41.28	0.0281	74.49	10.39	0.0269	7.37	30.00	0.00
S3.4	47.75	0.0412	79.41	4.35	0.0281	14.03	0.00	0.00
S3.5	47.09	0.0745	76.80	9.55	0.0519	7.00	37.50	0.00
S4.1	43.18	0.0457	100.71	9.97	0.0221	23.39	30.00	0.00
S4.2	48.08	0.0421	105.36	7.09	0.0228	31.88	0.00	0.00
S5.1	48.50	0.0263	99.92	7.22	0.0211	27.23	7.14	0.00
S5.2	55.14	0.0441	90.17	7.35	0.0328	12.44	12.50	0.00
S6.1	35.00	0.0211	173.60	4.52	0.0150	33.93	10.00	0.00
S6.2	0.00	0.0000	0.00	0.00	0.0000	0.00	100.00	0.00
S7	42.36	0.0212	154.29	9.84	0.0212	46.78	36.36	0.00

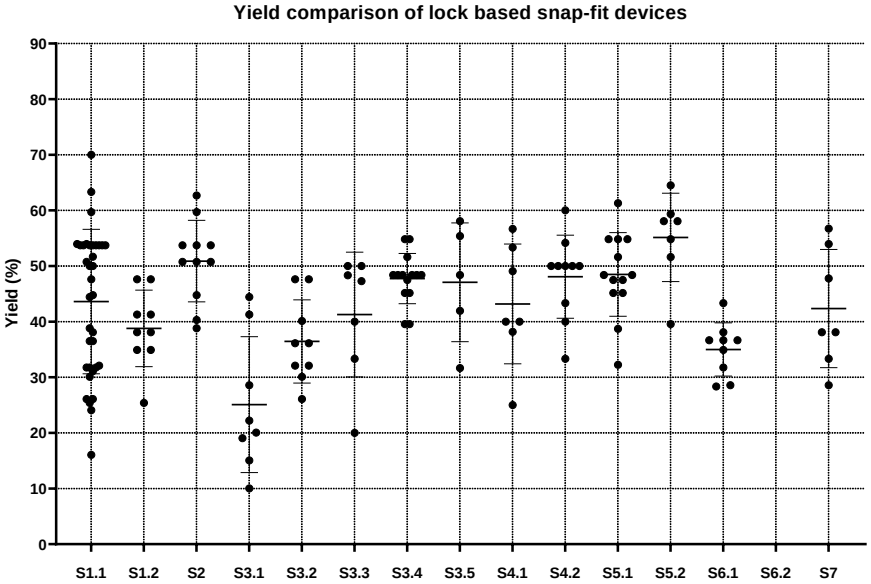

Figure 7.10: Yield comparison of all iterations of lock-based 3D printed snap-fit devices.

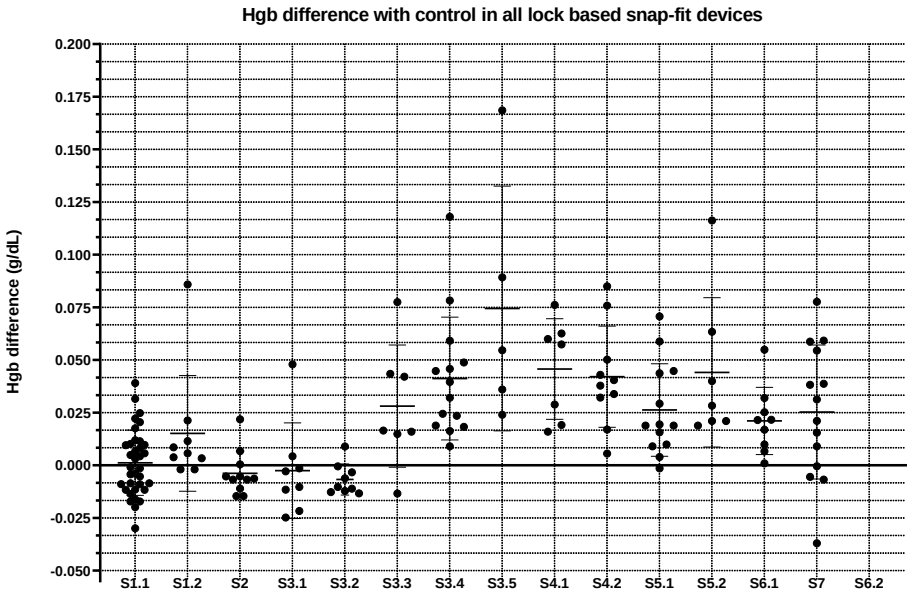

Figure 7.11: Comparison of plasma quality among all iterations of lock-based 3D printed snap-fit devices, measured as haemoglobin concentration difference with centrifuged controls.

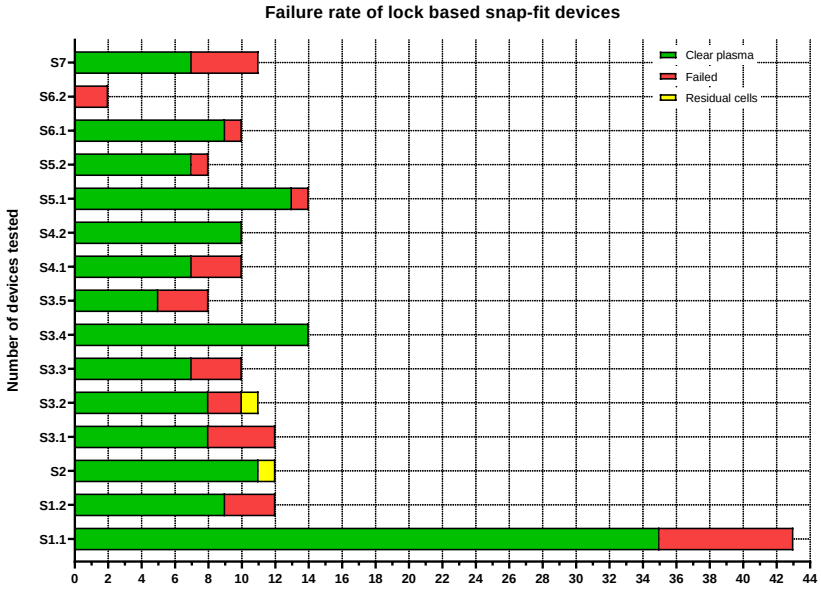

Figure 7.12: Total and partial failure rate comparison of all iterations of lock-based 3D printed snap-fit devices.

7.5 Results and discussion of locator-based "snap-fit" 3D printed devices

7.5.1 Effect of feature modifications

The best performing iterations of lock-based devices were S1.1 and S2 due to the relatively high yield, good plasma quality and acceptable failure rate. As such, these devices were used as the starting point for the development of the locator-based snap-fit devices. Table 7.3 summarises the feature modifications attempted to improve both the manufacturability and performance of the plasma separation modules. Each feature is discussed in detail below.

Table 7.3: Features explored during the development of locator-based 3D printed devices. First and second lock mechanism refer to the designs described in section 5.3.6 of chapter 5.

Device ID	Membrane slot height (mm)	Pattern	Lock mechanism
L1.1	0.35	None	First
L1.2	0.36	None	First
L2.1	0.40	None	First
L2.2	0.40	SP	First
L2.3	0.40	SF	First
L2.4	0.40	K	First
L2.5	0.40	K2	First
L2.6	0.40	SP2	First
L3.1	0.40	None	Second
L3.2	0.40	SP	Second
L3.3	0.40	SF	Second
L3.4	0.40	K	Second

Membrane compression

The L1.1 and L1.2 devices were the only type with a membrane slot with height $<$ 0.4 mm. Although this did not have a direct effect on device performance, it was observed that during the assembly process the edge of the membrane closer to the locator was pinched against the bottom layer, occasionally causing membrane damage. To resolve this issue, all the subsequent devices were fitted with a 0.4 mm high membrane slot, which successfully prevented the membrane from being compressed on the locator side.

Effect of plasma collection pattern

Different collection patterns placed underneath the membrane were tested to determine whether they would improve the plasma separation process in the snap-fit 3D printed devices. Figure 7.13 shows all patterns used throughout this study, which were fitted on devices L2.1 to L2.6. Some of these patterns were previously introduced and tested with the bonded devices, as explained in section 6.4.1 of chapter 6.

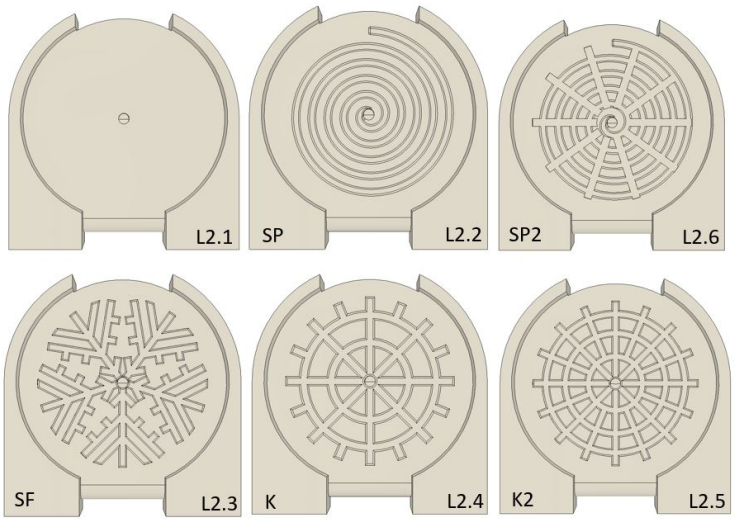

Figure 7.13: Labelled bottom layers with patterns used in the development of locator-based snap-fit devices, matched to the corresponding device ID.

Overall, the patterns had a positive effect on the device performance. All devices fitted with a pattern performed better than the pattern-less control (L2.1) in terms of yield, plasma quality and extraction time. Patterns SP and SF in L2.2 and L2.3 were particularly successful, with a yield of 56.88% and 58.71% respectively, excellent plasma quality and a low failure rate (0% for L2.2 and 14.3% for L2.3). The remaining patterns had either lower yield or a significantly higher failure rate. As such, the SP and SF patterns were selected for further analysis with the final devices.

Lock mechanism

Section 5.3.6 of chapter 5 offered an in-depth description of the two different lock mechanisms developed for the locator-based devices. All L3 devices were designed with the second mechanism in place, which ensures a much easier and successful assembly process. The patterns tested are shown in figure 7.14, where they are also compared to the L2 devices. All of the L3 devices performed poorly compared to the L2 counterpart, with lower yield and higher failure and visible residual cell percentage. The plasma quality and the extraction time, however, remained good and the assembly process was far superior to the L2 devices, which often required pliers to be assembled and had a high assembly failure rate. Given that the reused L3 devices performed better than their fresh counterpart, the L3 devices were tested again with better input samples, with the results being discussed in section 7.5.4.

7.5.2 Re-usability analysis

To determine whether it was possible to safely and successfully reuse the snap-fit devices, some of locator-based devices tested were disassembled, cleaned, disinfected and re-tested up to two times. The full procedure used to clean and disinfect the used devices is given below:

1. The used devices were first disassembled. Device parts that still contained blood after disassembly were scrubbed with 70% Ethanol and a toothbrush.

2. All parts were placed inside a waterproof container and soaked for 15 minutes in

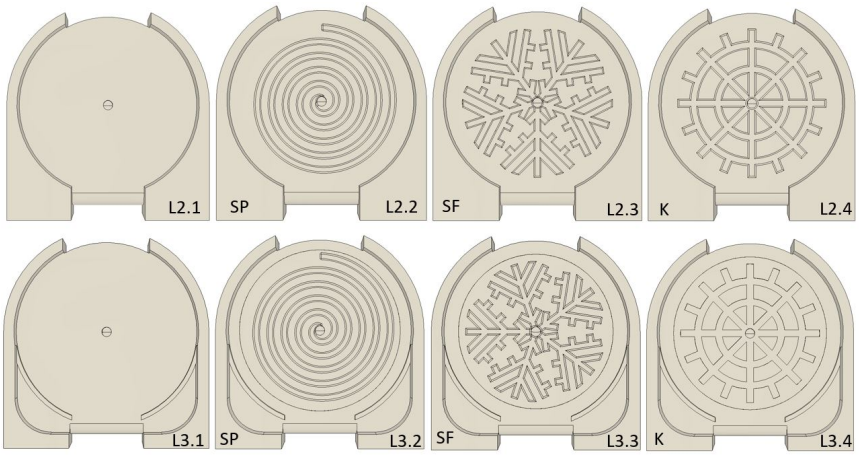

Figure 7.14: Labelled bottom layer of devices used in the lock mechanism comparison.

a TriGene ADVANCE disinfectant solution available in the laboratory.

3. The parts were then rinsed 3x times in tap water, scattered onto an absorbent tissue and left to dry completely.

As can be seen in table 7.4, the yield of reused devices did not differ significantly from that of fresh devices and the plasma quality was slightly lower in reused L2 devices. The reused L3 devices performed better on average than their fresh counterparts both in terms of yield and plasma quality, indicating that perhaps the input samples of the fresh devices had a negative effect on their performance.

The failure rate and visible residual cell percentage, however, was significantly worse in the reused devices and was progressively worsened by repeated use, with the RR devices having by far the highest failure and visible residual cell rate. This is likely due to a combination of material and snap-fit degradation due to the disinfection process and repeated assembly/disassembly. The weakened material at the top layer was unable to maintain a consistent level of membrane compression, leading to blood passing around the membrane and through the outlet. In summary, the snap-fit devices can be reused, although with higher probability of failure than fresh devices.

7.5.3 Data analysis

The test results from all device iterations are shown in table 7.4, where R and RR denote devices that have been reused once and twice respectively.

Yield

Figure 7.15 gives an overview of the average yield of the locator-based devices. The highest volume of available plasma extracted was seen in L2.2 (56.88%) and L2.3 (58.71%), although a large percentage of the device iterations also achieved an average yield $\geq$50%.

Plasma quality

Figure 7.16 shows the average difference in haemoglobin concentrations between the plasma extracted with the devices and the centrifuged control plasma prepared from the

Table 7.4: Comparison of locator based snap-fit devices. The parameters used are described in table 6.2 of chapter 6.

	Average			Standard Deviation				
Device ID	**Yield (%)**	**Hgb diff. (g dL^{-1})**	**Extraction time (s)**	**Yield (%)**	**Hgb diff. (g dL^{-1})**	**Extraction time (s)**	**Failure rate (%)**	**Visible RBCs (%)**
L1.1	44.09	−0.0142	96.00	5.48	0.0016	16.97	0.00	33.33
L1.2	51.61	−0.0125	88.50	2.28	0.0030	18.31	33.33	16.66
L1.2_R	36.9	−0.0073	106.50	3.08	0.0026	19.50	0.00	0.00
L2.1	49.65	−0.0098	93.43	4.81	0.0044	17.15	0.00	0.00
L2.1_R	46.4	−0.0079	79.20	1.51	0.0014	4.49	30.00	20.00
L2.2	56.88	−0.0027	86.77	9.25	0.0100	12.31	0.00	7.14
L2.2_R	51	0.0098	111.75	8.62	0.0029	14.29	0.00	0.00
L2.3	58.71	−0.0034	84.27	6.92	0.0162	13.50	14.29	35.71
L2.3_R	55	0.0132	75.60	9.31	0.0125	2.94	0.00	40.00
L2.4	53.85	−0.0086	80.67	5.38	0.0030	4.78	30.77	0.00
L2.4_R	51.52	0.0048	82.13	6.78	0.0034	4.48	0.00	20.00
L2.5	51.77	−0.0018	88.00	9.60	0.0098	15.02	6.67	33.33
L2.5_R	50.00	0.0111	78.00	3.97	0.0061	0.00	50.00	25.00
L2.6	53.52	−0.0028	82.00	6.92	0.0162	4.00	23.08	15.38
L3.1	44.45	−0.0031	100.77	8.87	0.0109	24.95	11.11	14.81
L3.1_R	45.10	0.0049	92.20	7.28	0.0149	18.18	26.09	30.43
L3.1_RR	42.77	0.0022	78.00	9.56	0.0130	6.00	58.33	25.00
L3.2	46.51	0.0044	87.00	7.00	0.0131	15.04	17.65	17.65
L3.2_R	49.85	0.0054	83.44	4.78	0.0193	10.62	10.53	21.05
L3.2_RR	49.95	−0.0002	85.25	6.76	0.0076	13.72	7.14	35.71
L3.3	42.50	0.0031	89.31	9.12	0.0126	13.83	11.76	29.41
L3.3_R	49.93	−0.0030	84.82	4.44	0.0057	11.94	11.11	50.00
L3.3_RR	56.24	−0.0029	83.50	5.42	0.0100	16.65	57.14	21.43
L3.4	44.78	0.0142	85.07	5.07	0.0249	21.44	21.05	26.32
L3.4_R	52.40	0.0041	88.67	5.22	0.0203	17.33	26.32	31.58
L3.4_RR	54.67	0.0005	87.75	6.72	0.0058	19.43	42.86	21.43

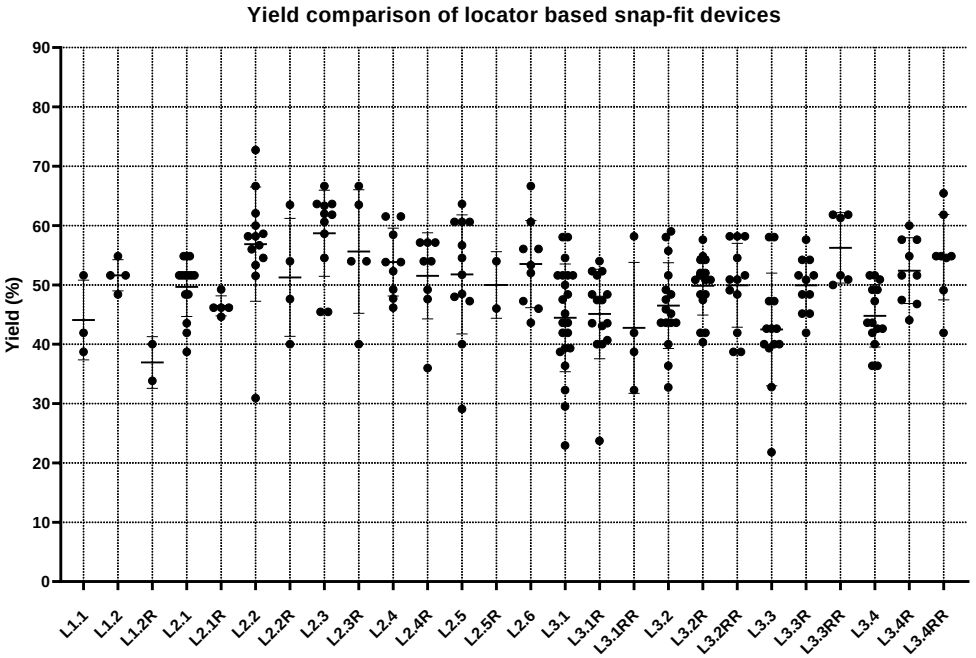

Figure 7.15: Yield comparison of all iterations of locator-based 3D printed snap-fit devices.

same sample. With the exception of a few outliers, most devices produced plasma that was very close with the controls in terms of quality. The L3.1 devices, in particular, had the highest number of data points and yet consistently produced good quality plasma, even in the reused versions. L2.1 and L2.4 also performed particularly well, with most or all of the extracted plasma being of higher quality than the centrifuged counterpart.

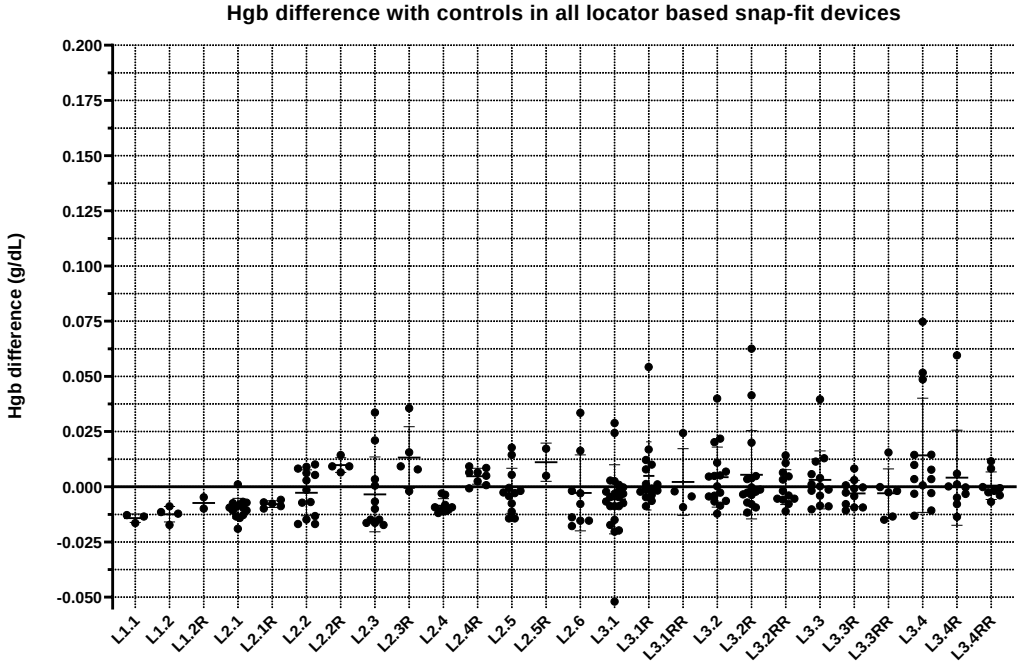

Figure 7.16: Comparison of plasma quality among all iterations of locator-based 3D printed snap-fit devices, measured as haemoglobin concentration difference with centrifuged controls.

Failure rate

Figure 7.17 shows the number of devices tested per iteration, along with their failure rate and number of devices that outputted plasma with visible residual RBCs. L2.1 and L2.2 devices, in particular, stand out for their 0% failure rate with 14 devices tested for each type.

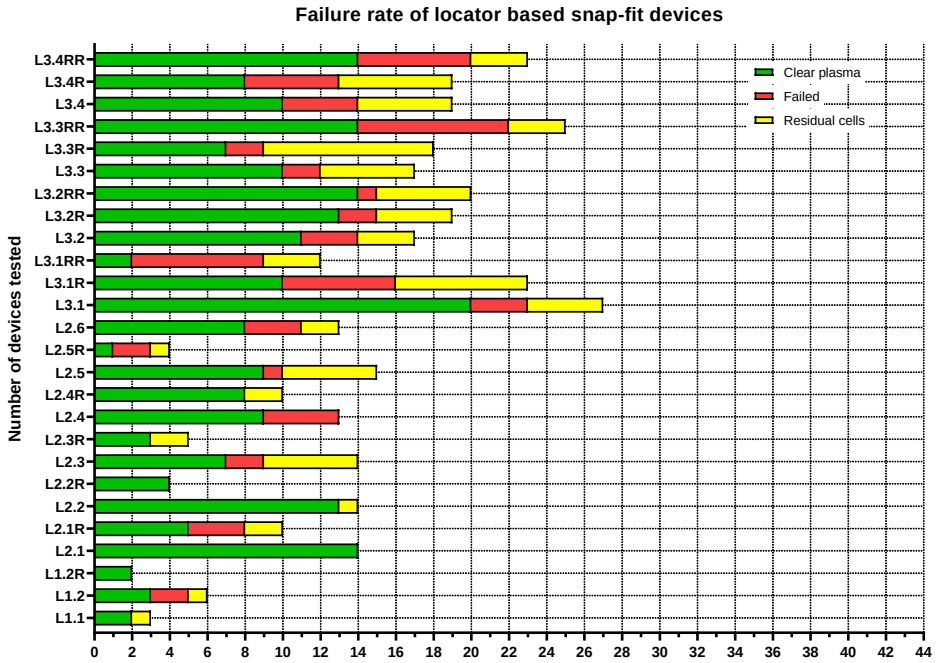

Figure 7.17: Total and partial failure rate comparison of all iterations of locator-based 3D printed snap-fit devices.

7.5.4 Retesting of locator-based L3 devices

Table 7.5: Haematocrit, Hgb concentration and number of devices tested for all samples to use the initial, initial reused and retested L3 devices. W. Avg is the weighted average of Hct and Hgb concentrations, while n is the number of devices tested.

	Retested			Initial			Initial reused		
	Hct (%)	Hgb ($g\,dL^{-1}$)	n	Hct (%)	Hgb ($g\,dL^{-1}$)	n	Hct (%)	Hgb ($g\,dL^{-1}$)	n
Sample 1	40	0.0331	42	39	0.0467	38	50	0.0569	19
Sample 2	37	0.0461	21	45	0.0600	39	38	0.0567	26
Sample 3	40	0.0584	30	38	0.0733	12	41	0.0733	28
Sample 4	36	0.0355	15						
W. Avg	38.86	0.0430		41.49	0.0561		42.27	0.0631	

This section covers the retesting of the L3 devices. Due to time constraints and general sample scarcity, a large percentage of the L3 devices were tested with poor quality samples which were likely a few days old by the time they reached the laboratory. The centrifuged control plasma from such samples was visibly affected by haemolysis

Table 7.6: Comparison of retested locator-based L3 devices. The parameters used are described in table 6.2 of chapter 6.

	Average			Standard Deviation				
Device ID	**Yield (%)**	**Hgb diff. (g dL^{-1})**	**Extraction time (s)**	**Yield (%)**	**Hgb diff. (g dL^{-1})**	**Extraction time (s)**	**Failure rate (%)**	**Visible RBCs (%)**
L3.2	53.98	0.0110	99.00	7.79	0.0121	24.03	15.38	23.08
L3.2_R	63.28	0.0121	103.41	7.00	0.0153	20.71	25.00	16.67
L3.2 all	58.63	0.0116	101.21	7.39	0.0137	22.37	20.19	19.87
L3.3	59.43	0.0026	100.36	6.02	0.0040	18.38	26.67	40.00
L3.3_R	64.85	0.0069	88.29	4.02	0.0104	13.83	29.17	33.33
L3.3 all	62.14	0.0048	94.32	5.02	0.0072	16.10	27.92	36.67
L3.4	60.00	0.0025	96.00	5.90	0.0097	29.14	20.00	13.33
L3.4_R	60.93	0.0050	96.00	8.08	0.0057	37.81	53.33	13.33
L3.4 all	60.46	0.0038	96.00	6.99	0.0077	33.48	36.67	13.33

and had high concentrations of haemoglobin. A comparison of the control plasma haematocrit and Hgb concentration from each sample used to test and retest the L3 devices is shown in table 7.5.

The samples used for the retesting of the L3 devices had a lower average Hct and Hgb concentration than the samples used in the initial tests. The increased Hgb content was partly due to the higher Hct and mostly a consequence of the significant haemolysis of the RBCs in the samples. The results of the retesting are summarised in table 7.6, which show a dramatic yield improvement compared to the initial L3 devices tested, likely due to the increased sample quality. The term "all" refers to the merged data of the fresh and reused devices, which are also presented separately.

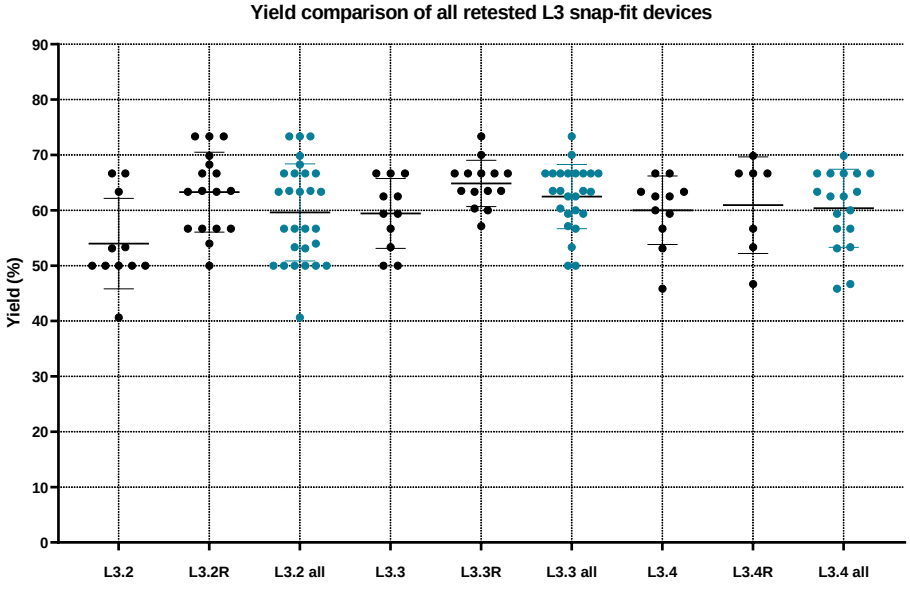

Figure 7.18: Yield comparison of all retested L3 snap-fit devices.

Yield

The average yield of the retested L3 devices is shown in in figure 7.18. With the exception of the L3.2 devices, all designs had an average yield ~60%, which is extremely good for a microfiltration plasma separation device.

Plasma quality

Figure 7.19 shows the Hgb difference between the plasma collected with the L3 devices and their respective control plasma. The plasma quality of most devices was close to that of the controls, with the L3.3 and L3.4 devices performing better than the L3.2 ones (average Hgb difference of $0.0048\,\mathrm{g\,dL^{-1}}$, $0.0038\,\mathrm{g\,dL^{-1}}$ and $0.0116\,\mathrm{g\,dL^{-1}}$ respectively).

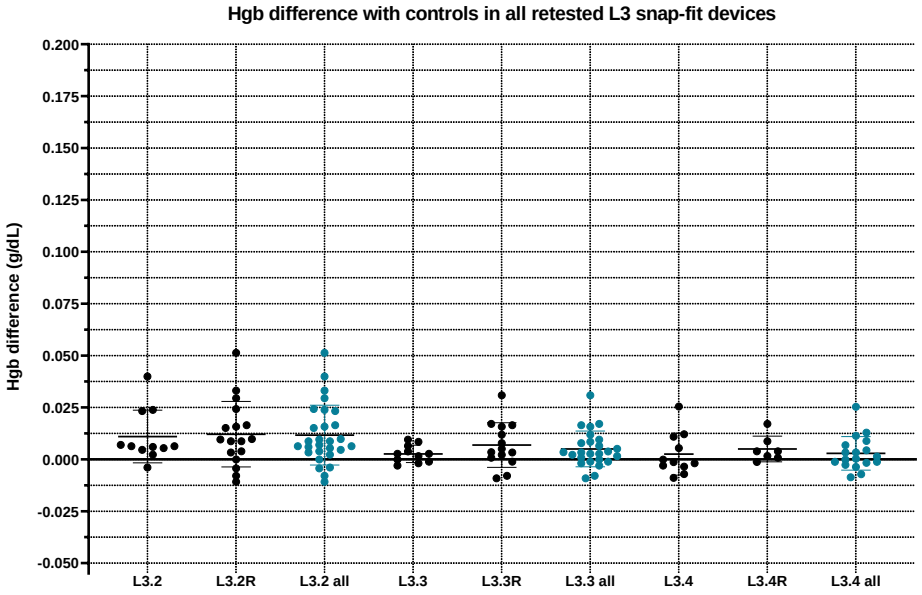

Figure 7.19: Comparison of plasma quality among all retested L3 snap-fit devices, measured as haemoglobin concentration difference with centrifuged controls.

Failure rate

The failure rate and visible residual cell percentage of the retested L3 devices is shown in figure 7.20. As observed previously, reused devices had a higher probability of failure. Overall, the failure rate is clearly high, particularly for the L3.3 and L3.4 devices, indicating that perhaps the locator mechanism needs to be adjusted to be more sturdy and exert more pressure at the edge of the membrane to prevent blood to flow to the downstream area of the membrane.

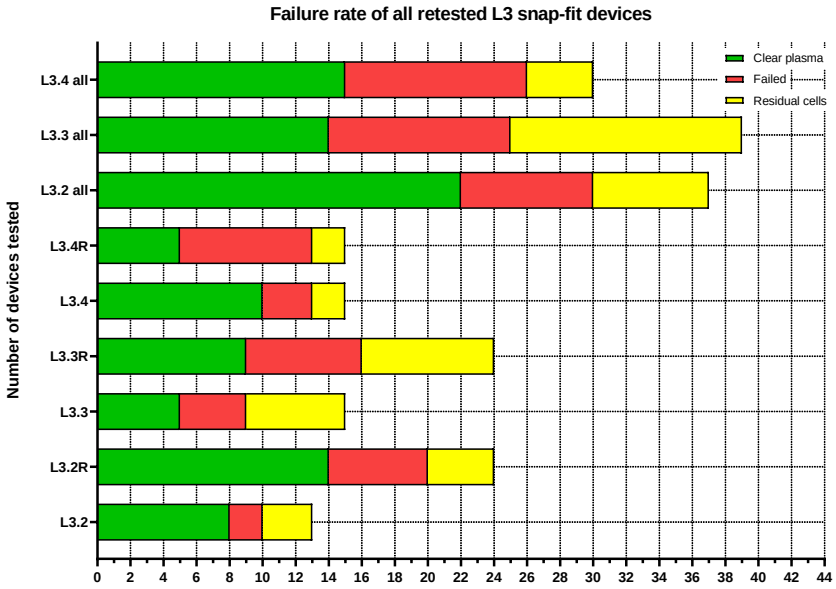

Figure 7.20: Total and partial failure rate comparison of all retested L3 snap-fit devices.

7.6 Effect of sample quality and Hct on device performance

This section discusses the effect of sample quality and Hct on the performance of the locator-based L3 devices. Table 7.7 shows the average yield, Hgb concentration difference with controls and failure rate of all L3 devices tested (both initial and retested merged are included) as a function of the Hct of the initial sample.

Table 7.7: Average yield, Hgb concentration difference with controls, failure rate and visible residual cell % of all L3 devices tested with different samples of varying Hct (35 to 50%), given along with the total number of devices tested.

Sample Hct (%)	35	36	37	38	39	40	41	45	50
Avg Yield (%)	45.54	53.26	61.46	48.13	41.43	61.94	49.58	46.69	52.67
Avg $\triangle$Hgb ($g\,dL^{-1}$)	0.0015	0.0049	0.0048	−0.0057	−0.0023	−0.0018	−0.0022	0.0123	0.0593
Failure rate (%)	37.50	6.67	33.33	13.51	12.00	19.44	14.29	35.29	42.11
Residual cell (%)	37.50	40.00	23.81	33.78	12.00	19.44	25.00	17.65	36.84
Total tested	8	15	21	74	25	72	28	68	19

While the yield appears largely unaffected by the increasing Hct %, both the average Hgb and failure rate experienced a sharp increase when the 45% and 50% Hct samples were used. This could be caused by a number of factors:

1. Waiting time before extraction: the Vivid GR manufacturers claim that the membrane requires a longer time to filter out plasma from samples with higher Hct. As such, adding a short waiting time before extracting the plasma from the devices

depending on sample Hct could lead to improved results.

2. Potential device issues with membrane size: a slightly larger membrane could reduce surface fouling and decrease haemolysis, although the yield and extraction time might be negatively affected.

3. Differences in equine and human RBCs: the Vivid GR membranes are designed to filter out human RBCs. Equine RBCs are slightly smaller in diameter, so this could have an impact on membrane performance when a larger cell percentage is present.

The failure rate of the 35% Hct sample was also high, although few data points were collected. It is worth noting that no equine sample was received with a natural Hct of 45% or 50%. Instead, plasma was removed from a few particularly good samples with low Hct to obtain these percentages. This was done to test the devices with a wide range of Hct within human physiological levels (36–46% in females and 41–53% in males[6].). The additional mixing necessary for this procedure inevitably led to significant haemolysis that could be easily noticed through visual inspection. As such, the samples were already compromised to some extent before testing.

L3 devices that were disassembled, disinfected and reused have been noted to have a higher failure rate in general compared to unused devices. To remove the potential effect of the reused L3 devices, the analysis was repeated for unused devices only. The results are shown in table 7.8, which includes data points for both initial and retested devices. Although the failure rate for the 45% Hct samples improved, the average Hgb concentration was still significantly higher compared to the lower Hct samples. Overall, further work is required to find out the exact cause of the increased haemolysis and failure rate when equine samples with higher haematocrit are used. The devices should first be tested with human blood in the 40-50% Hct range to eliminate inter-species differences in RBC diameter as a potential cause. Then, device features such as membrane size and compression at the edges should be adjusted until a more satisfactory result is obtained. Unfortunately, neither was possible throughout the duration of this project due to laboratory limitations and time constraint.

Table 7.8: Average yield, Hgb concentration difference with controls, failure rate and visible residual cell % of fresh L3 devices tested with different samples of varying Hct (36 to 45%). The number of total devices tested is also given.

Sample Hct (%)	36	38	39	40	45
Avg Yield (%)	53.26	49.58	41.43	59.50	41.69
Avg Hgb (g dL^{-1})	0.0049	−0.0139	−0.0023	0.0066	0.0196
Failure rate (%)	6.67	10.71	12.00	33.33	17.65
Residual cell (%)	40.00	32.14	12.00	16.67	14.71
Total tested	15	28	25	30	34

7.7 Summary

This chapter discussed the development of a range of 3D printed devices that relied on a snap-fit mechanism to easily connect two layers with a plasma separation membrane sandwiched in between. The first “lock-based” mechanism consisted of a series of

radial cantilever hooks placed around the edges of the device, while the final and most successful "locator-based" design made use of a locator feature and a single cantilever hook. The locator-based devices proved to be a definite improvement over the bonded 3D printed devices in terms of manufacturability, as the device layers can be first printed and post-processed independently, then easily and quickly joined with a membrane in between using the snap-fit mechanism.

A variety of features were analysed in an attempt to improve the device performance, including three different patterns placed at the downstream area of the membrane designed to facilitate the plasma collection process. Although none of the patterns tested could be conclusively said to be superior compared to the others, they all led to yield improvements compared to pattern-less devices. As the devices can be disassembled, disinfected and reassembled, a re-usability analysis was also carried out to establish whether the devices could be successfully re-used a number of times. While the general performance was unaffected, the failure rate was observed to increase significantly with every attempt at reusing the devices following disinfection.

The most successful locator-based device tested was the L2.2 version, with an average yield of 56.88%, a Hgb concentration in the extracted plasma lower than the centrifuged controls and an average fast exaction time of 87 seconds. Only one step was required for operating the device and the only accessory needed was a means of producing a gentle pressure drop at the outlet (a manual pipette was used in this study). Out of the 14 devices tested with this version, none failed and all produced plasma with purity $\geq$ 99.9%.

Overall, these devices are a happy compromise between design simplicity and performance. To the author's knowledge, no other research publication utilizes integral snap-fit mechanisms to secure a membrane in a plasma separation device. The devices not only perform well compared to other ones in the literature, but they are also extremely simple to fabricate, as the parts can be 3D printed using most modern resin-based printers (even the most affordable ones) and the assembly is easy and quick thanks to the intuitive snap-fit mechanism. The performance of each device version was thoroughly analysed so that other researchers can make an informed decision as to whether to use any part of this work in their studies. As developed, the devices can either serve as a stand-alone module or can be integrated in a larger lab-on-a-chip platform that requires sample preparation abilities.

Chapter 8

Additional work

8.1 Integrated 3D printed components

The possibility of creating 3D printed actuators, valves and air-tight reservoirs that could be integrated in the devices was briefly explored. Although the components were not integrated in the devices tested with blood, their further development could result in a self-powered device capable of more complex operations, all requiring no external power or user expertise. The components were fabricated using tough and flexible transparent resins. Mixes of the two at varying percentages were also tested without success.

8.1.1 Air-tight enclosures

The first step in the development of water and air-tight enclosures for the storage of reagents on-chip consisted in copying existing designs found in everyday objects. An example is the snap-fit enclosure shown in figure 8.1, which was printed using flexible resin to create the thin hinge that connects the top and bottom parts. The circular gap in the bottom layer was meant to compress a ring protruding from the top layer to create a seal. Flexible resin proved to be the correct choice for the hinge, allowing it to be printed correctly when supports were used during the print. However, the snap-fit mechanism at the front of the device, meant to lock the top and bottom parts, could not be engaged due to the resin's flexibility. Printing the part with tough resin resulted in a successful snap-fit, a broken hinge and no seal between the parts. Various mixes of tough and flexible transparent resins were attempted (50-50%, 25-75% and 75-25% of tough and flexible resin respectively) without success. The 25-75% flexible-tough mix behaved similarly to the flexible resin. The 50-50% mix resulted in an unsuccessful hinge and snap-fit, while the 75-25% mix was difficult to differentiate from tough resin alone.

A common way to achieve air-tight enclosures is through the use of gaskets, which are mechanical seals that, when compressed, fill the gaps between two mating surfaces, thus preventing the passage of fluids. First, 3D printed enclosures were tested using commercially available o-rings, that is rubber rings of circular cross section. The dimensions of the o-ring gland in the enclosure were calculated using the Apple Rubber Seal Design Guide[1]. The o-rings were successful in preventing fluid flow outside of

[1] https://www.applerubber.com/src/pdf/seal-design-guide.pdf

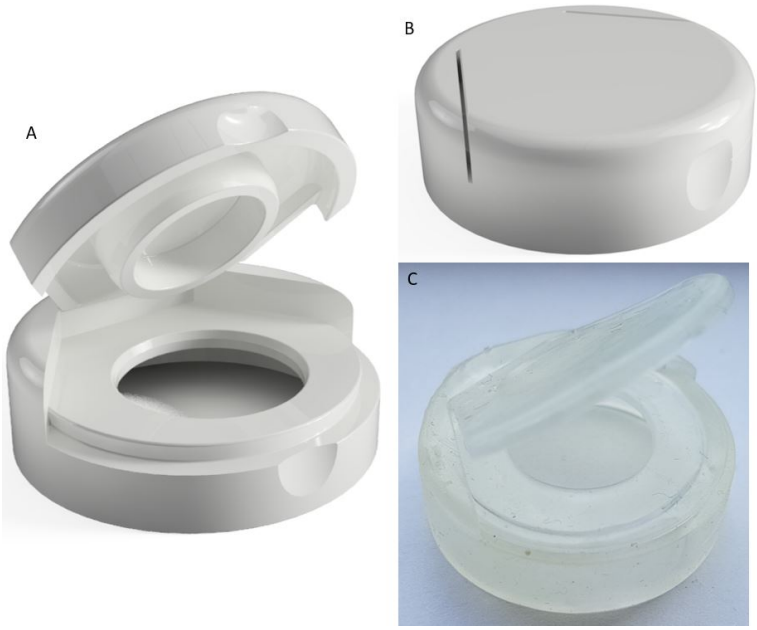

Figure 8.1: Design and 3D printed object of the first enclosure attempted. A) Rendered version of the enclosure. The top and bottom parts are connected through a hinge and the edges connect through a snap-fit mechanism. B) Closed version of the enclosure, with the snap-fit mechanism engaged. C) Object 3D printed using flexible resin.

snap-fit and threaded enclosures when fluid was injected inside a device with a 10 mL syringe (Becton Dickinson) fitted with a piece of silicone tubing.

Several gaskets were then developed and printed with flexible resin in order to achieve the same seal as the store bought o-rings. Gaskets with circular and square cross sections were first tested without success, as the flexible resin does not present the same properties as rubber and would not compress at the same rate. Different designs adapted from the Parker Gask-O-Seal® and Integral Seal™ Handbook[2] were 3D printed with flexible resin using a range of settings. While curing time and temperature did not affect the shape or elasticity of the gasket, changing the layer height produced a slight difference in the gasket cross section as can be seen in figure 8.2.

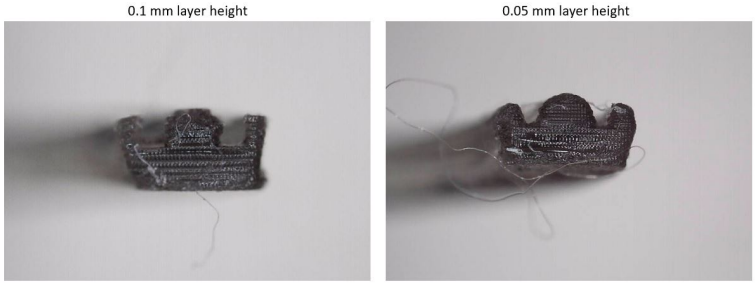

Figure 8.2: Effect of layer height settings on the cross section of gaskets 3D printed with flexible resin.

figure 8.3 shows the L-shaped designs that were developed and tested. Although not as effective as standard o-rings, these gaskets blocked the passage of fluid more successfully than their 3D printed predecessors due to the fact that both parts of the gasket are

[2]https://www.parker.com/literature/Seal%20Group/CSS%205124.pdf

compressed simultaneously. The four iterations show how the gasket was progressively adapted to fit within the device through trial and error. Overall, the 3D printing of gaskets was not fully successful due to the tendency of the flexible resin used to harden with lower temperatures <22°C and only regain its flexibility when exposed to higher temperature. This led to a significant reduction in the flexibility and elasticity properties of the material, rendering it unsuitable for sealing components.

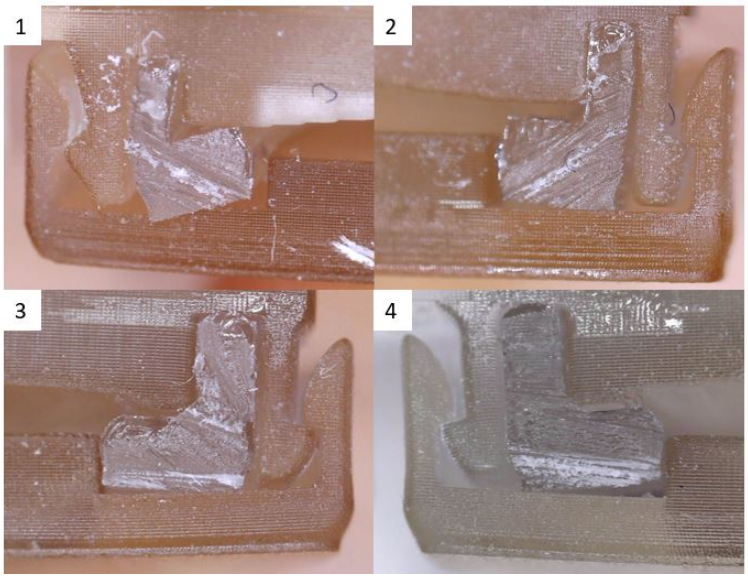

Figure 8.3: Four different 3D printed L-gasket designs fitted inside a snap-fit enclosure.

8.1.2 Valves

Three types of valves were explored, which were inspired by common types of mechanical valves commonly used in hydraulic operations. The objective of the valves was to enable fluid flow from inlet to outlet in one direction only. In a microfiltration plasma separation device context, this would prevent the backflow of plasma and reabsorption by the membrane once pressure application stops, as was often observed in the PMMA devices. All valves were tested using a similar object that consisted of an inlet and outlet with a valve placed in between the two. Both inlets and outlets had a diameter of 5 mm, which perfectly matched the tip of a 10 mL syringe fitted with a piece of silicone tubing. The valves were tested by pushing water mixed with red food colouring from the outlet to the inlet using the syringes, with the idea that a successful valve would prevent the liquid from reaching the inlet.

Flap valves consist of a "swinging door" that is pushed open by the passage of liquid in one direction and closed shut by the liquid when passage in the other direction is attempted. The main advantage of this valve type is that it is self-operating, without needing any action from the user during usage. In the 3D printed test objects, the valve itself was printed with flexible resin, while the test body was printed with tough transparent resin. A few iterations of this valve type were attempted, with the final one shown in figure 8.4. Unfortunately the flexible resin proved to be too tough and inflexible for this application due to its lack of elasticity. Although the valve prevented some liquid flow from outlet to inlet, it was not able to completely prevent the liquid from reaching the inlet and was therefore unsuccessful.

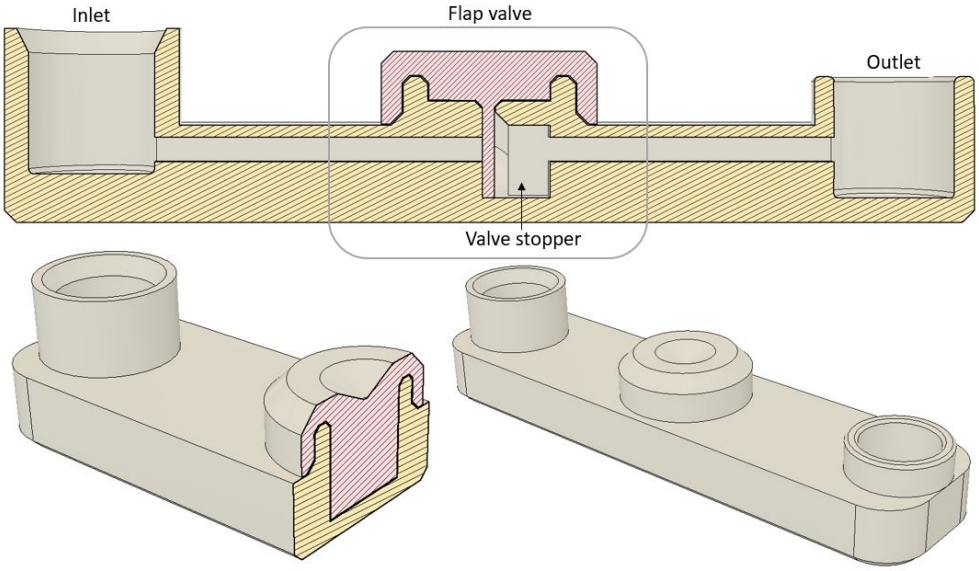

Figure 8.4: Annotated cross section of the test device body and the flap valve. At the bottom are a second cross section along the width of the device and the full design. The valve stopper prevented the valve from bending excessively and ensured it was in the best position to be closed shut by an outlet to inlet flow.

Another type of valve explored consisted in a rearranged version of a plug valve, which are traditionally conical or cylindrical and rotate inside the valve body to control the flow of liquids. An advantage of plug valves over other types is their ability to fine-tune the liquid flow, allowing progressively larger amounts through depending on how much the valve is turned. However, unlike flap valves, they have to be operated by the user. A 3D printed attempt at recreating a plug valve can be seen in figure 8.5, which shows how the user can control the liquid flow by turning the valve handle. Although better than the flap valves, a small amount of liquid still leaked through the clearance gaps necessary for the assembly of the valve and eventually reached the inlet when high pressures were applied with the syringe.

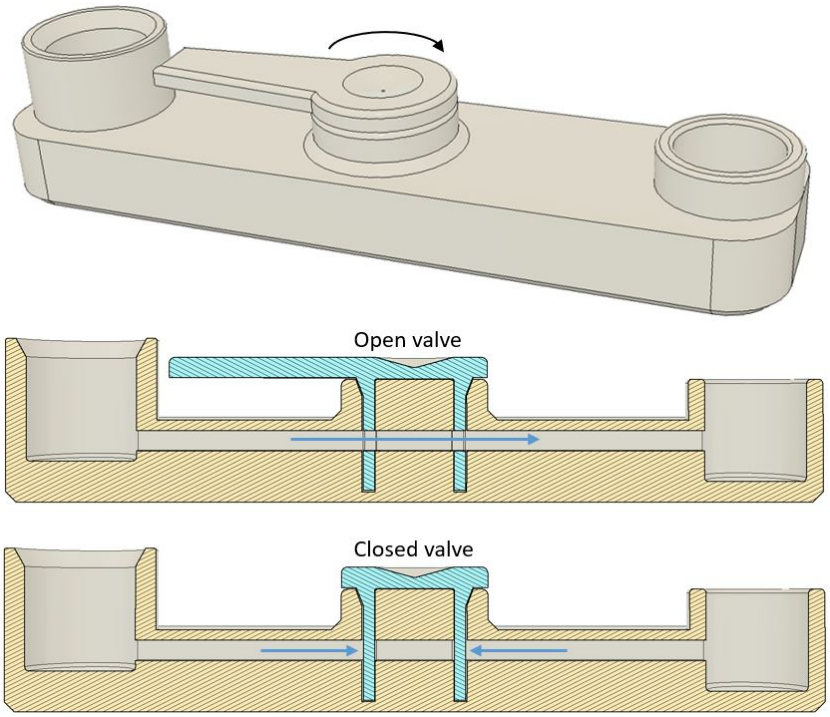

Figure 8.5: Design and cross section schematics of the 3D printed plug valve. The valve is shown both in its open and close configuration.

Needle valves consist in a threaded, needle-shaped plug that allows precise flow regulation within a channel. Tightening the valve progressively constricts the flow until it is stopped. Needle valves were the most successful type of 3D printed valve developed, with the five main designs attempted shown in figure 8.6. All "needles" were 3D printed using tough transparent resin. The first attempt consisted of a wide threaded needle that was partially successful at restricting the flow of water. In the second design, the tip of the longer needle was dipped into resin and re-cured, giving the tip a thin elastic layer that allowed valve to effectively close the gap between inlet and outlet and prevent liquid flow when fully tightened. However, the large surface area of the valve led to the thin flexible resin coating disintegrating and falling off with repeated use. In the third design, the valve tip was much thinner and, when dipped in flexible resin, less prone to resin damage and material loss. In the fourth design the needle was no longer dipped into flexible resin. Instead, a gasket printed with flexible resin was compressed by a threaded part, referred to as the gasket holder. When inserted in the gap, the tough needle valve walls pressed against the flexible gasket creating a seal. The fifth design relied on the same principle as the fourth, but the threaded connection was placed further up along the gasket holder.

Design number four was the most successful type, as it was capable of withstanding the pressure from the 10 mL syringe used for testing when the user attempted to press its plunger all the way. Because no formal burst test was carried out, it is not known precisely what internal pressure the design could handle before leakage and/or breakage occurred.

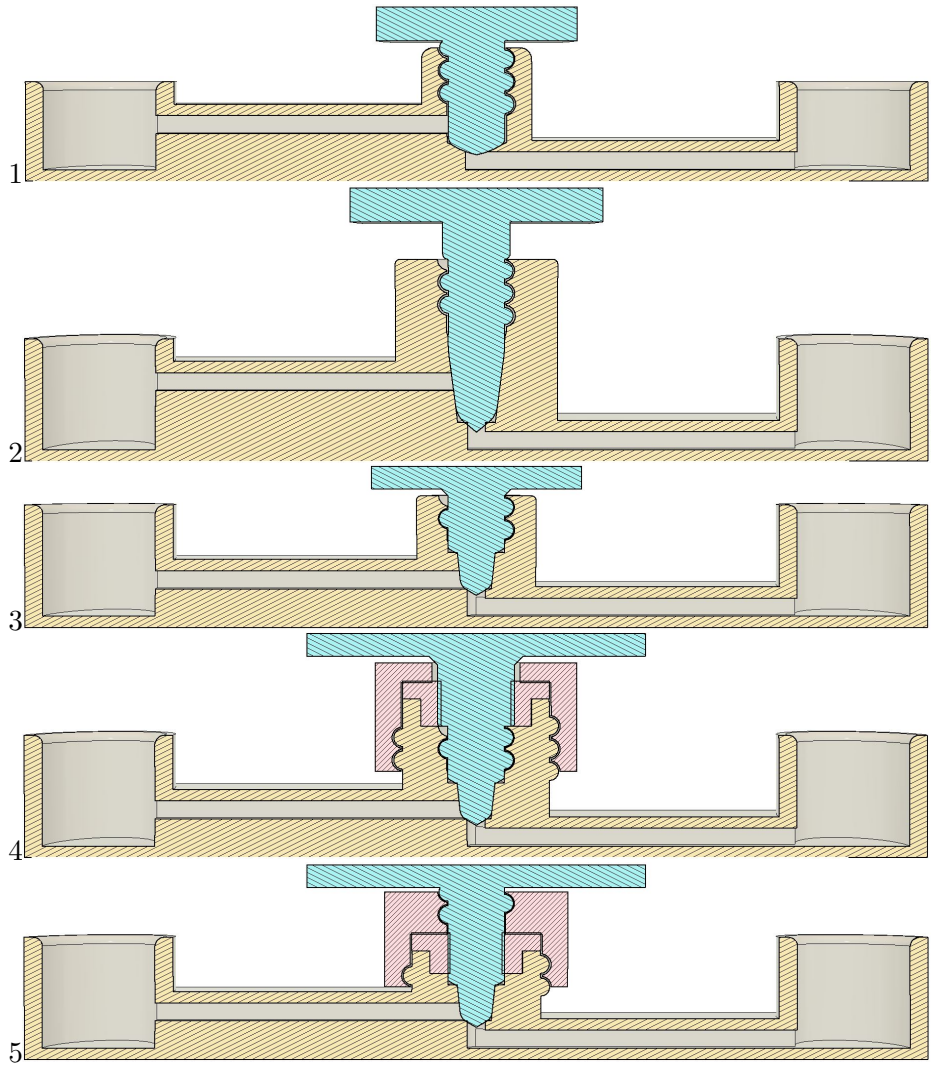

Figure 8.6: Five different designs of needle valve attempted.

8.1.3 Actuators

Different mechanical 3D printed objects were developed in at attempt at integrating components that could drive the flow of liquids within the devices. Button designs were tested first, but as the resin is not extremely flexible they were difficult to push all the way down. The design shown in figure 8.7 was, on the other hand, easy to operate by squeezing its sides and inserting it inside a device. The actuator was able to drive water through the test object shown in figure 8.8, but could not actuate the flow of plasma within the 3D printed plasma separation devices tested with blood. As such, more work is necessary to identify the correct pump dimensions that would allow fluid actuation in a microfiltration device.

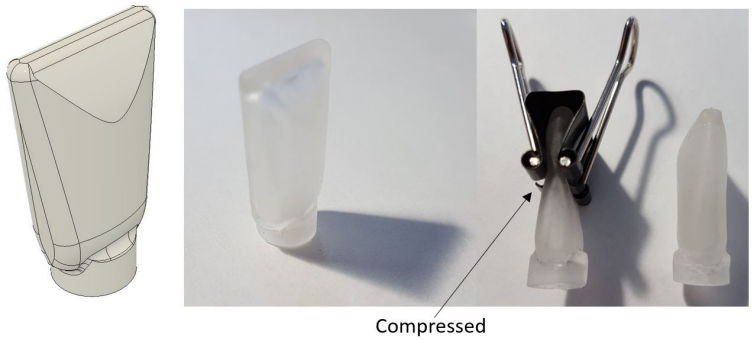

Figure 8.7: Design of the squeezable mini bottle used to drive the fluid flow within a device. The bottle is first squeezed and then inserted on an outlet, then released to initiate the fluid flow. The object is also shown 3D printed with flexible resin and compressed with a paper clip.

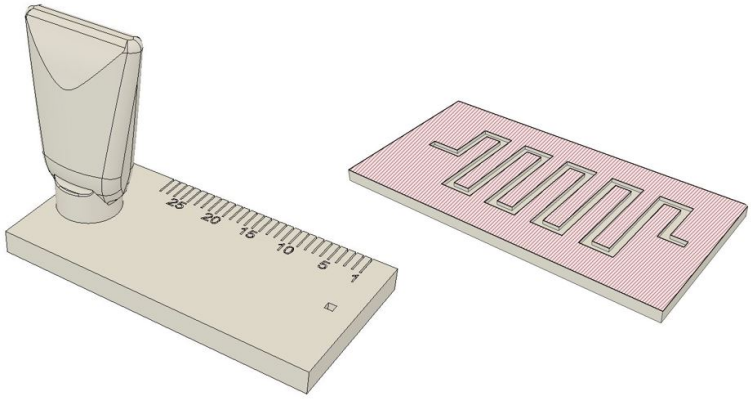

Figure 8.8: Test object used to determine whether the squeezable actuator was able to drive the flow of water in a 3D printed device. The cross section is shown to highlight the serpentine channel inside the test device.

Syringes are widely used to drive fluid flow in microfluidic devices. Several types of miniaturised 3D printed syringes were developed, consisting of a syringe barrel printed with tough transparent resin and a plunger printed with flexible resin (either blue or transparent). The designs can be seen in figure 8.9. The first design was largely unsuccessful, as it was difficult to insert the flexible plunger inside the barrel and to extract it back again due to the absence of a handle. In the second design, the plunger was fitted with flexible flaps that easily bent to create a seal against the syringe barrel. The plunger insertion was easier than the previous design and the miniaturised syringe initiated the flow of water to some extent in a test device. However, the flexible resin of the flaps suffered from degradation due to bending and friction, which led to the presence of resin residuals in the liquid extracted. To resolve this issue, in the third design the plunger was enclosed within the outside of the barrel and an external layer to avoid material release inside the liquid. The presence of double walls made the plunger insertion and extraction process rather difficult due to increased friction between the flexible resin and the tough resin walls. This often led to the plunger handle breaking and detaching from the plunger body, which remained inserted in the barrel object. The fourth design resolved this problem, as the plunger was only in contact with the outside of the barrel and was therefore easy to insert and extract. Progressive material loss occurred in this design as well, causing the plunger to become progressively looser

and ineffective.

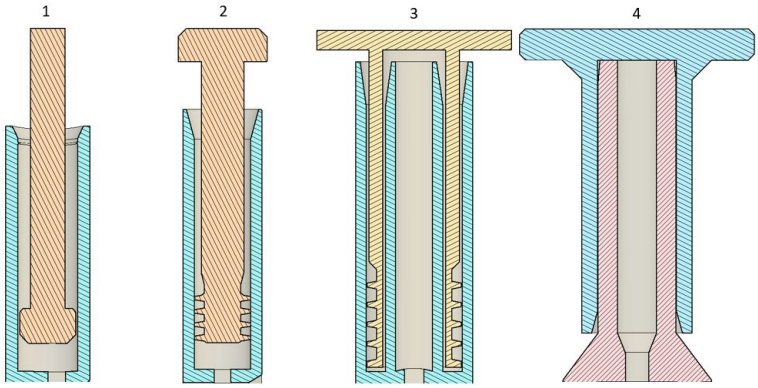

Figure 8.9: Cross section of the syringe designs tested throughout this study.

A few of these plungers were incorporated inside early versions of 3D printed devices to determine whether they could potentially drive the flow of water through a membrane. The first of these devices, shown in figure 8.10 incorporated a valve, a plunger and a membrane holder printed with blue flexible resin. This design was unsuccessful due to water leaking at the valve, which was removed in the second design shown in favour of a bonded syringe barrel fitted with a different plunger design. The new miniaturised syringe setup was able to drive the flow of water from a test membrane into the barrel as can be seen in figure 8.11.

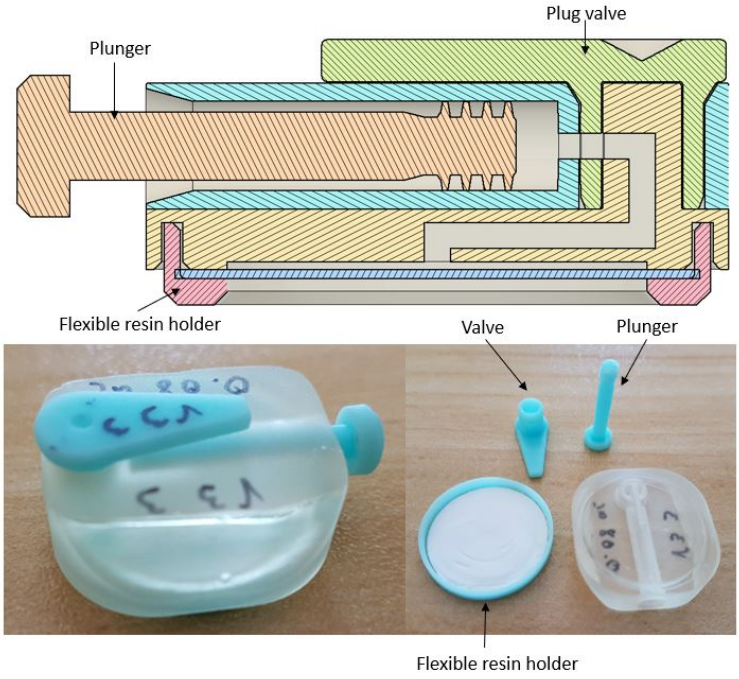

Figure 8.10: Example of the second plunger design integrated into a test device, shown as design cross section and actual 3D printed parts, both assembled and disassembled.

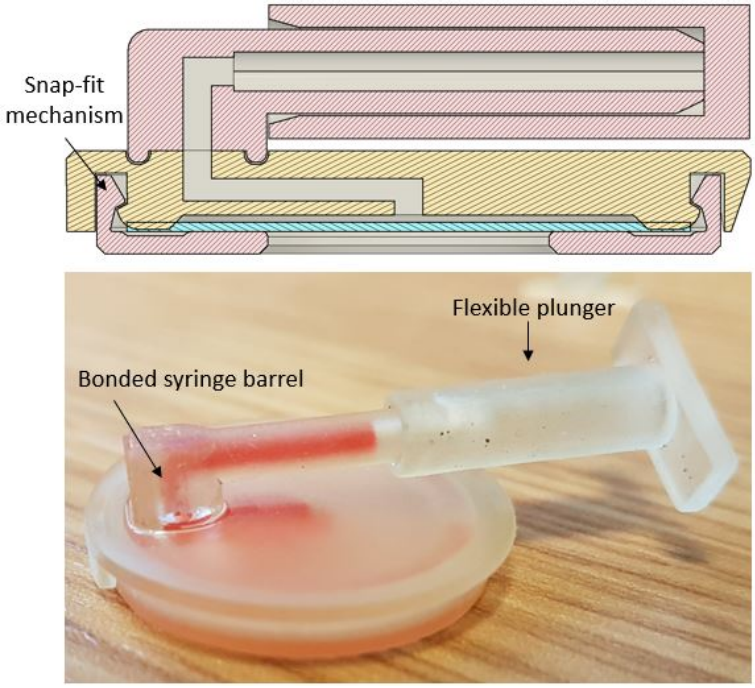

Figure 8.11: Example of the fourth plunger design integrated into a test device, showing both the design cross section and a functional device tested with water and red food colouring.

To minimise the surface area of the flexible resin exposed to friction, another method was used that relied on a L-gasket compressed by a threaded gasket holder, which enabled the gasket to form a seal when pushed against the syringe barrel as shown in figure 8.12. figure 8.13 demonstrates how the plunger successfully actuated the flow from the air-tight reservoir through the open valve and into the plunger itself. As with its predecessor, however, this type of gasket could only be used a limited amount of times before the resin would degrade and the plunger become too lose and ineffective.

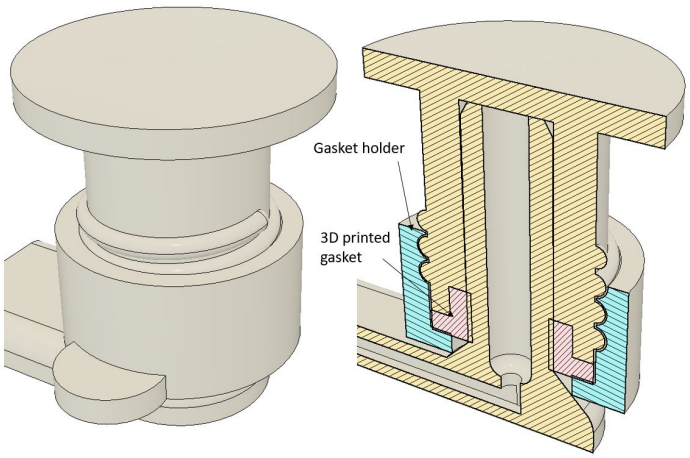

Figure 8.12: Design of the last actuator design developed with a compressed L-gasket, shown as full design (left) and labelled cross-section (right).

Figure 8.13: Top: example of all air-tight enclosure, needle valve and actuator integrated into a single device and tested with water and red food colouring. Bottom: view of the same device from a different angle.

Unfortunately the integrated components could not be developed further (for example by including them in the last iterations of 3D printed devices) and tested with blood due to time constraints.

8.2 Integrated surface modification patterns

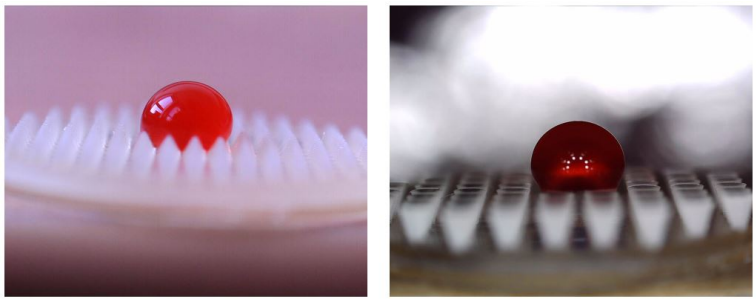

Figure 8.14: Example of dyed water droplets placed on patterns meant to increase surface hydrophobicity.

Liu et al. [51] has shown that placing a hydrophobic surface in the layer downstream of the membrane can lead to reduced protein absorption within the device and an enhanced plasma separation process. The idea of introducing patterns that could increase the hydrophobicity of the cured resin was briefly explored by attempting to print different patterns, which were tested with dyed water. As shown in figure 8.14, some

patterns proved to be successful at temporarily increasing the contact angle. However, any movement of the 3D printed object led to the droplet being absorbed within the pattern. As such, more work is required to explore this idea so that it can potentially be incorporated into a 3D printed plasma separation device.

Chapter 9

Conclusions and future work

9.1 Summary

Sample preparation in the form of separation of plasma/serum from blood cells is a strict requirement for many clinical tests and diagnostic procedures. Miniaturised devices designed to replicate clinical assays at the point-of-care should therefore be capable of performing sample preparation as part of the assay protocol. Many of these miniaturised devices make use of lab-on-a-chip and microfluidic-based technologies to manipulate the flow of liquids. However, due to the complexity and non-Newtonian properties of blood, sample preparation is difficult to perform in the small quantities required by microfluidic devices and remains therefore a challenge, particularly in research settings. An ideal plasma separation device needs to meet the following criteria:

- Achieve a high yield, that is extract a large amount of good quality plasma.
- Perform a quick extraction, ideally within a few minutes.
- Extract plasma that contains no residual cells from the original sample and has a low Hgb concentration, which indicates that minimal haemolysis occurred during the separation process.
- Be easy to operate without requiring a number of complex steps for the user to follow.
- Be affordable, simple to fabricate and amenable to mass manufacturing.

This work set out to develop successful prototypes of low-cost plasma separation modules that met the above criteria and could be potentially incorporated into, or expanded to become full point-of-care devices. A comprehensive characterisation of the devices was performed to address all of the main issues in sample preparation for point-of-care testing, which are often overlooked in the current literature.

The microfiltration-based plasma separation modules were developed using two different methods: laser ablation of PMMA layers, then bonded using an optimised ethanol-assisted thermal bonding technique, and MSLA 3D printing using UV-curable resins. The innovative aspect of the PMMA devices consisted in the use of a commercially available metered device for the collection of capillary blood samples (the Minivette®) to actuate the blood flow and push the plasma towards the outlet of the device. Conversely, in the 3D printed devices a pipette was used to induce a partial vacuum within

the devices and collect the separated plasma. Although a few 3D printed devices have been reported in the literature, none utilised the concept of integral snap-fit attachments to simplify the membrane integration and device assembly process. Additionally, to the author's knowledge, no study on point-of-care plasma separation devices analysed their device performance as thoroughly as in this work, where the average yield, haemoglobin concentration of the plasma, extraction time, number of devices tested and failure rate were discussed for each device iteration, along with the each of the features explored.

9.1.1 PMMA devices

The PMMA devices consisted of 6 layers cut to shape using a CO_2 laser cutter and bonded together using an optimized ethanol-assisted thermal bonding method. A commercially available polysulfone plasma separation membrane (VividTM GR, Pall) was integrated in the devices during the bonding process. For their successful operation, the devices required two steps: the insertion of a filled Minivette inside the inlet and the pressing of the Minivette plunger after a 2 minute waiting time.

The results from a successful type of PMMA device were published at the µTAS 2019 conference. The two latest versions, developed after the conference, performed better than their published counterpart, with a low failure rate and an average yield of 57.27% and 54.85% and Hgb content of 0.9 and 0.96 $g\,dL^{-1}$ for the V18 and B3 versions respectively. Schematics and results from all devices can be found in chapter 4, section 4.3.

Figure 9.1 shows an annotated version of table 4.1 from chapter 4. The B3 devices were highlighted as the overall best due to their high yield, low failure rate (7.89%) and relatively low (when compared with similar devices) Hgb concentration in the extracted plasma. B3 was also the only version that was operated in a "bottom-up" configuration, where the device was filled from the bottom with the upstream side of the membrane facing downwards. This setup exploits cell sedimentation during the waiting time to ideally reduce the risk of haemolysis during the filtration process.

	Device ID	Yield (%)	Hgb ($g\,dL^{-1}$) (analyser)	Hgb ($g\,dL^{-1}$) (UV-vis)	Failure rate (%)	% with plasma $\geq$ 25 µL
Published devices →	V4	47.66	0.1256	N/A	26.23	47.54
	V9	50.88	0.3333	N/A	7.69	61.54
	V7	60.91	0.3000	N/A	50.00	28.57
	V10	50.86	0.3400	N/A	16.67	66.67
	V11	54	0.1944	N/A	7.14	85.71
	V12	25	0.1500	N/A	50.00	16.67
	V13	49.09	0.2111	N/A	0.00	87.50
	V15	44.67	0.1000	N/A	50.00	33.33
	V17	47.86	0.1143	N/A	25.00	75.00
	V18	57.275	N/A	0.0900	33.33	66.67
Best devices →	B3	54.85714	0.1313	0.0960	7.89	89.47

Figure 9.1: Annotated version of the comparison table 4.1 from chapter 4, highlighting the overall winner among all device versions tested.

9.1.2 3D printed devices

3D printing is a fast-growing technology that is quickly gaining traction as a viable rapid prototyping method for point-of-care devices. The improvements in print quality and reliability, along with a significant reduction in equipment and materials cost, make even affordable resin-based 3D printers capable of producing meso to microfluidic devices. Here, a low cost MSLA 3D printer was used to manufacture plasma separation devices, which were specifically designed to take full advantage of this fabrication method.

The devices developed in this project were labelled "bonded" or "snap-fit" depending on the method of assembly used. As the name implies, the bonded devices consisted of two 3D printed layers bonded together with a membrane sandwiched in the middle. To achieve a high strength bond, the same resin using in the printing process was deposited in a dedicated channel prior to joining the two layers, which were then cured normally as per post-processing print procedure.

The snap-fit devices, on the other hand, relied on a snap-fit mechanism to mechanically join two parts together while squeezing the edges of the membrane to prevent blood from spilling over and reaching the outlet. Figure 9.2 summarises the structural differences between the two device types, along with the different designs used. Both were operated in one step and no waiting time was required between sample introduction and plasma collection.

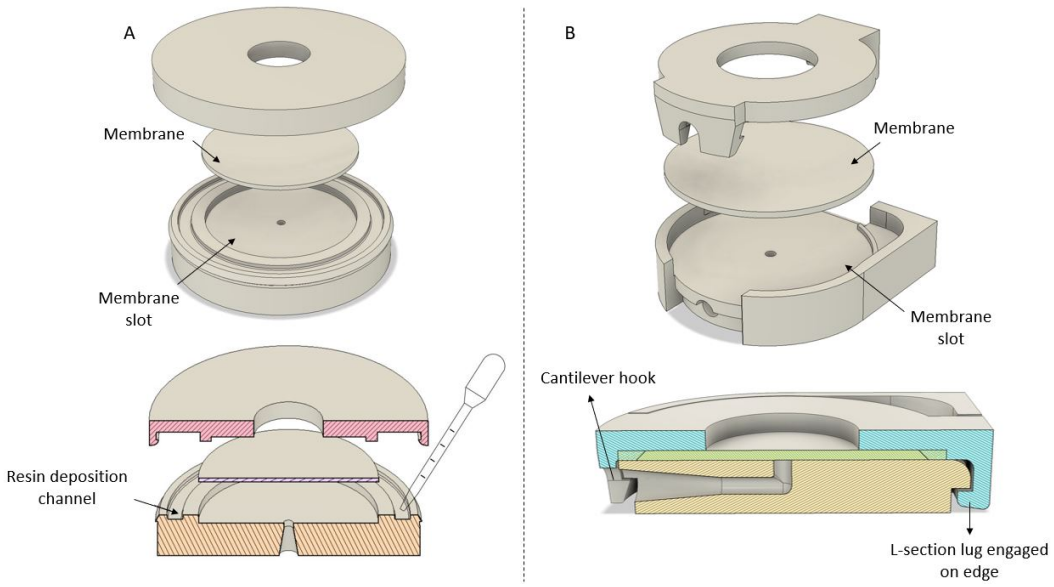

Figure 9.2: At the top, schematics of bonded (A) and snap-fit devices (B), while at the bottom are diagrams showing the bonding procedure and the locator-based snap-fit mechanism.

Bonded devices

Due to the small size of the 3D printer used, the bonded 3D printed devices could be fabricated in batches of maximum eight devices. The top and bottom layers were printed separately and the plasma separation membrane was placed within the grooves prior to resin insertion in the deposition channel. As can be seen in figure 9.3, out of all the devices tested the B4 device versions were the best performing ones, with a consistent yield $> 50\%$ and Hgb difference with controls $\leq 0\,\mathrm{g\,dL^{-1}}$, which indicates that the devices produced plasma extremely similar (and sometimes better) in quality

	Average			Standard Deviation				
Device ID	Yield (%)	Hgb diff. ($g\,dL^{-1}$)	Extraction time (s)	Yield (%)	Hgb diff. ($g\,dL^{-1}$)	Extraction time (s)	Failure rate (%)	Visible RBCs (%)
B1	57.70	0.0147	183.84	7.72	0.0161	41.29	28.57	0
B2	55.18	0.0247	104.00	8.48	0.0142	27.45	20	0
B3.1	45.63	0.0739	120.17	7.12	0.0561	23.40	0	0
B3.2	29.89	0.0745	152.49	23.32	0.0355	18.14	0	0
B4.1	50.59	-0.0011	68.43	9.03	0.0114	12.68	20	13.33
B4.2	51.34	-0.0005	76.11	10.35	0.0095	14.82	4.65	9.3
B4.3	54.84	0.0001	71.53	5.02	0.0074	6.02	16.66	4.16
B4.4	53.11	-0.0016	70.00	7.79	0.0053	5.20	12.5	8.33
B5	43.07	0.0001	84.92	8.16	0.0062	19.81	12.5	6.25
B6	50.16	0.0020	91.85	6.77	0.0047	20.43	6.25	12.5
B7.1	56.89	0.0174	96.55	10.00	0.0098	18.35	6.25	25
B7.2	49.44	0.0039	75.00	10.34	0.0104	7.94	12.5	12.5
B7.3	45.40	0.0096	70.90	10.24	0.0159	13.90	12.5	18.75
B8.1	41.19	0.0495	131.83	7.28	0.0302	32.49	12.5	0
B8.2	45.12	-0.0086	126.00	2.40	0.0095	7.35	0	0

Figure 9.3: Annotated version of table 6.2 from chapter 6, . Although promising in terms of yield, the B1 devices required an excessive separation time, had a high failure rate and produced poor quality plasma. High yield and excessive haemolysis were also observed in B7.1. Overall, B4.2 was the most successful device due to its acceptable yield, excellent plasma quality, short extraction time and low failure rate.

compared with centrifuged controls. The extraction time was also excellent, with a total plasma collection time from direct blood insertion between 68 and 76 seconds.

A range of different features were explored in each device version to determine their impact on the separation process. The features analysed in the B4 versions were inlet and outlet positioning in the absence of membrane supports at the downstream side, as explained in chapter 6, table 6.1. Out of all B4 versions, B4.2 (with central inlet and outlet placement) was the most reliable as it had the lowest failure rate, and therefore the overall best among all bonded devices.

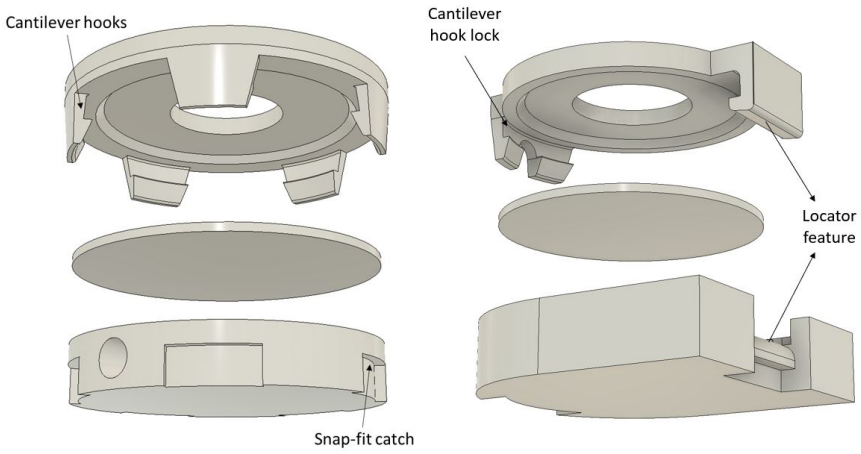

Figure 9.4: Exploded views of lock-based (left) and locator-based (right) devices with their respective integral snap-fit mechanism.

An enzyme-linked immunosorbent assay (ELISA) for the detection of antibodies to the Bovine Respiratory Syncytial Virus (BRSV) was used to determine whether the plasma extracted was suitable for immunoassay testing. Six bovine samples were used to test 36 B4.2 devices, with 6 devices being used per sample, and the results closely matched those of the centrifuged controls, confirming the suitability of the extracted plasma for testing.

Snap-fit devices

The snap-fit devices were designed to be simpler to manufacture, assemble and mass-produce than their bonded counterpart. Being smaller than the bonded devices, up to 14 devices could be fabricated in one batch. After printing and post-processing the layers independently, the membrane was placed in the dedicated slot at the bottom layer and the two layers were connected using the integrated snap-fit mechanism. The devices could be easily disassembled by lifting up the cantilever tab and disengaging the mechanism, a method familiar to most users as it is commonly seen in plastic battery covers. The disassembled devices could them be disinfected after use and re-assembled when needed up to 3 times, although this procedure increased the device's failure rate during testing.

The two main types of snap-fit devices developed were named "lock-based" and "locator-based" due to the different snap-fit mechanisms used, which are shown in figure 9.4. The locator-based devices proved to be more successful due a better overall performance and increased usability. Several plasma collection patterns were also evaluated for their ability to successfully help wicking plasma out of the downstream surface of the membrane. As can be seen in the annotated table shown in figure 9.5, many of the device versions performed well with a yield $> 50\%$ and Hgb concentration difference with controls $\leq 0\,\mathrm{g\,dL^{-1}}$: L2.1, L2.1R, L2.2, L2.3, L2.4, L2.5, L2.6, L3.2R, L3.2RR, L3.3R, L3.3RR, L3.4R, L3.4RR. Out of those, L2.1 and L2.2 had the lowest failure and residual cell rate and can therefore be considered the most successful device versions.

	Average			Standard Deviation				
Device ID	Yield (%)	Hgb diff. ($g\,dL^{-1}$)	Extraction time (s)	Yield (%)	Hgb diff. ($g\,dL^{-1}$)	Extraction time (s)	Failure rate (%)	Visible RBCs (%)
L1.1	44.09	−0.0142	96.00	5.48	0.0016	16.97	0.00	33.33
L1.2	51.61	−0.0125	88.50	2.28	0.0030	18.31	33.33	16.66
L1.2_R	36.9	−0.0073	106.50	3.08	0.0026	19.50	0.00	0.00
L2.1	49.65	−0.0098	93.43	4.81	0.0044	17.15	0.00	0.00
L2.1_R	46.4	−0.0079	79.20	1.51	0.0014	4.49	30.00	20.00
L2.2	56.88	−0.0027	86.77	9.25	0.0100	12.31	0.00	7.14
L2.2_R	51	0.0098	111.75	8.62	0.0029	14.29	0.00	0.00
L2.3	58.71	−0.0034	84.27	6.92	0.0162	13.50	14.29	35.71
L2.3_R	55.	0.0132	75.60	9.31	0.0125	2.94	0.00	40.00
L2.4	53.85	−0.0086	80.67	5.38	0.0030	4.78	30.77	0.00
L2.4_R	51.52	0.0048	82.13	6.78	0.0034	4.48	0.00	20.00
L2.5	51.77	−0.0018	88.00	9.60	0.0098	15.02	6.67	33.33
L2.5_R	50.00	0.0111	78.00	3.97	0.0061	0.00	50.00	25.00
L2.6	53.52	−0.0028	82.00	6.92	0.0162	4.00	23.08	15.38
L3.1	44.45	−0.0031	100.77	8.87	0.0109	24.95	11.11	14.81
L3.1_R	45.10	0.0049	92.20	7.28	0.0149	18.18	26.09	30.43
L3.1_RR	42.77	0.0022	78.00	9.56	0.0130	6.00	58.33	25.00
L3.2	46.51	0.0044	87.00	7.00	0.0131	15.04	17.65	17.65
L3.2_R	49.85	0.0054	83.44	4.78	0.0193	10.62	10.53	21.05
L3.2_RR	49.95	−0.0002	85.25	6.76	0.0076	13.72	7.14	35.71
L3.3	42.50	0.0031	89.31	9.12	0.0126	13.83	11.76	29.41
L3.3_R	49.93	−0.0030	84.82	4.44	0.0057	11.94	11.11	50.00
L3.3_RR	56.24	−0.0029	83.50	5.42	0.0100	16.65	57.14	21.43
L3.4	44.78	0.0142	85.07	5.07	0.0249	21.44	21.05	26.32
L3.4_R	52.40	0.0041	88.67	5.22	0.0203	17.33	26.32	31.58
L3.4_RR	54.67	0.0005	87.75	6.72	0.0058	19.43	42.86	21.43

Figure 9.5: Annotated version of table 7.4 (chapter 7). R and RR refer to devices reused once and twice respectively. The device versions marked by the green rectangles performed well in terms of yield and plasma quality, but had issues with high failure rate and plasma purity (marked in orange). The two device versions fully highlighted in green (L2.1 and L2.2) were considered the most successful, as they had a combination of good yield, plasma quality and purity and low failure rate.

9.2 Future work

9.2.1 Further device testing

The following list outlines further work that, although planned, could not be carried out due to time and work environment constraints:

- Testing of 3D printed devices with fresh human blood.
- Exploration of device scalability: can the devices be scaled up or down to accommodate different input sample volumes without compromising their performance?
- Testing of the devices using a range of different membranes to determine whether any of them would lead to better results than the Vivid GR membrane from Pall.
- Further testing of 3D printed adaptations of designs developed for the laser-cut PMMA devices to compare the effectiveness of the two manufacturing methods directly.

Fresh human blood testing

The Vivid GR membranes used throughout this project were developed to be used with human blood. The equine samples sourced for device testing were not only of poor quality on average, but equine red blood cells differ from human ones in that their diameter is slightly smaller, potentially complicating their filtration using membrane pores developed to successfully filtrate human cells.

As such, testing the devices with human blood extracted right before the experiments (as in the case of the PMMA devices) would provide the best indication of real device performance and usefulness in a clinical setting.

Figure 9.6 offers an example of human plasma samples collected from 3D printed bonded devices. Capillary blood with 35% haematocrit was collected from a healthy volunteer through a finger-prick using a lancet device and a 100 µL EDTA coated Minivette. The Hct was established during a normal routine blood count though the National Health Service close to the time of device testing. The blood was then divided into two 50 µL batches, one for each device to be tested. The average plasma volume collected was 16.5 µL, which corresponds to a 50.7% yield. The plasma appeared clear to visual examination and no residual cells were observed during extraction, which in laboratory cell testing (chapter 3, section 3.4) translated to no residual cells being detected in the plasma. Although the samples could not be analysed in the laboratory due to lack of permissions, this shows that analysis with fresh human blood is not only possible, but is also likely to improve the testing results compared to equine blood.

Device scalability

Adapting the diameter of the membrane and the device size to a range of input sample volumes would provide important information on the scalability of the 3D printed devices, that is whether they would remain effective with either larger or smaller blood samples than the 50 µL used throughout this study. This can be easily tested given the parametric nature of the designs, where adjusting the diameter of the membrane automatically leads to the creation of a device with corrected dimensions.

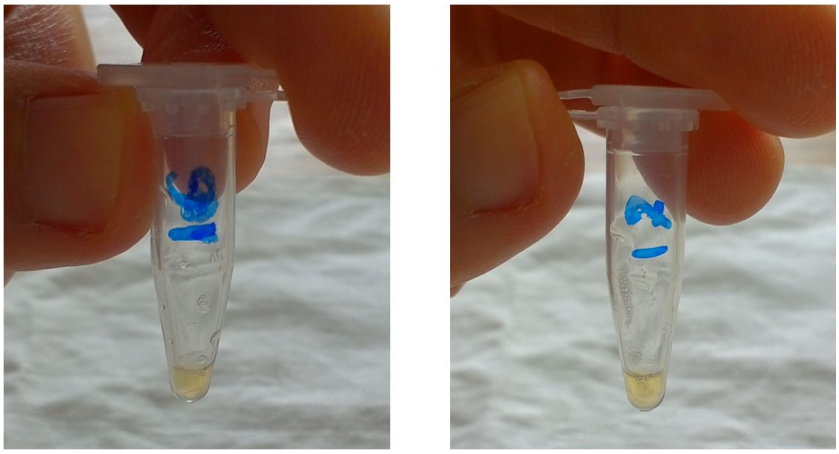

Figure 9.6: Two human plasma samples obtained using B4.2 devices and 50 µL of fresh capillary blood as input. The plasma volume collected was 16 µL (left) and 17 µL (right).

Different membranes

To determine whether a more successful performance could be achieved with different pore-sizes and membrane architectures, the devices should be tested with a range of membranes capable of performing plasma separation from human blood cells. The following are examples of such membranes, for which samples were obtained but could not be used due to time constraints:

- Whatman GE Healthcare LF1, MF1, FUSION 5, VF2 and Nuclepore (0.1 µm pores).
- Merck Durapore PVDF (0.22 µm pores).

3D printed adaptation of laser-cut PMMA devices

The adaptation of the design of laser-cut PMMA devices to a 3D printing-based fabrication process was explored with one PMMA device design and a 50 µL sample. Further exploring the use of the Minivette in 3D printed devices, particularly with the same input blood volume and "bottom-up" setup similar to the B3 iteration of the PMMA devices (chapter 4, figure 4.15) would provide a better and more direct comparison between the two manufacturing methods when used to produce a similar product.

9.2.2 Biosensor integration

The sample preparation devices can be upgraded to point-of-care testing devices by integrating a sensing component consisting of a functionalised surface and a detection mechanism into the device body. The detection could be based on colorimetric, chemiluminescence and/or electrochemical methods. An example of this can be seen in the work of Cheah et al. [109], who created a 3D-printed sample preparation platform integrated with a nanoscale field-effect-transistor (FET) biosensor. The latter FET biosensor was placed on a PCB carrier, which was located underneath the 3D printed body consisting of a sample and wash buffer inlets and a waste chamber, as shown in figure 9.7. A ×10 diluted finger-prick blood sample was placed inside the sample inlet over a plasma separation membrane. At the same time, a washing buffer was introduced into a second inlet fitted with a dissoluble sacrificial delay valve. The plasma

filtered by the membrane immediately reached the sensing area while the buffer's release was delayed. Once the valve dissolved and failed, the buffer was able to reach the sensor's surface and wash away the plasma, which was then pushed into the waste chamber and collected by an absorbent pad. The authors tested both a commercially available membrane (Pall GF) and a porous monolithic membrane photopolymerised *in-situ* within the sample inlet and reported a similar performance between the two. The authors noted that the sample had to be diluted so that volume could be large enough to guarantee an autonomous extraction through hydrostatic pressure. Moreover, they claim that the dilution of the sample did not affect the immunoassay, as the FET sensor had a high enough sensitivity to detect low analyte concentrations. The device detected $1.4\,\mathrm{pg\,mL^{-1}}$ of SARS-CoV-2 nucleocapsid protein within 25 minutes and with minimal operator intervention.

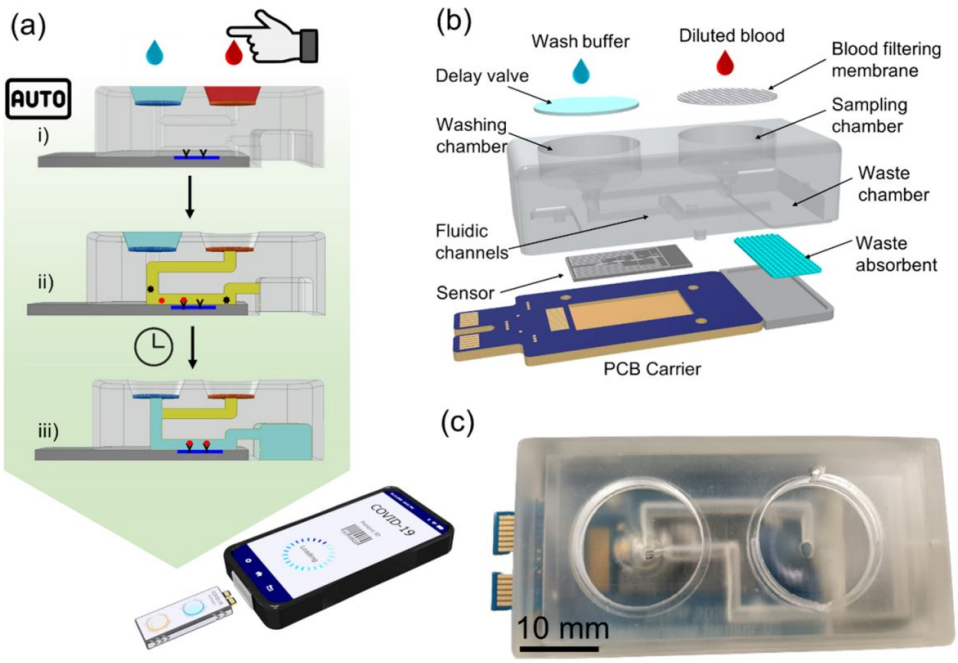

Figure 9.7: a) Cross-section of the 3D printed body of the device with labelled channels and flow diagram. b) Labelled schematic representation of the device and the FET biosensor. c) Image of the assembled device. Figure reproduced as it appears in the work of developed Cheah et al. [109] with permission from the American Chemical Society.

In the 3D printed devices developed throughout this project, the plasma could be seen passively accumulating downstream of the membrane once the blood was absorbed by the membrane. As such, the sensing components could be placed directly in contact with the downstream area of the membrane to perform analyte detection on-site after the plasma is passively separated by the membrane. Alternatively, the sensors could be placed in a separate plasma collection chamber as shown in chapter 5, section 5.3.2, which would fill with plasma driven by suction applied at the outlet using a pipette or other methods.

The resin itself could also be modified in a way that facilitates the use of sensing methods, for example by modifying it to impart electrically conductive properties. Although expensive conductive resins are commercially available, DIY methods also appear in the literature. An example is the work of Hanon et al. [110], who developed a protocol to successfully 3D print test components from resin mixed with graphene

powder. The authors recommended to keep the percentage of graphene powder between 0.5% and 1% of the total resin volume and to mix it thoroughly for at least 5 minutes with a vortex mixer. Lowering the height of each printed layer also increased the chance of success, as the resulting resin is darker or more opaque meaning that the UV light does not penetrate as far into the layer to cure it.

9.2.3 Adaptation to plastic injection moulding

Design for manufacturing (DFM) refers to the designing of products in such a way that they can be produced efficiently in large numbers using as little material as possible, with the objective to reduce overall cost without overly compromising output quality. Design for assembly (DFA), on the other hand, focuses on producing designs that are easily assembled, minimising the number of assembly steps, the time required and, consequently, costs.

The 3D printed devices were developed with the concept of "design for manufacturing and assembly" in mind, which is reflected by the following:

- Resin use was minimised by designing thin parts printable without supports and pads.
- The printing time was greatly reduced by selecting a flat orientation and adapting the design to print successfully under flat conditions.
- The assembly complexity was progressively reduced throughout the development of the 3D printed devices to the point where assembly and disassembly of the locator-based devices (particularly L3 models) are both simple and intuitive, requiring no previous training and being achievable by anyone with minimal instructions.
- Some designs have the potential to be adapted to injection moulding, which is the most common manufacturing method for plastic products.

An interesting future development would see the full adaptation of the 3D printed snap-fit devices to injection moulding using plastic materials. This would reduce the individual cost of each device, as plastic injection moulding is widely used and automated. Should the device be expanded into a full point-of-care device with integrated sensors, this step would be important in its future commercialisation.

9.3 Final remarks

The 3D printed devices outperformed their PMMA counterpart in all aspects, with higher average plasma yield and quality, lower extraction time and simpler operational steps. Moreover, the equipment necessary for the fabrication of the 3D printed devices was far more accessible both in terms of cost and simplicity of usage, thus greatly simplifying the manufacturing process. The most successful out of the 3D printed devices could collect up to 56.88% of the available plasma without inducing significant haemolysis during the separation process, as indicated by their minimal haemoglobin concentration difference with control plasma samples prepared using standard centrifugation techniques.

The plasma collected using one of the device types developed was used to successfully perform an immunoassay for the detection of antibodies to BRSV, with results closely

resembling those from centrifuged plasma controls, indicating low protein loss within the devices as previously confirmed by other studies in the literature that used similar membrane and materials. Finally, the snap-fit 3D printed devices are more eco-friendly than most alternatives, as they were produced using a plant-based biodegradable resin and can potentially be disassembled, disinfected and re-used. If 3D printed with high temperature-resistant resins, the devices can be easily autoclaved, which is the standard sterilisation procedure in most laboratories.

In conclusion, low-cost plasma separation devices were developed that successfully separated a significant percentage of the total available plasma with little to no haemolysis occurring during the extraction. The devices required minimal equipment for their operation and were easy to fabricate, assemble and use. A range of fabrication methods were explored that allow a sensing component to be integrated with the plasma separation module to create a full point-of-care device. Although this could not attempted during this project due to time constraints, it remains an interesting challenge for the future. The development of these plasma separation devices can hopefully contribute to the creation of point-of-care devices or lab-on-a-chip components that require pure plasma for their analyses.

Appendix A

ImageJ - Contact angle plugin basic 5 points algorithm

1. The user inputs the coordinates for exactly 5 points, the first two for the baseline ($p1_x, p1_y$ and $p2_x, p2_y$) and the other to define the droplet (x_1, y_1 to x_3, y_3). First the baseline of the droplet of the form $y = mx + q$ is found using points $p1$ and $p2$. Then the coordinates of the center of the circle (x_0, y_0) are calculated using the system of equations describing the circle passing through the three points:

$$\begin{aligned} &(1) \quad (x_1 - x_0)^2 + (y_1 - y_0)^2 = r^2 \\ &(2) \quad (x_2 - x_0)^2 + (y_2 - y_0)^2 = r^2 \\ &(3) \quad (x_3 - x_0)^2 + (y_3 - y_0)^2 = r^2 \end{aligned}$$

   Once the coordinates for the center are known, the radius of the circle can be found by calculating the distance from the center to one of the points.

2. The intersection points between the circle and the baseline are calculated by substituting the baseline equation $y = mx + q$ into the equation of the circle $(x - x_0)^2 + (y - y_0)^2 = r^2$ to obtain:

$$(x - x_0)^2 + (mx + q - y_0)^2 = r^2.$$

   Solving for x allows the calculation of the discriminant $\Delta = b^2 - 4ac$, where:

$$\begin{aligned} a &= (1 + m^2) \\ b &= 2(-x_0 + mq - my_0)) \\ c &= (x_0^2 + q^2 + y_0^2 - 2qy_0 - r^2). \end{aligned}$$

3. Δ is then used to perform a sanity check. If $\Delta = 0$ the baseline intersects the circle only once, meaning that the contact angle is 180°. If $\Delta < 1$ the baseline does not intersect the circle, indicating that the droplet is in a suspended state and is not touching the substrate, in which case the contact angle cannot be calculated. Finally, if $\Delta > 1$ the baseline intersect the circle in two points $I1$ and

$I2$ such that:

$$I1_x = \frac{-b + \sqrt{\Delta}}{2a}, \qquad I1_y = mI1_x + q$$
$$I2_x = \frac{-b - \sqrt{\Delta}}{2a}, \qquad I1_y = mI2_x + q.$$

4. The distance between $I1$ and $I2$ is then calculated, which describes the droplet base width w.

5. The height of the droplet h can then found in two steps. First, the distance d between the centre of the circle (x_0, y_0) and the baseline $y = mx + q$ is calculated as follows:
$$d = \frac{mx_0 - y_0 + 1}{\sqrt{m^2 + 1}}.$$
The distance d is then subtracted from the radius of the circle r to obtain $h = r - d$.

6. A right triangle is obtained by connecting w and h. Let the opposite angle to h be called ϕ. The contact angle θ is then given by $\theta = 2 \times \phi$, which is proven using the alternate segment theorem as illustrated in Figure A.1.

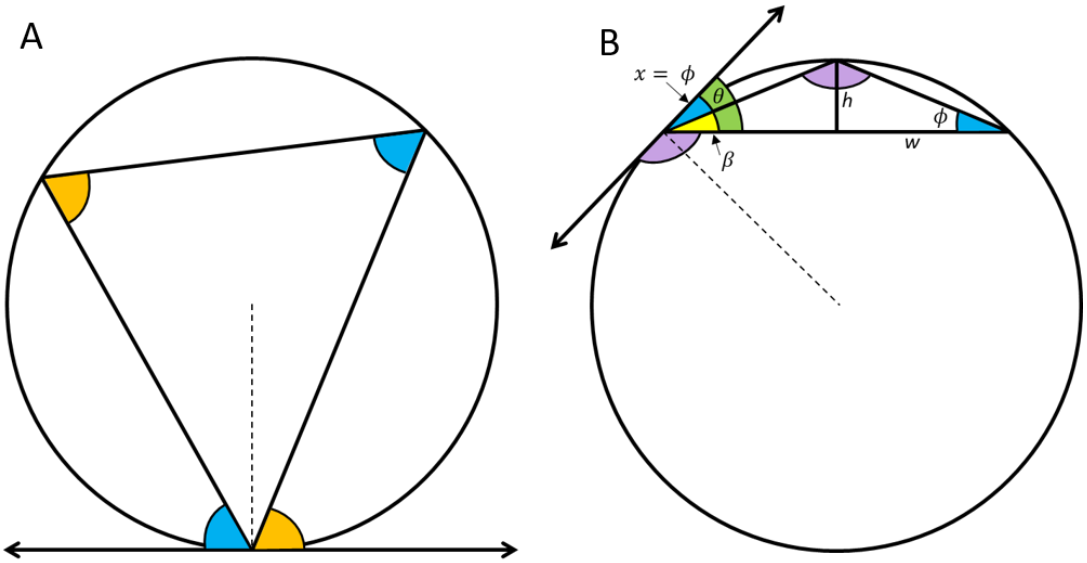

Figure A.1: A) Classic illustration of the alternate segment theorem. B) Alternate segment theorem applied to the contact angle measurement. Due to the theorem it can be seen that $x = \phi$, where ϕ is the angle opposite to h. But the angle β is also equal to ϕ, meaning that $\theta = 2\phi$.

Appendix B

PMMA engraving analysis - code for curve construction

The MATLAB code and data used to generate the curve shown in figure 3.6 of chapter 3.

```
CD = [0.191 0.223 0.286 0.342 0.443 0.574 0.857];
MD = [0.196 0.219 0.281 0.34 0.451 0.586 0.839];
Avg = [0.193 0.221 0.283 0.341 0.447 0.58 0.848];

x = [80 70 60 50 40 30 20];

xi = linspace(20, 80, 100);

p = polyfit(x, Avg, 2);
Avg\_yi = polyval(p, xi);

figure(1)
plot(x, CD, 'o')
hold on
plot(x, MD, 'o')
hold on
plot(xi, Avg\_yi, '-r', 'LineWidth',2)
hold off
grid

depth = interp1(xi,Avg\_yi,55,"spline")
```

A total of seven data points (the average of all data points for each engraving setting tested) was used in order to construct the curve. Leave-one-out cross validation was used to determine which degree of polynomial to use in fitting the data. In this procedure, we leave out one data point, fit a polynomial of degree m and n to the remaining data and use these curves to predict the value of the point we left out. The process is repeated for every point in the dataset, after which we can check which degree polynomial minimises the error between the actual data and the predicted values.

The MATLAB code used to implement this procedure can be found below. The Avg_error values give us the root mean square errors for each degree of polynomial, with the values 0.1190, 0.0586, 0.0488, 0.0276 obtained respectively for degrees 1st, 2nd, 3rd and 4th. It is clear that the quadratic polynomial predicts the data better than the linear one. The third and fourth degree perform even better. However, since our data set is only 7 points, we don't want to use a degree to close to the total number of points. As such, the quadratic polynomial was chosen over the rest to fit the data.

```
Avg = [0.193 0.221 0.283 0.341 0.447 0.58 0.848];
x = [80 70 60 50 40 30 20];

xi = linspace(0,100,1000);
error1 = [];
error2 = [];
error3 = [];
error4 = [];

for i = 1:7
a = [];
b = [];

for j = 1:7
if j ~= i
a = [a Avg(j)];
b = [b x(j)];
end
end

p1 = polyfit(b,a,1);
p2 = polyfit(b,a,2);
p3 = polyfit(b,a,3);
p4 = polyfit(b,a,4);

e1 = abs(polyval(p1,x(i))-Avg(i));
e2 = abs(polyval(p2,x(i))-Avg(i));
e3 = abs(polyval(p3,x(i))-Avg(i));
e4 = abs(polyval(p4,x(i))-Avg(i));
error1 = [error1 e1^2];
error2 = [error2 e2^2];
error3 = [error3 e3^2];
error4 = [error4 e4^2];

figure(i)
plot(x,Avg,'o');
hold on
plot(xi,polyval(p1,xi),'r');
hold on
plot(xi,polyval(p2,xi),'g');
hold on
plot(xi,polyval(p3,xi),'m');
```

```
hold on
plot(xi,polyval(p4,xi),'k');
hold off
end

Avg_error1 = sqrt(sum(error1)/7);
Avg_error2 = sqrt(sum(error2)/7);
Avg_error3 = sqrt(sum(error3)/7);
Avg_error4 = sqrt(sum(error4)/7);
```

Appendix C

Haemoglobin Standard Curve - supporting information

C.1 Derivation of Allen's correction method

This section offers a step-by-step guide to the derivation of Allen's formula to reliably subtract the absorption due to interferents from the spectrum of a mixture containing the target substance.

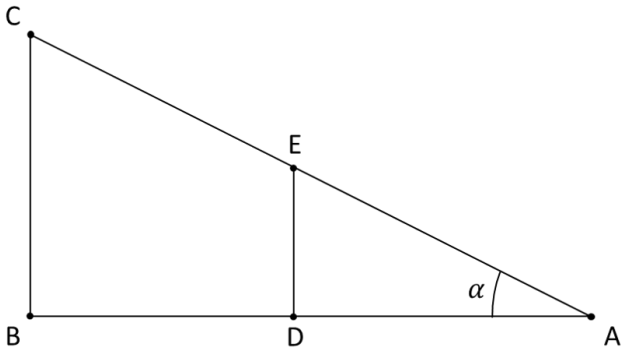

Figure C.1: Supporting figure for Lemma 1.

Lemma 1. *Given a triangle ABC with a line DE parallel to the side BC, as shown in Figure C.1, then:*

$$\frac{AD}{AB} = \frac{DE}{BC}.$$

Proof. Let $\angle\, BAC$ be α. Then:

$$\begin{aligned}
&\tan(\alpha) = \frac{DE}{AD} && \text{from triangle } ADE \\
&\tan(\alpha) = \frac{BC}{AB} && \text{from triangle } ABC \\
\implies \quad &\frac{BC}{AB} = \frac{DE}{AD} \quad \implies && \frac{AD}{AB} = \frac{DE}{BC}.
\end{aligned}$$

□

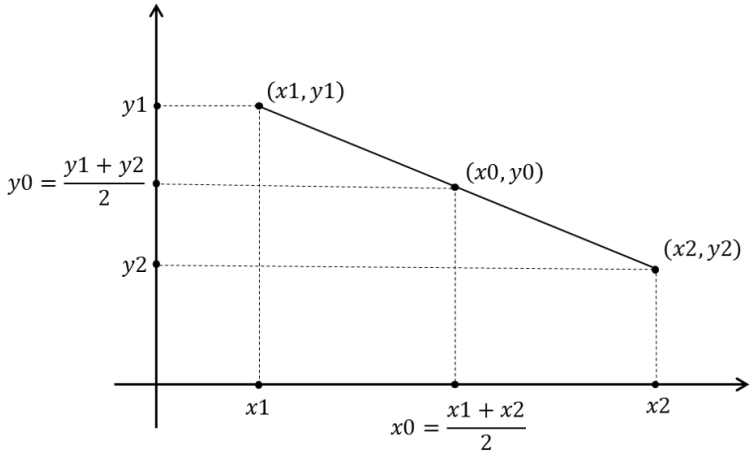

Figure C.2: Supporting figure for Lemma 2.

Lemma 2. *Given two points (x_1, y_1) and (x_2, y_2), the y-component of the point lying on the line joining the two points with x-component halfway between x_1 and x_2 is itself halfway between y_1 and y_2.*

Proof. Let the desired point be (x_0, y_0) as shown in Figure C.2. Since x_0 is halfway between x_1 and x_2 we know that

$$x_0 = \frac{x_1 + x_2}{2}.$$

The equation of the line joining (x_1, y_1) and (x_2, y_2) is then

$$y - y_1 = \frac{y_2 - y}{x_2 - x_1}(x - x_1).$$

Since (x_0, y_0) lies on this line, it must satisfy the equation

$$y_0 - y_1 = \frac{y_2 - y}{x_2 - x_1}\left(\frac{x_1 + x_2}{2} - x_1\right) \implies y_0 - y_1 = \frac{y_2 - y_1}{2} \implies y_0 = \frac{y_1 + y_2}{2}.$$

□

Theorem 1. *Consider a positive valued curve on the set $[a, c]$ with a unique maximum at $\frac{a+c}{2}$, and a positive valued straight line on the set $[a, c]$ that lies underneath the curve. Given an arbitraty $x = x_0$, let OD_{x_0} be the y-component of the curve at x_0, DI_{x_0} be the y-component of the line at x_0 and $DA_{x_0} = OD_{x_0} - DI_{x_0}$. Let CDA_{x_0} be the difference between the y-component of the curve at x_0 and the y-component of the line that joins the two end points of the curve at x_0. Then the following result holds:*

$$DA_{\frac{a+c}{2}} - \frac{DA_a + DA_c}{2} = OD_{\frac{a+c}{2}} - \frac{OD_a + OD_c}{2} = CDA_{\frac{a+c}{2}} \tag{C.1}$$

Proof. Let fd be a line parallel to the x-axis. Then by lemma 1

$$\frac{fe}{fd} = \frac{he}{gd}.$$

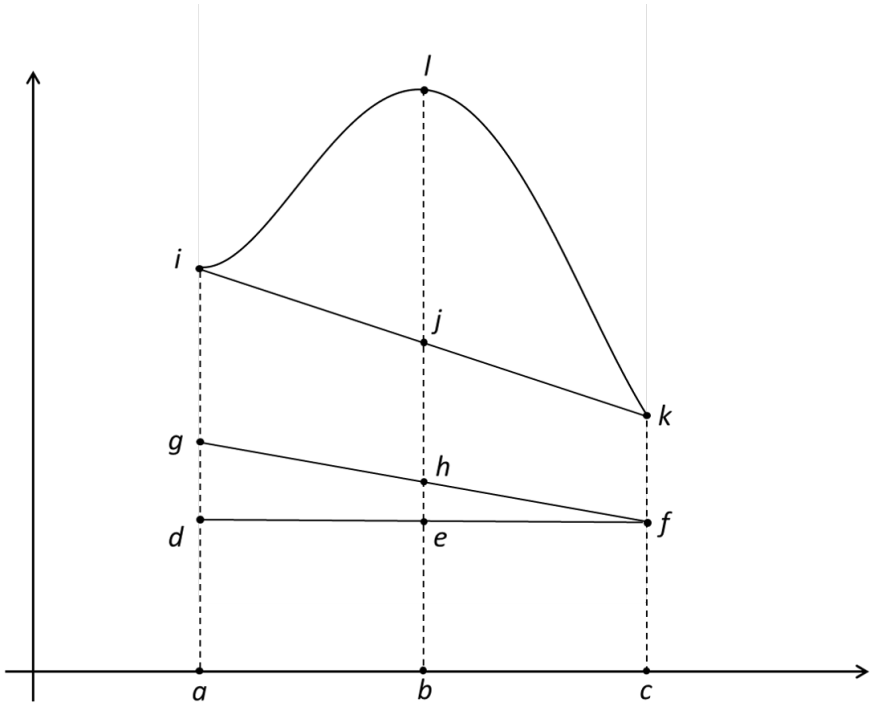

Figure C.3: Supporting figure for the proof of Theorem 1.

Because b is the point on the x-axis corresponding to the maximum l, by hypothesis $ab = bc$. Notice that

$$\begin{aligned} eb = fc &\implies he + fc = hb \implies he = hb - fc \\ da = fc &\implies gd + fc = ga \implies = gd = ga - fc. \end{aligned}$$

Then

$$\frac{hb - fc}{ga - fc} = \frac{fe}{fd} = \frac{1}{2} \implies hb = fc + \frac{ga - fc}{2}. \tag{C.2}$$

Substituting the following into Equation C.2

$$\begin{aligned} hb &= lb - lh \\ fc &= kc - kf \\ af &= ia - ig \end{aligned}$$

we have that:

$$lb - lh = kc - kf + \frac{(ia - kc) + (kf - ig)}{2} \tag{C.3}$$

$$\implies lb - lh = \frac{kc + ia}{2} - \frac{kf + ig}{2} \tag{C.4}$$

$$\implies lb - \frac{kc + ia}{2} = lh - \frac{kf + ig}{2} \tag{C.5}$$

But

$$\begin{aligned} ia &= OD_a \\ lb &= OD_b \\ kc &= OD_c \\ ig &= DA_a \\ lh &= DA_b \\ kf &= DA_c \end{aligned}$$

and $b = \frac{a+c}{2}$, so we can rewrite Eq. C.5 as

$$OD_{\frac{a+c}{2}} - \frac{OD_c + OD_a}{2} = DA_{\frac{a+c}{2}} - \frac{DA_c + DA_a}{2}$$

Since $ab = bc$, by Lemma 2

$$jb = \frac{ia + kc}{2} \quad \text{and} \quad hb = \frac{ga + fc}{2}.$$

Notice that $jb - hb = lh - lj$, so:

$$lj = lh - \frac{ia + kc}{2} + \frac{ga + fc}{2} \tag{C.6}$$

$$\implies lj = lh - \frac{ig + kf}{2} \tag{C.7}$$

Given that $lj = CDA_b = CDA_{\frac{a+c}{2}}$, Eq. C.7 can also be written as

$$CDA_{\frac{a+c}{2}} = DA_{\frac{a+c}{2}} - \frac{DA_a + DA_c}{2}$$

□

Allen [96] chose as the target substance dehydroisoandrosterone (DA), an endogenous steroid hormone that can be found in urine samples. Its absorbance measurement is complicated by the presence the hormone pregnanediol and other interferents present in the hormone-free urinary blank (DI), which can vary significantly between samples. Note that the term optical density (OD) used by Allen is a synonym for absorbance [95].

When analysing the spectrum of an unknown solution containing the target substance, the measured absorption (OD) at every point is the sum of the target's and all the other interfering substances' absorbance, so that

$$OD = DA + DI.$$

Figure C.4 illustrates the spectra of dehydroisoandrosterone (1), pregnanediol (2) and urinary blank (3), along with a composite curve summing 1, 2 and 3. Allen claims that this composite curve resembles closely the absorption curves obtained from clinical samples, making this a suitable example to outline his correction method.

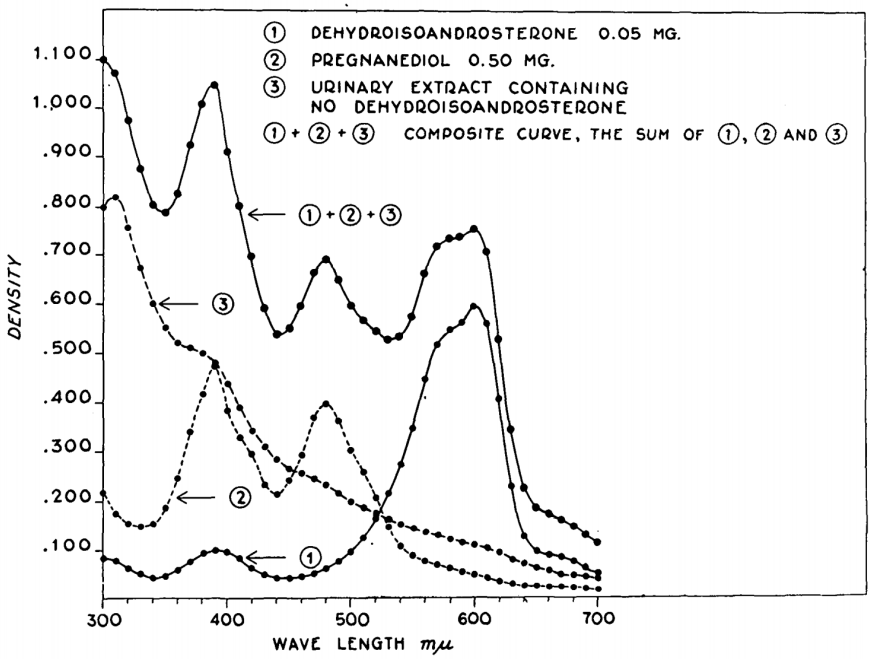

Figure C.4: Absorption curves given for 50 µg of pure dehydroisoandrosterone (1), 500 µg of pregnanediol (2) and a butyl alcohol extract of a clinical urine sample, which acts as urinary blank (3) as illustrated in Allen's work [96]. 1+2+3 is the composite curve obtained from the sum of the individual curves.

The spectrum of both interferents (2 and 3) is almost linear in the region near the target's curve (1) peak at 600 nm. Figure C.5 "zooms-in" on the area of interest around the peak of DA at 600 nm, representing curve 3, 2+3 and 1+2+3. The latter and the former were introduced in Figure C.4, while 2+3 shows the total absorption contribution of the combined interferents. The value obtained by subtracting the absorption values along the 2+3 from the 1+2+3 curve is due to the 50 µg of DA alone.

Theorem 1 can be applied if the composite curve of the interferents, in this case 2+3, can be approximated to a straight line at equidistant regions from the peak. Here the approximation is valid in the 560 to 640 nm range where both values are 40 nm away from the 600 nm peak, so

$$CDA_{600} = OD_{600} - \frac{(OD_{560} + OD_{640})}{2}. \tag{C.8}$$

Because the OD values are readily obtained from the spectrum of the unknown mixture, equation C.8 can be used even when the spectrum of the target substance is unknown[96]. Part of the target's absorbance is neglected during the calculation ($a'b'$ in Figure C.5), but can be included using the following if the target's spectrum is known to finally obtain line mb'

$$DA_{600} = OD_{600} - \frac{(OD_{560} + OD_{640})}{2} + \frac{(DA_{560} + DA_{640})}{2} \tag{C.9}$$

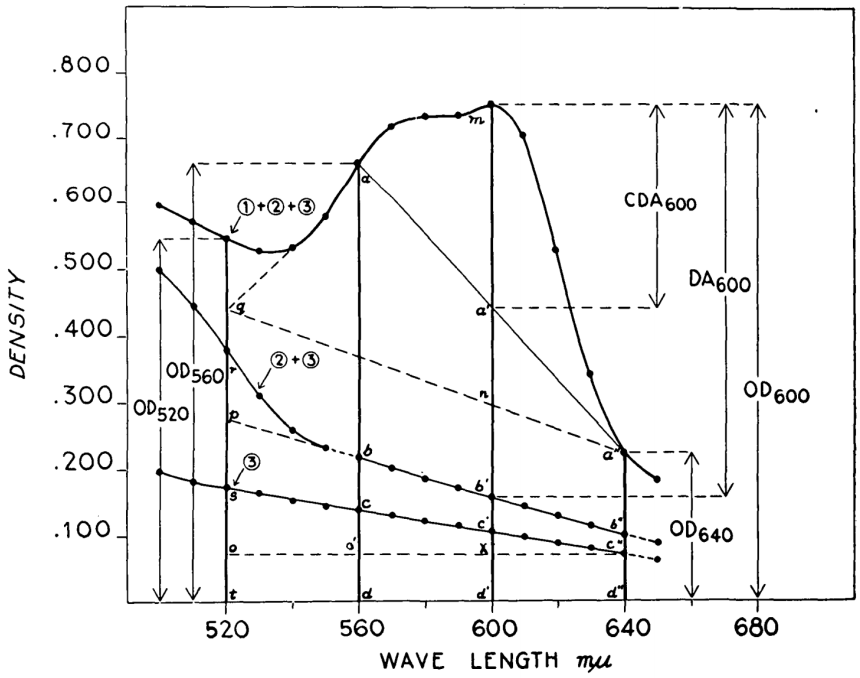

Figure C.5: Analysis of near *DA* peak region (600 nm) as depicted in Allen's work [96]. The four lines perpendicular to the wavelength axis at 520, 560, 600 (peak) and 640 nm intersect the curves at different points, each indicated by a letter.

The linear relationship between the absorption calculated using the equations presented and the concentration of target substance in the sample is illustrated in Figure C.6.

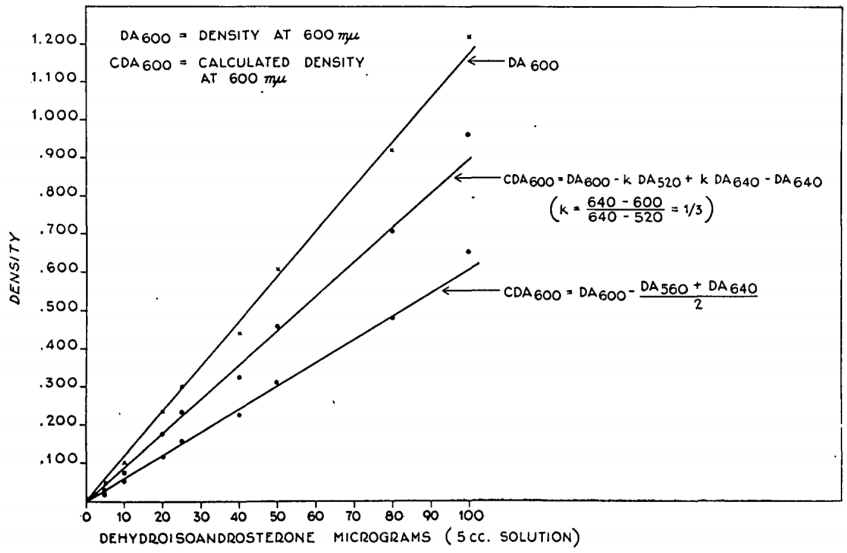

Figure C.6: Linear relationship between target substance *DA* concentration and the absorption calculated using Eq. C.8 and Eq. C.9, which were used to construct the lower and uppermost line respectively, as shown in Allen's paper [96].

C.2 Values collected for human blood standard curve

Table C.1: Values collected to construct the standard curve for the calculation of haemoglobin from human plasma samples with unknown concentrations. Five human blood samples (labelled A to E) collected from the SNBTS were diluted with a lysis buffer to obtain the starting solution, which was measured 3 times with the haematology analyser to produce the value shown. The H-value was then calculated using the absorption values at 562, 576 and 590 nm wavelengths. Dilutions 2 to 11 were used by the MATLAB script to produce the standard curve shown in Chapter 3, Section 3.6.2. The remaining data was outside the valid range of the UV-Vis spectrophotometer, and was therefore discarded.

Dilution number	Dilution factor	Solution (µL)	DPBS (µL)	A_H-values	A_Hgb ($g\,dL^{-1}$)	B_H-values	B_Hgb ($g\,dL^{-1}$)	C_H-values	C_Hgb ($g\,dL^{-1}$)	D_H-values	D_Hgb ($g\,dL^{-1}$)	E_H-values	E_Hgb ($g\,dL^{-1}$)
Starting sol.					5.23		5.06		5.3		3.7		5
1	1/20	50	950	0.0761	0.2617	0.0825	0.2533	0.0859	0.2650	0.2130	0.1850	0.0911	0.2500
2	1/66.66	300	700	0.2421	0.0785	0.2543	0.0760	0.2502	0.0795	0.2345	0.0555	0.2538	0.0750
3	1/133.33	500	500	0.1714	0.0393	0.1659	0.0380	0.1685	0.0398	0.1323	0.0278	0.1593	0.0375
4	1/166.66	800	200	0.1424	0.0314	0.1395	0.0304	0.1389	0.0318	0.1075	0.0222	0.1302	0.0300
5	1/208.33	800	200	0.1181	0.0251	0.1138	0.0243	0.1110	0.0254	0.0859	0.0178	0.1063	0.0240
6	1/260.41	800	200	0.0968	0.0201	0.0918	0.0195	0.0888	0.0204	0.0695	0.0142	0.0873	0.0192
7	1/325.52	800	200	0.0776	0.0161	0.0730	0.0156	0.0709	0.0163	0.0545	0.0114	0.0694	0.0154
8	1/406.90	800	200	0.0622	0.0129	0.0591	0.0125	0.0562	0.0130	0.0434	0.0091	0.0550	0.0123
9	1/508.62	800	200	0.0503	0.0103	0.0464	0.0100	0.0444	0.0104	0.0345	0.0073	0.0454	0.0098
10	1/1017.25	500	500	0.0247	0.0051	0.0233	0.0050	0.0220	0.0052	0.0167	0.0036	0.0217	0.0049
11	1/2034.50	500	500	0.0117	0.0026	0.0113	0.0025	0.0106	0.0026	0.0077	0.0018	0.0107	0.0025
12	1/2543.13	800	200	0.0091	0.0021	0.0087	0.0020	0.0081	0.0021	0.0060	0.0015	0.0079	0.0020

C.3 Values collected for equine blood standard curve

Table C.2: Values collected to construct the standard curve for the calculation of haemoglobin from equine plasma samples with unknown concentrations. Five equine blood samples (labelled A to E) collected from the Easter Bush Pathology Laboratory were prepared as discussed in Chapter 3, Section 3.6.3. Each dilution was thoroughly mixed using a vortex mixer (Fischer Scientific) at 1600 RPM and a pipette before 2.5 µL were deposited inside the spectrophotometer. The H-value was then calculated using the absorption values at 562, 576 and 590 nm wavelengths. All the H-values shown were used by the MATLAB script to produce the standard curve. The remaining data could not be measured as it was outside the valid range of the UV-Vis spectrophotometer.

Dilution number	Dilution factor	Solution (µL)	PBS (µL)	A_H-values	A_Hgb ($g\,dL^{-1}$)	B_H-values	B_Hgb ($g\,dL^{-1}$)	C_H-values	C_Hgb ($g\,dL^{-1}$)	D_H-values	D_Hgb ($g\,dL^{-1}$)	E_H-values	E_Hgb ($g\,dL^{-1}$)
Starting sol.					6.3		6.1		6.9		6.1		2.5
1	1/2	200	200		3.15		3.05		3.45		3.05		1.25
2	1/4	200	200		1.58		1.53		1.73		1.53		0.63
3	1/8	200	200		0.7875		0.7625		0.8625		0.7625		0.3125
4	1/16	200	200		0.3938		0.3813		0.4313		0.3813	0.1475	0.1563
5	1/32	200	200	0.1943	0.1969	0.1767	0.1906	0.2302	0.2156	0.1845	0.1906	0.0625	0.0781
6	1/64	200	200	0.0760	0.0984	0.0678	0.0953	0.0948	0.1078	0.0827	0.0953	0.0430	0.0625
7	1/80	200	50	0.0582	0.0788	0.0548	0.0763	0.0668	0.0863	0.0567	0.0763	0.0307	0.0500
8	1/100	200	50	0.0412	0.0630	0.0408	0.0610	0.0503	0.0690	0.0447	0.0610	0.0255	0.0400
9	1/125	200	50	0.0257	0.0504	0.0302	0.0488	0.0338	0.0552	0.0318	0.0488	0.0162	0.0320
10	4/625	200	50	0.0232	0.0403	0.0217	0.0390	0.0260	0.0442	0.0238	0.0390	0.0128	0.0256
11	3/586	200	50	0.0167	0.0323	0.0152	0.0312	0.0202	0.0353	0.0157	0.0312	0.0100	0.0205
12	1/244	200	50	0.0122	0.0258	0.0103	0.0250	0.0152	0.0283	0.0142	0.0250	0.0070	0.0164
13	1/305	200	50	0.0088	0.0206	0.0085	0.0200	0.0110	0.0226	0.0090	0.0200	0.0028	0.0131
14	2/763	200	50	0.0067	0.0165	0.0062	0.0160	0.0075	0.0181	0.0073	0.0160	0.0032	0.0105
15	1/477	200	50	0.0048	0.0132	0.0035	0.0128	0.0038	0.0145	0.0037	0.0128		
16	1/596	200	50	0.0038	0.0106	0.0027	0.0102	0.0035	0.0116				

C.4 MATLAB code for derivation of standard curve

C.4.1 Human blood

Standard_curve_main.m

```
[xi,y_mean] = standard_curve();
% Requires an array of H values to convert as input.
H = [];
hgb = h_value_to_hgb(H,xi,y_mean)
```

standard_curve.m

```
% Function to load standard curve data and calculate y_mean
function [xi,y_mean] = standard_curve()
data = load('Standard_curve_data.mat');
data = data.UVVisstandardcurveS8;

% For each dataset, load variables from table
x = data(1:10,{'A'});
y = data(1:10,{'A_Hgb'});
% Convert to arrays
a_x = table2array(x);
a_y = table2array(y);

x = data(1:10,{'B'});
y = data(1:10,{'B_Hgb'});
b_x = table2array(x);
b_y = table2array(y);

x = data(1:10,{'C'});
y = data(1:10,{'C_Hgb'});
c_x = table2array(x);
c_y = table2array(y);

x = data(1:10,{'D'});
y = data(1:10,{'D_Hgb'});
d_x = table2array(x);
d_y = table2array(y);

x = data(1:10,{'E'});
y = data(1:10,{'E_Hgb'});
e_x = table2array(x);
e_y = table2array(y);

xi = linspace(0, 0.2, 5000); % Standard curve range

% Interpolate to new x values
ayi = interp1(a_x(:), a_y(:), xi(:), 'linear', 'extrap');
byi = interp1(b_x(:), b_y(:), xi(:), 'linear', 'extrap');
cyi = interp1(c_x(:), c_y(:), xi(:), 'linear', 'extrap');
```

```
dyi = interp1(d_x(:), d_y(:), xi(:), 'linear', 'extrap');
eyi = interp1(e_x(:), e_y(:), xi(:), 'linear', 'extrap');

% Calculate mean of y values
y_mean = mean([ayi byi cyi dyi eyi], 2);
xs = [a_x b_x c_x d_x e_x];
ys = [a_y b_y c_y d_y e_y];

plot_curves(xi,y_mean,xs,ys);
end

% Function to plot the curve
function [] = plot_curves(xi,y_mean,xs,ys)
figure(1)
plot(xs(:,1), ys(:,1), '-k')
hold on
plot(xs(:,2), ys(:,2), '-k')
hold on
plot(xs(:,3), ys(:,3), '-k')
hold on
plot(xs(:,4), ys(:,4), '-k')
hold on
plot(xs(:,5), ys(:,5), '-k')
hold on
plot(xi, y_mean, '-r', 'LineWidth',2)
hold off
grid
legend('A', 'B', 'C', 'D', 'E', 'Mean', 'Location','N')
end
```

h_value_to_hgb.m

```
% Find hemoglobin value given the corresponding H value
function [Hgb] = h_value_to_Hgb(H,xi,y_mean)
Hgb = [];
for i = 1:length(H)
temp_hgb = interp1(xi,y_mean,H(i),"spline");
Hgb = [Hgb temp_hgb];
end
end
```

Data used for the construction of the curve

C.4.2 Equine blood

eq_standard_curve_main.m

```
[xi,y_mean] = eq_standard_curve();
% Requires an array of H values to convert as input.
H = [0.0235];
```

A	A_Hgb	B	B_Hgb	C	C_Hgb	D	D_Hgb	E	E_Hgb
0.2421	0.0785	0.254289	0.076	0.250207	0.0795	0.234521	0.0555	0.253754	0.075
0.171406	0.03925	0.165874	0.038	0.168483	0.03975	0.13233	0.02775	0.159305	0.0375
0.142393	0.0314	0.139531	0.0304	0.138897	0.0318	0.107461	0.0222	0.130218	0.03
0.118062	0.02512	0.113846	0.02432	0.110991	0.02544	0.085945	0.01776	0.106306	0.024
0.096768	0.020096	0.09181	0.019456	0.088789	0.020352	0.069488	0.014208	0.087287	0.0192
0.077644	0.016077	0.072977	0.015565	0.070932	0.016282	0.054457	0.011366	0.069355	0.01536
0.062177	0.012861	0.059065	0.012452	0.056248	0.013025	0.043367	0.009093	0.055048	0.012288
0.050265	0.010289	0.046423	0.009961	0.044383	0.01042	0.034499	0.007274	0.045439	0.00983
0.02472	0.005145	0.02333	0.004981	0.02195	0.00521	0.016656	0.003637	0.021688	0.004915
0.011717	0.002572	0.011251	0.00249	0.010618	0.002605	0.007721	0.001819	0.01065	0.002458

```
hgb = eq_h_value_to_hgb(H,xi,y_mean)
```

eq_standard_curve.m

```
% Function to load standard curve data and calculate y_mean
function [xi,y_mean] = eq_standard_curve()

data = load('eq_standard_curve_data.mat');
data = data.HgbcurvedataS5;

% For each dataset, load variables from table
x = data(1:12,{'A'});
y = data(1:12,{'A_Hgb'});
% Convert to arrays
a_x = table2array(x);
a_y = table2array(y);

x = data(1:12,{'B'});
y = data(1:12,{'B_Hgb'});
b_x = table2array(x);
b_y = table2array(y);

x = data(1:12,{'C'});
y = data(1:12,{'C_Hgb'});
c_x = table2array(x);
c_y = table2array(y);

x = data(1:12,{'D'});
y = data(1:12,{'D_Hgb'});
d_x = table2array(x);
d_y = table2array(y);

x = data(1:12,{'E'});
y = data(1:12,{'E_Hgb'});
e_x = table2array(x);
e_y = table2array(y);

xi = linspace(0, 0.25, 5000); % Eq standard curve range (lowest expected H-value,
```

```
%highest expected H-value, number of points in between);

% Interpolate to new x values
ayi = interp1(a_x(:), a_y(:), xi(:), 'linear', 'extrap');
byi = interp1(b_x(:), b_y(:), xi(:), 'linear', 'extrap');
cyi = interp1(c_x(:), c_y(:), xi(:), 'linear', 'extrap');
dyi = interp1(d_x(:), d_y(:), xi(:), 'linear', 'extrap');
eyi = interp1(e_x(:), e_y(:), xi(:), 'linear', 'extrap');

y_mean = mean([ayi byi cyi dyi eyi], 2);

% Plot against the other interpolations
ys = [ayi byi cyi dyi eyi];
plot_curves(xi, y_mean, ys)
end

% Plotting function
function [] = plot_curves(xi, y_mean, ys)
figure(1)
plot(xi, ys(:,1), '-k')
hold on
plot(xi, ys(:,2), '-k')
hold on
plot(xi, ys(:,3), '-k')
hold on
plot(xi, ys(:,4), '-k')
hold on
plot(xi, ys(:,5), '-k')
hold on
plot(xi, y_mean', '-r', 'LineWidth', 2)
hold off
grid
legend('A', 'B', 'C', 'D', 'E', 'Mean', 'Location','N')
end
```

eq_h_value_to_hgb.m

```
% Find hemoglobin value given the corresponding H value
function [Hgb] = h_value_to_Hgb(H,xi,y_mean)

Hgb = [];
for i = 1:length(H)
temp_hgb = interp1(xi, y_mean, H(i), "spline");
Hgb = [Hgb temp_hgb];
end
end
```

Data used for the construction of the curve

A	A_Hgb	B	B_Hgb	C	C_Hgb	D	D_Hgb	E	E_Hgb
0.194333	0.1969	0.176667	0.190625	0.230167	0.215625	0.1845	0.190625	0.1475	0.15625
0.076	0.0984	0.067833	0.095313	0.094833	0.107813	0.082667	0.095313	0.0625	0.078125
0.058167	0.0788	0.054833	0.07625	0.066833	0.08625	0.056667	0.07625	0.043	0.0625
0.041167	0.0630	0.040833	0.061	0.050333	0.069	0.044667	0.061	0.030667	0.05
0.025667	0.0504	0.030167	0.0488	0.033833	0.0552	0.031833	0.0488	0.0255	0.04
0.023167	0.0403	0.021667	0.03904	0.02600	0.04416	0.023833	0.03904	0.016167	0.032
0.016667	0.032256	0.015167	0.031232	0.020167	0.035328	0.015667	0.031232	0.012833	0.0256
0.012167	0.025805	0.010333	0.024986	0.015167	0.028262	0.014167	0.024986	0.01	0.02048
0.008833	0.020644	0.0085	0.019988	0.011	0.02261	0.009	0.019988	0.007	0.016384
0.006667	0.016515	0.006167	0.015991	0.0075	0.018088	0.007333	0.015991	0.002833	0.013107
0.004833	0.013212	0.0035	0.012793	0.003833	0.01447	0.003667	0.012793	0.003167	0.010486
0.003833	0.01057	0.002667	0.010234	0.0035	0.011576	0	0	0	0

Appendix D

Conference publication

The following paper:

G. Deiana, A. J. Conde, C. McCarthy, J. Dear, S. Smith, and M. Kersaudy-Kerhoas, 'MICROFLUIDIC DEVICE FOR THE SEPARATION OF BLOOD PLASMA FROM CAPILLARY SAMPLES'

was presented at the Miniaturized Systems for Chemistry and Life Sciences (µTAS 2019) in Oct. 2019 and is available online here.

MICROFLUIDIC DEVICE FOR THE SEPARATION OF BLOOD PLASMA FROM CAPILLARY SAMPLES

Giulia Deiana[1], Alvaro J. Conde[2,3], Conni McCarthy[2,3], James Dear[3], Stewart Smith[1] and Maïwenn Kersaudy-Kerhoas[2,3*]

[1] School of Engineering, University of Edinburgh, UK

[2] Institute of Biological Chemistry, Biophysics and Bioengineering, Heriot-Watt University, UK

[3] College of Medicine and Veterinary Medicine, University of Edinburgh, UK

ABSTRACT

In this paper, we report a cost-effective, disposable microfluidic microfiltration device for the fast separation of capillary volumes of undiluted whole blood. The proposed device is operated without power or specialist equipment, requiring only a commercial metered device (Minivette®, Sarstedt) used for the collection of blood from a finger prick to actuate the blood flow in a dead-end filtration setup. The device can extract 27.7 ± 6 µL of 100% pure plasma from 100 µL of undiluted whole blood in three minutes.

KEYWORDS: Blood plasma separation, sample preparation, point-of-care testing, microfluidics.

INTRODUCTION

The integrity of blood samples is of paramount importance for several clinical tests, which become unreliable when samples are compromised by hemolysis. Notable examples are assays for cardiac troponins, the leading biomarker for the detection of acute myocardial infarction (among the leading causes of death worldwide) [1] and circulating cell-free nucleic acids, which are used in many emerging applications such as the assessment and prediction of athletic performance [2]. The inclusion of microfluidic methods in medical diagnostics can lead to faster and cheaper tests, along with the possibility of point-of-care use. By testing immediately at the patient's side, errors due to the collection, transportation, handling and preparation of samples could be significantly reduced. However, one of the major hurdles preventing microfluidic devices from being widely adopted in clinical settings is the difficulty of isolating pure plasma from minute amounts of blood and at the point-of-care.

Several microfiltration devices for the separation of whole blood in the 100-300 µL range can be found in the literature [4-7]. A succinct comparison is offered in Table 1 with regards to the main parameters in sample preparation: yield, purity, dilution ratio, extraction time and hemoglobin (Hgb) levels. Most of these devices rely on bulky and expensive external pumps for their operation or necessitate careful pipetting of blood.

We have developed a low cost, disposable microfluidic microfiltration device for the fast separation of 100 µL of undiluted whole blood. The proposed device does not necessitate any power source or specialist equipment for its operation, requiring only a commercial metered device used for the collection of blood from a finger prick (Minivette®, Sarstedt) to actuate the blood flow in a dead-end filtration setup.

Table 1: Comparison of studies reviewed. N/C entries were not communicated by the authors. Average hematocrit level for yield calculation from other studies was set at 45%.

Study	Sample volume	Yield	Purity	Hgb (g/dL)	Dilution	Extraction time	External pumps
Homsy *et al.* [4]	100 µL	12%	N/C	N/C	None	7-10 min	Yes
Liu *et al.* [5]	200 µL	33%	N/C	N/C	None	10 min	No
Su *et al.* [6]	300 µL	20%	99%	N/C	None	5 min	Yes
Aota *et al.* [7]	200 µL	34%	92.5%	2.5×10^{-4}	None	20 min	Yes
This study	100 µL	27.7 ± 6 %	100%	0.1	None	3 min	No

EXPERIMENTAL

The device consists of 6 layers of Poly(methyl methacrylate) (PMMA) and a polysulfone plasma separation membrane (Vivid™ GR, Pall) (Fig 1.A). Layers 5 and 6 were functionalized by immersion in a 1 M NaOH solution for 2 minutes to render the surface hydrophilic. The layers were bonded using an optimised ethanol-assisted thermal bonding method previously described by our group [3]. Briefly, all PMMA layers were cut to

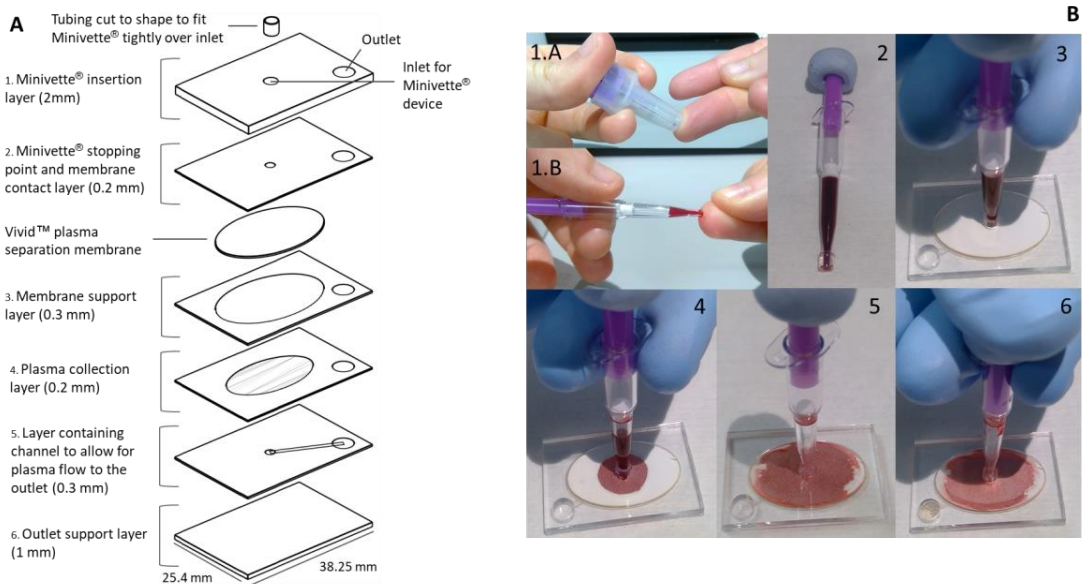

Fig 1. A) Exploded view of the separation device. All layers are laser-cut in cast PMMA. B) Device operation. 1) The Minivette® is filled with capillary blood. 2) Cap and laboratory tubing (1.57 mm I.D. and 3.18 mm O.D.) cut to 3 mm height are fitted on the filled Minivette®. 3) The Minivette® is inserted into the device's inlet. 4) The user presses the Minivette® plunger gently and immediately releases it. This allows the membrane to start wicking the blood out of the Minivette® 5) Once the Minivette® is completely emptied, the user waits 2 minutes for the plasma to accumulate in the collection layer. 6) The user presses the Minivette® plunger and the plasma fills the outlet, ready for collection.

size using a CO_2 laser cutter (Epilog Laser Mini 18) and cleaned with ethanol to remove fabrication debris and dust particles from the surface. The individual layers were stacked on top of each other in the correct order, sprayed with a small amount of ethanol and subsequently bonded at 70 °C and 13.7 MPa using a hot press for 3 minutes. The entire fabrication process requires less than 15 minutes and is amenable to mass manufacturing. The operational steps of the device are described in Fig 1.B.

Fresh venous blood was extracted on the day of the experiments from a healthy volunteer (NHS REC 19/ES/0056) using a EDTA K3 Monovette. To prepare the control plasma, 600 µL of whole blood was pipetted in a 2 mL Eppendorf container and centrifuged in an Eppendorf Minispin centrifuge at 1600 g for 10 min. The resulting supernatant was then transferred into a clean container and centrifuged again at 12,045 g for another 10 minutes. All samples were characterised using a hematology analyser (Beckman Coulter Ac·T diff 2TM hematology).

RESULTS AND DISCUSSION

The novelty of our approach resides in the use of the Minivette® as an actuation mechanism to accelerate the extraction of plasma. In order to measure the maximal and minimal pressure that can be applied using the 100 µL Minivette®, the collection device was wrapped in parafilm, filled with 100 µL of venous blood and immediately fitted into a pressure sensor setup (LabSmith). The maximal pressure obtained by pressing the plunger as fast as possible was measured as 9.24 kPa over 1 second, while 2-2.5 kPa were recorded for a slower 3 seconds long injection. The averaged measurements data is presented in Fig 2.A.

In order to characterise the separation performance of the device, a total of 39 devices were tested with fresh blood (43.1% Hct). Once the Minivette® was filled, the extraction process only required three minutes. The separated plasma was collected from the outlet of the device, transferred into a clean container and subsequently characterised with the hematology analyser. The collected average plasma volume was 27.7 µL, which corresponds to 48.7% of the total available plasma (Fig 2.B). All the plasma extracted with the device was 100% pure, meaning that no red blood cells were detected in the filtrate. The plasma collected with the device contained more platelets (2.9 vs 2 cells $x10^3/\mu L$) and marginally more white blood cells (0.215 vs 0.2 cells $x10^3/\mu L$) (Fig 2.C). Centrifuged control plasma and device plasma were both measured as 0.1 g Hgb/dL, which is the lowest detectable Hgb level of the hematology analyser (Fig 2.D).

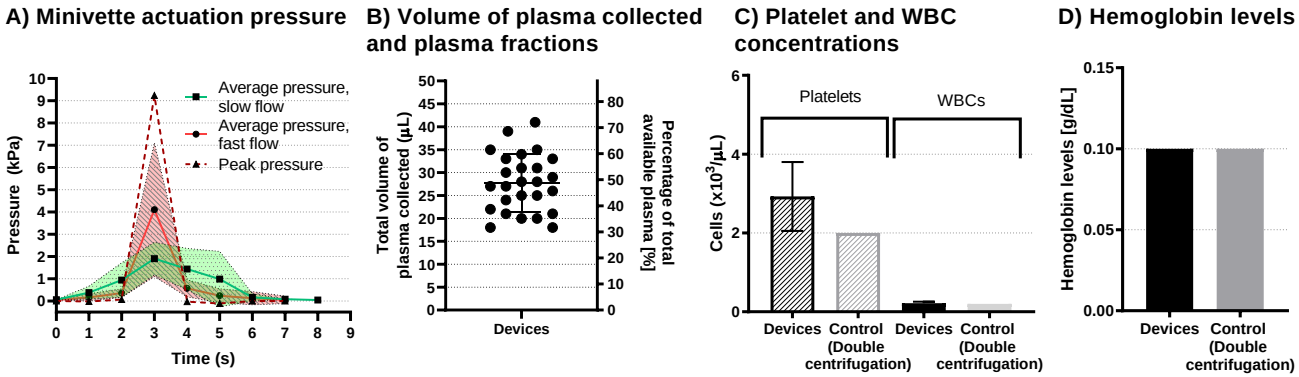

Fig 2. A) Average pressure obtainable with the 100 µL Minivette® during fast and slow injections into the device. 1 Hz acquisition rate. Device resistance was not accounted for B) Plasma volume/yield and percentage of available plasma collected for each device that did not experience failure due to manufacturing defects. C) Platelets and WBC count of device and control plasma. D) Hemoglobin levels of device plasma and control plasma.

CONCLUSION

When designing a microfluidic filtration device, plasma quality, yield and extraction speed need to be carefully balanced to produce a clean filtrate. We focused on minimising extraction time and operational and fabrication complexity. Our device is low cost, easy to use, amenable to mass manufacturing and capable of producing 100% pure plasma in three minutes without requiring external components or the application of negative pressure at the outlet. The devices tested extracted an average of 27.7 µL from 100 µL of blood. Hemoglobin levels of the plasma were measured at ≤ 0.1g/dL (hematology analyser limit), which were similar to the centrifugation control. Future work will focus on acquiring data for several different healthy donors, improving the robustness of the device and characterising the plasma with a bioassay such as insulin measurement.

ACKNOWLEDGEMENTS

This project was funded by the Engineering and Physical Sciences Research Council (EPSRC) through the EPSRC Centre for Doctoral Training in Intelligent Sensing and Measurement (EP/L016753/1). MKK acknowledges EPSRC EP/R00398X/1.

REFERENCES

[1] C. Puelacher et al., "Effects of hemolysis on the diagnostic accuracy of cardiac troponin I for the diagnosis of myocardial infarction," International Journal of Cardiology, vol. 187, pp. 313–315, May 2015.

[2] N. Haller et al., "Circulating, cell-free DNA as a marker for exercise load in intermittent sports," PLOS ONE, vol. 13, no. 1, p. e0191915, Jan. 2018.

[3] A. Liga et al., "Safe and cost-effective rapid-prototyping of multilayer PMMA microfluidic devices," Microfluid. Nanofluidics, vol. 20, no. 12, Dec. 2016.

[4] A. Homsy et al., "Development and validation of a low cost blood filtration element separating plasma from undiluted whole blood," Biomicrofluidics, vol. 6, no. 1, p. 012804, Mar. 2012.

[5] C. Liu et al., "A high-efficiency superhydrophobic plasma separator," Lab. Chip, vol. 16, no. 3, pp. 553–560, 2016.

[6] X. Su et al., "A low cost, membranes based serum separator modular," Biomicrofluidics, vol. 12, no. 2, p. 024108, Mar. 2018.

[7] A. Aota et al., "Microchip-based Plasma Separation from Whole Blood via Axial Migration of Blood Cells," Anal. Sci., vol. 27, no. 12, p. 1173, 2011.

CONTACT

*m.kersaudy-kerhoas@hw.ac.uk

Bibliography

[1] H. Teymourian, A. Barfidokht, and J. Wang, "Electrochemical glucose sensors in diabetes management: An updated review (2010–2020)," vol. 49, no. 21, pp. 7671–7709.

[2] M. Kersaudy-Kerhoas and E. Sollier, "Micro-scale blood plasma separation: From acoustophoresis to egg-beaters," vol. 13, no. 17, p. 3323.

[3] R. Mariella, "Sample preparation: The weak link in microfluidics-based biodetection," vol. 10, no. 6, pp. 777–784.

[4] M. Toner and D. Irimia, "Blood-on-a-Chip," vol. 7, no. 1, pp. 77–103.

[5] J. M. Ward, S. Cherian, and M. A. Linden, "19 - Hematopoietic and Lymphoid Tissues," in *Comparative Anatomy and Histology (Second Edition)* (P. M. Treuting, S. M. Dintzis, and K. S. Montine, eds.), pp. 365–401, Academic Press.

[6] L. Dean, *Blood Groups and Red Cell Antigens*. National Center for Biotechnology Information (US).

[7] A. Blann and N. Ahmed, *Blood Science: Principles and Pathology*. John Wiley & Sons, Incorporated.

[8] G. Pop, D. Duncker, M. Gardien, P. Vranckx, S. Versluis, D. Hasan, and C. Slager, "The clinical significance of whole blood viscosity in (cardio)vascular medicine," vol. 10, no. 12, pp. 512–516.

[9] R. E. Moore, "An Historical Perspective on the Clinical Diagnostic Laboratory," in *Molecular Diagnostics: For the Clinical Laboratorian* (W. B. Coleman and G. J. Tsongalis, eds.), pp. 3–10, Humana Press.

[10] F. T. Fischbach and M. B. Dunning, *A Manual of Laboratory and Diagnostic Tests [Edited by] Frances Talaska Fischbach, Marshall Barnett Dunning III*. Wolters Kluwer Health, 9th edition ed.

[11] K. D. McClatchey, R. W. Weinberg, R. E. Reter, and M. Lerner, *Clinical Laboratory Medicine / Kenneth D. McClatchey, Editor ; Ruth W. Weinberg, Acquisition Editor ; Raymond E. Reter, Developmental Editor ; Mark Lerner, Cover Designer*. Lippincott Williams & Wilkins, second edition. ed.

[12] M. Laposata, *Laboratory Medicine The Diagnosis of Disease in the Clinical Laboratory / Michael Laposata*. McGraw-Hill's AccessMedicine, McGraw-Hill Education LLC,, 2nd edition ed.

[13] P. Bonini, M. Plebani, F. Ceriotti, and F. Rubboli, "Errors in Laboratory Medicine," vol. 48, no. 5, pp. 691–698.

[14] G. Lippi, N. Blanckaert, P. Bonini, S. Green, S. Kitchen, V. Palicka, A. J. Vassault, and M. Plebani, "Haemolysis: An overview of the leading cause of unsuitable specimens in clinical laboratories," vol. 46, no. 6, pp. 764–772.

[15] D. Wild, C. Sheehan, and S. Binder, "Introduction to Immunoassay Product Technology in Clinical Diagnostic Testing," in *The Immunoassay Handbook*, pp. 509–515, Elsevier.

[16] A. St John and C. P. Price, "Existing and Emerging Technologies for Point-of-Care Testing," vol. 35, no. 3, pp. 155–167.

[17] J. H. Nichols, "Point-of-Care Testing," in *The Immunoassay Handbook*, pp. 455–463, Elsevier.

[18] R. Tang, H. Yang, J. R. Choi, Y. Gong, M. You, T. Wen, A. Li, X. Li, B. Xu, S. Zhang, Q. Mei, and F. Xu, "Capillary blood for point-of-care testing," vol. 54, no. 5, pp. 294–308.

[19] L. Heireman, P. Van Geel, L. Musger, E. Heylen, W. Uyttenbroeck, and B. Mahieu, "Causes, consequences and management of sample hemolysis in the clinical laboratory," vol. 50, no. 18, pp. 1317–1322.

[20] S. F. Green, "The cost of poor blood specimen quality and errors in preanalytical processes," vol. 46, no. 13-14, pp. 1175–1179.

[21] L. Thomas, "Haemolysis as Influence & Interference Factor," vol. 13, no. 4, pp. 95–98.

[22] P. J. Howanitz, C. M. Lehman, B. A. Jones, F. A. Meier, and G. L. Horowitz, "Clinical Laboratory Quality Practices When Hemolysis Occurs," vol. 139, no. 7, pp. 901–906.

[23] J. A. Snyder, M. W. Rogers, M. S. King, J. C. Phillips, J. F. Chapman, and C. A. Hammett-Stabler, "The impact of hemolysis on Ortho-Clinical Diagnostic's ECi and Roche's elecsys immunoassay systems," vol. 348, no. 1, pp. 181–187.

[24] G. Lippi, D. Giavarina, M. Gelati, and G. L. Salvagno, "Reference range of hemolysis index in serum and lithium-heparin plasma measured with two analytical platforms in a population of unselected outpatients," vol. 429, pp. 143–146.

[25] G. Lippi and J. Cadamuro, "Visual assessment of sample quality: Quo usque tandem?," vol. 56, no. 4, pp. 513–515.

[26] International Organization for Standardization, "ISO 22870:2016."

[27] T. Shu, H. Hunter, Z. Zhou, Y. Sun, X. Cheng, J. Ma, L. Su, X. Zhang, and M. J. Serpe, "Portable point-of-care diagnostic devices: An updated review," vol. 13, no. 45, pp. 5418–5435.

[28] S. Sachdeva, R. W. Davis, and A. K. Saha, "Microfluidic Point-of-Care Testing: Commercial Landscape and Future Directions," vol. 8, p. 1537.

[29] K. J. Land, D. I. Boeras, X.-S. Chen, A. R. Ramsay, and R. W. Peeling, "REASSURED diagnostics to inform disease control strategies, strengthen health systems and improve patient outcomes," vol. 4, no. 1, pp. 46–54.

[30] W. S. Mielczarek, E. A. Obaje, T. T. Bachmann, and M. Kersaudy-Kerhoas, "Microfluidic blood plasma separation for medical diagnostics: Is it worth it?," vol. 16, no. 18, pp. 3441–3448.

[31] S. Tripathi, Y. V. B. Varun Kumar, A. Prabhakar, S. S. Joshi, and A. Agrawal, "Passive blood plasma separation at the microscale: A review of design principles and microdevices," vol. 25, no. 8, p. 083001.

[32] S. Tripathi, Y. V. B. Varun Kumar, A. Prabhakar, S. S. Joshi, and A. Agrawal, "Performance study of microfluidic devices for blood plasma separation—a designer's perspective," vol. 25, no. 8, p. 084004.

[33] S. Tripathi, Y. V. B. Kumar, A. Agrawal, A. Prabhakar, and S. S. Joshi, "Microdevice for plasma separation from whole human blood using bio-physical and geometrical effects," vol. 6, no. 1.

[34] S. Tripathi and A. Agrawal, "Blood Plasma Microfluidic Device: Aiming for the Detection of COVID-19 Antibodies Using an On-Chip ELISA Platform," vol. 5, no. 2, pp. 217–220.

[35] A. Prabhakar, Y. V. B. V. Kumar, S. Tripathi, and A. Agrawal, "A novel, compact and efficient microchannel arrangement with multiple hydrodynamic effects for blood plasma separation," vol. 18, no. 5-6, pp. 995–1006.

[36] A. Vázquez-Guardado, S. Barkam, M. Peppler, A. Biswas, W. Dennis, S. Das, S. Seal, and D. Chanda, "Enzyme-Free Plasmonic Biosensor for Direct Detection of Neurotransmitter Dopamine from Whole Blood," vol. 19, no. 1, pp. 449–454.

[37] S. Yang, A. Ündar, and J. D. Zahn, "A microfluidic device for continuous, real time blood plasma separation," vol. 6, no. 7, pp. 871–880.

[38] M. Kersaudy-Kerhoas, D. M. Kavanagh, R. S. Dhariwal, C. J. Campbell, and M. P. Y. Desmulliez, "Validation of a blood plasma separation system by biomarker detection," vol. 10, no. 12, p. 1587.

[39] M. Rafeie, J. Zhang, M. Asadnia, W. Li, and M. E. Warkiani, "Multiplexing slanted spiral microchannels for ultra-fast blood plasma separation," vol. 16, no. 15, pp. 2791–2802.

[40] M. Robinson, H. Marks, T. Hinsdale, K. Maitland, and G. Coté, "Rapid isolation of blood plasma using a cascaded inertial microfluidic device," vol. 11, no. 2, p. 024109.

[41] S. Thorslund, O. Klett, F. Nikolajeff, K. Markides, and J. Bergquist, "A hybrid poly(dimethylsiloxane) microsystem for on-chip whole blood filtration optimized for steroid screening," vol. 8, no. 1, pp. 73–79.

[42] S. Thorslund, O. Klett, F. Nikolajeff, K. Markides, and J. Bergquist, "A hybrid poly(dimethylsiloxane) microsystem for on-chip whole blood filtration optimized for steroid screening," vol. 8, no. 1, pp. 73–79.

[43] A. Homsy, P. D. van der Wal, W. Doll, R. Schaller, S. Korsatko, M. Ratzer, M. Ellmerer, T. R. Pieber, A. Nicol, and N. F. de Rooij, "Development and validation of a low cost blood filtration element separating plasma from undiluted whole blood," vol. 6, no. 1, p. 012804.

[44] J. Hauser, G. Lenk, J. Hansson, O. Beck, G. Stemme, and N. Roxhed, "High-Yield Passive Plasma Filtration from Human Finger Prick Blood," vol. 90, no. 22, pp. 13393–13399.

[45] Q. Gao, Y. Chang, Q. Deng, and H. You, "A simple and rapid method for blood plasma separation driven by capillary force with an application in protein detection," vol. 12, no. 20, pp. 2560–2570.

[46] J. Kim, J. Yoon, J.-Y. Byun, H. Kim, S. Han, J. Kim, J. H. Lee, H.-S. Jo, and S. Chung, "Nano-Interstice Driven Powerless Blood Plasma Extraction in a Membrane Filter Integrated Microfluidic Device," vol. 21, no. 4, p. 1366.

[47] A. Aota, S. Takahashi, K. Mawatari, Y. Tanaka, Y. Sugii, and T. Kitamori, "Microchip-based Plasma Separation from Whole Blood via Axial Migration of Blood Cells," vol. 27, no. 12, p. 1173.

[48] P.-C. Chen, C.-C. Chen, and K.-C. Young, "Characterization of thermoplastic microfiltration chip for the separation of blood plasma from human blood," vol. 10, no. 5, p. 054112.

[49] K. Aran, A. Fok, L. A. Sasso, N. Kamdar, Y. Guan, Q. Sun, A. Ündar, and J. D. Zahn, "Microfiltration platform for continuous blood plasma protein extraction from whole blood during cardiac surgery," vol. 11, no. 17, pp. 2858–2868.

[50] C. Liu, M. Mauk, R. Gross, F. D. Bushman, P. H. Edelstein, R. G. Collman, and H. H. Bau, "Membrane-Based, Sedimentation-Assisted Plasma Separator for Point-of-Care Applications," vol. 85, no. 21, pp. 10463–10470.

[51] C. Liu, S.-C. Liao, J. Song, M. G. Mauk, X. Li, G. Wu, D. Ge, R. M. Greenberg, S. Yang, and H. H. Bau, "A high-efficiency superhydrophobic plasma separator," vol. 16, no. 3, pp. 553–560.

[52] "Vivid™ Plasma Separation Membrane - Diagnostics."

[53] K. Kadimisetty, K. Yin, A. M. Roche, Y. Yi, F. D. Bushman, R. G. Collman, R. Gross, L. Feng, and C. Liu, "An integrated self-powered 3D printed sample concentrator for highly sensitive molecular detection of HIV in whole blood at the point of care," vol. 146, no. 10, pp. 3234–3241.

[54] X. Su, S. Zhang, S. Ge, M. Chen, J. Zhang, J. Zhang, and N. Xia, "A low cost, membranes based serum separator modular," vol. 12, no. 2, p. 024108.

[55] Y. Ma, X. Cao, X. Feng, Y. Ma, and H. Zou, "Fabrication of super-hydrophobic film from PMMA with intrinsic water contact angle below 90°," vol. 48, no. 26, pp. 7455–7460.

[56] D. G. Waugh and J. Lawrence, "Wettability characteristics variation of PMMA by means of CO2 laser generated surface patterns," in *International Congress on Applications of Lasers & Electro-Optics*, pp. 1236–1244, Laser Institute of America.

[57] X. Su, J. Zhang, D. Zhang, Y. Wang, M. Chen, Z. Weng, J. Wang, J. Zeng, Y. Zhang, S. Zhang, S. Ge, J. Zhang, and N. Xia, "High-Efficiency Plasma Separator Based on Immunocapture and Filtration," vol. 11, no. 4, p. 352.

[58] C. Park, H.-R. Kim, S.-K. Kim, I.-K. Jeong, J.-C. Pyun, and S. Park, "Three-Dimensional Paper-Based Microfluidic Analytical Devices Integrated with a

Plasma Separation Membrane for the Detection of Biomarkers in Whole Blood," vol. 11, no. 40, pp. 36428–36434.

[59] B. Kim and S. Choi, "Smart Pipette and Microfluidic Pipette Tip for Blood Plasma Separation," vol. 12, no. 2, pp. 190–197.

[60] S. Vemulapati and D. Erickson, "Portable Resource-Independent Blood–Plasma Separator," vol. 91, no. 23, pp. 14824–14828.

[61] C. E. Nwankire, M. Czugala, R. Burger, K. J. Fraser, T. M. O'Connell, T. Glennon, B. E. Onwuliri, I. E. Nduaguibe, D. Diamond, and J. Ducrée, "A portable centrifugal analyser for liver function screening," vol. 56, pp. 352–358.

[62] A. J. Mach, J. H. Kim, A. Arshi, S. C. Hur, and D. Di Carlo, "Automated cellular sample preparation using a Centrifuge-on-a-Chip," vol. 11, no. 17, p. 2827.

[63] A. P. Wong, M. Gupta, S. S. Shevkoplyas, and G. M. Whitesides, "Egg beater as centrifuge: Isolating human blood plasma from whole blood in resource-poor settings," vol. 8, no. 12, pp. 2032–2037.

[64] J. Brown, L. Theis, L. Kerr, N. Zakhidova, K. O'Connor, M. Uthman, Z. M. Oden, and R. Richards-Kortum, "A Hand-Powered, Portable, Low-Cost Centrifuge for Diagnosing Anemia in Low-Resource Settings," vol. 85, no. 2, pp. 327–332.

[65] M. S. Bhamla, B. Benson, C. Chai, G. Katsikis, A. Johri, and M. Prakash, "Hand-powered ultralow-cost paper centrifuge," vol. 1, no. 1, pp. 1–7.

[66] "Microfluidic ChipShop."

[67] A. Liga, J. A. S. Morton, and M. Kersaudy-Kerhoas, "Safe and cost-effective rapid-prototyping of multilayer PMMA microfluidic devices," vol. 20, no. 12.

[68] B. S. Yilbas, "1 - Introduction," in *The Laser Cutting Process* (B. S. Yilbas, ed.), pp. 1–4, Elsevier.

[69] A. Liga, J. A. S. Morton, and M. Kersaudy-Kerhoas, "Safe and cost-effective rapid-prototyping of multilayer PMMA microfluidic devices," vol. 20, no. 12.

[70] "Properties of Plastics," in *Plastics Product Design*, pp. 11–30, John Wiley & Sons, Ltd.

[71] H. Duan, L. Zhang, and G. Chen, "Plasticizer-assisted bonding of poly(methyl methacrylate) microfluidic chips at low temperature," vol. 1217, no. 1, pp. 160–166.

[72] A. Ongaro, N. Howarth, V. La Carrubba, and M. Kersaudy-Kerhoas, "Rapid Prototyping for Micro-Engineering and Microfluidic Applications: Recycled PMMA, a Sustainable Substrate Material,"

[73] L.-M. Chi and W.-g. Wu, "Mechanism of hemolysis of red blood cell mediated by ethanol," vol. 1062, no. 1, pp. 46–50.

[74] O. V. Tyulina, M. J. Huentelman, V. D. Prokopieva, A. A. Boldyrev, and P. Johnson, "Does ethanol metabolism affect erythrocyte hemolysis?," vol. 1535, no. 1, pp. 69–77.

[75] A. Gebhardt and J.-S. Hötter, *Additive Manufacturing: 3D Printing for Prototyping and Manufacturing*. Carl Hanser Verlag GmbH & Co. KG.

[76] H. Gao, D. V. Kaweesa, J. Moore, and N. A. Meisel, "Investigating the Impact of Acetone Vapor Smoothing on the Strength and Elongation of Printed ABS Parts," vol. 69, no. 3, pp. 580–585.

[77] N. Zohdi and R. C. Yang, "Material Anisotropy in Additively Manufactured Polymers and Polymer Composites: A Review," vol. 13, no. 19, p. 3368.

[78] "Validating Isotropy in SLA 3D Printing."

[79] A. Bagheri and J. Jin, "Photopolymerization in 3D Printing," vol. 1, no. 4, pp. 593–611.

[80] S. Razavi Bazaz, N. Kashaninejad, S. Azadi, K. Patel, M. Asadnia, D. Jin, and M. Ebrahimi Warkiani, "Rapid Softlithography Using 3D-Printed Molds," vol. 4, no. 10, p. 1900425.

[81] S. C. Ligon, B. Husár, H. Wutzel, R. Holman, and R. Liska, "Strategies to Reduce Oxygen Inhibition in Photoinduced Polymerization," vol. 114, no. 1, pp. 557–589.

[82] H. Bruus, *Theoretical Microfluidics*. Oxford University Press, illustrated edition ed.

[83] M. Taylor, A. J. Urquhart, M. Zelzer, M. C. Davies, and M. R. Alexander, "Picoliter Water Contact Angle Measurement on Polymers," vol. 23, no. 13, pp. 6875–6878.

[84] J. Drelich, J. D. Miller, and R. J. Good, "The Effect of Drop (Bubble) Size on Advancing and Receding Contact Angles for Heterogeneous and Rough Solid Surfaces as Observed with Sessile-Drop and Captive-Bubble Techniques," vol. 179, no. 1, pp. 37–50.

[85] M. A. Galin, J. C. Salamone, A. P. Olson, and A. W. Tuberville, "Chemical effects of alkali on polymethylmethacrylate intraocular lenses," vol. 21, no. 2, pp. 354–357.

[86] L. A. Bosworth, W. Hu, Y. Shi, and S. H. Cartmell, "Enhancing Biocompatibility without Compromising Material Properties: An Optimised NaOH Treatment for Electrospun Polycaprolactone Fibres," vol. 2019, p. e4605092.

[87] S.-M. Choi, W.-K. Yang, Y.-W. Yoo, and W.-K. Lee, "Effect of surface modification on the in vitro calcium phosphate growth on the surface of poly(methyl methacrylate) and bioactivity," vol. 76, no. 1, pp. 326–333.

[88] V. Goodship and D. K. Jacobs, *Polyvinyl Alcohol: Materials, Processing and Applications*, vol. Vol.16. Smithers Rapra Technology.

[89] Y. Zhang, G. Ping, N. Kaji, M. Tokeshi, and Y. Baba, "Dynamic modification of poly(methyl methacrylate) chips using poly(vinyl alcohol) for glycosaminoglycan disaccharide isomer separation," vol. 28, no. 18, pp. 3308–3314.

[90] I. Shahzadi, M. Bashir, S. Bashir, and M. H. Inayat, "Thermally assisted coating of PVA for hydrophilic surface modification of PMMA microchannel for oil in water emulsion," in *2018 15th International Bhurban Conference on Applied Sciences and Technology (IBCAST)*, pp. 51–54.

[91] H. Yu, Z. Z. Chong, S. B. Tor, E. Liu, and N. H. Loh, "Low temperature and deformation-free bonding of PMMA microfluidic devices with stable hydrophilicity via oxygen plasma treatment and PVA coating," vol. 5, no. 11, pp. 8377–8388.

[92] T. Yoshida, M. Prudent, and A. D'Alessandro, "Red blood cell storage lesion: Causes and potential clinical consequences," vol. 17, no. 1, pp. 27–52.

[93] J. A. Sanders and W. W. Orrison, "Functional Magnetic Resonance Imaging," in *Functional Brain Imaging*, pp. 239–326, Elsevier.

[94] N. Adili, M. Melizi, and H. Belabbas, "Species determination using the red blood cells morphometry in domestic animals," vol. 9, no. 9, pp. 960–963.

[95] S. M. Nilapwar, M. Nardelli, H. V. Westerhoff, and M. Verma, "Chapter four - Absorption Spectroscopy," in *Methods in Enzymology* (D. Jameson, M. Verma, and H. V. Westerhoff, eds.), vol. 500 of *Methods in Systems Biology*, pp. 59–75, Academic Press.

[96] W. M. Allen, "A SIMPLE METHOD FOR ANALYZING COMPLICATED ABSORPTION CURVES, OF USE IN THE COLORIMETRIC DETERMINATION OF URINARY STEROIDS," vol. 10, no. 1, pp. 71–83.

[97] C. M. Cripps, "Rapid method for the estimation of plasma haemoglobin levels.," vol. 21, no. 1, pp. 110–112.

[98] R. A. Malinauskas, "Plasma Hemoglobin Measurement Techniques for the In Vitro Evaluation of Blood Damage Caused by Medical Devices," vol. 21, no. 12, pp. 1255–1267.

[99] E. Sollier, H. Rostaing, P. Pouteau, Y. Fouillet, and J.-L. Achard, "Passive microfluidic devices for plasma extraction from whole human blood," vol. 141, no. 2, pp. 617–624.

[100] V. VanDelinder and A. Groisman, "Separation of Plasma from Whole Human Blood in a Continuous Cross-Flow in a Molded Microfluidic Device," vol. 78, no. 11, pp. 3765–3771.

[101] D. A. Grosenbaugh, J. O. Alben, and W. W. Muir, "Absorbance Spectra of Inter-Species Hemoglobins in the Visible and Near Infrared Regions," vol. 7, no. 1, pp. 36–42.

[102] A. E. Jakus, "An Introduction to 3D Printing—Past, Present, and Future Promise," in *3D Printing in Orthopaedic Surgery*, pp. 1–15, Elsevier.

[103] R. W. Messler, "1 - INTRODUCTION TO INTEGRAL MECHANICAL ATTACHMENT," in *Integral Mechanical Attachment* (R. W. Messler, ed.), pp. 1–25, Butterworth-Heinemann.

[104] P. R. Bonenberger, *The First Snap-Fit Handbook: Creating and Managing Attachments for Plastics Parts*. Carl Hanser Verlag GmbH & Co. KG, 3 ed.

[105] R. W. Messler, "4 - ELASTIC INTEGRAL MECHANICAL ATTACHMENTS OR INTERLOCKS," in *Integral Mechanical Attachment* (R. W. Messler, ed.), pp. 103–142, Butterworth-Heinemann.

[106] "Snap Fits and Hinges," in *Plastics Product Design*, pp. 169–194, John Wiley & Sons, Ltd.

[107] E. Nader, S. Skinner, M. Romana, R. Fort, N. Lemonne, N. Guillot, A. Gauthier, S. Antoine-Jonville, C. Renoux, M.-D. Hardy-Dessources, E. Stauffer, P. Joly, Y. Bertrand, and P. Connes, "Blood Rheology: Key Parameters, Impact on Blood Flow, Role in Sickle Cell Disease and Effects of Exercise," vol. 10.

[108] Z. Onódi, C. Pelyhe, C. Terézia Nagy, G. B. Brenner, L. Almási, A. Kittel, M. Manček-Keber, P. Ferdinandy, E. I. Buzás, and Z. Giricz, "Isolation of High-Purity Extracellular Vesicles by the Combination of Iodixanol Density Gradient Ultracentrifugation and Bind-Elute Chromatography From Blood Plasma," vol. 9.

[109] E. Cheah, D. P. Tran, M. T. Amen, R. D. Arrua, E. F. Hilder, and B. Thierry, "Integrated Platform Addressing the Finger-Prick Blood Processing Challenges of Point-of-Care Electrical Biomarker Testing," vol. 94, no. 2, pp. 1256–1263.

[110] M. M. Hanon, A. Ghaly, L. Zsidai, Z. Szakál, I. Szabó, and L. Kátai, "Investigations of the Mechanical Properties of DLP 3D Printed Graphene/Resin Composites," vol. 18, no. 8, pp. 143–161.